Hydrodynamic analysis and numerical modelling of heave plates for floating wind turbines

Seung-Yoon Han

COLLEGE SCIENCES DOCTORAL DE L'INGENIERIE PAYS DE LA LOIRE ET DES SYSTEMES

CENTRALE NANTES

MÉMOIRE DE DOCTORAT DE

L'ÉCOLE CENTRALE DE NANTES

ÉCOLE DOCTORALE N° 602
Sciences de l'Ingénierie et des Systèmes
Spécialité : *Mécanique des Milieux Fluides*

Par
Seung-Yoon HAN

Hydrodynamic analysis and numerical modelling of heave plates for floating wind turbines

Projet de recherche doctoral présenté et soutenu à l'École Centrale de Nantes, le 2 Avril 2024
Unité de recherche : UMR 6598, Laboratoire de recherche en Hydrodynamique, Énergétique et Environnement Atmosphérique (LHEEA)

Rapporteurs avant soutenance :

Antonio SOUTO-IGLESIAS	Full professor, Universidad Politécnica de Madrid
Harry B. BINGHAM	Full professor, Technical University of Denmark

Composition du Jury :

Président :	Antonio SOUTO-IGLESIAS	Full professor, Universidad Politécnica de Madrid
Examinateurs :	Erin E. BACHYNSKI-POLIĆ	Full professor, Norwegian University of Science and Technology
	Harry B. BINGHAM	Full professor, Technical University of Denmark
Directeur de recherches doctorales :	David LE TOUZÉ	Professeur des universités, École Centrale de Nantes
Co-enc. de recherches doctorales :	Benjamin BOUSCASSE	Chargé de recherche, École Centrale de Nantes
	Vincent LEROY	Maître de Conférences, École Centrale de Nantes

ACKNOWLEDGEMENTS

This Ph.D. work has been carried out at Ecole Centrale Nantes (ECN) in the FLOAWER (FLOAting Wind Energy netwoRK) project. The project has received funding from the European Union's Horizon 2020 research and innovation programme under Marie Skolodowska-Curie grant agreement N°860879. Additional support was provided by the HP_Flow project in the WEAMEC framework (West Atlantic Marine Energy Community) and with funding from the Pays de la Loire Region (France) and European Regional Development Fund.

First and foremost, I would like to express my sincere gratitude to my supervisors, Prof. David Le Touzé, Dr. Benjamin Bouscasse, and Prof. Vincent Leroy. Their outstanding guidance and supervision throughout my Ph.D. study created a comfortable and competitive research environment. This environment allowed me to focus on my research subject with passion, dedication, and hard work, which led to significant development and growth in both work and life. I would also like to thank Dr. Jean-Christophe Gilloteaux for his initial supervision of the project.

I extend my sincere appreciation to committee members, Prof. Antonio Souto-Iglesias, Prof. Harry B. Bingham, and Prof. Erin E. Bachynski-Polić. Their effort in reviewing my thesis and providing valuable discussions on the experimental, theoretical, and numerical approaches were instrumental in shaping the final version of my thesis. Additionally, I am very grateful to Prof. Krish Thiagarajan Sharman for providing his insights into hydrodynamics on heave plates. Furthermore, I am very thankful to Dr. Riccardo Mariani for hosting and supervising me in the floating wind industry, BW-Ideol, and for collaborating with other experts.

I am deeply grateful to Prof. Sun Hong Kwon, Dr. Sime Malenica, and Dr. Ju Hyuck Choi for encouraging me to embark on this challenging and meaningful journey. I also appreciate the support of Prof. Young-Myung Choi and Dr. Young Jun Kim in helping me and my family settle well in Nantes. Their support has helped me stay motivated and complete my journey smoothly from start to finish.

I want to express my gratitude to all my colleagues in LHEEA for creating an inspiring and relaxing work environment. I am grateful for the friendship and cooperation of Dr. Shinwoong Kim, Dr. In-Chul Kim, Dr. Ruddy Kurnia, Gaspard Engel, Dr. Maxim Canard, Dr. Théo Descamps, Dr. Sithik Aliyar, Matthieu Tierno, and my fellow Ph.D. students. In addition, I am thankful to

Prof. Félicien Bonnefoy and Dr. Sylvain Delacroix for their invaluable assistance in conducting extensive test campaigns comprising thousands of test cases. I would also like to thank the tank testing team for their support in designing, preparing, and operating the model tests.

To my friends in the FLOAWER network, thank you for the incredible journey and discussion throughout these last three years. I am very fortunate to have the opportunity to do my Ph.D. alongside such a wonderful and intelligent group of people. In particular, I would like to thank Prof. Sandrine Aubrun and Florent Jubé for their coordination and management of the project. The dedicated training, dissemination, and outreach activities significantly contributed to developing my knowledge, network, technical, and soft skills.

Last but not least, I would like to express my love and gratitude to my wife, Hyun-Jee, and our daughter, Yoojoo. Your unwavering love and endless support have been the foundation of my Ph.D. journey in France. I also extend my warmest thanks to my family back in South Korea, especially my parents and parents-in-law, for their love and encouragement despite being far from home for more than three years.

CONTENTS

LIST OF FIGURES

LIST OF TABLES

CHAPTER 1

INTRODUCTION

1.1 Context of Ph.D. program

The main objective of this Ph.D. thesis is to obtain a thorough understanding of the physics involved in the flow, free surface, and hydrodynamic load behaviors around the submerged heave plates designed for floating offshore wind turbines. The second objective is to create a comprehensive hydrodynamic database using experimental and numerical methods. Finally, the study aims to identify the validity domain for the state-of-the-art engineering tools used to model heave plates and improve them based on the knowledge gained from the experimental and numerical analysis.

In the framework of “HP_Flow" project funded by WEAMEC (West Atlantic Marine Energy Community), an experimental campaign was conducted for various geometries, column-diameter/heave-plate diameter ratios, and drafts in the hydrodynamic and ocean engineering tank at Ecole Centrale Nantes. Numerical simulations were carried out with an in-house variant of OpenFOAM dedicated to wave-structure interaction through the coupling with accurate deterministic wave propagation solvers.

The Ph.D. research activities have been supported by the EU project FLOAWER (FLOAting WindEnergy nertwoRk). This project has received funding from the European Union’s Horizon H2020 research and innovation programme under the Marie Skłodowska-Curie grant agreement N° 860879. The FLOAWER project aims to train 13 early-stage researchers (ESRs) in the required multi-disciplinary engineering fields to better develop floating wind turbine (FWT) technologies under the constraint of minimizing the levelized cost of energy (LCOE). The program provided me with six leading-edge trainings addressing the state-of-the-art scientific and transversal needs of the FWT sector. Additionally, two secondments were completed during the study – one in the industrial partner BWIdeol and the other in academia at the Norwegian University of Science and Technology (NTNU). A list of research activities can be found in Appendix A.

1.2 Damping plate in floating platforms

Damping plates are used as appendages to the floating structure to suppress excessive motion responses. Their shape depends on the characteristics of the floater: bilge keels on ships, heave plates on floating offshore platforms, and skirts on buoys.

For ships, the roll motion is a key element in the design and the operation of ships in waves for the safety of crew and cargo. The bilge-keel is designed to increase viscous damping and reduce roll motion. The viscosity carries non-linearity and makes the roll damping estimation difficult. The damping can be predicted by experimental or numerical analysis and also by the empirical formula called the ITH method (Ikeda, Tanaka, and Himeno). Himeno (1981) summarized the damping predictions for conventional ships based on damping components, including hull friction, vortices, waves, lift, and bilge keel. The method can predict damping as a function of the amplitude and frequency of the roll motion and of the principal dimensions of the vessel with reasonable accuracy. ITTC (International Towing Tank Community, ITTC (2021)) selected this method as a recommendation. In engineering design tools, the method is practically used to estimate the ship roll damping for evaluating ship performance, such as seakeeping and maneuvering.

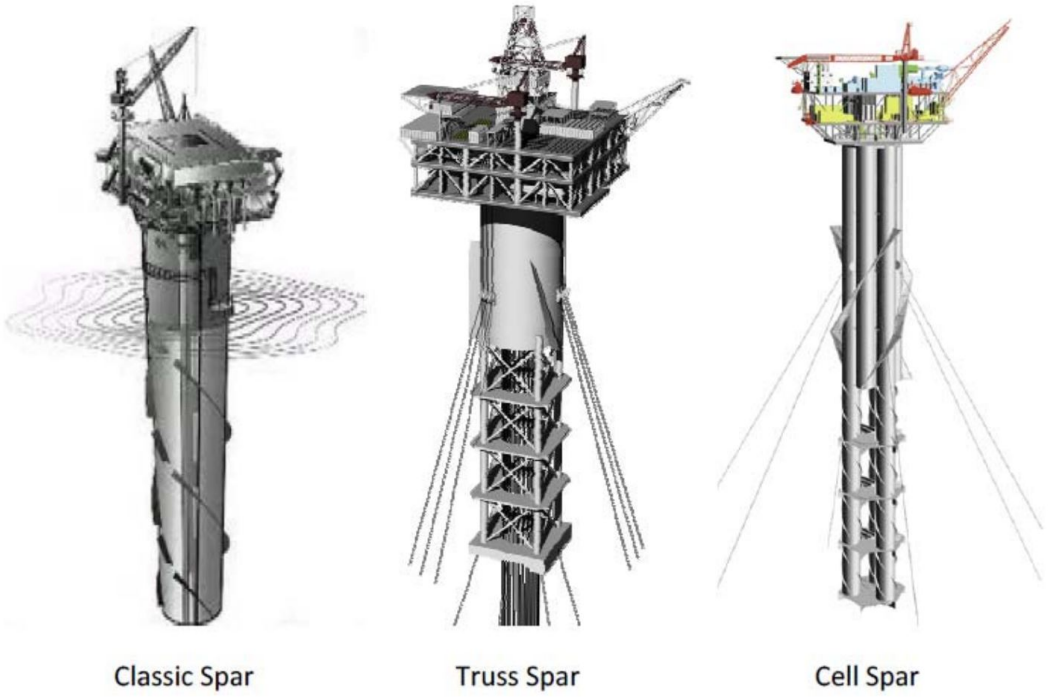

Figure 1.1 – Generations of the offshore spar platform (from Kurian et al. (2013))

With offshore platforms, the heave response induced by the nonlinear wave loads is one of the quantities of interest. This is especially important with Tension Leg Platforms (TLP) and classic Spar platforms, which have very small damping in heave. Haslum and Faltinsen (1999) presented the vulnerability of the classic Spar platform to heave resonance in waves and discussed alternative Spar shapes to increase damping and added mass. Thiagarajan and Troesch (1998) and Thiagarajan et al. (2002) noted the effects of adding a plate on the heave motion of the TLP and Spar, not only increasing the damping of the system but also shifting the resonant period from the dominant wave periods due to the added mass. This finding led to the transition in the design of the Spar platform from the classical Spar (single circular cylinder with constant cross section) to the truss spar (circular cylinder with truss and plates) or the cell spar (multiple circular cylinders with truss and plates) as shown in Figure 1.1. This is because the mass from the submerged draft can be substituted by the added mass from the plates.

Recently, heave plates have found widespread adoption in the design of the foundations of FWTs, as illustrated in Figure 1.2 from Roddier et al. (2010) and Choisnet Thomas (2013). These plates are typically assembled at the bottom of the floater. For semi-submersible floaters (Roddier et al. (2010); Lopez-Pavon et al. (2015); Pegalajar-Jurado et al. (2018); Robertson et al. (2020)), the heave plates have a larger diameter than the column. Meanwhile, barge-like floaters are equipped with small plates called skirts to reduce the heave, roll, and pitch motion responses.

(a) Windfloat, Roddier et al. (2010) **(b)** Floatgen, Choisnet Thomas (2013)

Figure 1.2 – Floating wind turbine substructures with heave plates

1.3 Modelization of heave plates in seakeeping analysis

A floating structure is an object that pierces an interface between the air and water, known as a free surface. It stays afloat due to the buoyancy force, corresponding to the amount of displaced fluid (as described by Archimedes' principle). When there are no environmental disturbances, the floating structure stays in an equilibrium position where the mass of the floating structure and buoyancy forces are balanced. However, when waves generated from far away reach the structure, they disrupt the fluid pressure and viscous effect around the structure, resulting in forces being exerted on the body. These forces cause the structure to respond by moving and vibrating, and the free surface deforms into a complex shape. The responses can be intricate and non-linear when the waves are large and steep. Moreover, the responses affect the surrounding fluid, causing friction and generating vortices.

The complex nonlinear interactions between fluids and floating bodies are studied in the seakeeping theory. Historically, solving Navier-Stokes equations with the free surface was unaffordable. The problem is simplified by assuming an incompressible, inviscid fluid and irrotational flow named potential flow. It is then solved at a given order of non-linearity, deduced using Taylor series expansions and Stokes perturbation series based on the wave steepness and relative body motion amplitude. The forces induced by the waves and motions are decomposed into components supposedly superimposable (e.g., diffraction and radiation). Then, the body motion $\mathbf{x}$ can be solved using the following equation of motions expressed in the equilibrium position:

$$(m+A)\,\ddot{\mathbf{x}} + B\dot{\mathbf{x}} + C\mathbf{x} = \mathbf{f}_{wave} \tag{1.1}$$

where m is the mass of the floating system and C is a restoring coefficient. A, B, and $\mathbf{f}_{wave}$ are hydrodynamic coefficients, which refer to added mass, damping and wave excitation force coefficients, respectively. These hydrodynamic coefficients are necessary to solve the equation of motion. While the mass and restoring coefficients can be calculated geometrically, obtaining hydrodynamic coefficients requires additional efforts, such as using boundary element method (BEM) solvers and analytical methods (e.g., McCamy and Fuchs (1954)).

For most seakeeping problems, potential flow theory is affordable to achieve appropriate accuracy of these coefficients for engineering purposes of evaluating loads and responses efficiently to cover the whole design scenarios (ultimate design state, fatigue limit state, serviceability limit state, see Bureau Veritas Rule Note (NI572)). Therefore, the engineering design tools are mostly based on potential flow theory which requires first the evaluation of linear hydrodynamic coefficients involving wave excitation forces, added mass and damping. As

the linear hydrodynamic coefficients are obtained by neglecting non-linear and viscous effects, some tuning on these coefficients and additional terms are needed for common engineering practices. This is particularly important in some cases, for example, when the floater is equipped with heave plates (or bilge keel, skirts).

Modelling heave plates in engineering design tools remains a challenging task. The reason behind this is that the engineering models require tuning by retrieving hydrodynamic coefficients from experiments or numerical simulations that solve the Navier-Stokes equations. These experiments and simulations focus on extracting the hydrodynamic coefficients, which divide the entire physical fluid-structure interaction problem into subproblems: hydrodynamic loads in oscillatory flows and wave excitation loads on the fixed body.

Extensive experimental studies helped accumulate some physical understanding of the hydrodynamic loads on heave plates in various engineering configurations, from classical offshore platforms to floating wind turbines (see Table 1.1). The characteristics of motion response and plate geometries were adapted based on the type of floaters. Most of the studies employed the forced oscillation technique in calm water to measure the hydrodynamic loads and provided the added mass and damping (or drag) coefficients with a focus on the heave motion.

Table 1.1 – Previous experimental studies on floating structures with heave plates

Author(s)	Floater type	Technique	Type of motion	Configuration
Thiagarajan and Troesch (1998)	Offshore platform	Forced[1]	Heave	Column with plate
Cozijn et al. (2005)	CALM buoy	Forced	Surge, Heave, Pitch	Column with plate
Tao and Dray (2008)	Offshore platform	Forced	Heave	Isolated plate
Molin et al. (2007)	Subsea equipment	Forced	Heave	Isolated plate
Wadhwa and Thiagarajan (2009)	Subsea equipment	Forced	Heave	Isolated plate
Sudhakar and Nallayarasu (2011)	Offshore platform	Free[2]	Heave, Pitch	Column with plate
An and Faltinsen (2013)	Subsea equipment	Forced	Heave	Isolated plate
Li et al. (2013)	Offshore platform	Forced	Heave	Isolated plate
Lopez-Pavon and Souto-Iglesias (2015)	FWT	Forced	Heave	Column with plate
Tian et al. (2017)	Offshore platform	Forced	Heave	Isolated plate
Zhu and Lim (2017)	FWT	Forced , free	Heave	Column with plate
Zhang and Ishihara (2018)	FWT	Forced	Heave	Column with multiple plates
Thiagarajan and Moreno (2020)	FWT	Forced	Heave	Column with plate
Robertson et al. (2020)	FWT	Forced , free	Surge, heave, pitch	Full substructure
Abazari et al. (2021)	General offshore	Forced	Heave	Isolated plate
Zhang et al. (2023)	FWT	Forced	Heave	Column with plate

[1]Forced oscillation tests, [2]Free decay tests

1.4 Hydrodynamic loads on plates in oscillatory flow

In the seakeeping problem, the hydrodynamic loads in oscillatory flow are identified as added mass and damping components, described in Faltinsen (1990). In general, these hydrodynamic coefficients can be obtained from free decay and forced oscillation tests in still water. With free decay tests, the added mass and damping coefficients can be extracted at the natural period from the time series of motion response. On the other hand, with forced oscillation tests, the coefficients can be acquired for all the periods of interest (e.g., wave excitation periods). Heave plate hydrodynamic properties in the literature are generally driven by the surrounding flow characteristics. The flow is usually defined by two non-dimensional parameters.

1.4.1 Flow parameters

The effects of heave plates on hydrodynamic loads have been explored with two categories of governing parameters: flow parameters and geometry parameters. The flow is mainly oscillatory around the plate, so the Keulegan-Carpenter number (KC) and the frequency parameter (β) are typically selected as flow parameters to investigate their influence on the hydrodynamics loads, especially with the heave motion. They are defined as:

$$KC = \frac{2\pi\xi}{D_d}, \qquad \beta = \frac{(D_d)^2 f}{\nu} \tag{1.2}$$

where ξ and f are the amplitude and frequency of the motion of interest, D_d is the diameter of the plate, and ν is the kinematic viscosity of the fluid.

Graham (1980) studied the force induced by flow separation and vortex shedding on a sharp-edged cylinder in oscillatory flow based on the discrete vortex method. It was shown that the forces are proportional to KC in the low KC number regime ($KC < 1$). Details of the flow behavior in the low KC regime of the oscillating plate are presented in Tao and Thiagarajan (2003b). Three different vortex shedding regimes were observed with their numerical model, visually identified as independent, interactive and uni-directional vortex shedding, depending on the KC number.

Low KC numbers were considered in these previous studies of oscillating flat plates. This is reasonable for TLPs and Spar platforms, which have a moderate heave response in ocean waves owing to their mooring system or large draughts. However, when considering a monohull floater with a large water plane area, such as a barge or a semi-submersible platform in extreme

sea states, the KC number should be increased. For KC numbers ranging in $0.15 \leq KC \leq 3.15$, Tian et al. (2017) provided experimentally hydrodynamic characteristics for various geometries. In addition, Thiagarajan and Moreno (2020) introduced a relative KC number, $KC_{rel} = \frac{2\pi A_{rel}}{D_d}$, to describe the wave effects on the hydrodynamic coefficients, where A_{rel} is a relative amplitude of motion with respect to a wave elevation.

The second flow parameter, the frequency parameter β, is shown to have a smaller influence on the hydrodynamic coefficients than the KC number when the plate is deeply submerged (An and Faltinsen (2013); Lopez-Pavon and Souto-Iglesias (2015)). In shallow draft condition, Molin et al. (2007) carried out tank testing with an isolated plate with 5 cm immersion, corresponding to a submerged depth to the plate diameter ratio of 0.08. The experimental measurements showed that the hydrodynamic coefficients depend on the frequency in that case. Especially in short motion periods, numerical models based on potential flow estimate the added mass and damping well. They observed that the added mass is negative over the lower periods from both the numerics and the measurements. An and Faltinsen (2013) also determined in their experimental and numerical study that the drag coefficients of the solid and perforated plates are largely affected by the free surface.

1.4.2 Heave plate geometry and layout

Several geometric configurations have been investigated for an isolated plate, and with the addition of a column. Tian et al. (2017) experimentally investigated the influence of the plate thickness ratio (t_d/D_d with the plate thickness, t_d) on the added mass and damping. They found a critical ratio defining thin and thick plates based on the relationship between the thickness ratio and the hydrodynamic coefficients. The influence of the edge corner shape was also studied in (Li et al. (2013); Tian et al. (2017)). It shows that the plates with sharp edges could provide more added mass than the plates with rounded and triangular corners. Meanwhile, the damping is almost independent of the shape, at least for $KC < 1.0$. Lopez-Pavon and Souto-Iglesias (2015) studied the influence of the reinforced plate on the hydrodynamic coefficient by adding a vertical flap at the edge. As a result, it was found that the hydrodynamic damping was significantly decreased due to the reduction of the vortex on the reinforced plates.

Perforated plates were proposed to improve the hydrodynamic performances by Downie et al. (2000). The perforation ratio of the disk, τ, was investigated by forced heave oscillation model tests with isolated plates in Tao and Dray (2008). From the results, the disks with porosity were found to produce less added mass and more damping. At very low KC, a significant increase in damping is observed by making the heave plate porous. An and Faltinsen (2013)

proposed a numerical model and showed that when the KC number is small, the damping is primarily caused by the flow through perforated openings. However, with a large KC, the flow separating from the outer edge of the plate dominates the hydrodynamic damping. Tian et al. (2017) presented that the damping of the perforated plate is larger than the solid plate one at low KC but found the opposite at large KC. On the other hand, the perforated plates produce lower added mass than the solid ones at all KC numbers. Furthermore, it was found that the perforated hole size is not significant for the hydrodynamic coefficients.

The influences of free surface and seabed effects on the added mass and damping coefficients were studied using experiments (Wadhwa and Thiagarajan (2009); Wadhwa et al. (2010)). In the experiments, an isolated plate in forced oscillation was considered with different geometric ratios (h/D_d and d/D_d, where h is the elevation from the seabed and d is the draft of the plate. The added mass and damping coefficients were found to increase with the proximity to the boundary (seabed and free surface). Furthermore, a critical KC value was found where the linear trend of the coefficients with KC is broken even in the low KC number. Numerical simulations by Garrido-Mendoza et al. (2014, 2015) followed, and the numerical results presented a similar behavior to the experiments. It was found that the effect of the free surface on the damping is more dominant than that of the seabed at the same distance ratio ($h/D_d = d/D_d$). In the case of shallow draft, the drag coefficients of the solid and perforated plate are greatly affected by the free surface (An and Faltinsen (2013)).

In actual engineering applications, the heave plate is necessarily connected to the platform and often to a column, and this influences the flow. The effect of the diameter ratio (heave plate diameter over column diameter, D_c) on the added mass and damping was presented by Thiagarajan et al. (2002) for $D_d/D_c = 1.0, 1.1, 1.2$ and 1.3. From the experimental and numerical results, the added mass and damping normalized with, respectively, the displaced mass of the model and the critical damping, increase with the disk diameter ratio as $(D_d/D_c)^3$ for the added mass and $(D_d/D_c)^2$ for the damping. Recently, Zhang et al. (2023) carried out forced oscillation tests in a calm water tank with different diameter ratios ranging from 1.5 to 2.5. It confirms that the added mass and damping are dependent on the diameter ratio. According to the theoretical added mass formulation proposed by Tao et al. (2007), the non-dimensional added mass and damping decrease with the diameter ratio at a given heave amplitude.

1.4.3 Hydrodynamic coefficients of heave plates

Empirical formulas for the added mass are summarized in Table 1.2. Sarpkaya (2010) introduced the theoretical form of the added mass for an isolated plate, which is equivalent to the mass of an ellipsoid of water around the plate. The added mass of a single heave plate attached at the bottom of a cylinder was presented based on a theoretical approach in Tao et al. (2007), by neglecting the contribution of the cylinder. These two formulas show that heave added mass is highly dependent on geometry. Later, Zhang and Ishihara (2018) proposed a correction factor and introduction of the cross-sectional shape parameter of the heave plate using Large Eddy Simulations. The formula of Tao et al. (2007) was modified to refine the added mass definition as a function of KC.

Table 1.2 – Formulations of added mass for heaving plates

Configuration	Section	Added mass	Reference
Isolated heave plate	Cir.	$A_{33} = \frac{1}{3}\rho D_d^3$	Sarpkaya (2010)
A cylinder with heave plate	Cir.	$A_{33} = \frac{1}{12}\rho(2D_d^3 + 3\pi D_d^2 z - \pi^3 z^3 - 3\pi D_c^2 z), \quad z = \frac{1}{\pi}\sqrt{D_d^2 - D_c^2}$	Tao et al. (2007)
	Cir., Oct., Rec.	$A_{33} = f_{r1}\left(k^3 - \frac{1}{4}\left[3r_d^2\sqrt{k^2 - r_d^2} + \left(k - \sqrt{k^2 - r_d^2}\right)^2\left(2k + \sqrt{k^2 - r_d^2}\right)\right]\right)$, $k = k_1 \cdot k_2, \quad k_1 = 1 + 0.2KC, \quad k_2 = \begin{cases} 1.00; & \text{Circular heave plate} \\ 0.95; & \text{Octagonal heave plate} \\ 0.75; & \text{Square heave plate} \end{cases}$ $f_{r1} = \frac{1}{3}\rho D_d^3$	Zhang and Ishihara (2018)

• Note: Cir., Oct., Rec. are the circular, octagonal, and rectangular cross section of plate, respectively.

Thiagarajan and Troesch (1994, 1998) showed that the heave damping coefficient is composed of friction and form drag from their experiments. The friction drag refers to the damping due to the shear stress over the body's wet surface and is dominant at very low KC numbers, depending on the viscosity. On the other hand, the form drag refers to the damping due to the normal stress over the wet surface, which is induced by flow separation and vortex shedding at the edges. This type of damping shows a linear trend with large KC numbers.

In the study by Graham (1980), the form drag coefficient was demonstrated theoretically for a two-dimensional isolated edge in oscillatory flow. The equation for the coefficient is given in Table 1.3. Tao and Thiagarajan (2003a) adjusted this equation to predict the drag on a cylinder with a heave plate based on the characteristics of the vortex shedding regimes. Zhang and Ishihara (2018) improved this formula by performing numerical simulations. They proposed drag coefficients as functions of the aspect ratio ($r_t = t_d/D_d$), KC number, and shape correction factors for circular, octagonal, and square cross sections. The drag coefficient for a single heave plate configuration is bounded by 12 based on experimental studies by Lopez-Pavon and Souto-Iglesias (2015). It is worth noting that the drag is obtained from the equivalent damping.

Table 1.3 – Formulations of drag coefficient for heaving plates

Configuration	Section	Drag coefficient	Reference
Isolated heave plate	Cir.	$C_d = A(KC)^n$ $A = \begin{cases} 11.8 \\ 5.7 \end{cases}, n = \begin{cases} -1/3 & \text{for flat plate} \\ 0 & \text{for diamond cylinder} \end{cases}$	Graham (1980)
A cylinder with heave plate	Cir.	$C_d = A(KC)^n$ $A = \begin{cases} 0.15 \\ 2.5 \\ 4.0 \end{cases}, n = \begin{cases} -3/4 & \text{for independent vortex shedding} \\ -1/5 & \text{for interactive vortex shedding} \\ -1/4 & \text{for uni-directional vortex shedding} \end{cases}$	Tao and Thiagarajan (2003a)
	Cir., Oct., Rec.	$C_d = min\left\{1.7 r_t^{-1/3.7} (KC)^{-1/k_3}, 12\right\}$ $k_3 = \begin{cases} 2.5 & \text{for circular heave plate} \\ 2.5 & \text{for octagonal heave plate} \\ 3.0 & \text{for square heave plate} \end{cases}$	Zhang and Ishihara (2018)

1.5 Wave excitation loads

Predicting the wave loads exerted on an FWT is necessary for the design of the substructure, mooring lines, and power cables. The loads significantly influence the dynamic response of the FWT system, potentially leading to extreme responses, drift motions, and vibrations due to system resonance. Therefore, accurately evaluating the wave loads acting on FWTs is crucial for designing systems that can operate robustly for production in harsh offshore environments throughout their design life.

The wave loads in ocean engineering are commonly categorized into three different frequency regimes (DNV-RP-C205 (2010)): wave frequency (WF), low frequency (LF), and high frequency (HF). The dominant contribution to the wave loads comes from the wave frequency regime, where the waves carry most of their energy. Accordingly, the design of the FWT systems aims to avoid having their natural frequencies fall within the wave frequency range by adjusting their natural frequencies to be lower or higher than the wave frequencies.

Nonlinear wave-wave and wave-body interactions result in low- and high-frequency wave loads, which become more prominent with higher wave nonlinearity. Although the wave loads at low and high-frequency regimes are comparatively smaller than those at the wave frequency regime, they are still critical factors to consider in engineering, such as station-keeping and fatigue assessment, because of their ability to trigger resonant behavior. Specifically, the low-frequency wave loads are known as “mean drift loads" or “slowly varying drift loads," which can cause significant horizontal and vertical motions of moored structures. On the other hand, the high-frequency wave loads can excite high-frequency resonant responses of stiff systems (e.g., tendons of tension leg platforms), commonly referred to as “ringing" in the transient state and “springing" in the steady state as described in Molin (2023).

The wave loads on a fixed body can be evaluated using a diffraction theory based on the potential flow hypothesis. This approach does not take into account the contribution of the motion response to the wave load. The loads are decomposed into the zeroth-, first-, second-, and higher-order components by using the perturbation series with respect to the wave steepness parameter ($\varepsilon = k_0 A$ with wavenumber, k_0, and wave amplitude, A). Analytical solutions can be found for a fixed vertical circular cylinder. For the first-order wave loads, McCamy and Fuchs (1954) and Garrett (1971) solved the linear diffraction problem on bottom-mounted and truncated cylinders. The theory was extended by Kim and Yue (1989) to the pure second-order wave loads on the truncated cylinder in regular waves. Kim and Yue (1990) presented the second-order sum- and difference-frequency loads using an interaction of two wave frequency

components called bichromatic waves. Furthermore, Malenica and Molin (1995) presented a complete third-order wave load theory on the bottom-mounted vertical cylinder to investigate the ringing phenomenon. Faltinsen et al. (1995) introduced the FNV (Faltinsen, Newman and Vinje) method to compute the higher-order wave loads.

Dedicated wave tank testing campaigns were conducted to study the linear and nonlinear wave loads acting on a fixed model in regular waves with angular frequency $\omega = 2\pi/T$ where T is the wave period. The loads measured by a force transducer are interpreted using Fourier analysis, resulting in obtaining the harmonic components (0^{th}, ω, 2ω, 3ω, ...), and compared with the corresponding order of nonlinearity from the potential flow theory. For instance, Mavrakos and Grigoropoulos (1994) presented the horizontal wave forces and moments on a truncated cylinder obtained using Fast Fourier Transform (FFT). The higher harmonics of the wave loads (up to the fifth harmonic) obtained by the Fourier transform were reported by Boo (2006) for the truncated cylinder and by Kristiansen and Faltinsen (2017) for the bottom-mounted cylinder. Both considered various wave steepnesses and compared the harmonics with the corresponding orders computed by the FNV method.

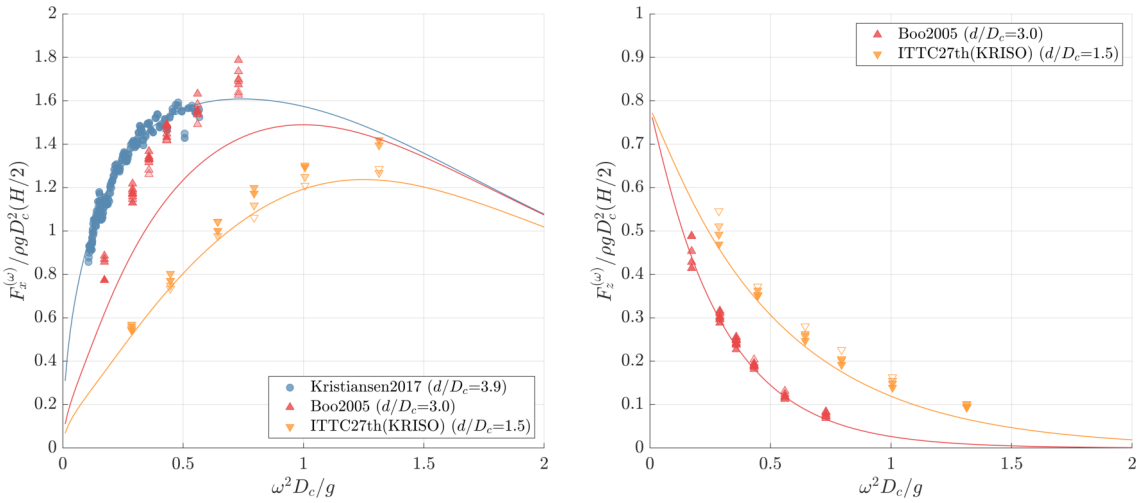

(a) Horizontal wave forces **(b)** Vertical wave forces

Figure 1.3 – Nondimensional first harmonics of horizontal and vertical wave forces on a vertical circular cylinder in the literature. Lines are the results using the linear potential theory.

Figure 1.3 presents the first-order hydrodynamic loads on the vertical circular cylinder in the literature. It is worth noting that the literature mainly concentrates on horizontal wave forces with only limited discussion on vertical forces. The wave loads are given as a function of the non-dimensional wave frequency $\omega^2 D_c/g$. The draft ratio d/D_c represents the

cylinder configurations for both bottom-mounted and truncated cylinders. In general, the first harmonic wave loads, non-dimensionalized as $F^{(\omega)}/\rho g D_c^2(H/2)$, are described well by the linear potential flow theory (McCamy and Fuchs (1954); Garrett (1971)), which evaluates the forces analytically.

Besides, the slowly varying drift forces, which are in the low-frequency regime, can also be measured by generating bichromatic waves in the wave tank. Fonseca et al. (2011) carried out experiments with a fixed buoy in monochromatic and bichromatic waves. The wave loads were reported as the first harmonics of two wave components (ω_1, ω_2) as well as the difference frequency component, $\omega_1 - \omega_2$. The harmonic components were obtained by standard Fourier analysis as well as by the least-square methods using second harmonic approximation.

These theoretical and experimental methods have been extensively used in many applications to estimate the wave loads acting on floating wind turbines. In particular, numerous engineering models are time-domain solvers relying on a hydrodynamic database calculated using linear potential flow theory. However, engineering models have difficulties in modelling the heave plates of a floater and often require calibration of hydrodynamic coefficients based on experimental data or computational fluid dynamic (CFD) simulations. Despite these efforts, the models tend to underpredict the nonlinear wave loads, as reported in Lopez-Pavon et al. (2015); Simos et al. (2018); Robertson et al. (2017, 2020); Robertson and Wang (2021); Fonseca et al. (2022). Therefore, further research is needed to understand better the wave loads on floating wind turbines equipped with heave plates.

1.6 Contributions of the present work

This study aims to investigate the hydrodynamic loads exerted on heave plates during typical waves and motions. The study focuses on the design characteristics of floating wind turbines, which differ from conventional offshore structures. Compared to conventional platforms, the floating substructures of FWTs have a lower submerged depth and a larger motion response, resulting in the heave plate being positioned closer to the free surface. Therefore, the study examines various heave plate diameters, considering the free surface proximity across a wide range of flow parameters.

The hydrodynamic loads are examined with three approaches at different levels of fidelity: potential flow theory, computational fluid dynamics (CFD), and physical wave tank testing. Through the different approaches, it has been concluded that the presence of a heave plate significantly affects wave excitation loads. Furthermore, the motion parameters and

geometrical characteristics of the plate affect the hydrodynamic load. The following specific contributions are achieved from the present study.

Potential flow theory (low-fidelity model): An analytical method has been developed for the robust modelling of heave plates using potential flow theory. The method presents generalized first-order analytical solutions for a truncated circular cylinder with a heave plate mounted at the bottom. The solutions cover the linear diffraction and radiation of water wave problems, including surge, heave, and pitch motions. The numerical modelling of the heave plate has also been studied using the Boundary Element Method (BEM) solvers HydroStar (Bureau Veritas (2020)) and Nemoh (Kurnia and Ducrozet (2023)). The hydrodynamic loads on thin and thick heave plate configurations are verified using the analytical solutions. The validity region of the potential flow theory is identified in comparison with the experiments done during the "HP_Flow" project under various submergence conditions.

CFD methods (medium and high-fidelity model): A Navier-Stokes equation solver (CFD) is validated with the experimental data of the HiPRWind project (Lopez-Pavon and Souto-Iglesias (2015); Anglada-Revenga et al. (2020)), compared in terms of flow around the heave plate and hydrodynamic loads. The results show that using the turbulence model ($k-\omega$ SST) permits to get a flow behavior around the heave plate in good agreement with PIV tests (Anglada-Revenga et al. (2020)). Numerical simulations of a fixed truncated cylinder with a heave plate in regular waves are then performed, which are in good agreement with the present experimental measurements. The simulations revealed that the waves induce strong flow separation around the plate edge. Additionally, drag coefficients are obtained based on the results of the simulations.

Experiments (high-fidelity model): Dedicated experiments are performed with varying drafts and diameters of the plate, as well as motion amplitudes and frequencies, to account for the diversity of FWT designs. A detailed experimental setup is introduced toward achieving a high-fidelity hydrodynamic database, including added mass, damping and wave loads. An extensive experimental campaign is conducted in two configurations: a fixed model with incident waves and a forced oscillating model in calm water. Heave plate effects on the loads are studied as a function of flow parameters, including the amplitude and frequency of the waves and motions. Five different plate configurations, including a perforated plate, are tested to investigate the influence of the geometry on the loads. Additionally, the study examines the

proximity of the heave plate to the free surface by considering different submerged depths. As a result, the experimental outcomes can be stressed as (1) wave diffraction loads at deep and shallow drafts and (2) added mass and damping at different submerged depths.

1.7 Thesis outlines

Chapter 1. Introduction This chapter presents an overview of studies regarding hydrodynamic loads on heave plates. Applications of the plates in floating offshore industries are introduced to reduce dynamic responses by enhancing the hydrodynamic added mass and damping. The physical analysis of the oscillating plate flow in the literature is introduced. The main contributions of the present research to the scientific community are highlighted.

Chapter 2. Theoretical background This chapter describes the theoretical framework used in the present study. It covers the equations of motion, which mainly focus on wave-structure interaction. The force components, including inertia, gravity, constraints and fluid loads, are defined in this chapter. In particular, the fluid loads are modeled based on the viscous flow and potential flow models. The physical interpretations of the added mass and damping are derived based on the energy equations.

Note: Each chapter below is written as a "quasi-stand alone" dedicated to a single scientific topic, isolated and concentrated based on published and submitted papers listed in Appendix A.

Chapter 3. Development of analytical methods This chapter introduces the first-order analytical theory on a truncated vertical circular cylinder with a circular plate to solve linear wave diffraction/radiation problems. The domain decomposition method is employed based on small wave and motion amplitudes hypothesis. Linearized velocity potentials are derived in each subdomain and matched on subdomain interfaces employing pressure and normal velocity continuity. The analytical expressions of physical quantities are provided for the first-order hydrodynamic loads as well as the mean drift forces and wave elevations.

Chapter 4. Validation of numerical models for heave plates Numerical modelling of the heave plate is discussed in this chapter. The analytical and numerical modelling of thick and thin heave plates is verified using the Boundary Element Method (BEM). Modelling the thin plate is further studied using CFD methods. The use of the turbulence model is validated with

the experiments in terms of flow velocity and hydrodynamic loads including added mass and damping.

Chapter 5. Experimental designs and setup This chapter provides an overview of the experimental designs and setups considered in the experimental project "HP Flow", funded by WEAMEC. The chapter includes a detailed introduction to the experimental setup, which covers the captive system, model configurations, and acquisition systems. Additionally, the chapter describes preliminary tests performed to prepare for the experimental measurements, including wave calibrations, hammer tests, and the estimation of the inertia matrix of the model.

Chapter 6. Wave diffraction loads on a circular cylinder with a heave plate In this chapter, the results of experimental measurements on wave diffraction loads at deep and shallow submerged depths are presented. The study provides information on the horizontal and vertical wave forces acting on a vertical and surface-piercing circular cylinder with a heave plate under monochromatic and bichromatic waves. The research examines the impact of the heave plate on the force time histories and the representative harmonics at different frequency components such as the zeroth-, first-, second-, sum-, and difference-frequency components. To support the experimental campaign up to the second-order computation, the study employs the BEM solver (HydroStar). Furthermore, dedicated CFD simulations are performed to visualize the flow around the heave plates. The study also introduces a simplified approach based on Morison's equation to model the flow separation effects as the viscous drag forces.

Chapter 7. Hydrodynamic loads on an oscillating circular cylinder with a heave plate This chapter presents the results of hydrodynamic loads for surge, heave, and pitch oscillations of a vertical and surface-piercing circular cylinder with a heave plate. The hydrodynamic loads are obtained by subtracting the inertia, gravity, and linear hydrostatic loads from the measured loads by a six-component force transducer. Harmonic components of the loads are investigated. The first harmonics of the measured force are interpreted into added mass and damping coefficients. The coefficients are investigated with the flow parameters (motion amplitude and frequency) and heave-plate characteristics, including plate diameter, porosity, and the proximity of the free surface.

Chapter 8. Conclusions This chapter summarizes the main findings and contributions of the present study to the scientific and floating wind turbine communities.

CHAPTER 2

THEORETICAL BACKGROUND

In this chapter, we discuss the theoretical framework employed in the present study. The chapter primarily focuses on the equations of motion, specifically on wave-structure interaction. The force components, including inertia, gravity, constraint, and fluid loads, are defined. A detailed explanation of fluid loads models based on the viscous flow and potential flow models is presented.

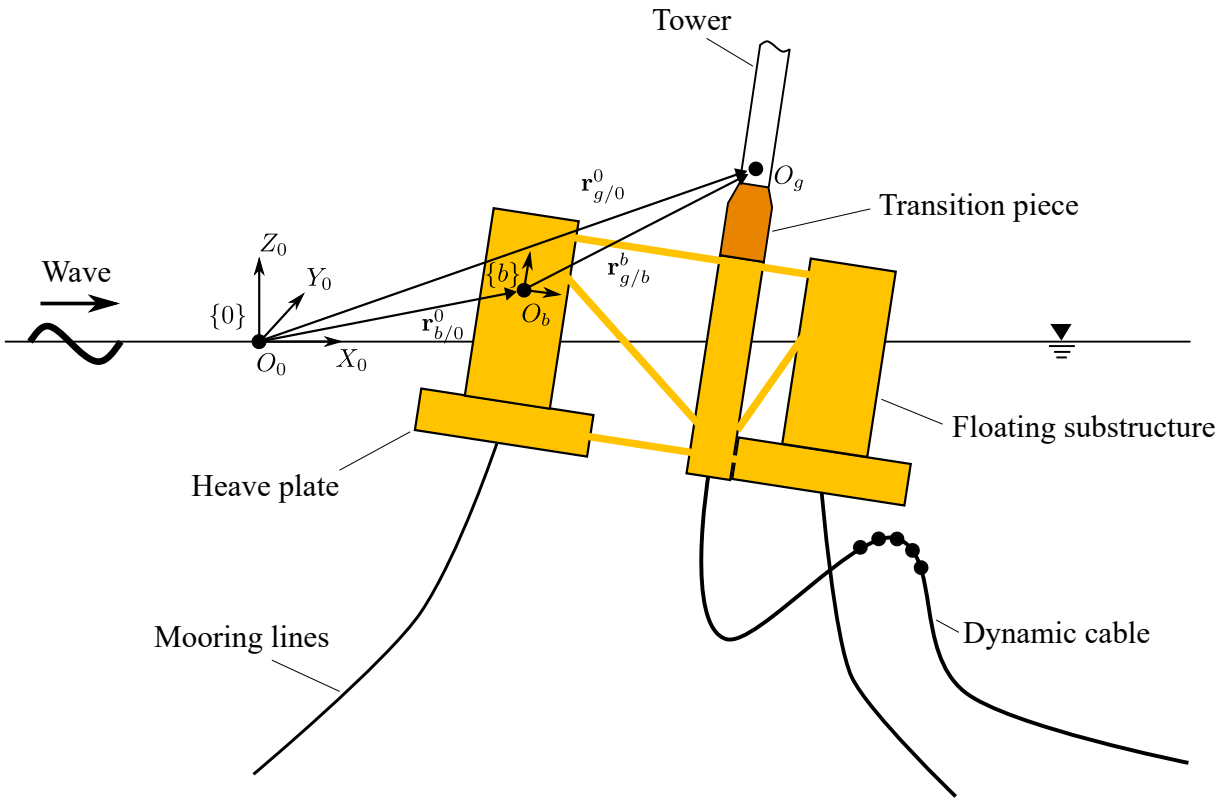

Figure 2.1 – Description of reference frames for the floating wind turbine substructure.

2.1 Rigid body kinetics for floating structures

An example of a semi-submersible type of substructure for floating wind turbines is illustrated in Figure 2.1. The superstructures, including the blade and turbine, are omitted to focus on wave-structure interaction. Note that the superstructure is connected to the substructure via a transition piece. The floating substructure is moored by steel chains or synthetic fiber for station keeping. The dynamic cable is connected to the floater to transmit the electricity produced by the wind turbine to the power substation. Waves are considered to be the only environmental load on structures.

To describe the rigid body response of the substructure, two reference frames are introduced:

- The Galilean reference frame, denoted as $\{0\}$, is defined with the axes $(\mathbf{X}_0, \mathbf{Y}_0, \mathbf{Z}_0)$. The origin, O_0, of the reference system is fixed to the Earth. Here, we define O_0 as the initial position of the body located on the free surface at rest before perturbation due to waves.
- The body-fixed reference frame $\{b\}$ is a moving coordinate frame with axes $(\mathbf{X}_b, \mathbf{Y}_b, \mathbf{Z}_b)$. The origin O_b is fixed on the moving body.

The rotation matrix $R_b^0(\Theta_{nb})$ from $\{b\}$ to $\{0\}$ is introduced with Tait-Bryan angles (Yaw ψ, Pitch θ, and Roll ϕ) where $\Theta_{nb} = [\phi, \theta, \psi]^T$ is the angle between the two reference frames $\{0\}$ and $\{b\}$:

$$R_b^0 = \begin{bmatrix} \cos\psi\cos\theta & -\sin\psi\cos\phi + \cos\psi\sin\theta\sin\phi & \sin\psi\sin\phi + \cos\psi\cos\phi\sin\theta \\ \sin\psi\cos\theta & \cos\psi\cos\phi + \sin\phi\sin\theta\sin\psi & -\cos\psi\sin\phi + \sin\phi\cos\phi\sin\theta \\ -\sin\theta & \cos\theta\sin\phi & \cos\theta\cos\phi \end{bmatrix} \tag{2.1}$$

Note that the rotation matrix from $\{0\}$ to $\{b\}$ can be obtained from the inverse transformation $R_0^b(\Theta_{0b}) = R_b^0(\Theta_{0b})^{-1}$.

Following the notation expressed in Fossen (2011), the position of the floater can be described with the following vectors:

- $\mathbf{r}_{b/0}^0$ is the vector from O_0 to O_b expressed in the Galilean reference frame.
- $\mathbf{r}_{G/0}^0$ is the vector from O_0 to O_G expressed in the Galilean reference frame. where O_G is the center of gravity fixed on the body.
- $\mathbf{r}_{G/b}^b$ is the vector from O_G to O_b expressed in the body-fixed reference frame. The distance of $\mathbf{r}_{G/b}^b$ is constant from the hypothesis of the rigid body.

2.1.1 Equations of rigid body motion

The equations of motion at the origin of the body-fixed reference frame are derived from the Newton-Euler equations (see Fossen (2011)):

$$\begin{aligned} m\left(\frac{d\mathbf{V}_{b/0}^{b}}{dt}+\boldsymbol{\omega}_{b/0}^{b}\times\mathbf{V}_{b/0}^{b}+\frac{d\boldsymbol{\omega}_{b/0}^{b}}{dt}\times\mathbf{r}_{G/b}^{b}+\boldsymbol{\omega}_{b/0}^{b}\times(\boldsymbol{\omega}_{b/0}^{b}\times\mathbf{r}_{G/b}^{b})\right)&=\mathbf{F}_{b}^{b}\\ I_{b}\frac{d\boldsymbol{\omega}_{b/0}^{b}}{dt}+\boldsymbol{\omega}_{b/0}^{b}\times I_{b}\boldsymbol{\omega}_{b/0}^{b}+m\mathbf{r}_{G/b}^{b}\times\left(\frac{d\mathbf{V}_{b/0}^{b}}{dt}+\boldsymbol{\omega}_{b/0}^{b}\times\mathbf{V}_{b/0}^{b}\right)&=\mathbf{M}_{b}^{b}\end{aligned} \tag{2.2}$$

where m is the total mass of the floating structure, I_b is the moment of inertia about position O_b. $\mathbf{V}_{b/0}^{b}$ and $\boldsymbol{\omega}_{b/0}^{b}$ are the velocity and angular velocity vectors from O_0 to O_b expressed in the body-fixed reference frame b (superscript). $\mathbf{F}_{b}^{b}$ and $\mathbf{M}_{b}^{b}$ on the RHS of the equation are the forces and moments acting on a point of the body, O_b. On the other hand, the terms on the LHS can be defined as inertia forces and moments:

$$\begin{aligned} \mathbf{F}_{i}^{b}&=m\left(\frac{d\mathbf{V}_{b/0}^{b}}{dt}+\boldsymbol{\omega}_{b/0}^{b}\times\mathbf{V}_{b/0}^{b}+\frac{d\boldsymbol{\omega}_{b/0}^{b}}{dt}\times\mathbf{r}_{G/b}^{b}+\boldsymbol{\omega}_{b/0}^{b}\times(\boldsymbol{\omega}_{b/0}^{b}\times\mathbf{r}_{G/b}^{b})\right)\\ \mathbf{M}_{i}^{b}&=I_{b}\frac{d\boldsymbol{\omega}_{b/0}^{b}}{dt}+\boldsymbol{\omega}_{b/0}^{b}\times I_{b}\boldsymbol{\omega}_{b/0}^{b}+m\mathbf{r}_{G/b}^{b}\times\left(\frac{d\mathbf{V}_{b/0}^{b}}{dt}+\boldsymbol{\omega}_{b/0}^{b}\times\mathbf{V}_{b/0}^{b}\right)\end{aligned} \tag{2.3}$$

These inertia loads can be computed using the translational and rotational vectors with the inertia information.

2.1.2 Forces and moments on the floating body

For the floating substructure, the forces F_b^b and moments M_b^b are decomposed into gravity, fluid, and constraint load contributions.

$$\begin{aligned} \mathbf{F}_{b}^{b}&=\mathbf{F}_{g}^{b}+\mathbf{F}_{f}^{b}+\mathbf{F}_{c}^{b}\\ \mathbf{M}_{b}^{b}&=\mathbf{M}_{g}^{b}+\mathbf{M}_{f}^{b}+\mathbf{M}_{c}^{b}\end{aligned} \tag{2.4}$$

where subscripts g, f, and c stand for the gravity, fluid and constraint loads. The constraint forces and moments are considered mooring forces if the body has mooring lines or dynamic cables.

The gravity forces and moments expressed in $\{b\}$ are calculated using the following

equation,

$$\begin{aligned}\mathbf{F}_g^b &= (R_b^0(\Theta_{0b}))^{-1}\mathbf{F}_g^0 = -mg\begin{bmatrix}-\sin\theta\\ \sin\phi\cos\theta\\ \cos\phi\cos\theta\end{bmatrix}\\ \mathbf{M}_g^b &= \mathbf{r}_{G/b}^b \times \mathbf{F}_g^b = -mg\begin{bmatrix}\mathbf{y}_{G/b}^b\cos\theta\cos\phi - \mathbf{z}_{G/b}^b\cos\theta\sin\phi\\ -\mathbf{x}_{G/b}^b\cos\theta\cos\phi - \mathbf{z}_{G/b}^b\sin\theta\\ \mathbf{x}_{G/b}^b\cos\theta\sin\phi + \mathbf{y}_{G/b}^b\sin\theta\end{bmatrix}\end{aligned} \tag{2.5}$$

where $\mathbf{F}_g^0 = [0,0,-mg]^T$ is the gravity force expressed in the Galilean reference frame with gravity acceleration ($g = 9.81$ m/s^2) and $\mathbf{r}_{G/b}^b = [\mathbf{x}_{G/b}^b, \mathbf{y}_{G/b}^b, \mathbf{z}_{G/b}^b]^T$ is the position of the center of gravity.

The forces and moments exerted by the fluid denoted as $\mathbf{F}_f^b$ and $\mathbf{M}_f^b$, respectively, can either be measured through tank testing or modeled numerically. Chapter 5 presents an experimental method for measuring the fluid loads. Other different techniques can be used to model fluid loads, such as solving the Navier-Stokes equations for viscous flow or Laplace and Bernoulli's equations for potential flow. Further information regarding this topic will be discussed in Sections 2.2 and 2.3.

2.2 Viscous flow theory

In order to model the fluid loads on a floating substructure, a physical problem is introduced as shown in Figure 2.2. This problem focuses on a single column of the substructure. A three-dimensional fluid domain denoted by Ω is considered as a control volume that is enclosed by various boundary surfaces including the free surface S_F, body surface S_B, sea bottom S_b, and the lateral surface S_C.

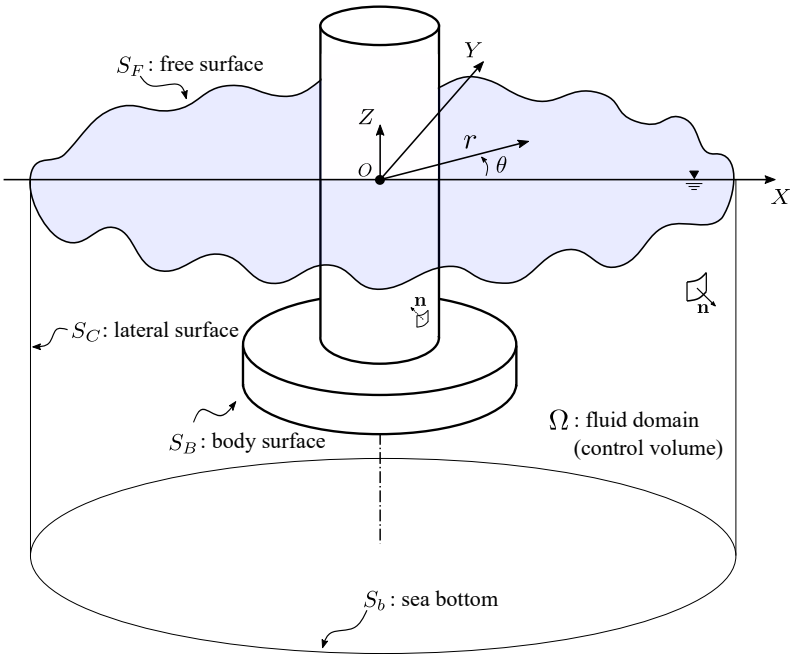

Figure 2.2 – Description of the physical problem in the fluid domain closed by the free surface, bottom, lateral, and body boundaries.

2.2.1 Governing equations

The incompressible Navier Stokes equations for a Newtonian fluid are employed:

$$\nabla \bullet \mathbf{u} = 0 \tag{2.6}$$

$$\rho \frac{D\mathbf{u}}{Dt} = \rho \nabla G + \mathrm{div}(\sigma) \tag{2.7}$$

where D/Dt represents the material derivative, $\mathbf{u}$ stands for the flow velocity vector, ρ is the fluid density, σ is the stress tensor. This study considers only the gravity force field $\nabla G = \mathbf{g}$ as a generic specific body force, where G is a potential field, $G = -gz$.

By assuming an incompressible Newtonian fluid, the stress tensor can be written as:

$$\boldsymbol{\sigma} = -p\mathbf{I} + 2\mu\mathbf{D}, \tag{2.8}$$

where $\mathbf{D}$ is the rate of strain tensor, i.e. $\mathbf{D} = (\nabla\mathbf{u} + \nabla\mathbf{u}^T)/2$ and μ is the dynamic viscosity coefficient. The vorticity vector $\boldsymbol{\omega}$ is calculated from the velocity field as $\boldsymbol{\omega} = \nabla \times \mathbf{u}$.

2.2.2 Hydrodynamic and hydrostatic loads on the floating body

The fluid forces and moments can be expressed by integrating the stress on the wetted body surface as,

$$\begin{bmatrix} \mathbf{F}_f^b \\ \mathbf{M}_f^b \end{bmatrix} = -\iint_{S_B} \boldsymbol{\sigma} \bullet n_i dS, \qquad \text{i} = 1 \sim 6 \tag{2.9}$$

where σ is the stress tensor in the incompressible Newtonian fluid, S_B is the instantaneous wetted body surface, n_i are the six components of the generalized unit surface normal vector pointing out of the fluid domain, $(n_1, n_2, n_3) = \mathbf{n}$ and $(n_4, n_5, n_6) = \mathbf{r} \times \mathbf{n}$. $\mathbf{r}$ is the position vector on the body surface from O_b.

To discuss the static contribution, a dynamic pressure is introduced in the following equation.

$$p_d = p - \rho\mathbf{g} \bullet \mathbf{x} \tag{2.10}$$

where p_d is the dynamic pressure (Rusche (2003)) and the last term on RHS can be interpreted as a static pressure. $\mathbf{x}$ is the position vector, and $\mathbf{g} = [0, 0, -g]$ is the gravity acceleration.

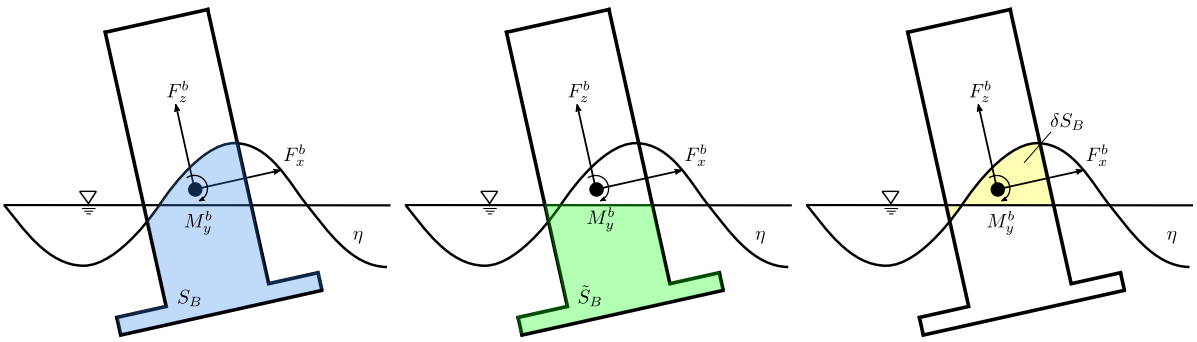

(a) Wetted surface, S_B **(b)** Wetted surface, $\tilde{S}_B$ **(c)** Wetted surface, δS_B

Figure 2.3 – Definition of the wetted surfaces of a moving body in waves of free surface elevation η. S_B: total wetted body surface, $\tilde{S}_B$: wetted body surface under the mean free surface level, δS_B: variation of the wetted body surface.

The fluid loads can be decomposed with the definitions of the wetted body surface illustrated in Figure 2.3.

$$\begin{bmatrix} \mathbf{F}_f^b(t) \\ \mathbf{M}_f^b(t) \end{bmatrix} = \iint_{S_B} p_d n_i dS - \iint_{S_B} 2\mu \mathbf{D} \bullet n_i dS + \iint_{\delta S_B} \rho \mathbf{g} \bullet \mathbf{x} n_i dS + \iint_{\tilde{S}_B} \rho \mathbf{g} \bullet \mathbf{x} n_i dS \tag{2.11}$$

where S_B is the total wetted body surface in waves naturally caused by wave-structure interaction, including incident, diffracted, and radiated waves. $\tilde{S}_B$ is the wetted body surface of the moving body below the mean free surface, and δS_B is the difference between S_B and $\tilde{S}_B$.

The first three terms of Eq. (2.11) are the dynamic contributions to the fluid loads. The first and second terms are the hydrodynamic pressure and viscous forces on S_B. The third term is the hydrodynamic contribution of the hydrostatic pressure on δS_B due to the disturbed free surface. Therefore, the hydrodynamic loads can be defined as below.

$$\begin{bmatrix} \mathbf{F}_{hd}^b \\ \mathbf{M}_{hd}^b \end{bmatrix} = \iint_{S_B} p_d n_i dS - \iint_{S_B} 2\mu \mathbf{D} \bullet n_i dS + \iint_{\delta S_B} \rho \mathbf{g} \bullet \mathbf{x} n_i dS \tag{2.12}$$

The last term of Eq. (2.11) provides the hydrostatic loads on $\tilde{S}_B$ which can be defined as:

$$\begin{bmatrix} \mathbf{F}_{hs}^b \\ \mathbf{M}_{hs}^b \end{bmatrix} = \iint_{\tilde{S}_B} \rho \mathbf{g} \bullet \mathbf{x} n_i dS \tag{2.13}$$

where the hydrostatic loads can be further described with the hydrostatic forces expressed in the Galilean reference frame, $\mathbf{F}_{hs}^0(t) = [0, 0, \rho g \nabla]^T$ as follows,

$$\mathbf{F}_{hs}^b = (R_b^0(\Theta_{0b}))^{-1} \mathbf{F}_{hs}^0 = \rho g \nabla \begin{bmatrix} -\sin\theta \\ \sin\phi\cos\theta \\ \cos\phi\cos\theta \end{bmatrix} \tag{2.14}$$

where ∇ is the immersed volume in calm water.

The hydrostatic moments are then expressed as:

$$\mathbf{M}_{hs}^b(t) = \mathbf{r}_{B/b}^b \times \mathbf{F}_{hs}^b(t) = \rho g \nabla \begin{bmatrix} y_{B/b}^b \cos\theta\cos\phi - z_{B/b}^b \cos\theta\sin\phi \\ -x_{B/b}^b \cos\theta\cos\phi - z_{B/b}^b \sin\theta \\ x_{B/b}^b \cos\theta\sin\phi + y_{B/b}^b \sin\theta \end{bmatrix} \tag{2.15}$$

where $\mathbf{r}_{B/b}^b = [x_{B/b}^b, y_{B/b}^b, z_{B/b}^b]^T$ is the position vector of the center of buoyancy expressed in

$\{b\}$. The immersed volume in calm water is calculated by integrating the hydrostatic pressure on the time-varying wetted body surface.

2.2.3 Energy of the fluid around an oscillating body

In this section, we focus on the oscillating body problem without incident waves. As the body moves through the fluid, it causes disturbances in both the fluid around the body and the free surface. While the bottom and lateral boundaries remain fixed, the body and free-surface boundaries are changing with time. This body motion yields mechanical energy $\mathscr{E}_M$ in the system, which can be expressed as the sum of the potential and kinetic energies as follows:

$$\mathscr{E}_M = \mathscr{E}_P + \mathscr{E}_K \tag{2.16}$$

where $\mathscr{E}_K = \iiint_\Omega \rho \frac{\mathbf{u}^2}{2} dV$ and $\mathscr{E}_P = \iiint_\Omega -\rho G dV$ denote the kinetic energy and potential energy of the fluid domain Ω, respectively.

Taking the time derivative of the mechanical energy, the following equation is obtained using the transport theorem (e.g., Bouscasse (2015)) for the fluid volume Ω and the momentum equation as

$$\dot{\mathscr{E}}_M = \iiint_\Omega \mathrm{div}(\sigma) \cdot \mathbf{u} dV + \iint_S \rho \left(\frac{\mathbf{u}^2}{2} - G \right) (\mathbf{v} - \mathbf{u}) \, dS \tag{2.17}$$

where the first term is the mechanical power in the fluid, and the second term is the energy flux across the boundary surface with a velocity of the boundary surface, $\mathbf{v}$.

Using the divergence theorem and tensor identities presented in Colagrossi et al. (2015), the first term in Eq. (2.17) can be further decomposed into two surface integrals and one volume integral as follows:

$$\iiint_\Omega \mathrm{div}(\sigma) \cdot \mathbf{u} dV = \iint_S (\sigma \cdot \mathbf{n}) \cdot \mathbf{u} dS - 2 \iint_S \mu \, (\nabla \mathbf{u}\mathbf{u}) \cdot \mathbf{n} dS - \iiint_\Omega \mu \omega^2 dV \tag{2.18}$$

where the first term is the power caused by the stress on each boundary surface, the second is the power linked to the viscous deformation of the fluid domain, and the last is the dissipation due to the enstrophy.

By imposing the boundary conditions with an assumption of no stress on the free surface, the equation of the mechanical energy balance can be obtained as follows:

$$\dot{\mathscr{E}}_M = -P^{pressure}_{fluid/body} - P^{viscosity}_{fluid/body} + \dot{\mathscr{E}}_\omega + \dot{\mathscr{E}}_{FS} + \dot{\mathscr{E}}_C \tag{2.19}$$

where the first two terms are pressure and viscous powers of the fluid acting on the body surface, $\dot{\mathscr{E}}_{FS}$ is the power of the viscous deformation on the free surface, $\dot{\mathscr{E}}_{\omega}$ is the enstrophy dissipation, and $\dot{\mathscr{E}}_{C}$ is the power flux on the lateral boundary surface. These terms on the RHS are given as:

$$
\begin{aligned}
P_{fluid/body}^{pressure} &= \iint_{S_B} p\boldsymbol{u}\cdot\boldsymbol{n}dS \\
P_{fluid/body}^{viscosity} &= \iint_{S_B} \mu(\boldsymbol{\omega}\times\boldsymbol{n})\cdot\boldsymbol{u}dS \\
\dot{\mathscr{E}}_{\omega} &= -\iiint_{\Omega_C} \mu\boldsymbol{\omega}^2 dV \\
\dot{\mathscr{E}}_{FS} &= -2\iint_{\partial\Omega_F} \mu(\nabla\boldsymbol{u}\boldsymbol{u})\cdot\boldsymbol{n}dS \\
\dot{\mathscr{E}}_{C} &= -\iint_{\partial\Omega_C} p\mathbf{u}\cdot\mathbf{n}dS - \iint_{S_C} \mu(\boldsymbol{\omega}\times\mathbf{n})\cdot\mathbf{u}dS + \iint_{S_B} \rho\left(\frac{\mathbf{u}^2}{2}-\mathbf{G}\right)(\mathbf{v}-\mathbf{u})\cdot\mathbf{n}dS
\end{aligned}
\tag{2.20}
$$

Assuming harmonic oscillation of motion with motion period T, we can obtain the following equation by averaging over one cycle with an operator $<\bullet>=\frac{1}{T}\int_t^{t+T}\bullet dt$.

$$
\left\langle P_{fluid/body}^{total}\right\rangle = \left\langle\dot{\mathscr{E}}_{\omega}\right\rangle + \left\langle\dot{\mathscr{E}}_{FS}\right\rangle + \left\langle\dot{\mathscr{E}}_{C}\right\rangle \tag{2.21}
$$

where $\left\langle P_{fluid/body}^{total}\right\rangle = \left\langle P_{fluid/body}^{pressure}\right\rangle + \left\langle P_{fluid/body}^{viscosity}\right\rangle$ and the averaged time derivative of the mechanical energy over one period $\left\langle\dot{\mathscr{E}}_{M}\right\rangle$ is zero.

2.2.4 Hydrodynamic damping from the energy equation

For the sake of simplicity, hereinafter, we consider a 1 degree of freedom (DOF) prescribed motion defined with a periodic function as follows,

$$X = \overline{\xi} \cos \omega t \tag{2.22}$$

where $\overline{\xi}$ is the amplitude of the motion with angular frequency $\omega = 2\pi/T$.

In a typical linear framework used in engineering applications, the fluid force on the oscillating free surface-piercing body is modeled as an added mass and damping, which are in-phase and out-of-phase of the motion:

$$-A\ddot{X} - B\dot{X} - KX = F^{total}_{fluid/body} \tag{2.23}$$

where A, B, and K stand for the added mass, damping and hydrostatic coefficients in 1 DOF. $\ddot{X}$ and $\dot{X}$ are the acceleration and velocity of the motion, respectively.

To recover the added mass and damping coefficient from a measured or simulated non-linear force $F^{total}_{fluid/body}$, the orthogonality of the cosine function is used., The added mass and damping are obtained by time averaging over a single motion period as:

$$A - \frac{1}{\omega^2}K = -\frac{2}{\omega^4 \overline{\xi}^2}\left\langle F^{total}_{fluid/body}\ddot{X}\right\rangle, \qquad B = -\frac{2}{\omega^2 \overline{\xi}^2}\left\langle F^{total}_{fluid/body}\dot{X}\right\rangle \tag{2.24}$$

Note that the added mass and the damping coefficients from the above expression represent only the contribution from the first harmonic component of the fluid forces.

Therefore, an explicit expression of the linear damping can be derived by substituting the total power $\left\langle P^{total}_{fluid/body}\right\rangle$ as $\left\langle F^{total}_{fluid/body}\dot{X}\right\rangle$ into Eq. (2.21):

$$B = B_\omega + B_{FS} + B_C \tag{2.25}$$

where

$$\begin{aligned} B_\omega &= -\frac{2}{\omega^2 \overline{\xi}^2}\left\langle \dot{\mathscr{E}}_\omega \right\rangle, \\ B_{FS} &= -\frac{2}{\omega^2 \overline{\xi}^2}\left\langle \dot{\mathscr{E}}_{FS} \right\rangle, \\ B_C &= -\frac{2}{\omega^2 \overline{\xi}^2}\left\langle \dot{\mathscr{E}}_C \right\rangle \end{aligned} \tag{2.26}$$

It is shown that the damping B comprises three main components: damping due to the dissipation of enstrophy (B_ω), damping caused by free surface effects (B_{FS}), and radiated damping on the lateral surface (B_C). In engineering, damping can be interpreted in various ways. For instance, in the case of a heaving circular cylinder with a heave plate at large submersion depth, the contribution of $\dot{\mathscr{E}}_{FS}$ and $\dot{\mathscr{E}}_C$ is negligible as there is no interaction between the free surface and the heave plate, meaning no radiated waves. As a result, the heave damping can be expressed as a function of enstrophy given in Garrido-Mendoza Carlos A. (2015).

$$B \approx B_\omega \tag{2.27}$$

On the other hand, under further simplifying assumptions, especially the potential flow assumption, the damping can be further simplified in specific application cases where these assumptions are valid (see Section 2.3). Therefore, it is important to note that depending on the particular physical problems in the fluid domain, special care may be needed when applying this interpretation to select the damping components in the applications.

2.3 Potential flow theory

In some application cases, the perfect fluid (inviscid and incompressible fluid) and irrotational flow assumptions can be employed, leading to a large simplification of the general Navier-Stokes equations used in the previous section. The flow velocity for the irrotational flow can then be derived as $\mathbf{u} = \nabla\Phi(\mathbf{x},t)$, where $\Phi(\mathbf{x},t)$ is a scalar velocity potential. The continuity equation for incompressible fluid (Eq. (2.6)) becomes the Laplace equation ($\nabla^2\Phi = 0$), while the momentum equation (Eq. (2.7)) becomes the unsteady Bernoulli's equation. The velocity potential satisfies the boundary conditions on the free surface, sea bottom, body surface, and the radiation condition.

2.3.1 Governing equations

Figure 2.4 illustrates the linearized physical problem with incident wave propagating in the positive X-direction. The boundary value problems (BVP) can be formulated using Taylor series expansions suggested by Stokes and linearized with small wave and motion amplitude assumptions. The mean wetted body surface is given as $\overline{S}_B$ where only the body surface under the mean free surface level is presented. The linearized free surface is defined on $z = 0$. The lateral boundary is replaced by the S_∞ surface positioned far away from the body at $r = \infty$.

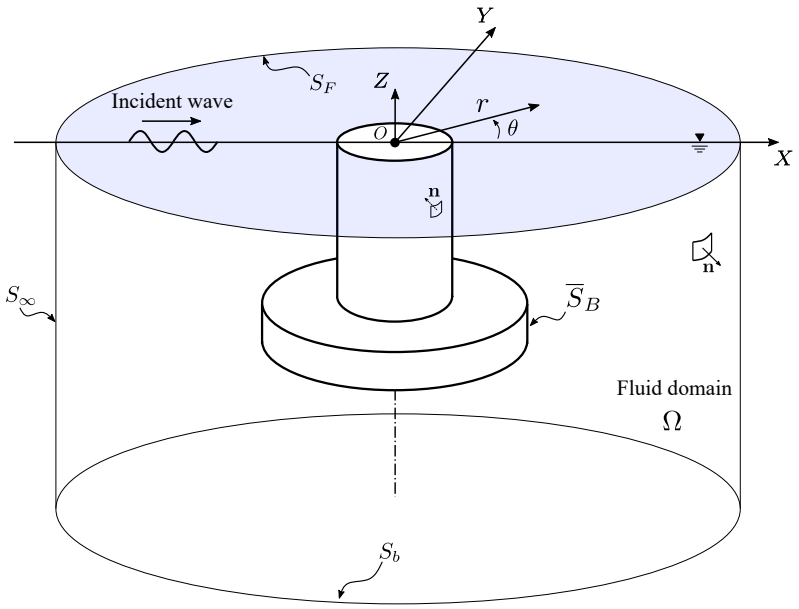

Figure 2.4 – Description of the physical problem in the linearized fluid domain closed by the free surface, bottom, lateral, and body boundaries.

With the time-periodic velocity potential expressed as $\Phi(\mathbf{x},t) = \mathfrak{Re}\{\phi(\mathbf{x})e^{-i\omega t}\}$, the linearized BVP for ϕ is summarized below.

$$\begin{aligned}
&\text{Laplace equation:} \quad \nabla^2\phi = 0 \quad \text{in} \quad \Omega \\
&\text{Free surface boundary condition:} -\frac{\omega^2}{g}\phi + \frac{\partial\phi}{\partial z} = 0 \quad \text{on} \quad S_F \\
&\text{Body boundary condition:} \quad \frac{\partial\phi}{\partial n} = \mathbf{v}\bullet\mathbf{n} \quad \text{on} \quad \overline{S}_B \\
&\text{Bottom boundary condition:} \quad \frac{\partial\phi}{\partial z} = 0 \quad \text{on} \quad S_b \\
&\text{Radiation condition:} \quad \lim_{k_0 r\to\infty} r^{1/2}\left(\frac{\partial\phi}{\partial r} - ik_0\phi\right) = 0 \quad \text{on} \quad S_\infty
\end{aligned} \tag{2.28}$$

where $\mathbf{v}$ is the velocity of the body surface and $\mathbf{n}$ is a normal vector of the body surface pointing out of the fluid domain.

In the linearized wave-structure interaction problem, the velocity potential can be decomposed into the incident wave ϕ_I, diffraction ϕ_D, and radiation ϕ_R potentials as:

$$\phi = \phi_I + \phi_D + \phi_R = \phi_I + \phi_D + \sum_{j=1}^{6}\left(-i\omega\xi_j\phi_j\right) \tag{2.29}$$

where $j = 1 \sim 6$ stands for the modes of the six degrees of freedom, and ϕ_j is a unit amplitude radiation potential with complex motion amplitude ξ_j.

The body boundary condition is then expressed using linear superposition as,

$$\frac{\partial\phi_D}{\partial n} = -\frac{\partial\phi_I}{\partial n}, \qquad \frac{\partial\phi_j}{\partial n} = n_j \quad \text{on} \quad \overline{S}_B \tag{2.30}$$

where the first body boundary condition stands for the wave-fixed body interaction called diffraction problem, and the second stands for the moving body in the absence of incident waves named radiation problems.

In engineering applications, boundary element methods (BEMs) based on boundary integral equations with free-surface Green functions are practically used to solve the diffraction-radiation problem. The methods involve discretizing the body boundary into a finite number of panels, which allows for handling complex body geometries. Various forms of the integral equation were presented by Lee et al. (1996) and Malenica and Chen (1998) to eliminate irregular frequency, which is a numerical problem related to the interior boundary value problem. Recently, He et al. (2021) proposed a combined boundary integral equation

method based on two flow models for more efficient computation. This thesis introduces an analytical method in Chapter 3 for a truncated vertical circular cylinder with a circular plate.

2.3.2 Linear hydrodynamic and hydrostatic loads

In linear potential flow, the loads acting on the floating body are computed by integrating the pressure on the wetted body surface at the rest position, as there is no viscosity contribution in the stress tensor (see Equation (2.8)).

$$\mathbf{f} = \iint_{\overline{S}_B} p\mathbf{n}dS \tag{2.31}$$

where $\mathbf{f}$ denotes the generalized loads, the integration is made on the mean wetted body surface $\overline{S}_B$.

The pressure is obtained from the linearized Bernoulli's equation,

$$p = -\rho g z + i\omega\rho\phi \tag{2.32}$$

where the first term corresponds to the hydrostatic pressure and the second term denotes the hydrodynamic pressure.

Therefore, the hydrostatic and hydrodynamic loads can be defined as,

$$\begin{aligned} \mathbf{f}_{hs} &= -\rho g \iint_{\overline{S}_B} (z)\,\mathbf{n}dS \\ \mathbf{f}_{hd} &= i\omega\rho \iint_{\overline{S}_B} \left(\phi_I + \phi_D + \sum_{j=1}^{6} -i\omega\xi_j\phi_j\right)\mathbf{n}dS \end{aligned} \tag{2.33}$$

Furthermore, the first two terms in the hydrodynamic loads are called the linear wave excitation loads (or wave diffraction loads), where the loads act on the fixed body as:

$$\mathbf{f}_{ext} = i\omega\rho \iint_{\overline{S}_B} (\phi_I + \phi_D)\,\mathbf{n}dS \tag{2.34}$$

where the first term is often called the "Froude-Krylov force" generated by the undisturbed incident waves.

The loads induced by the radiation potential are interpreted as the added mass and wave damping expressed as,

$$A_{w,ij} + i\frac{B_{w,ij}}{\omega} = \rho \iint_{\overline{S}_B} \phi_j n_i dS \tag{2.35}$$

where $A_{w,ij}$ and $B_{w,ij}$ are the added mass and wave damping coefficients. The subscripts i and j stand for the component i of the normal vector to the body surface and the sinusoidal motion in the mode j.

2.3.3 Energy of the fluid around an oscillating body

This section considers the radiation problem when forcing the body motion without incident waves. The energy equation Eq. (2.21) simplifies for a potential flow as

$$\left\langle P^{pressure}_{fluid/body} \right\rangle = \left\langle \dot{\mathscr{E}}_C \right\rangle \tag{2.36}$$

where the energy flux on the lateral surface located far away from the body ($\dot{\mathscr{E}}_C \to \dot{\mathscr{E}}_\infty$) is,

$$\dot{\mathscr{E}}_\infty = -\iint_{S_\infty} p\mathbf{u}\bullet\mathbf{n}dS - \rho \iint_{S_\infty} \mathbf{u}\bullet\mathbf{n}\left(\frac{\boldsymbol{u}^2}{2} - G\right) dS \tag{2.37}$$

By using the pressure from the linearized Bernoulli's equation and the radiation condition in Equation (2.28), the equation can be rewritten as a function of the wave damping, $B_{w,jj}$:

$$\left\langle \dot{\mathscr{E}}_\infty \right\rangle = -\frac{1}{2}\omega^2 |\xi_j|^2 B_{w,jj} \tag{2.38}$$

where the energy radiated away from the structure by the waves is proportional to the wave-damping coefficients as stated in Linton and McIver (2001a). Furthermore, wave damping is a function of the amplitude of the radiated waves in the far field, which can be derived using the asymptotic form of the velocity potential.

As a result, the damping B in Eq. (2.25) can be simplified by neglecting the first two terms, $\dot{\mathscr{E}}_\omega$ and $\dot{\mathscr{E}}_{FS}$, due to the virtue of the potential flow theory. In addition, by putting the lateral boundary far from the body, "far-field" ($\dot{\mathscr{E}}_C \to \dot{\mathscr{E}}_\infty$), the damping B is interpreted as the wave radiated damping.

$$B \approx B_w \tag{2.39}$$

On the other hand, the relations of the added mass with the energy can be derived using the kinetic energy and potential energy of the fluid as presented in Linton and McIver (2001b).

$$\langle \mathscr{E}_K \rangle - \langle \mathscr{E}_P \rangle = \frac{1}{4}\omega^2 |\xi_i|^2 A_{w,ii} \tag{2.40}$$

where $\mathscr{E}_K = \frac{1}{2}\rho \iiint_\Omega \nabla\Phi_R \bullet \nabla\Phi_R dV$ and $\mathscr{E}_P = \frac{1}{2}\rho g \iint_{S_F} \eta_R^2 dS$ are the kinetic energy and potential

energy and η_R is the free surface elevation of radiated waves.

From the above equation, one can note that when the potential energy is increased due to the dominant effects of the free surface, the added mass decreases. Conversely, the added mass increases when the kinetic energy increases in the absence of radiated waves.

CHAPTER 3

DEVELOPMENT OF ANALYTICAL METHODS

A first-order analytical theory of a truncated and surface-piercing vertical circular cylinder with a circular plate mounted at the bottom of the cylinder is generalized to solve the linear wave diffraction and radiation problems based on potential flow and the hypothesis of small wave and motion amplitudes. The domain is decomposed, and the linearized velocity potentials are derived in each subdomain and matched on each subdomain interface employing pressure and normal velocity continuity. The linear hydrodynamic loads obtained with the analytical method are compared with the results of linear boundary element method (BEM) solvers. This chapter is written based on the paper (Han et al. (2024)).

3.1 Introduction

In marine hydrodynamics, potential flow theory is well established by assuming that the fluid is incompressible and inviscid and that the flow is irrotational. In a linear context combining small wave amplitude and motion displacement, the entire wave-body interaction problem can be split into two typical subproblems: diffraction and radiation problems (e.g., see Faltinsen (1990)). These subproblems correspond to a fixed body in incident waves and an oscillating body in calm water. In diffraction problems, the hydrodynamic loads are the result of the interaction between the body and the incident waves, known as wave diffraction loads. The radiation problems describe the hydrodynamic loads caused by the body motions. The loads are typically interpreted as added mass and damping representing the loads components proportional to the acceleration and velocity, respectively.

The diffraction-radiation problems have been extensively studied for the conventional cylindrical structure commonly used in ocean engineering for fixed or floating foundations. A monopile substructure installed at the sea bed is an example represented by a bottom-mounted circular cylinder, and floating substructures such as TLP (Tension Leg Platform), SPAR, and

semi-submersible platforms can also be characterized as truncated circular cylinders. These fundamental shapes have long been studied by hydrodynamicists to understand better the complex mechanisms involving both linear and nonlinear hydrodynamics.

For the bottom-mounted vertical circular cylinder, McCamy and Fuchs (1954) introduced a mathematical model to solve the diffraction problem in finite depth. Malenica and Molin (1995) developed semi-analytical solutions up to the third order to compute the nonlinear horizontal wave forces. Faltinsen et al. (1995) introduced nonlinear diffraction theory, so-called FNV methods, to evaluate the nonlinear horizontal loads up to the third-order harmonics on the cylinder at infinite water depth. Later, Kristiansen and Faltinsen (2017) generalized the FNV methods to an arbitrary order of harmonics in finite water depth. They focused on the third harmonic load and showed good agreement with their regular wave experiments for small and medium wave steepnesses.

On the other hand, the truncated circular cylinder, which can be considered a floating body, introduces several challenges related to diffraction and radiation. Garrett (1971) presented the analytical model for the diffraction problem of a truncated vertical circular cylinder to evaluate the first-order horizontal and vertical forces and moments. The fluid domain was separated into external and internal domains. In addition, matching conditions were implemented on the interface to ensure the continuity of pressure and normal velocity. This method was named the matched eigenfunction expansions method (MEEM) (e.g., see Linton and McIver (2001b)). Later, attempts to solve the non-linear problem were made by Huang and Taylor (1996) and Teng and Kato (2002) up to the second and third order.

Regarding the radiation problem, Yeung (1981) computed the added mass and damping coefficients on the truncated vertical circular cylinder by solving the radiation problem analytically. A particular solution was presented to satisfy the body boundary condition due to the body motions. A similar explanation for the heave motion was given by McIver and Evans (1984), where the occurrence of negative added mass is discussed using kinetic and potential energy.

Bhatta and Rahman (2003) presented the generalized solutions for the radiation and diffraction problems on the truncated cylinder. The computational results of wave excitation, added mass, and damping were provided in Bhatta (2011). Malenica (2012) summarized the generalized solutions by adding various physical aspects regarding vertical cylinders, including hydroelasticity, array of cylinders, and small forward speed. The analytical expressions of the cylinder for submerged bottom-standing and floating conditions can be found in Li and Liu (2019). Additionally, analytical solutions for other shapes, such as a hemisphere (Hulme (1982))

and a sphere (Linton (1991)), are also available in the literature.

Recently, some analytical studies have been done on a circular plate attached to the truncated cylinder. This so-called "heave plate" has been widely used on floating platforms to reduce wave-induced motion responses, particularly heave motion, by increasing the added mass and damping (Haslum and Faltinsen (1999)). The heave plate is now frequently used in floating offshore wind turbines as well. Cong et al. (2019) focused on the diffraction problem to evaluate analytically the first-order wave excitation and the mean drift force. Koh and Cho (2016) solved the heave radiation problem on the truncated cylinder with dual damping plates based on the MEEM. Moreau et al. (2022) presented the analytical expressions of diffraction and radiation to solve the motion response of the bottomless circular cylinder with a moonpool and bilge boxes by introducing particular solutions on the box regions. The analytical models were successfully adjusted to match their experimental measurements by including additional viscous damping, which is not considered in the potential flow theory.

The viscous effects of heave plates with a vertical cylinder were examined through experiments or numerical analysis by focusing on heaving motions in Thiagarajan et al. (2002); Tao and Thiagarajan (2003a); Tao et al. (2007); Lopez-Pavon and Souto-Iglesias (2015). Considerable knowledge has been obtained on hydrodynamic loads, specifically on the added mass and damping governed by flow parameters (e.g., Keulegan-Carpenter number, KC, and Reynolds number, Re) and geometrical parameters (e.g., diameter, thickness, and porosity of the plate). In general, viscous damping of the heave plate is obtained by assuming no wave contribution to the total (or equivalent) damping. This approach is appropriate in the context of classical offshore structures, such as SPAR and TLP, which typically operate at deep submerged depths. For floating wind turbines, however, the wave damping induced by the heave plate is significant because free surface interactions occur due to relatively shallow depths. Therefore, the damping needs to be carefully computed using potential flow theory to obtain the precise contribution of viscous damping.

Numerical methods are widely used in hydrodynamic modeling for various applications, including evaluating the performance of wave energy converters (WECs) (Kim and Cho (2021); Cheng et al. (2022a,b)). A comparative study of open-source codes (Nemoh and HAMS) and a commercial code (WAMIT) was conducted by Sheng et al. (2022) to guide the hydrodynamic modeling of WECs. The study focused on fundamental cylindrical structures and concluded that open-source software generally provides accurate results. However, the codes gave different hydrodynamic coefficients for the thin heave plate due to the different numerical schemes employed. Therefore, hydrodynamic modeling of the thin plate remains a challenge.

The objective of this study was to establish an analytical approach for robust hydrodynamic modeling of heave plates. Generalized first-order analytical solutions for a truncated circular cylinder with a heave plate mounted at the bottom of the cylinder are given. The solutions cover the linear diffraction and radiation of water wave problems, including surge, heave, and pitch motions. Linearized velocity potentials in the regime of small wave and motion amplitudes are presented on the decomposed fluid domain. The problems are solved using the matched eigenfunction expansion method (MEEM) following a similar approach to that of Koh and Cho (2016); Cong et al. (2019); Moreau et al. (2022). The first-order hydrodynamic loads are calculated for the cylinder with thick and thin plates and verified using BEM solvers.

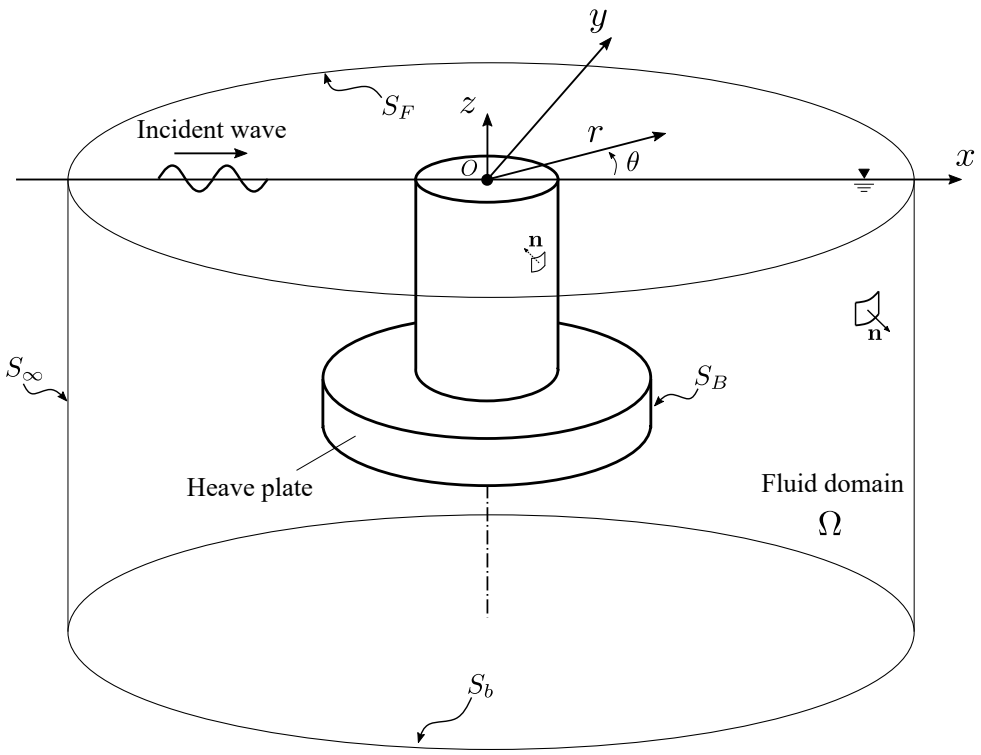

Figure 3.1 – Description of the problem for a truncated circular cylinder with a circular plate mounted at the bottom.

3.2 Mathematical description

A truncated circular cylinder with a circular plate mounted at the bottom of the cylinder is considered as shown in Figure 3.1. The fluid domain, Ω, is filled with an inviscid and incompressible fluid, and the velocity field is assumed irrotational. The right-handed and body-fixed coordinate system is defined on the undisturbed free surface (at $z = 0$) with the z-axis pointing upward. The incident waves propagate in the positive x-direction. The body geometry is represented by three parameters: the radius of the cylinder R_c $(= D_c/2)$, the radius of the plate R_d $(= D_d/2)$, and the thickness t_d. Here, D_c, and D_d stand for the diameter of the cylinder and the plate. The body is immersed at the draft d, and the distance from the undisturbed free surface to the top of the heave plate is $d_c (= d - t_d)$. The bottom S_b is assumed to be flat and placed at the water depth h.

3.2.1 Governing equation and boundary conditions

With the assumptions of potential flow and periodicity of the problem with frequency ω, the flow is determined by the complex velocity potential $\Phi(r,\theta,z,t) = \phi(r,\theta,z)e^{-i\omega t}$. The spatial function, ϕ, satisfies the following governing equation in the fluid domain,

$$\nabla^2\phi(r,\theta,z) = 0 \quad \text{in} \quad \Omega \tag{3.1}$$

where ∇^2 is the Laplace operator in cylindrical coordinates.

To solve the governing equation, boundary conditions are established on the free surface (S_F), the bottom boundary (S_b), and the body boundary (S_B). After linearization using Taylor series expansion by assuming small wave amplitude and motion displacement, the boundary conditions can be obtained with respect to the mean position:

$$-\frac{\omega^2}{g}\phi + \frac{\partial\phi}{\partial z} = 0, \quad z = 0 \quad \text{on} \quad S_F \tag{3.2}$$

$$\frac{\partial\phi}{\partial z} = 0, \quad z = -h \quad \text{on} \quad S_b \tag{3.3}$$

$$\frac{\partial\phi}{\partial n} = \mathbf{V}\bullet\mathbf{n} \quad \text{on} \quad S_B \tag{3.4}$$

$$\lim_{k_0 r\to\infty} r^{1/2}\left(\frac{\partial\phi}{\partial r} - ik_0\phi\right) = 0 \quad \text{on} \quad S_\infty \tag{3.5}$$

where **V** is the velocity vector of the moving body, **n** is the normal vector pointing out of the fluid domain, k_0 is the wave number, and g stands for the gravity acceleration.

The velocity potential ϕ is decomposed into the sum of the diffraction potential ϕ_D and the radiation potential ϕ_R.

$$\phi(r,\theta,z) = \phi_D(r,\theta,z) + \phi_R(r,\theta,z) \tag{3.6}$$

In this study, the diffraction potential includes the contribution of the incident wave potential ϕ_I to simplify the mathematical expression.

The body boundary condition in Equations (3.4) becomes two body boundary conditions after using the linear superposition expressed as,

$$\frac{\partial \phi_D}{\partial n} = 0 \qquad \text{on} \quad S_B \tag{3.7}$$

$$\frac{\partial \phi_R}{\partial n} = \mathbf{V} \bullet \mathbf{n} \qquad \text{on} \quad S_B \tag{3.8}$$

where the boundary condition (3.7) is for the diffraction problem, in which the structure is fixed in the incident waves, and Equation (3.8) is for the radiation problem, in which the body is oscillating harmonically in the absence of incident waves.

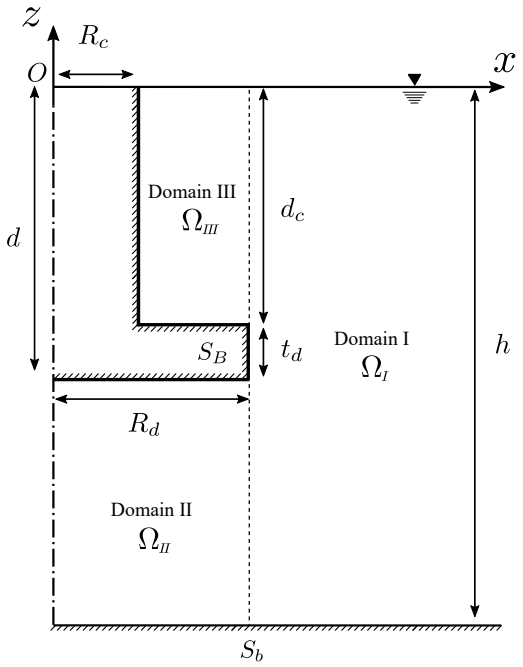

Figure 3.2 – Decomposed fluid domain.

This chapter develops the general solutions to the diffraction and radiation problems using domain decomposition methods. The entire fluid domain is divided into three subdomains, which are one outer domain (Ω_I) and two inner domains (Ω_{II} and Ω_{III}) shown in Figure 3.2. Two additional boundary conditions are introduced on the interface between the outer and inner domains (at $r = R_d$) through the continuity of pressure and normal velocity.

3.2.2 Diffraction problem

This section introduces the general solution to the diffraction problem expressed in each of the three domains. The diffraction potential that satisfies the governing equation (3.1) can be expressed as an eigenfunction expansion considering the boundary conditions of each domain. In the outer domain, Ω_I, the diffraction potential is further decomposed into the incident wave potential and perturbed potential,

$$\phi_D^I(r,\theta,z) = \phi_I^I(r,\theta,z) + \phi_P^I(r,\theta,z) \tag{3.9}$$

with the superscript indicating the fluid domain.

The incident wave potential of constant finite depth is given in cylindrical coordinates (r,θ,z) as,

$$\phi_I^I(r,\theta,z) = -\frac{igA}{\omega}\sum_{m=0}^{\infty}\varepsilon_m i^m J_m(k_0 r)\frac{\cosh k_0(z+h)}{\cosh k_0 h}\cos m\theta \tag{3.10}$$

where A is the wave amplitude, J_m is a Bessel function of the first kind with order m, and ε_m is the Neumann symbol defined by $\varepsilon_0 = 1$ and $\varepsilon_m = 2$, $m \geq 1$.

The perturbed wave potential satisfies the radiation condition and can be expressed with an eigenfunction expansion:

$$\phi_P^I(r,\theta,z) = -\frac{igA}{\omega}\sum_{m=0}^{\infty}\varepsilon_m i^m\left[\sum_{n=0}^{\infty}A_{mn}U_{mn}(r)f_n(z)\right]\cos m\theta \tag{3.11}$$

where A_{mn} are the unknown coefficients that the matching conditions will determine.

The functions $U_{mn}(r)$ are defined by:

$$U_{mn}(r) = \begin{cases} H_m^{(1)}(k_0 r), & n = 0 \\ K_m(k_n r), & n \geq 1 \end{cases} \tag{3.12}$$

where $H_m^{(1)}$ is a Hankel function of the first kind and K_m is a modified Bessel function of the

second kind.

The basis functions $f_n(z)$ that are orthogonal over the interval $-h < z < 0$ are given as,

$$f_n(z) = \begin{cases} \cosh k_0(z+h)/\cosh k_0 h, & n = 0 \\ \cos k_n(z+h)/\cos k_n h, & n \geq 1 \end{cases} \tag{3.13}$$

where k_n are the eigenvalues determined by the dispersion relation $\omega^2/g = k_0 \tanh k_0 h = -k_n \tan k_n h$. The eigenvalues k_n correspond to the propagating ($n = 0$) and the evanescent wave modes ($n \geq 1$), respectively.

In the domain Ω_{II}, the diffraction potential is different from that of Ω_I, as the top boundary condition is not a free-surface condition but a body boundary condition given by the plate:

$$\phi_D^{II}(r,\theta,z) = -\frac{igA}{\omega} \sum_{m=0}^{\infty} \varepsilon_m i^m \left[\sum_{n=0}^{\infty} B_{mn} V_{mn}(r) Z_n(z) \right] \cos m\theta \tag{3.14}$$

where B_{mn} are the unknown coefficients, and the functions $V_{mn}(r)$ are given as,

$$V_{mn}(r) = \begin{cases} (r/R_d)^m, & n = 0 \\ I_m(\alpha_n r)/I_m(\alpha_n R_d), & n \geq 1 \end{cases} \tag{3.15}$$

where I_m is the modified Bessel function of the first kind. The vertical basis functions, $Z_n(z) = \cos \alpha_n(z+h)$, are orthogonal in the interval from $-h$ to $-d$, where $\alpha_n = n\pi/(h-d)$ are the eigenvalues.

Lastly, the diffraction potential of the remaining domain (Ω_{III}) is written as an eigenfunction expansion,

$$\phi_D^{III}(r,\theta,z) = -\frac{igA}{\omega} \sum_{m=0}^{\infty} \varepsilon_m i^m \left[\sum_{n=0}^{\infty} \left(C_{mn} X_{mn}(r) + D_{mn} W_{mn}(r) \right) F_n(z) \right] \cos m\theta \tag{3.16}$$

where C_{mn} and D_{mn} are the unknown coefficients, and the functions $X_{mn}(r)$, $W_{mn}(r)$ are given as

$$\begin{aligned} X_{mn}(r) &= \begin{cases} J_m(\beta_0 r)/J_m(\beta_0 R_c), & n = 0 \\ I_m(\beta_n r)/I_m(\beta_n R_c), & n \geq 1 \end{cases} \\ W_{mn}(r) &= \begin{cases} Y_m(\beta_0 r)/Y_m(\beta_0 R_c), & n = 0 \\ K_m(\beta_n r)/K_m(\beta_n R_c), & n \geq 1 \end{cases} \end{aligned} \tag{3.17}$$

where Y_m is a Bessel function of the second kind.

The vertical basis functions, $F_n(z)$, are orthogonal within the interval of $-d_c < z < 0$ in Ω_{III}.

$$F_n(z) = \begin{cases} \cosh\beta_0(z+d_c)/\cosh\beta_0 d_c, & n=0 \\ \cos\beta_n(z+d_c)/\cos\beta_n d_c, & n \geq 1 \end{cases} \tag{3.18}$$

where the eigenvalues β_n are the roots of $\omega^2/g = \beta_0 \tanh\beta_0 d_c = -\beta_n \tan\beta_n d_c$.

3.2.3 Radiation problem

In the radiation problem studied in the frequency domain, the motions are given as,

$$\xi(t) = \mathrm{Re}\left\{ \xi_j e^{-i\omega t} \right\} \tag{3.19}$$

where ξ_j stands for a complex amplitude of motion in the j-th degree of freedom; here, we restrict the degrees of freedom to the surge, heave, and pitch motions ($j = 1,3,5$).

The radiation potential, ϕ_R, can be expressed by linear superposition to handle the body boundary condition in Equation (3.8) as:

$$\phi_R(r,\theta,z) = \sum_{j=1,3,5} -i\omega\xi_j\phi_j(r,z)\cos m\theta \tag{3.20}$$

where ϕ_j denotes a unit amplitude velocity potential in the j-th degree of freedom.

After introducing body velocity and ϕ_j into the body boundary condition (3.8), we obtain

$$\frac{\partial\phi_j}{\partial n}\cos m\theta = n_j \tag{3.21}$$

where the normal vector is defined as $\mathbf{n} = (n_1, n_2, n_3)$ and $\mathbf{r}\times\mathbf{n} = (n_4, n_5, n_6)$ and $\mathbf{r}$ is the position vector with respect to the reference point, O.

The general solution in each of the three domains is almost identical to the solution of the diffraction problem, with the difference that a particular solution $\psi_j(r,z)$ is needed for heave and pitch motions to satisfy the inhomogeneous body boundary conditions due to the presence of a forcing term. Compared to the previous diffraction problem, the solution will be considered only with $m = 0$ for heave (axisymmetric) and $m = 1$ for surge and pitch motions, thanks to the cosine functions appearing in the body boundary conditions of the radial direction.

The boundary value problem of the exterior domain (Ω_I) is expressed as,

$$\begin{aligned}
&\nabla^2\phi_j^I = 0 \quad \text{in} \quad \Omega \\
&-\frac{\omega^2}{g}\phi_j^I + \frac{\partial\phi_j^I}{\partial z} = 0 \quad \text{on} \quad z = 0 \\
&\frac{\partial\phi_j^I}{\partial z} = 0 \quad \text{on} \quad z = -h \\
&\frac{\partial\phi_j^I}{\partial r} = Q_j^I = \begin{cases} 1, & j = 1 \\ 0, & j = 3 \\ z, & j = 5 \end{cases}, \quad \text{on} \quad r = R_d
\end{aligned} \tag{3.22}$$

The linear velocity potential for the exterior domain (Ω_I) is very similar to the solution of the diffraction problem in Equation (3.11),

$$\phi_j^I(r,z) = \varepsilon_m \sum_{n=0}^{\infty} A_{mn} U_{mn}(r) f_n(z) \tag{3.23}$$

where the radiation condition is satisfied.

The interior domain (Ω_{II}) consists of the seabed ($z = -h$) and the body surface ($z = -d$). The boundary value problem is,

$$\begin{aligned}
&\nabla^2\phi_j^{II} = 0 \quad \text{in} \quad \Omega \\
&\frac{\partial\phi_j^{II}}{\partial z} = 0 \quad \text{on} \quad z = -h \\
&\frac{\partial\phi_j^{II}}{\partial z} = \begin{cases} 0, & j = 1 \\ 1, & j = 3 \\ -r, & j = 5 \end{cases}, \quad \text{on} \quad z = -d
\end{aligned} \tag{3.24}$$

where the inhomogeneous body boundary conditions need to be handled using particular solutions, especially for the heave and pitch motions.

The velocity potential in domain Ω_{II} is written as the sum of the homogenous solution and the particular solution $\psi_j^{II}(r,z)$ to satisfy the body boundary condition,

$$\phi_j^{II}(r,z) = \varepsilon_m \sum_{n=0}^{\infty} B_{mn} V_{mn}(r) Z_n(z) + \psi_j^{II}(r,z) \tag{3.25}$$

where the functions $V_{mn}(r)$ and $Z_n(z)$ are given in Equation (3.15) and in the text right above it. The particular solutions, $\psi_j^{II}(r,z)$, of the surge, heave, and pitch satisfying the governing equation, the bottom and body boundary conditions at $z=-d$and h are given as,

$$\psi_j^{II}(r,z)=\begin{cases}0, & j=1\\ \frac{-1}{4(h-d)}\left[r^2-2\left(z+h\right)^2\right], & j=3\\ \frac{1}{8(h-d)}\left[r^3-4r\left(z+h\right)^2\right], & j=5\end{cases} \tag{3.26}$$

Similar expressions for the particular solutions can be found in Bhatta (2011) and Koh and Cho (2016) for heave and in Moreau et al. (2022) for pitch motions.

The boundary value problem in domain Ω_{III} consists of the governing equation, the free-surface boundary condition, and the body boundary conditions on the cylinder and the heave plate surface.

$$\begin{aligned}&\nabla^2\phi_j^{III}=0 \quad \text{in} \quad \Omega\\ &-\frac{\omega^2}{g}\phi_j^{III}+\frac{\partial\phi_j^{III}}{\partial z}=0 \quad \text{on} \quad z=0\\ &\frac{\partial\phi_j^{III}}{\partial z}=\begin{cases}0, & j=1\\ 1, & j=3\\ -r, & j=5\end{cases}, \text{ on } \quad z=-d_c\\ &\frac{\partial\phi_j^{III}}{\partial r}=Q_j^{III}=\begin{cases}1, & j=1\\ 0, & j=3\\ z, & j=5\end{cases}, \text{ on } \quad r=R_c\end{aligned} \tag{3.27}$$

The general solution of the potential can be written as,

$$\phi_j^{III}(r,z)=\varepsilon_m\sum_{n=0}^{\infty}\left[C_{mn}X_{mn}(r)+D_{mn}W_{mn}(r)\right]F_n(z)+\psi_j^{III}(r,z) \tag{3.28}$$

where the functions $X_{mn}(r)$, $W_{mn}(r)$ and $F_n(z)$ were already given in the diffraction problem section. The particular solution, $\psi_j^{III}(r,z)$, satisfying the governing equation, the body boundary

condition at $z = -d_c$ and the free-surface boundary condition is expressed as,

$$\psi_j^{III}(r,z) = \begin{cases} 0, & j = 1 \\ z + \frac{g}{\omega^2}, & j = 3 \\ -\left(z + \frac{g}{\omega^2}\right) r, & j = 5 \end{cases} \tag{3.29}$$

This particular solution is also discussed in Koh and Cho (2016) for heave and in Moreau et al. (2022) for pitch motions.

3.2.4 Determination of the unknown coefficients

The general solutions developed with series of eigenfunctions are matched on the interface of subdomains based on the hypothesis of normal velocity and pressure continuity (see Garrett (1971)). The unknown coefficients in the diffraction and radiation potentials (A_{mn}, B_{mn}, C_{mn}, D_{mn}), are obtained from the linear sets of equations given by the velocity and pressure continuity. The infinite number of series in the eigenfunction expansions is truncated as a finite number. Here, we use different numbers of eigenmodes, N, in each domain, N_1, N_2, and N_3, since each subdomain shows a different convergence behavior with N, as reported in Moreau et al. (2022).

The first set of equations can be obtained using the continuity of the normal velocity as well as the body boundary condition on $r = R_d$ and $-h < z < 0$.

$$\begin{aligned} \int_{-h}^{0} \frac{\partial \phi^I}{\partial r} f_k(z) dz = \int_{-h}^{-d} \frac{\partial \phi^{II}}{\partial r} f_k(z) dz + \int_{-d}^{-d_c} Q_j^I f_k(z) dz \\ + \int_{-d_c}^{0} \frac{\partial \phi^{III}}{\partial r} f_k(z) dz, \quad k = 0,1,2,...,N_1 \end{aligned} \tag{3.30}$$

where Q_j^I is the forcing term of the body boundary condition on the heave plate thickness in the radial direction (e.g., $Q_j^I = 0$ in the diffraction and heave radiation problems).

Then we have two more sets of equations deriving from the pressure continuity on $r = R_d$, $-h < z < -d$ and $-d_c < z < 0$.

$$\int_{-h}^{-d} \phi^I Z_k(z) dz = \int_{-h}^{-d} \phi^{II} Z_k(z) dz, \quad k = 0,1,2,...,N_2 \tag{3.31}$$

$$\int_{-d_c}^{0} \phi^I F_k(z) dz = \int_{-d_c}^{0} \phi^{III} F_k(z) dz, \quad k = 0,1,2,...,N_3 \tag{3.32}$$

The last set of equations is deduced using the non-penetration condition on the cylinder surface on $r = R_c$ and $-d_c < z < 0$.

$$\int_{-d_c}^{0} \frac{\partial \phi^{III}}{\partial r} F_k(z) dz = \int_{-d_c}^{0} Q_j^{III} F_k(z) dz, \quad k = 0, 1, 2, ..., N_3 \tag{3.33}$$

where $Q_j^{III} = 0$ in the diffraction and heave radiation problems.

Substituting the velocity potentials of the diffraction or radiation problems into the above Equations from (3.30) to (3.33) gives the generalized linear system of equations for each Fourier mode, m:

$$\mathbb{A}_m = \mathbb{L}_m^{-1} \mathbb{R}_m \tag{3.34}$$

where $\mathbb{A}_m = [A_{m,0}, \cdots A_{m,N_1}, B_{m,0}, \cdots B_{m,N_2}, C_{m,0}, \cdots C_{m,N_3}, D_{m,0}, \cdots D_{m,N_3}]^T$ is the unknown coefficient matrix for the diffraction or radiation problems. A detailed description of $\mathbb{L}_m$ and $\mathbb{R}_m$ is given in Appendix B.1.

3.3 Physical quantities of interest

After determining the unknown coefficients of velocity potentials, interesting physical quantities can be obtained, such as flow velocity, pressure, loads, and free-surface elevations in the entire fluid domain Ω. This section focuses on the hydrodynamic loads and the radiated wave fields to compare with the numerical methods and experimental measurements.

3.3.1 Linear hydrodynamic loads

Linear hydrodynamic loads are calculated by integration of the hydrodynamic pressure on the mean wetted body surface S_B. The hydrodynamic pressure is obtained from Bernoulli's equation. Firstly, using the diffraction potential, the hydrodynamic loads considered as wave excitation forces and moments are expressed as,

$$F_i = i\rho\omega \iint_{S_B} \phi_D n_i dS \tag{3.35}$$

where subscript i represents the unit normal vector component of the body.

Secondly, with the radiation potential ϕ_R, the hydrodynamic loads induced by the body

motion are expressed as,

$$F_{rad,i} = \rho\omega^2 \sum_{j=1,3,5} \iint_{S_B} \xi_j \phi_j \cos(m\theta) n_i dS \tag{3.36}$$

where j = 1, 3, and 5 for surge, heave, and pitch motions.

Furthermore, in the radiation problem, the hydrodynamic loads ($F_{rad,i}$) are often interpreted as the added mass and damping by the following equations,

$$A_{ij} = \mathrm{Re}\left\{ \rho \iint_{S_B} \phi_j \cos(m\theta) n_i dS \right\}, \qquad B_{ij} = \mathrm{Im}\left\{ \rho\omega \iint_{S_B} \phi_j \cos(m\theta) n_i dS \right\} \tag{3.37}$$

where, A_{ij}, B_{ij} are the added mass and damping coefficients which are proportional to the acceleration and velocity of the body. The analytical expressions for wave excitation loads, added mass, and damping can be found in Appendix B.2.

3.3.2 Horizontal mean drift loads

Horizontal mean drift loads can be calculated with the linear velocity potential using Far-field methods introduced by Maruo (1960) and Newman (1967). Using momentum conservation, the expression for the horizontal mean drift force is given in Chiang et al. (2005):

$$\overline{F_x} = -\int_0^{2\pi} \rho r \cos\theta \left\{ \int_{-h}^{0} \frac{1}{4} \left(\frac{\partial \phi_D}{\partial r} \frac{\partial \phi_D^*}{\partial r} - \frac{\partial \phi_D}{\partial z} \frac{\partial \phi_D^*}{\partial z} \right) dz + \frac{\omega^2}{4g} |\phi_D|^2_{z=0} \right\} d\theta \tag{3.38}$$

where $r \to \infty$ and * denotes the complex conjugate. Here, we focus on the mean drift force for the diffraction problem.

With large r, the diffraction potential in Equation (3.9) can be expressed using the asymptotic formula for the Hankel function of the first kind, $H_m^{(1)}$, as,

$$\phi_D^I \sim \frac{-igA}{\omega} f_0(z) \left[e^{ik_0 r\cos\theta} + \left(\frac{2}{\pi k_0 r} \right)^{1/2} e^{i(k_0 r - \pi/4)} \sum_{m=0}^{\infty} \varepsilon_m i^m A_{m0} e^{-\frac{m\pi i}{2}} \cos m\theta \right] \tag{3.39}$$

where the evanescent eigenmodes vanish.

Substituting the asymptotic expression of the velocity potential in Equation (3.39) into Equation (3.38), the horizontal mean drift is obtained using the stationary phase method and the cosine identities given in Malenica and Molin (1995). The analytical expression of the mean

drift force given in Cong et al. (2019) is reported as,

$$\overline{F_x} = -\frac{\rho g A^2}{k_0}\frac{2k_0h+\sinh 2k_0h}{2\sinh 2k_0h}\,\mathrm{Re}\left\{2\sum_{m=0}^{\infty}\left(\mathscr{A}_m\mathscr{A}_{m+1}^{*}+\mathscr{A}_{m+1}\mathscr{A}_m^{*}+\varepsilon_m\mathscr{A}_m\right)\right\} \tag{3.40}$$

where $\mathscr{A}_m = i^m A_{m0} e^{-\frac{m\pi i}{2}}$.

3.3.3 Wave elevations

The free-surface elevation is obtained from the dynamic free-surface boundary condition as,

$$\eta(r,\theta) = \frac{i\omega}{g}\phi(r,\theta,z=0) \tag{3.41}$$

We can calculate the diffracted or radiated free-surface elevations in the fluid domains using the diffraction or radiation potentials.

CHAPTER 4

VALIDATION OF NUMERICAL MODELS FOR HEAVE PLATES

This chapter aims to validate two numerical models of different levels of fidelity: Boundary Element Method (BEM) and Computational Fluid Dynamics (CFD). The validations are carried out by comparing two models at the same level of fidelity, between:

(a) BEM solvers and analytical solutions both based on the potential flow theory,

(b) CFD solvers and experimental measurements, both obeying the Navier-Stokes equations.

The first one is a low-fidelity numerical model, potential flow-based, specifically the BEM with frequency domain free surface Green function. This model is compared to the analytical model developed in the previous Chapter 3. The study discusses the discretization of the heave plate and the computation of linear hydrodynamic coefficients from diffraction and radiation problems.

The other numerical model is a high-fidelity numerical solver called OpenFOAM which is based on the CFD method solving the Navier-Stokes equations. The study focuses on the forced heave oscillations and aims to validate the heave added mass and damping coefficients. The validation process involves comparing the flow field, hydrodynamic loads and coefficients to experimental data available in the literature. The study also discusses the selection of grid resolutions and the presence of turbulence models. This chapter is written based on the paper (Han et al. (2022, 2024)).

4.1 Potential flow solver

This section introduces boundary element methods (BEMs) based on potential flow theory. Heave plate modelling is presented using source and dipole methods, particularly for thin plates. The computations of linear and nonlinear wave diffraction loads are briefly outlined, together with numerical schemes. Open source and commercial BEM solvers, Nemoh (Kurnia

and Ducrozet (2023)) and HydroStar (Bureau Veritas (2020)), are utilized to solve the BVPs for the first- and second-order problems. These solvers discretize the boundary with panels to deal with boundary integral equations with a free surface Green function, known as the panel method. A single wave direction is considered in the positive x-direction.

4.1.1 Panel modelling with heave plates

In the panel method, heave plates can be modelled either by considering their thickness or assuming zero thickness. For the first case, the panels are modeled on the top, side, and bottom of the plate. A source formulation is used to solve the boundary integral equation by defining the velocity potential as a source distribution. On the other hand, the plate can also be modelled as a zero-thickness plate if the thickness is sufficiently small (thin plate) or the plate has porosity. A direct formulation is used to define the velocity potential by source and dipole distributions. Both the top and bottom of the panel are then considered as wetted surfaces. Furthermore, the porous effect can be modeled using Darcy's law, where the porosity is considered as a pressure drop condition linked to the water particle velocity (Chwang (1983)).

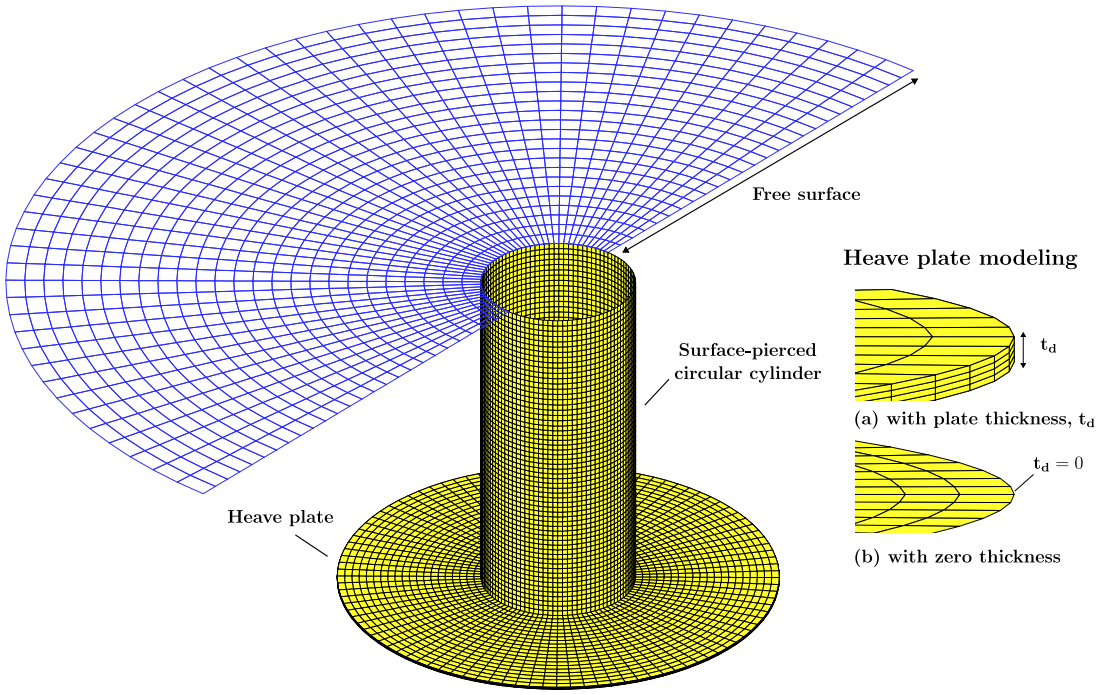

Figure 4.1 – Discretization of a truncated circular cylinder with a heave plate surrounded by a free surface for the first- and second-order computations by the Boundary Element Method: body (yellow), free surface (blue). Heave plate modelling is given: (a) with plate thickness t_d and (b) zero-thickness for source and dipole distribution methods.

An example of the panel model discretization on the cylinder and the heave plate is given in Figure 4.1. In this study, we use the source approach on the solid heave plate by using panels four times smaller than the plate thickness as illustrated in Figure 4.1 (a). On the other hand, the porous plate is modeled as a zero-thickness plate (see Figure 4.1 (b)) to use the direct approach. The free surface is modelled with a radius of $10D_d$ for the second-order computation. For the second-order computation, only the source method is available in HydroStar. Therefore, the second-order loads on the perforated plate can not be computed.

4.1.2 Verification study of the potential flow solver

The linear BEM solver is verified with two configurations of a truncated circular cylinder with a heave plate focusing on the first-order hydrodynamic loads. These configurations are based on the semi-submersible type of floating offshore wind platforms: DeepCWind (Robertson et al. (2014)), which has a thick heave plate, and HiPRWind (Lopez-Pavon and Souto-Iglesias (2015)), which is equipped with a thin plate. Dimensions of the models are given in Table 4.1. Further comparison of potential flow theory-based methods are presented in the following chapters: wave excitation forces up to 2nd order computation (Chapter 6) and added mass/damping (Chapter 7).

Table 4.1 – Dimensions of the vertical circular cylinders with circular plates ($h = 100.0$ m).

Parameter	Unit	Cylinder with thick plate	Cylinder with thin plate
D_c	m	12.0	7.0
D_d	m	24.0	20.0
d	m	20.0	15.5
t_d	m	6.0	0.1
D_d/D_c	-	2.0	2.9
d/D_c	-	1.7	2.2
t_d/D_d	-	0.25	0.005
Reference model	-	DeepCwind	HiPRWind

Two BEM solvers are studied: HydroStar and NEMOH. Both BEM codes solve boundary integral equations using the source method that satisfies the same governing equations and boundary conditions as the analytical method in Section 3.2. Additionally, the direct method in HydroStar, which is mixed with source and dipole methods, is used to handle the thin plate configuration. To compute the analytical solutions, the number of eigenmodes is selected

for each subdomain as N_1=100, N_2=100, and N_3=80, and the number of Fourier modes is chosen as M=15. The selected mode numbers are applicable for the thick and thin heave plate configurations.

a) Thick heave plate

Figure 4.2 shows the panel model discretization of the circular cylinder with the thick plate ($t_d/D_d = 0.25$) of the DeepCwind platform. The panels are evenly distributed on the wetted cylinder and plate surfaces, including the top, side, and bottom surfaces. The wetted surfaces refer to only one side of the panel, which is defined by the normal vectors pointing out of the body. Small-sized panels are selected to ensure high-resolution source distributions, while a symmetric body is considered to reduce the number of panels. As a result, the total number of panels used in the symmetric body is approximately 8,000.

Computations of the linear diffraction and radiation theory (MEEM) developed in Chapter 3 are shown in Figure 4.3. Non-dimensional linear hydrodynamic loads are compared with the source methods of HydroStar and NEMOH, including wave excitation loads, added mass and damping in surge, heave, and pitch. The results for the cylinder with the thick plate indicate good agreements between the analytical and the numerical solutions.

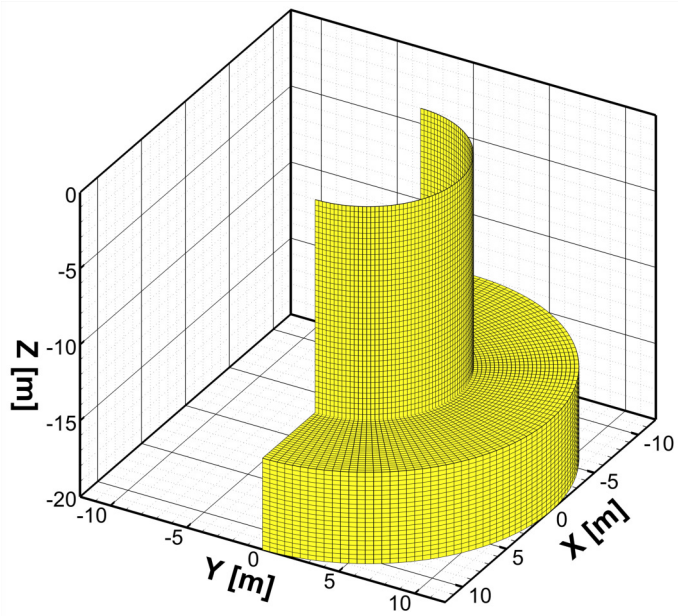

Figure 4.2 – Panel model discretization for the truncated cylinder with the thick heave plate of DeepCwind platform under the undisturbed free-surface level at $z = 0$.

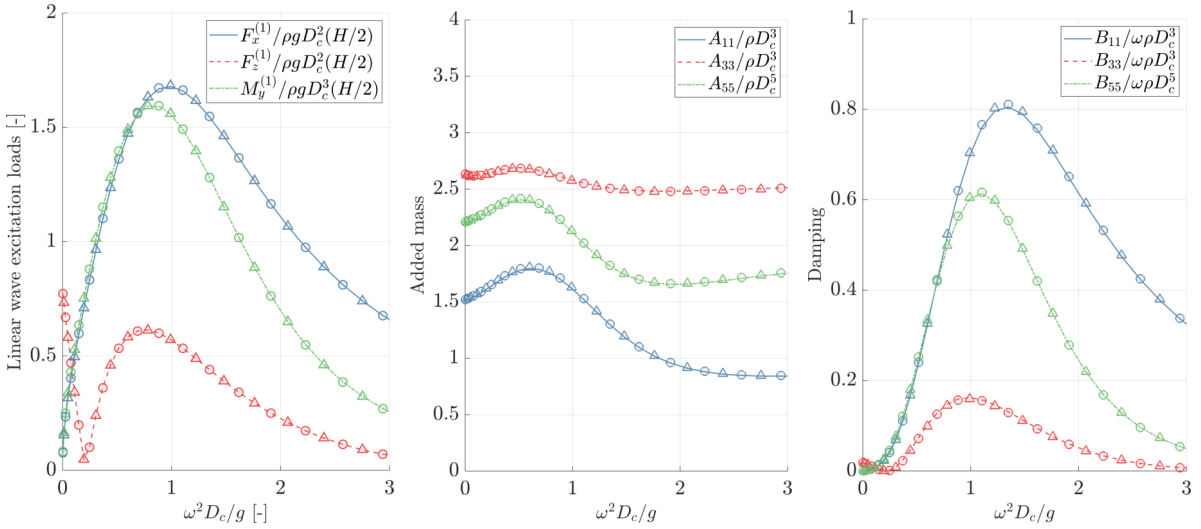

(a) Wave excitation loads **(b)** Added mass **(c)** Damping

Figure 4.3 – Non-dimensionalized wave excitation loads, added mass and damping for the truncated circular cylinder with a thick plate (lines: analytical (MEEM), △: NEMOH, and ◯: HydroStar).

b) Thin heave plate

The thin plate can be challenging for the source method in BEM solvers because the source and field points on the plate are in close proximity to each other. Therefore, two different approaches are studied to handle the thin plate of the HiPRWind model ($t_d/D_d = 0.005$). The first approach utilizes the source method with a panel model similar to that of the thick plate. This model presented in Figure 4.4a involves evenly distributed panels on both the cylinder and plate surfaces, resulting in a total of around 7,000 panels on the symmetric body. The second approach assumes that the thin plate has zero-thickness (see Figure 4.4b), meaning that both sides of the panels on the plate are defined as wetted surfaces. This approach uses the mixed panel method (Bureau Veritas (2020)) by distributing dipoles on the zero-thickness plate and sources on the cylinder surface. Since the dipoles cannot be used in a symmetric body representation in HydroStar, about 9,000 panels are utilized for the entire body. In general, the size of the panels is almost identical between the thin plate and zero-thickness models.

In Figure 4.5, the linear hydrodynamic loads on the cylinder with the thin plate are presented. The predictions made by NEMOH using the source method and HydroStar using both source and dipole methods are generally close to the results from the analytic method. Nonetheless, in contrast to the thick plate case, some deviations can be seen in the vertical wave excitation forces (F_z), as well as in the heave added mass (A_{33}) and damping

(B_{33}), and pitch added moment of inertia (A_{55}). The source methods for both HydroStar and NEMOH underpredict these hydrodynamic coefficients compared to the analytical method. In comparison, the dipole method of HydroStar provides a good agreement on the heave damping, but the added mass of heave and pitch is overestimated compared to the analytical method.

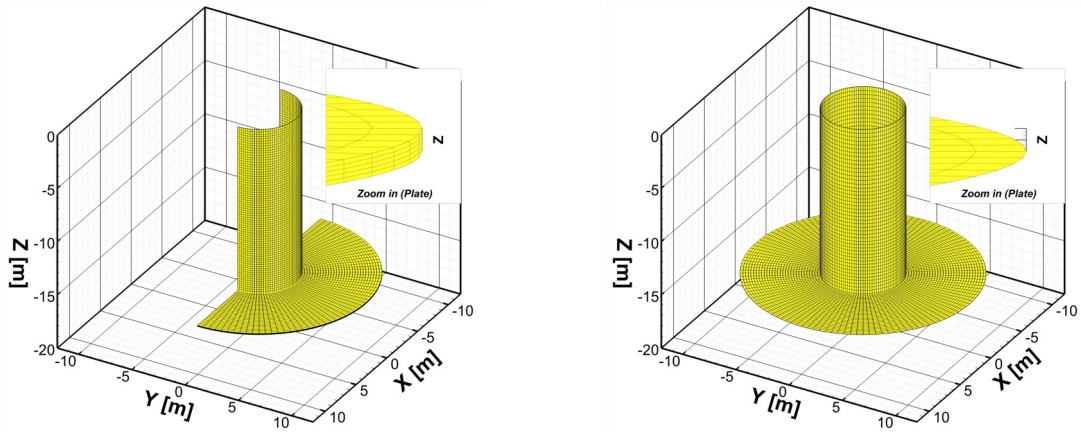

(a) Thin plate model for the source method

(b) Zero-thickness plate model for the dipole method

Figure 4.4 – Panel model discretizations for the truncated cylinder with the thin plate of the HiPRWind platform under the undisturbed free-surface level at $z = 0$.

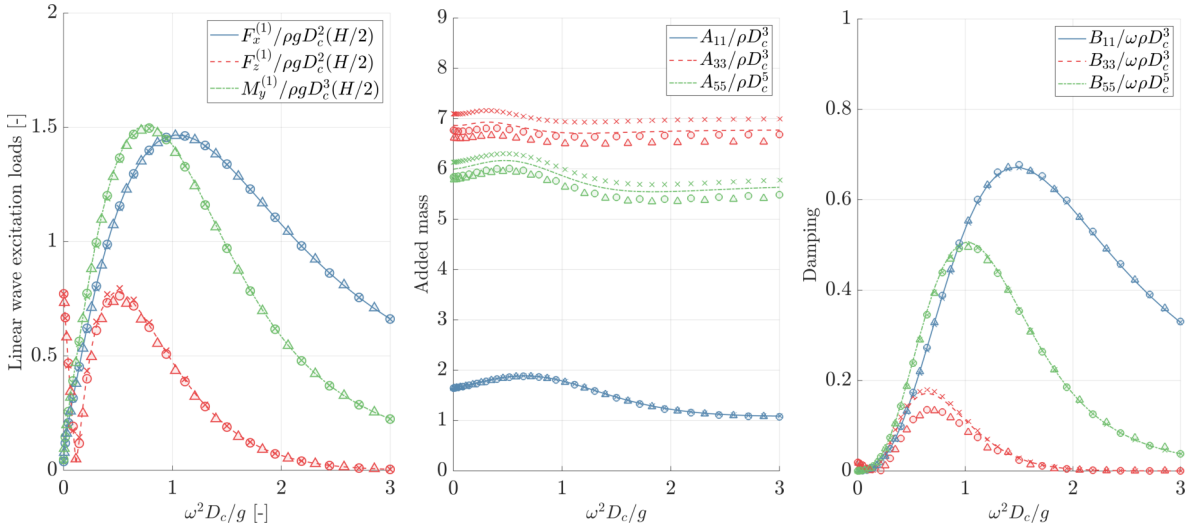

(a) Wave excitation loads

(b) Added mass

(c) Damping

Figure 4.5 – Non-dimensionalized wave excitation loads, added mass and damping for the truncated circular cylinder with a thin plate (lines: analytical (MEEM), △: NEMOH, ◯: HydroStar and ×: HydroStar with dipoles).

4.2 CFD numerical solver

In this section a computational fluid dynamics (CFD) solver based on OpenFOAM is used to obtain the hydrodynamic loads. Numerical results are compared to experimental results by considering the single circular cylinder with a heave plate of the HiPRWind platform undergoing forced heave oscillation motions. Specific choices in the numerical modelling are discussed, especially the presence or not of a turbulence model and the spatial resolution. The vorticity fields in the fluid domain are compared to the experimental results obtained by Particle Image Velocimetry (PIV) presented by Anglada-Revenga et al. (2020). The computed hydrodynamic loads on the cylinder with the heave plate are compared to the experimental results by Bezunartea-Barrio et al. (2020).

4.2.1 Numerical schemes and OpenFOAM

In the OpenFOAM framework, the in-house library, foamStar, is used to solve the wave-structure interaction problem. The foamStar library has been developed by Bureau Veritas and Ecole Centrale Nantes. It is based on *interDyMFoam*, a two-phase incompressible Reynolds Averaged Navier-Stokes Equations (RANSE) solver in OpenFOAM. The governing equations are solved using second-order finite volume discretization for the entire computational domain. Computational algorithms and applications are presented in Monroy et al. (2016); Choi et al. (2020); Kim (2022); Descamps (2023).

In *interDyMFoam*, the volume of fluid (VOF) method (Hirt and Nichols (1981)) is employed for capturing the interface between the air and water with an interface compression term C_α. The fluid in the whole domain is described by a phase indicator function α, which equals 0 if a cell is fully filled by air and 1 if a cell is fully filled by water. The interface is, therefore, located inside a cell where $0 < \alpha < 1$. Practically, the free surface is defined as the isosurface $\alpha = 0.5$.

The local density ρ and dynamic viscosity μ of the cell are defined as follows,

$$\rho = \alpha\rho_{water} + (1-\alpha)\,\rho_{air} \tag{4.1}$$

$$\mu = \alpha\mu_{water} + (1-\alpha)\,\mu_{air} + \mu_t \tag{4.2}$$

where ρ_{water}, ρ_{air} are the density of water (1000 kg/m^3) and air (1.2 kg/m^3). μ_{water}, μ_{air} are the linear dynamic viscosity of water (10^{-3} Ns/m^2) and air (10^{-5} Ns/m^2). μ_t stands for eddy

viscosity. The modified α transport equation (Rusche (2003)) derived from mass conservation is solved,

$$\frac{\partial \alpha}{\partial t} + \nabla \bullet (\mathbf{u}\alpha) + C_\alpha \nabla \{\mathbf{u}_r \alpha (1-\alpha)\} = 0 \tag{4.3}$$

where $\mathbf{u}_r = (\mathbf{u}_{water} - \mathbf{u}_{air})$ is the relative velocity between water and air at the interface. The last term on the left-hand side is a compression term, which enables the sharp interface to be kept artificially. Here, $C_\alpha = 0.2$ is used.

The *PIMPLE* scheme, a combination of *SIMPLE* and *PISO* algorithms, is employed to solve the governing equations (2.2) and the modified VoF equation. For the *PIMPLE* algorithm, 8 outer iterations for PIMPLE and 4 inner iterations for PISO are selected. A detailed flow chart of foamStar is presented in Descamps (2023).

Various time integration schemes, including Implicit Euler (Euler), Crank-Nicolson (CN) and second-order backward schemes (modified by Descamps (2023)), are available in foamStar with MULES (Multidimensional Universal Limiter with Explicit Solution, Damián and Nigro (2014)) to solve the α transportation equation. In engineering applications, the choice of time integration schemes is important as it significantly influences numerical stability and computational cost. In particular, the first-order Euler scheme is stable but results in significant wave dissipation during propagation as presented in Kim (2022). On the contrary, higher-order schemes (CN and backward) have been shown to improve numerical wave dissipation. However, these schemes are less stable and require more computational time than the Euler scheme. Therefore, the selection of a time integration scheme needs to be done depending on the problem of interest.

4.2.2 Validation of the CFD numerical solver in forced heave oscillation

The numerical solver, foamStar, is validated here in simulating the oscillating flow around a heave plate attached to the bottom of a circular cylinder. Experimental results from the HiPRWind project are used as a reference to validate the numerical model. The HiPRWind project focused on the design of a floating offshore wind platform with a semi-submersible floater and a 1.7 MW turbine. A single column with a circular heave plate is modeled based on the HiPRWind platform. The numerical results are compared with experimental measurements of the hydrodynamic forces measured by a multi-component force transducer (Lopez-Pavon and Souto-Iglesias (2015)) and velocity fields measured by PIV in Anglada-Revenga et al. (2020) to assess the accuracy of the numerical solver. The characteristics of the HiPRWind geometry and motion parameters are given in Table 4.2.

Table 4.2 – Dimensions and motion parameters of the HiPRWind experiments

Items	Values	Notes
D_c	0.35 m	Column diameter
D_d	1 m	Heave plate diameter
d	0.775 m	Draft
t_d	0.005 m	Heave plate thickness
a	0.05 m	Heave amplitude
ω	1.57 rad/s	Oscillation frequency
KC	0.314	Keulegan-Carpenter number
Re	78359	Reynolds number
β	249423	Frequency number
T_n	17.9 s	Natural period of the system
ω_n	1.57 rad/s	Natural angular frequency of the system
λ	20	Scale ratio

In foamStar, a motion solver called dynamicMotionSolverFvMesh is used to impose a vertical harmonic motion. The entire domain is moved with the prescribed body motions. The computational mesh is updated with respect to the displacement of body surfaces. The imposed body motion is set as a sinusoidal function in the heave direction. A single test case is selected from Anglada-Revenga et al. (2020) with $a = 0.05$ m of motion amplitude and $\omega = 1.57$ rad/s of oscillation angular frequency (KC = 0.314) expressed in 1:20 model scale. Displacements, velocities, and accelerations are defined by:

$$z(t) = a\sin\omega t, \qquad \dot{z}(t) = a\omega\cos\omega t, \qquad \ddot{z}(t) = -a\omega^2\sin\omega t \tag{4.4}$$

This study investigates two different computational domains: axisymmetric and 3D symmetric. An example of the 3D computational domain is illustrated in Figure 4.6a. In addition, two different grid resolutions (GRID A and GRID B) are tested to verify the influence of the grid size on the flow characteristics (see Figure 4.6b). The computational grids are generated using Star-CCM+ and transformed to the Openfoam format through ccm26ToFoam.

The test condition parameters are given in Table 4.3. According to Bezunartea-Barrio et al. (2020), no radiated waves were observed during the experiments of the heaving cylinder with the heave plate as the plate was deeply submerged ($d/D_c = 2.2$). Therefore, the Euler

scheme is used because wave propagation is not significant for the current test configuration. The time step is selected to keep the Courant number Co below 1 with the following equation,

$$Co = \frac{V_{max}\Delta t}{\Delta x} = \frac{a\omega\Delta t}{\Delta x} < 1 \tag{4.5}$$

where V_{max} is the maximum velocity of the body.

The turbulence model is selected as the $k-\omega$ SST turbulence model, and both with and without turbulence models are discussed. It is important to note that selecting a turbulence model can also affect the numerical wave damping. If wave propagation is important, it is recommended to use the free surface $k-\omega$ SST turbulence model. The boundary conditions for the 3D computational domains are summarized in Table 4.4. A wedge boundary condition is used for the axisymmetric computational domain instead of a symmetric boundary condition.

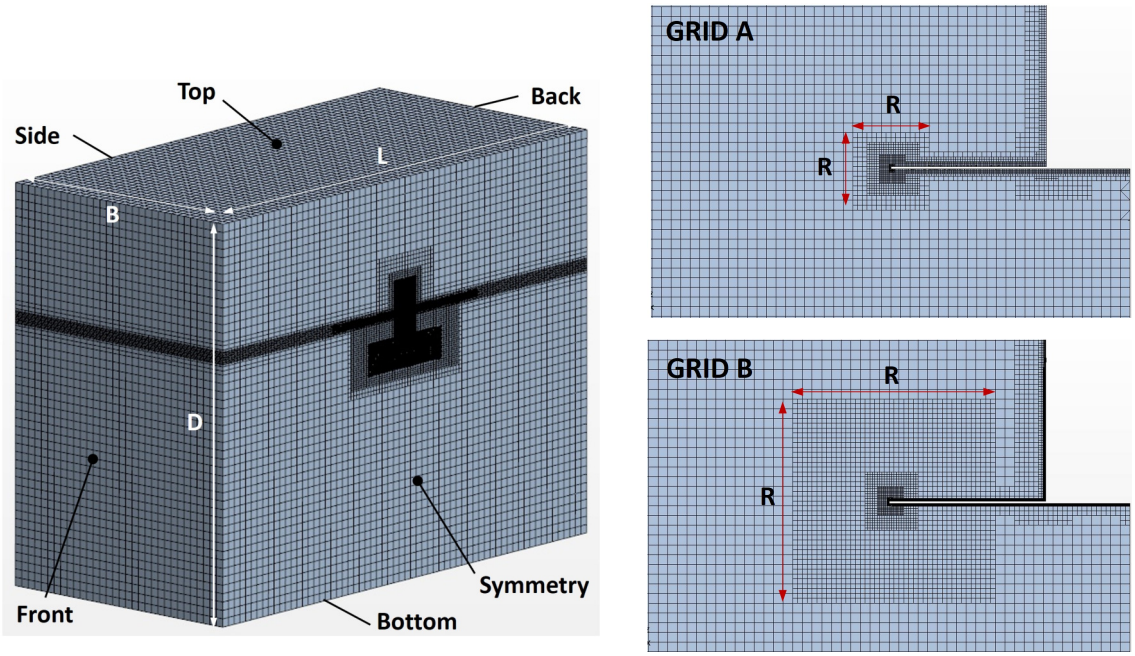

(a) 3D computational domain (symmetric)

(b) Grid refinement around the heave plate

Figure 4.6 – 3D computational domain and grid refinement zone around the heave plate. GRID A: R=0.16 m and w/o prismatic boundary layer; GRID B: R = 0.4 m and w/ prismatic boundary layer. The length, breadth and depth of the computational domain are set as $L = 10D_d$, $B = 5D_d$ and $D = 7.5D_d$.

Table 4.3 – Test cases of the CFD simulations for the forced heave oscillation.

Case ID	Grid refinement	Turbulence	Computational domain	dt	Min. cell	*Co*
C01	GRID A	$k-\omega$ SST	Axisym.[1]	0.001	0.00125 m	0.06
C02	GRID B	w/o	Axisym.	0.001	0.0002 m	0.4
C03	GRID B	$k-\omega$ SST	Axisym.	0.001	0.0002 m	0.4
C04	GRID A	$k-\omega$ SST	3D sym.[2]	0.002	0.00125 m	0.1
C05	GRID B	$k-\omega$ SST	3D sym.	0.001	0.0002 m	0.4

[1] Axisymmetric computational domain (Axisym.).
[2] 3D symmetric computational domain (3D sym.).

Table 4.4 – Boundary conditions used for forced heave oscillations.

	Top	Side/Bottom	Body	Symmetric
U	InletOutlet	fixedVlaue	movingWallVelocity	Sym.[1]
p_rgh	totalPressure	ZeroGradient	fixedFluxPressure	Sym.
α	inletOutlet	ZeroGradient	ZeroGradient	Sym.
k	zeroGradient	zeroGradient	kqRWallFunction	Sym.
ω	zeroGradient	zeroGradient	omegaWallFunction	Sym.
ν_t	calculated	calculated	nutUSpaldingWallFunction	Sym.

[1] The symmetric boundary condition (Sym.) for the 3D computational domain is replaced by a wedge boundary condition for the axisymmetric computational domain.

a) Flow fields

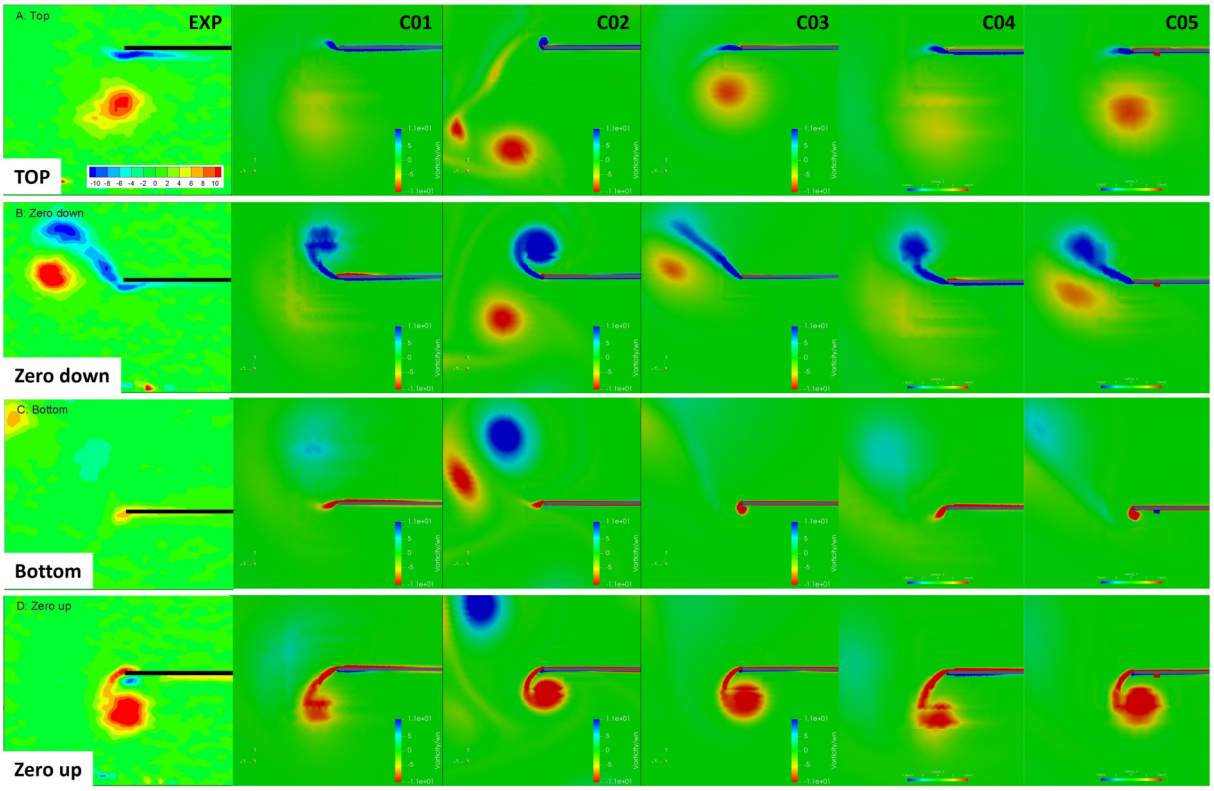

Figure 4.7 – Non-dimensional vorticity fields (ω_X/ω) at four representative positions: top, zero-crossing down, bottom, and zero-crossing up. CFD computations (C01-05) are compared to PIV measurements (EXP) from Anglada-Revenga et al. (2020).

Figure 4.7 shows the non-dimensional vorticity fields at different positions, including top, zero-crossing down, bottom, and zero-crossing up. The numerical results are compared to the averaged vorticity fields obtained from the PIV tests by Anglada-Revenga et al. (2020). The global behavior of the vorticity is well represented, showing a good agreement between the experiments in Anglada-Revenga et al. (2020) and the numerical simulations. Specifically, the flow captured by the fine GRID B (C03, C05) at the top position shows higher vorticity under the heave plate than the coarse GRID A (C01, C04). The GRID A leads to excessive dissipation of the vortices around the plate. Therefore, it has less influence on the vortices generated at the plate edge in the next step (zero-crossing down), and the shape of the newly generated vortices is shown to be freely curled. In contrast, for the fine grid, the emitted vortices (blue) at the zero-crossing down position are straightened rather than curled due to the influence of previous

vortices (red), which is similar to the experimental measurements. Besides, as expected, there is no significant difference between the results with the axisymmetric mesh and the 3D symmetric one.

The numerical setups (C01, C03, C04, C05) with the $k-\omega$ SST turbulence model effectively captures the interaction of the vorticity with the plate, allowing the vorticity field to be in good agreement with the experiment. In the absence of a turbulent model (C02), the vorticity field is not sufficiently dissipated in the fluid region and represents a largely different pattern compared to the experiment. This discrepancy is expected to result in a difference in the hydrodynamic damping since the damping is a function of vorticity, see Garrido-Mendoza et al. (2014).

b) Hydrodynamic Forces

Hydrodynamic loads on the cylinder with the heave plate are calculated as given in Section 2.2.2 and are compared with the experimental results published by Bezunartea-Barrio et al. (2020). Figure 4.8 presents the non-dimensional hydrodynamic forces together with the prescribed heave motion. The results show that the magnitude and phase of the forces agree well with the experimental results except for the case with no-turbulence model (C02). This happens because the vortex around the plate has a different shape and this results in a different force. It can be noticed however that the numerical results tend to overpredict the force, compared to the experiment, especially for the most converged results (C03, C05). The general behavior of the forces tends to be linear (harmonic) since this case is based on a low KC number (KC=0.314). It can be observed that the peaks of the fluid force are generated immediately after the change of direction of the heave motion.

c) Added mass and damping

Using the Fourier series approach, the added mass and damping over a period are obtained from the hydrodynamic force (F_{hd}) as follows:

$$A_{33}(t) = \frac{1}{\pi a \omega} \int_t^{t+T} F_{hd}(t) \sin \omega t dt, \quad C_a = \frac{A_{33}}{A_{33_{th}}} \tag{4.6}$$

$$B_{33}(t) = -\frac{1}{a\pi} \int_t^{t+T} F_{hd}(t) \cos \omega t dt, \quad C_b = \frac{B_{33}}{\omega A_{33_{th}}} \tag{4.7}$$

where C_a and C_b represent the non-dimensional added mass and damping coefficients, and $A_{33_{th}}$(=303 kg) is the theoretical added mass of a disc with a cylinder (Tao et al. (2007)).

Added mass and damping coefficients can be seen in Figure 4.9. The experimental result reaches the steady state faster than the numerical simulations, which might be the effect of the ramp function. This ramp function is not implemented in the numerical simulations. It can be observed that the results without the turbulence model do not converge to the experiment. On the other hand, the use of the turbulence model permits to effectively predict the added mass and damping. With the finest GRID B, the damping is accurately predicted both using the axisymmetric and 3D symmetric meshes, but the added mass is over-predicted, as was the force.

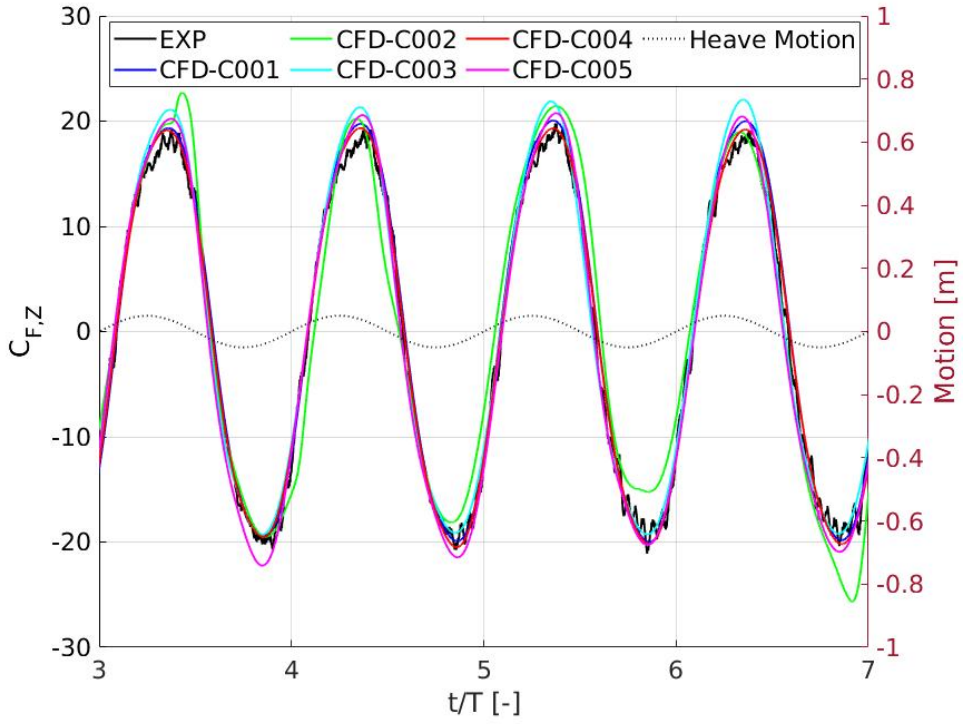

Figure 4.8 – Time histories of the hydrodynamic force coefficient C_F compared with the experimental measurements (Lopez-Pavon and Souto-Iglesias (2015)), and prescribed heave motion.

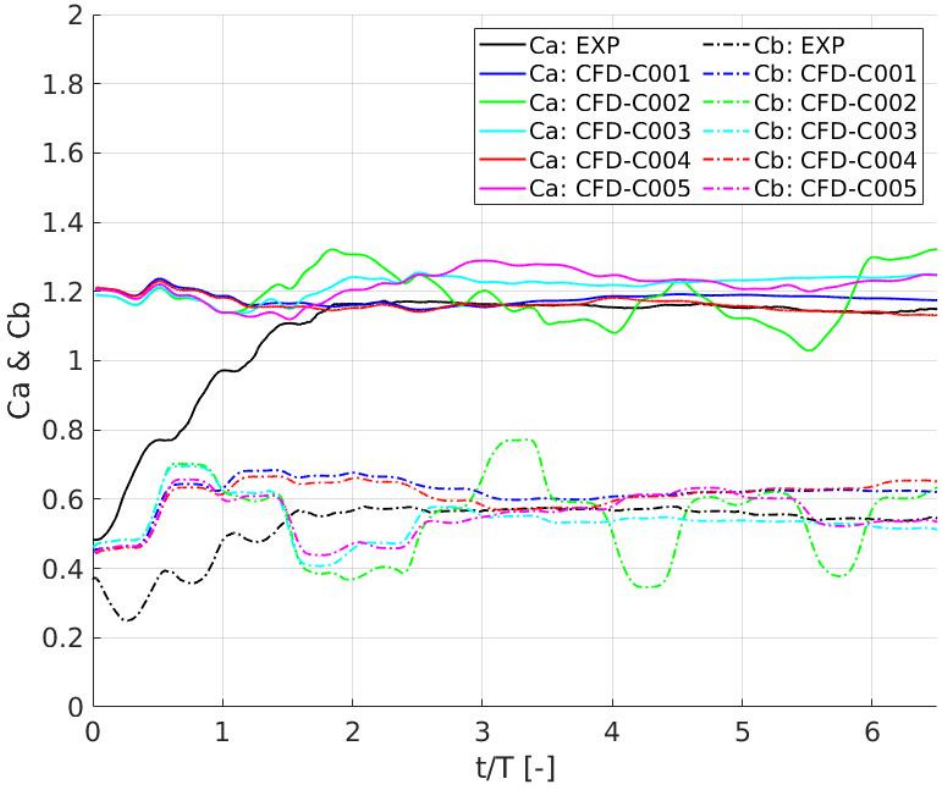

Figure 4.9 – Added mass and damping coefficients from the numerical simulations and the experiments (Lopez-Pavon and Souto-Iglesias (2015)).

CHAPTER 5

EXPERIMENTAL DESIGNS AND SETUP

The "HP Flow" project, which has been funded by WEAMEC, aims to develop a comprehensive understanding of the hydrodynamics on heave plates dedicated to floating wind platforms. Captive model test experiments were conducted to measure the hydrodynamic loads caused by waves or motions. The tests were carried out using a simplified experimental model: a truncated vertical and free-surface piercing circular cylinder. The model had heave plates of various sizes at the bottom, which were specifically designed for semi-submersible floaters used in the floating wind project. This chapter provides a general overview of the experimental setup, model configurations, acquisition systems, and the preparation of the experiments.

5.1 Introduction

The main objective of the experiments is to obtain the hydrodynamic loads on heave plates dedicated to the design characteristics of floating wind turbines (FWTs), which differ from conventional offshore structures such as TLP and SPAR platforms. The experiments aim to investigate three key aspects regarding the hydrodynamic loads based on the literature review: (1) flow characteristics, (2) plate geometrical characteristics, and (3) proximity to the free surface.

There are two main categories of experimental setups for studying the hydrodynamic loads on experimental models. The first is called **captive model tests**, which directly measures the loads acting on the model using a multi-component force balance installed on the model. This method uses motion mechanism platforms such as a Planar Motion Mechanism (PMM) or a hexapod to apply predetermined motions with specific degrees of freedom. Captive model tests are commonly used to obtain hydrodynamic coefficients to be utilized in mathematical models, particularly in seakeeping (equations of motion) and maneuvering (Maneuvering Modeling Group, MMG, model). Most studies have focused on wave-fixed body interaction or calm water-moving body interaction, as the mechanism platforms constrain the model.

The second is **moored tests**, which aim to measure the motions and the forces exerted

on the floating body. The exerted loads can be measured by load cells integrated into mooring lines. Additionally, the loads can be indirectly obtained using the stiffness of the mooring lines based on the floaters' movement. This setup also allows for free decay tests, which estimate the system's natural period and the damping occurring in this free oscillation. Although such tests are widely used as the setup reflects a more realistic design, setting up the mooring line arrangement and non-linear line dynamics (e.g., snapping) remains challenging. Furthermore, there is a limitation to investigating the hydrodynamic loads with a wide range of motion amplitudes and frequencies.

Therefore, the present study utilizes the captive model technique, which involves using a hexapod to induce specific body motions at a particular amplitude and frequency. The loads induced by the motions were measured by a force transducer. The experiment consists of two campaigns: one with a fixed model and incident waves (diffraction problem) and the other with a forced oscillating model without incident waves (radiation problem). For the first campaign, three long-crested waves are tested: monochromatic waves (a single regular wave), bichromatic waves (two regular wave components), and irregular waves. These waves allow the investigation of wave diffraction loads in different wave frequency regimes, namely low frequency, wave frequency, and high frequency. The second campaign tests pure surge, heave, and pitch sinusoidal motions with a wide range of motion amplitudes and frequencies. The study focuses on investigating the hydrodynamic loads that depend on the motion, plate properties, and proximity to the free surface. The added mass and damping are determined by analyzing the harmonic contents of the loads.

The following sections provide details about the wave tank facilities, the captive system, the experimental model configurations, acquisition systems, and the preliminary tests. The results of the measurements are presented in detail in Chapter 6 for the wave diffraction tests and in Chapter 7 for the radiation ones.

5.2 Hydrodynamic and ocean engineering tank

The experiments are carried out in the hydrodynamic and ocean engineering tank of Ecole Centrale Nantes (see Figure 5.1). The main dimensions of the tank are 48.4 m in length, 30.0 m in width, and 5 m in water depth h. The tank is equipped with a flap-type wave maker (composed of 48 flaps mounted on a hinge) to generate the waves and an absorbing beach with 9.7 m of length to reduce the reflected waves. The wave maker can generate regular waves with periods from 0.5 s to 5.0 s, and the maximum wave height is limited to 1.0 m.

Captive model tests are conducted to measure hydrodynamic loads induced by waves and body motions. The model is located 17.2 m away from the wave maker in a longitudinal direction and 15.0 m away from each side of the tank. The Galilean reference frame, $\{O\}$, is the earth-fixed coordinate system given by (O_0, X_0, Y_0, Z_0) where the origin of the frame O_0 is located on the free surface, 17.2 m from the wave maker in the x-direction and 15.0 m from the sidewall in the y-direction.

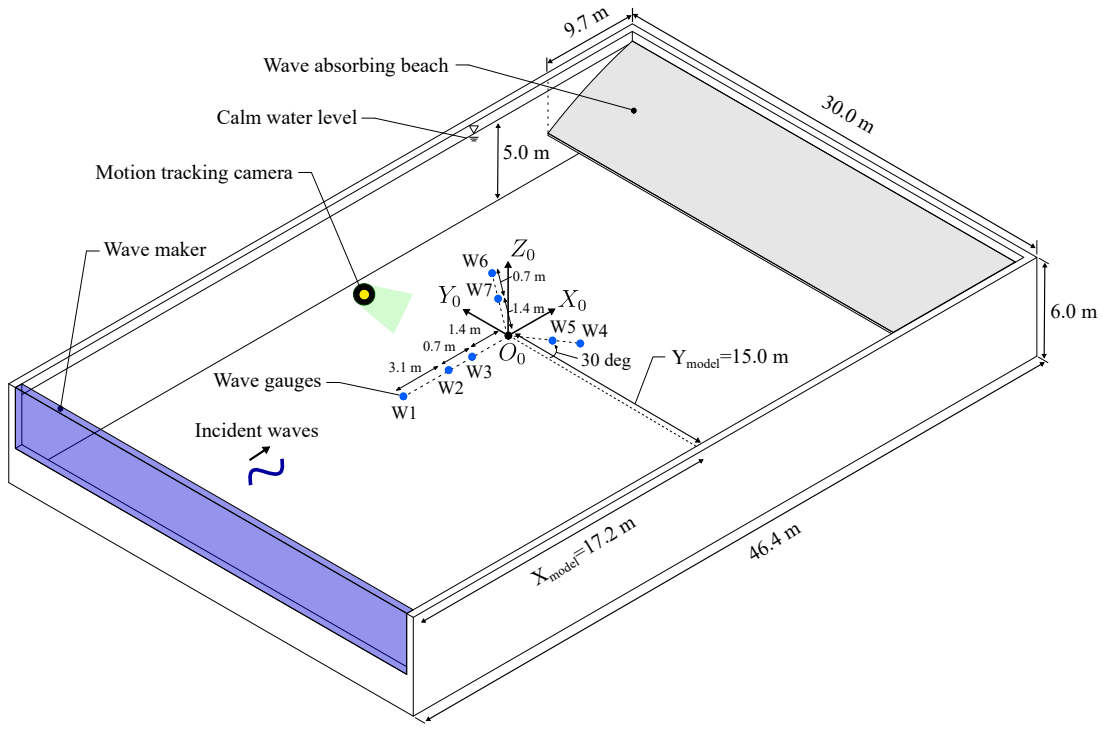

Figure 5.1 – The hydrodynamic and ocean engineering tank at Ecole Centrale Nantes. The Galilean reference system, (O_0, X_0, Y_0, Z_0) is defined as 17.2 m away from the wave maker and 15.0 m from the side wall. The positive x-axis is towards the wave-breaking beach, and the z-axis is pointing upward. Incident waves are propagating in positive x-direction.

5.3 Captive system

A captive model technique is employed to restrict or impose body motion as a function of amplitude ξ and frequency ω. The captive system consists of a tripod and hexapod, as shown in Figure 5.2a. The system is installed in the center of the tank. The tripod is a rigid, heavy jacket structure measuring 12.6 m wide and 7.2 m high. In particular, the free surface piercing part of the tripod has a truss structure to minimize interference caused by wave diffractions. The whole structure is firmly fixed at the bottom of the tank.

The hexapod, a forced motion generator, is equipped with fixed and mobile platforms, as illustrated in Figure 5.2b. The fixed platform is installed on the tripod, and the hexapod is placed above the free surface. The mobile platform is moved by six electric actuators within the operational limits described in Table 5.1. The experimental model is mounted on the mobile platform, and the hexapod imposes the motion with six degrees of freedom.

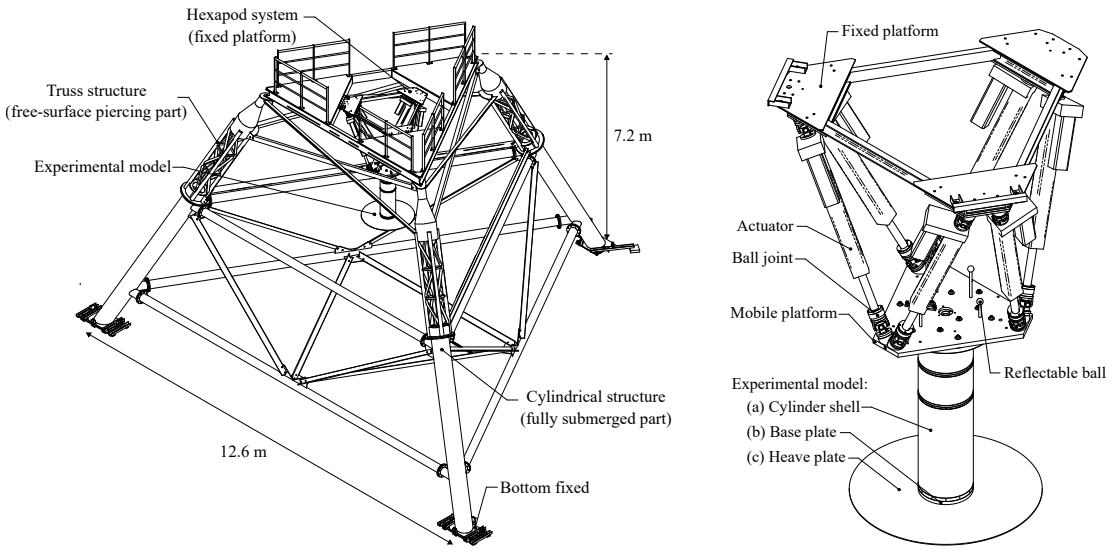

(a) Tripod structure **(b)** Hexapod system

Figure 5.2 – The captive system consists of the tripod and hexapod. The experimental model is mounted on the mobile platform of the hexapod.

Table 5.1 – Main characteristics of the hexapod

Motions	Displacement	Velocity	Acceleration	Frequency range	Precision
Surge	± 465 mm	± 1000 mm/s	± 20000 mm/s^2	0 - 3 Hz	± 1 mm
Sway	± 465 mm	± 1000 mm/s	± 20000 mm/s^2	0 - 3 Hz	± 1 mm
Heave	± 300 mm	± 600 mm/s	± 12000 mm/s^2	0 - 3 Hz	± 1 mm
Roll	± 30°	± 70 °/s	± 1200 °/s^2	0 - 3 Hz	± 0.1°
Pitch	± 30°	± 70 °/s	± 1200 °/s^2	0 - 3 Hz	± 0.1°
Yaw	± 45°	± 120 °/s	± 2000 °/s^2	0 - 3 Hz	± 0.1°

5.4 Experimental model with heave plates

The experimental model is designed as a single vertical, free-surface piercing circular cylinder with a circular plate mounted at the bottom. This model has three main components, as illustrated in Figure 5.3a: an outer cylinder shell, a base plate, and a heave plate. The cylinder shell is designed to be divided into three parts, which allows to consider three submerged drafts: deep, middle, and shallow. The shell is connected to the base plate and completely sealed for waterproofing. Additionally, the heave plate is mounted to the base plate and could be replaced by another plate.

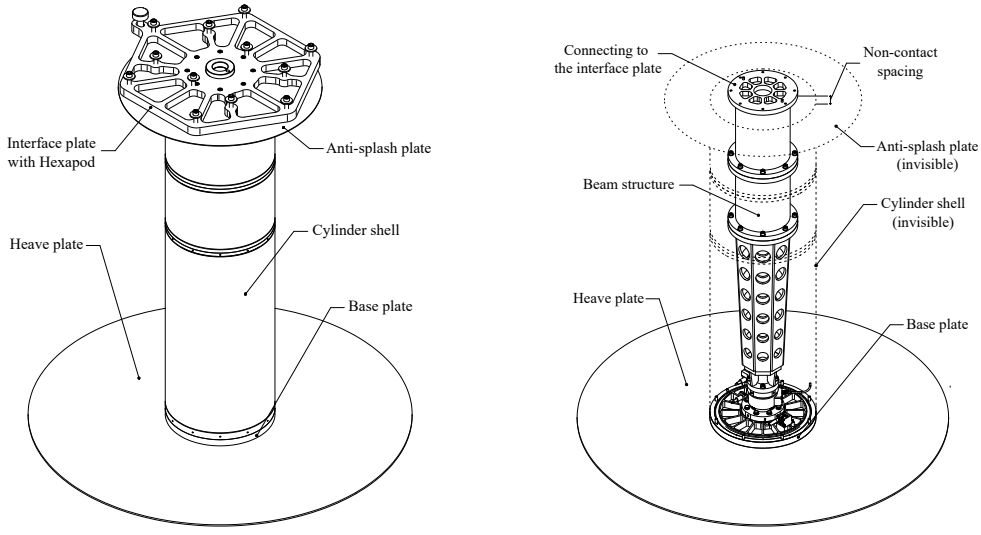

(a) Outlook of the model **(b)** Inside of the model

Figure 5.3 – General arrangement of the experimental model and beam structure.

Figure 5.3b illustrates the internal structure of the model. The base plate of the model is linked to a rigid beam structure through a force transducer. The beam structure is mounted on the hexapod using an interface plate. This arrangement enables measurement of the total load exerted on the cylinder and plate. The beam structure can also be separated into three smaller parts to adjust the draft easily. The height of the beam structure is higher than that of the cylinder to make the model independent of the hexapod. An anti-splash plate is installed on the top of the cylinder to prevent the water from overtopping due to wave run-ups or splashes, ensuring the safety of the sensors inside the cylinder.

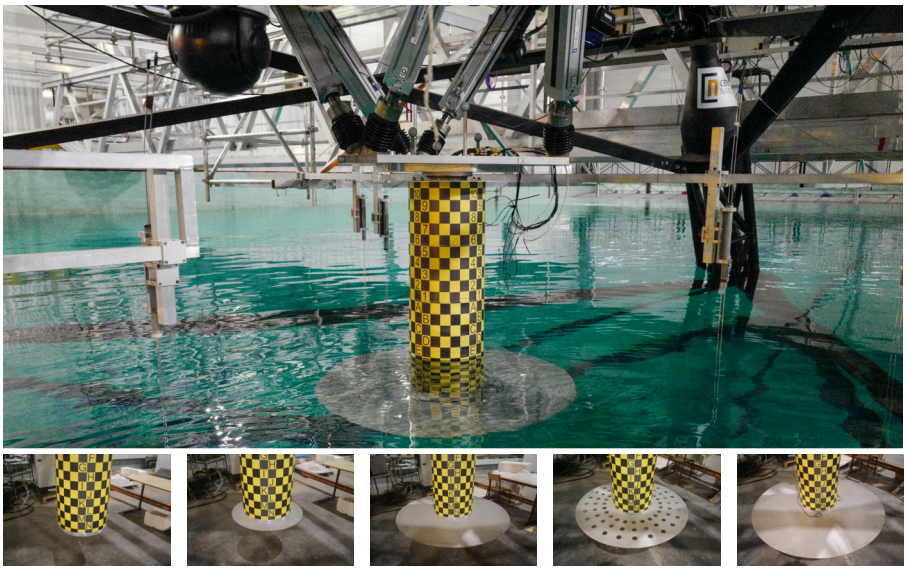

Figure 5.4 – The captive model in the wave tank: a truncated cylinder with a heave plate mounted at the bottom. Five heave plates with diameter ranging in $1.0 \leq D_d/D_c \leq 3.5$, including a perforated plate with 10% porosity ratio.

The main dimensions of the model configurations are summarized in Table 5.2. Five plate configurations are selected, represented by the cylinder diameter D_c and plate diameter D_d (see Figure 5.4). The plate diameter ratios (D_d/D_c) are adapted from real FWT projects, mostly semi-submersibles: e.g., Floatgen (Choisnet et al. (2016)), DeepCwind (Robertson et al. (2020)), HiPRWind (Lopez-Pavon et al. (2015)) and WindFloat platforms (Roddier et al. (2010)). In addition, a porous plate with porosity ratio τ=10 % is considered for the diameter ratio $D_d/D_c = 2.9$. The plate thickness t_d is 5 mm for all configurations. The effect of plate

aspect ratio (t_d/D_d) is not considered, as the plate is thin for all configurations. The detailed drawings are provided in Appendix C.

The center of the cylinder at rest is located at the origin of the Galilean reference frame, which is 17.2 m and 15.0 m from the wave maker and the side wall, respectively. The distance between the model and the tank bottom is 4.225 m based on the maximum submerged draft d = 0.775 m. Therefore, the wall boundary effect on the side and bottom of the tank is negligible in this study.

The heave plate is made of stainless steel to provide sufficient stiffness, while the other parts of the model are made of aluminum. Natural frequencies of the model are measured in both dry and wet conditions using hammer tests conducted inside and outside the wave tank (see Section 5.7.2). Each configuration has different natural frequencies due to variations in total mass and the plate's diameter. Multiple modes are observed, particularly because of the plate. The wet mode generally appears at a lower frequency than the dry mode due to the added mass of the fluid. Additionally, the frequency at the deep draft is slightly lower than at the shallow draft. Therefore, the lowest natural frequency is observed at around 5 Hz for the largest plate ($D_d/D_c = 3.5$) at the deep draft ($d/D_c = 2.2$). This value serves as a reference for the signal processing to filter out the structural response from the measured signal and determine the limit of harmonic analysis.

Table 5.2 – Dimensions of experimental models: a truncated circular cylinder with and without heave plates

Parameters	Unit	Model A	Model B	Model C	Model D	Model E
D_c	m	0.35	0.35	0.35	0.35	0.35
D_d	m	0.35	0.53	1.00	1.00	1.23
t_d	m	0.005	0.005	0.005	0.005	0.005
d	m	0.775, 0.250	0.775, 0.250	0.775[1], 0.500[2], 0.250[3]	0.775, 0.250	0.775, 0.250
Δ[4]	kg	74.6, 24.1	75.2, 24.7	78.0, 51.6, 27.5	78.0, 27.5	80.0, 29.5
m[5]	kg	36.9, 24.7	41.6, 29.5	64.2, 58.1, 52.1	60.9, 48.8	79.7, 67.6
τ	-	0.0	0.0	0.0	0.1	0.0
D_d/D_c	-	1.0	1.5	2.9	2.9	3.5
d/D_c	-	2.2, 0.7	2.2, 0.7	2.2, 1.4, 0.7	2.2, 0.7	2.2, 0.7
Note	-	Truncated cylinder	Truncated cylinder with heave plate			

[1]Deep draft ($d/D_c = 2.2$), [2]middle draft ($d/D_c = 1.4$), [3]shallow draft ($d/D_c = 0.7$).

[4] Δ is the mass of the displaced fluid, [5] m is the mass of the experimental model.

5.5 Instrumentation

The measurements include motion, motion-induced hydrodynamic loads, free surface elevation, accelerations, and strains on the plate. The sensors to measure the physical quantities of interest are introduced in this section.

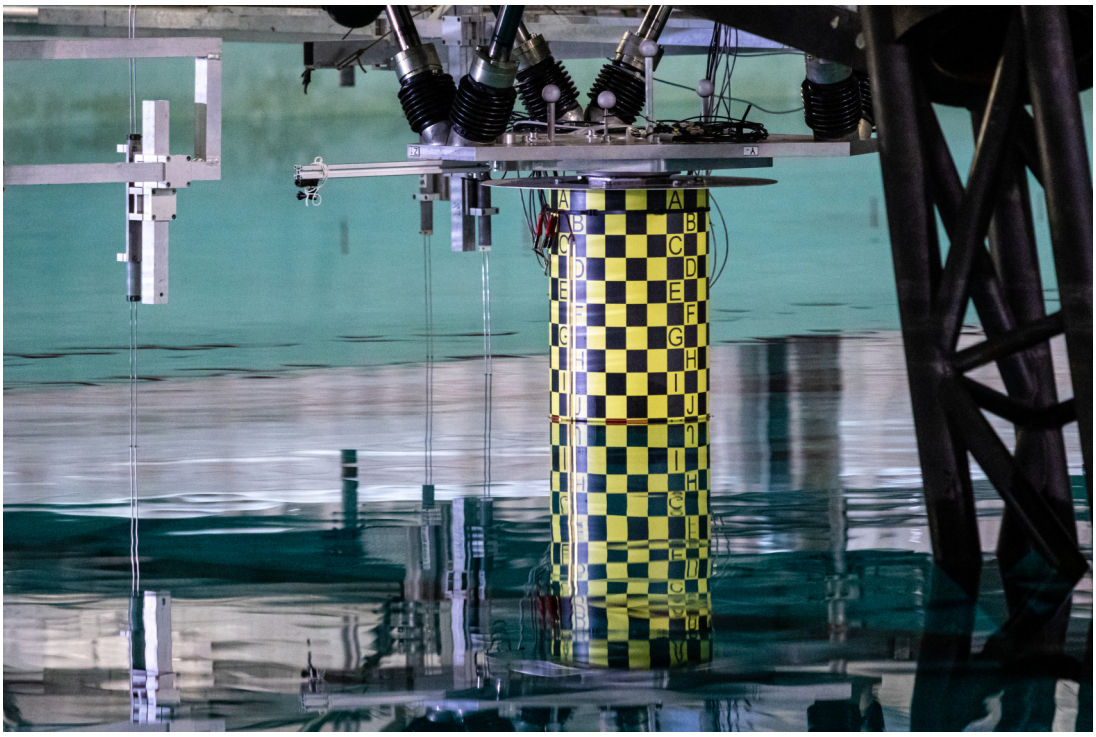

Figure 5.5 – Wave gauge arrangement for the resistive wave gauges around the truncated cylinder and the surface wave gauges on the cylinder's surface.

5.5.1 Sensors

Free surface elevations are measured by 8 resistive wave gauges installed in the ocean engineering tank (see Figure 5.5). The calibration factors (mm/V) are found before the installation using step-wise vertical movements in a large bucket with a water temperature similar to that of the wave tank. Wave gauge number 8 (WG 8) is first placed at the model's position (O_0) in the wave tank. This WG 8 measures incident waves without body interference. An iterative procedure is used to correct the measured waves in order to match the target value using an amplification factor on the wavemaker motion. The experimental model then replaces this wave gauge during the test campaign. WG1 is located between the model and the wave maker to measure the incident wave. The others (WG2-7) are distributed around the model to

measure the diffracted and radiated waves at intervals of 120 degrees in the circumferential direction and 1.4 m and 2.1 m from the center of the model at rest, O_0, in the radial direction as given in Figure 5.1. Additionally, 5 wave gauges are installed on the cylinder surface for the shallow draft configurations. They are evenly distributed on one side of the cylinder at 30-degree intervals to measure the wave run-up, including the weather and lee sides.

The 6 DOF body motions are recorded by a motion tracking system of Qualisys utilizing 3 cameras positioned around the model, fixed on the tripod. Four reflectable balls are installed on the hexapod (see Figure 5.5), and the cameras follow the movement of the balls. After installing the captive system in the tank, the Qualisys system is calibrated using an L-shaped calibration rod based on the hexapod mobile platform, where the reflectable balls are installed. This calibrated rod serves as a reference frame for the Qualisys system. The motion data is used to verify the movement against the prescribed motions of the hexapod and detect any deviation from the target motion. The velocity and acceleration of the model are calculated based on the measured motions.

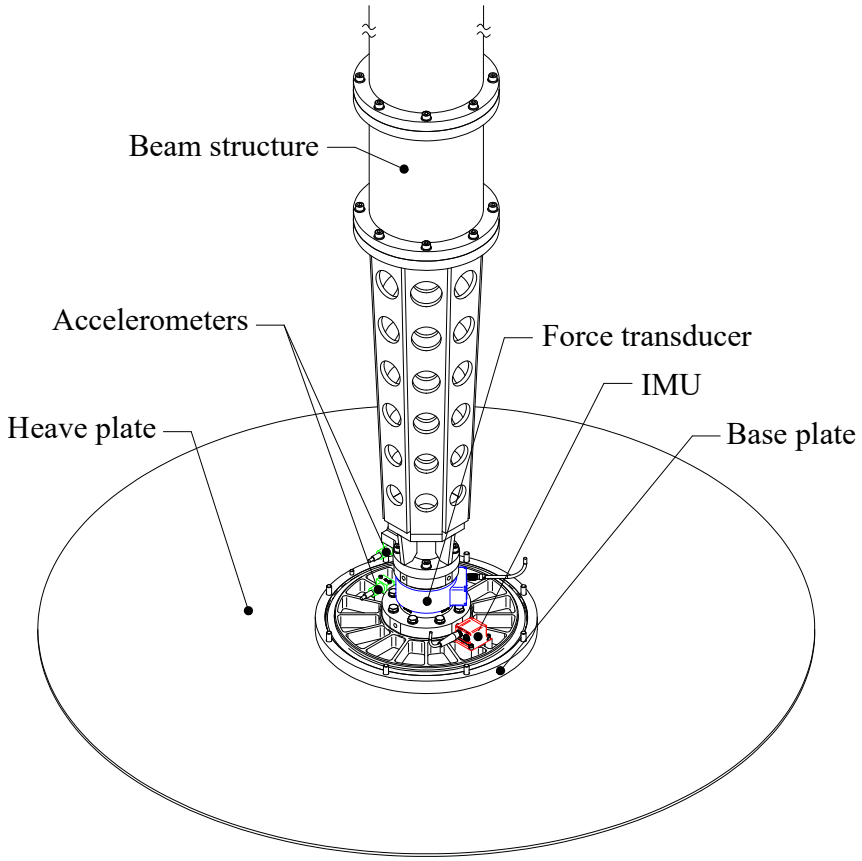

Figure 5.6 – General arrangement of the sensors inside of the cylinder shell: the force transducer (blue), IMU (red) and accelerometers (green).

Figure 5.6 presents sensor arrangements inside the cylinder shell. A six-component force transducer (HBM: MSC10-BG2) is installed between the heave plate and the beam structure. The nominal forces and moments of the transducer are 2 kN for F_x, 10 kN for F_z, and 0.15 kN•m for M_y. The sensor is chosen based on the possible range of measured loads computed by the numerical simulations. Furthermore, two accelerometers installed on the base plate and beam structure are used to check each structural vibration. An inertial measurement unit (IMU) is also utilized to check the Euler angles and angular rate to verify the measured motion signal by Qualisys.

The structural responses of the plate induced by loads are of interest for the present study. 9 strain gauges are installed only for the largest plate ($D_d/D_c = 3.5$) as shown in Figure 5.7. The gauges are divided into three sets (A, B, and C) and installed on the plate surface at a 45-degree angle corresponding to the front, side, and back of the cylinder. The strain gauges are also positioned close to the cylinder, 4 cm away from the cylinder, to obtain the highest strains. They are covered with silicon to make them waterproof, and the interference of the strain gauges on the flow is mitigated since the sensors and the cables are very thin.

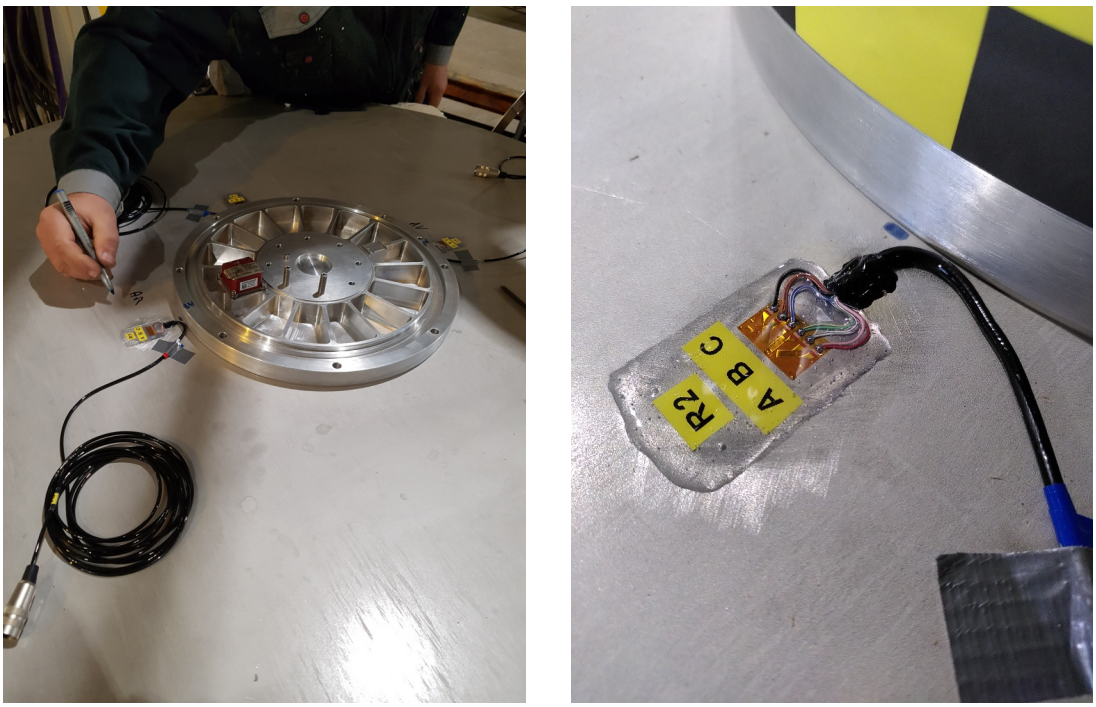

Figure 5.7 – Pictures of strain gauges on the largest heave plate ($D_d/D_c = 3.5$, Model E).

5.5.2 Reference frames of loads and motions

As the sensors are installed in different positions of the experimental model, the measured quantities, such as the forces, moments and 6 DOF motions, are expressed in their own reference frame. Therefore, a body-fixed coordinate system $\{b\}$, given by (O_b, X_b, Y_b, Z_b) is introduced to harmonize the physical quantities in a single reference frame. Tait-Bryan angles are defined with Yaw ψ, Pitch θ, and Roll ϕ based on the Galilean frame as illustrated in Figure 5.8. The origin of the body-fixed reference frame O_b is located on the free surface and the center line of the cylinder, allowing all quantities to be expressed in the same reference for different drafts. Therefore, the origins of both the Galilean and body-fixed reference frames are identical when the model is at rest. The measured quantities pass the transformation matrix to the body fixed frame, $\{b\}$.

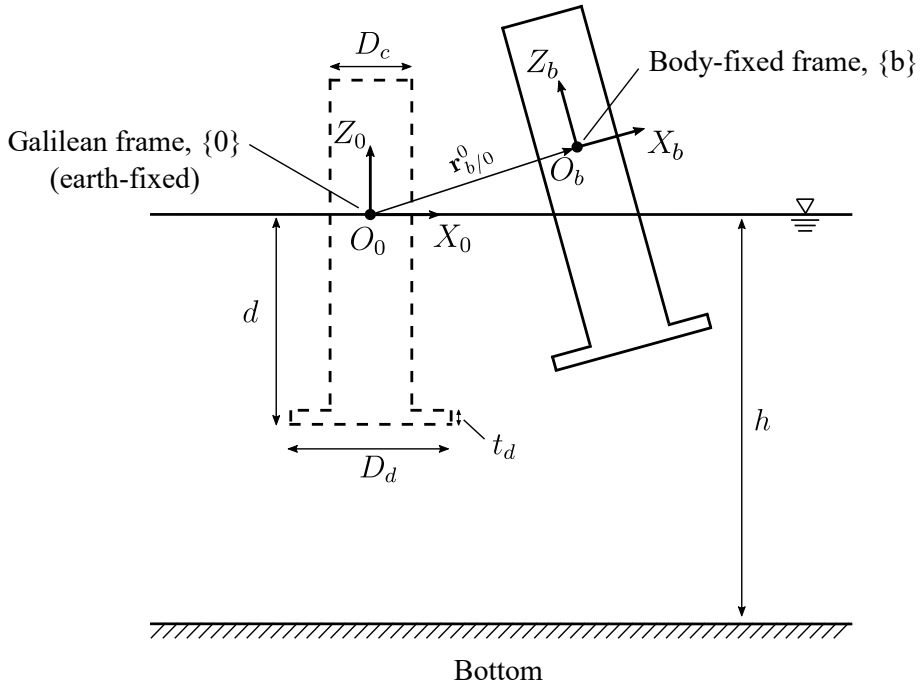

Figure 5.8 – The definitions of the Galilean reference frame and body-fixed reference frame.

5.6 Acquisition system

This section describes the acquisition system, from measurements to merged data files through synchronization.

5.6.1 System configuration

The design of the data acquisition system for the present study is shown in Figure 5.9. The entire acquisition system is managed by a Labview-based program called CN-Master, developed by LHEEA. This program is installed on the master computer and can communicate with the data acquisition software, Catman (HBM), and the motion tracking system Qualysis. The instruments, except for the motion tracking system, provide real-time physical quantities or voltage signals to the Catman software through a data acquisition system (DAQ), HBM Quantum, which can reduce power and ground noises. The voltage signals are processed using calibration factors in the Catman software and the software then exports the measured physical quantities in a data file for signal processing.

Two additional computers for wavemaker and Qualisys software are integrated into the master computer. The Qualisys software is linked to the camera and records the body motion in six degrees of freedom written in the Qualisys file format. The wavemaker software controls the wave generation with given wave condition parameters. The wavemaker motions are saved as a data file. The CN-Master can control the computers by sending a trigger to the other software with a designated sequence. For example, when the CN-Master starts the measurements, trigger #1 is sent to the Catman and Qualysis to begin recording all physical quantities and the hexapod's movements, respectively.

On the other hand, the hexapod system is an individual system that is not connected to the CN-Master. Those two systems need to communicate to synchronize all the signals with the hexapod motion. Therefore, to make a bridge between both systems, a pulse-like yaw motion is modeled in the hexapod motion called "hexapulse" before imposing the prescribed motions of interest. This allows the CN-Master to recognize the hexapod's movement through Qualisys instantly. When CN-Master detects the hexapulse, it sends an event to the Qualisys software within a given time from the peak time of the detected pulse. This event is stored in the Qualisys motion file. Simultaneously, the CN-Master sends trigger #2 to wavemaker to order the wavemaker to generate the waves. The trigger #2 is also stored in the Catman. Finally, when the flaps of the wavemaker start moving, the wavemaker software sends trigger #3 to Catman to record the actual start of the wavemaker. The detailed sequence with the trigger is illustrated in

Figure 5.9.

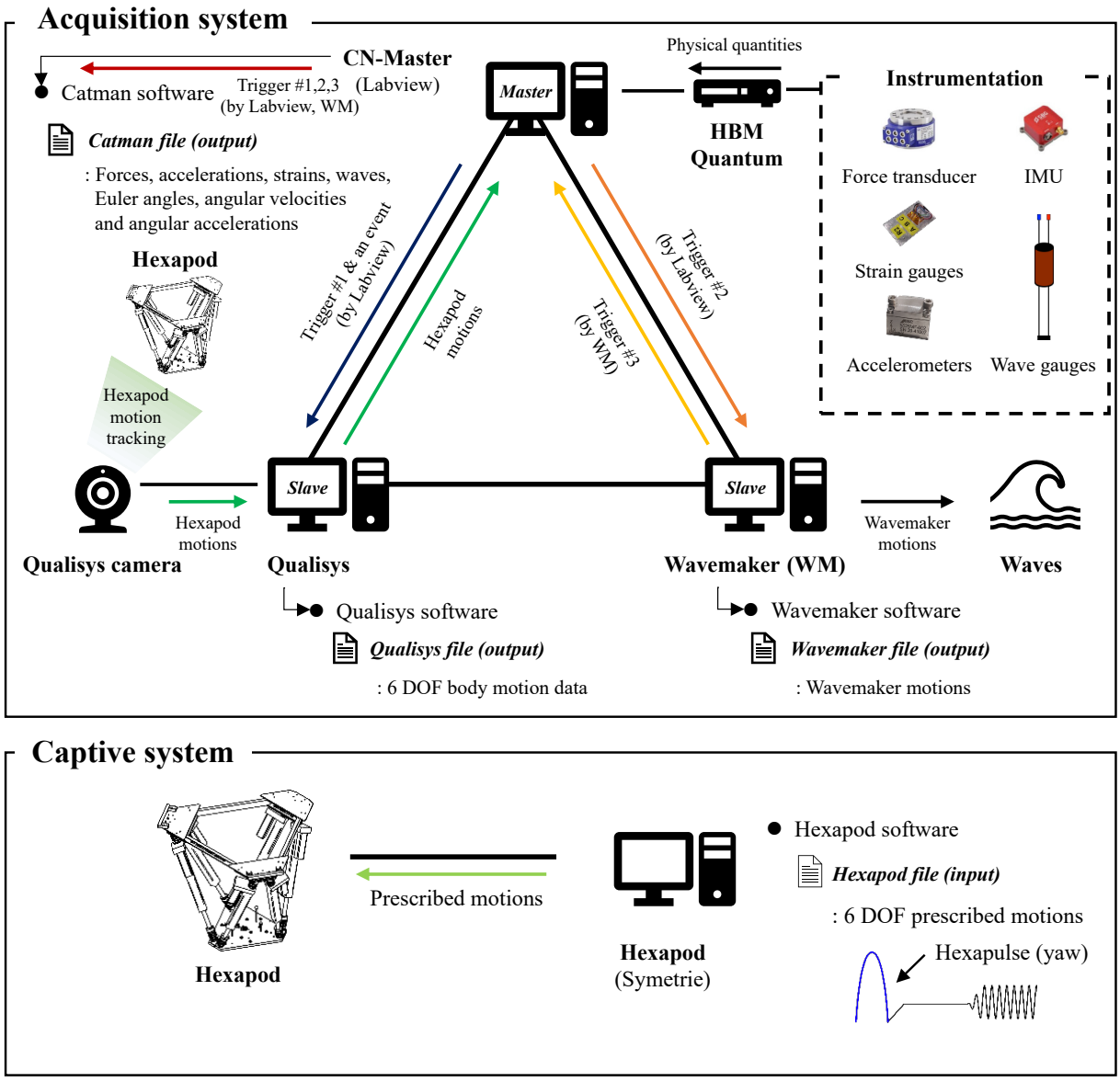

Figure 5.9 – Configurations for the acquisition system and hexapod system.

5.6.2 Synchronization

Synchronizing individual data files is essential for merging them into a single file. To achieve this, the hexapod motion involves three steps as illustrated in Figure 5.10: hexapulse (t_{hp}), pause for zeroing (t_p), and prescribed motions ($t_{mot} + 2 \times t_{ramp}$). The hexapulse is a pulse signal designed as a yaw motion with an amplitude of 1 deg and a period of $t_{hp} = 2$ s that minimizes the effects of body motions into the fluid.

After the hexapulse, the hexapod moves to the target position and waits for an additional $t_p = 30$ seconds to get the zeroing value, namely "pause for zeroing". If the test involves waves and imposed motions, CN-Master waits additionally to compensate for the time the waves arrive at the target position. This duration is determined by the phase velocity $V_p = \omega/k$ where ω is a circular frequency of waves and k is a wave number since the body motions need to be synchronized with the phase of the waves. Finally, the prescribed motion starts with a ramp function. Note that in the case of the diffraction test (without motions), the synchronization is done without the hexapulse when the wavemaker starts.

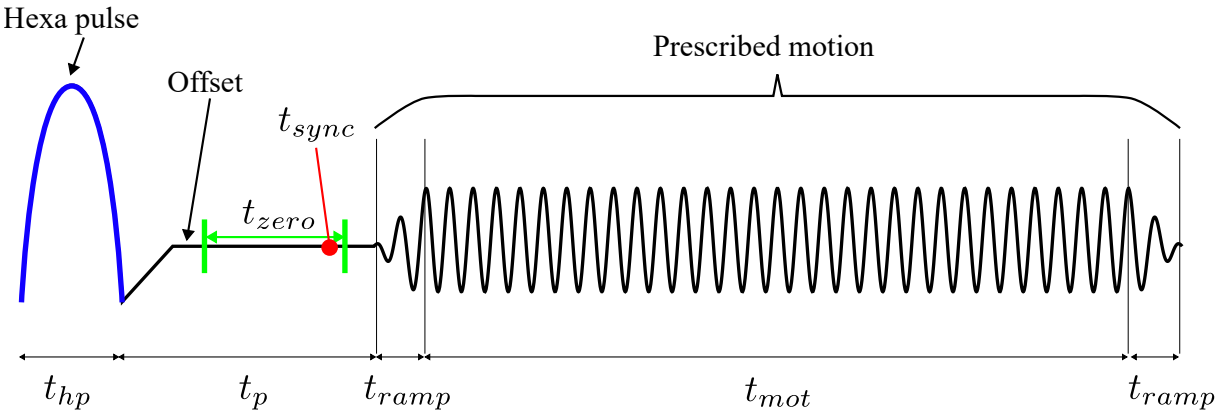

Figure 5.10 – Sequence of hexapod motions including a hexapulse for synchronizations.

After completing the measuring procedure, each software exports a data file. These files are merged into a single data set using an in-house Matlab-based program, CN-Analyser, and saved for each test case. All the physical data are then synchronized in time and merged into a single data file, with one column for time and one column for each measurement, see Figure 5.11.

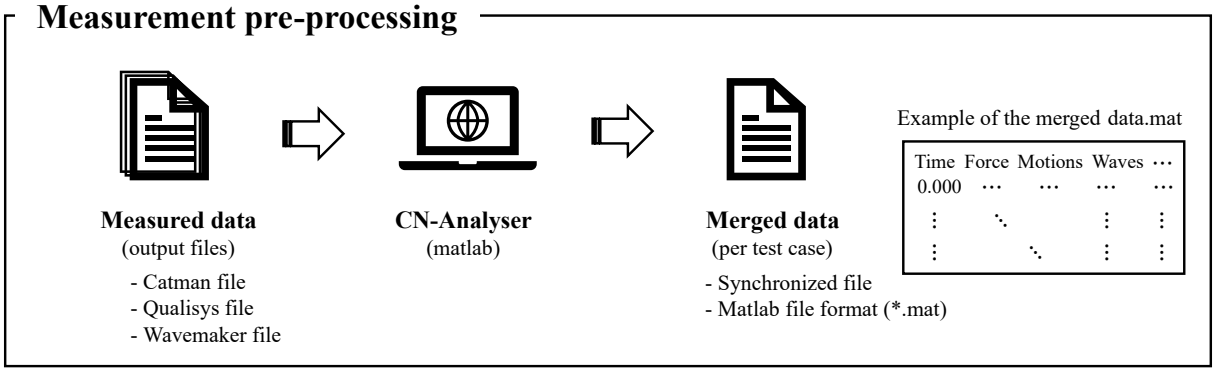

Figure 5.11 – Measurement pre-processing to merge the data files with synchronization.

5.7 Preliminary experiment

This section describes the preliminary experiments that were conducted before the wave tank testing to improve the accuracy of the results. These experiments consisted of wave calibrations, hammer tests, and forced oscillation tests in the air.

5.7.1 Wave calibrations

The wave maker generates waves using a transfer function derived from the linear potential flow theory. This linear transfer function causes a significant deviation when the nonlinear effects increase. Therefore, it is important to confirm the generated wave matches with the target wave, especially for non-linear waves. Furthermore, the waves tend to dissipate as they propagate in the wave tank due to the various sources (e.g., friction on the side wall of the tank) identified by Deike et al. (2012). Therefore, the wavemaker motions must be corrected to reach a target at a given position to improve the quality of the wave generation.

The present study selected three sets of regular waves for different wave steepnesses (H/λ) from 0.02 to 0.06 to investigate the non-linear effects. The regular wave parameters are given in Table 5.3. According to Le Méhauté's diagram (Le Méhauté (1976)), the selected regular waves correspond to Stokes 2nd and 3rd-order waves. A reference wave gauge was installed at the target position (O_0), where the model will be placed for the tests. For each wave condition, an amplification factor for the wavemaker motion was found through three iterative wave generations. These factors aim to correct the small deviation of the transfer function depending on the wave frequency and height. As a result, the generated waves reach the target wave height within a range of 5 % error with respect to the target as presented in Figure 5.12.

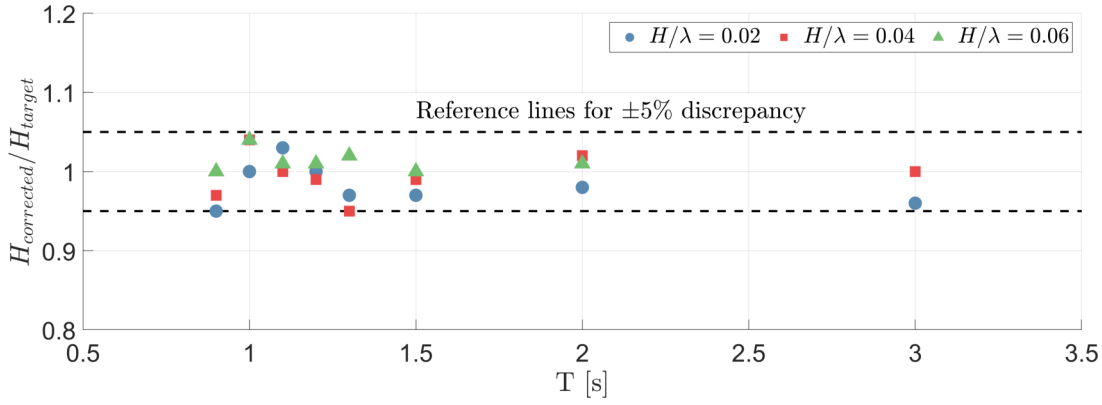

Figure 5.12 – Wave height difference between target waves and corrected regular waves.

Table 5.3 – Wave condition parameters for the regular waves.

H [m]	T [s]	H/λ	H/gT^2	kH	h/λ	h/gT^2	kh
0.025	0.9	0.02	0.003	0.12	3.94	0.63	24.7
0.031	1.0	0.02	0.003	0.12	3.19	0.51	20.0
0.038	1.1	0.02	0.003	0.13	2.64	0.42	16.6
0.045	1.2	0.02	0.003	0.13	2.22	0.35	13.9
0.053	1.3	0.02	0.003	0.13	1.89	0.30	11.9
0.070	1.5	0.02	0.003	0.12	1.42	0.23	8.9
0.120	2.0	0.02	0.003	0.12	0.80	0.13	5.0
0.280	3.0	0.02	0.003	0.13	0.36	0.06	2.3
0.051	0.9	0.04	0.006	0.25	3.89	0.63	24.5
0.062	1.0	0.04	0.006	0.25	3.15	0.51	19.8
0.076	1.1	0.04	0.006	0.25	2.61	0.42	16.4
0.090	1.2	0.04	0.006	0.25	2.19	0.35	13.8
0.110	1.3	0.04	0.007	0.26	1.86	0.30	11.7
0.140	1.5	0.04	0.006	0.25	1.40	0.23	8.8
0.250	2.0	0.04	0.006	0.25	0.79	0.13	5.0
0.550	3.0	0.04	0.006	0.25	0.36	0.06	2.2
0.076	0.9	0.06	0.010	0.36	3.82	0.63	24.0
0.094	1.0	0.06	0.010	0.36	3.10	0.51	19.5
0.113	1.1	0.06	0.010	0.36	2.56	0.42	16.1
0.135	1.2	0.06	0.010	0.36	2.15	0.35	13.5
0.158	1.3	0.06	0.010	0.36	1.83	0.30	11.5
0.211	1.5	0.06	0.010	0.36	1.38	0.23	8.7
0.375	2.0	0.06	0.010	0.36	0.77	0.13	4.9

Examples of calibrated wave profiles and their harmonic content at the wave period of 1.2 s for three wave steepnesses are shown in Figure 5.13. The figure presents 10 individual wave profiles (transparent lines) extracted from the wave time series that overlap for half of the wave period. By comparing with an averaged wave profile given in solid lines, it is noticed that the waves exhibit reasonable temporal repeatability. The first harmonic is predominant among the harmonic content. Higher harmonic components become more significant as the wave height increases. This effect is visible in the wave profile, which shows an increase in wave crest and a decrease in trough. CN-Stream (Ducrozet et al. (2019)), which is based on the stream function theory, accurately predicts the wave profiles measured in the experiment. This theory represents

the first three harmonics well, but the theoretical harmonic amplitudes gradually decrease, resulting in inconsistencies with the experiments as the harmonics get higher, which are linked to the confinement of the wave tank, viscous effects, and other experimental inaccuracies not accounted for in theory.

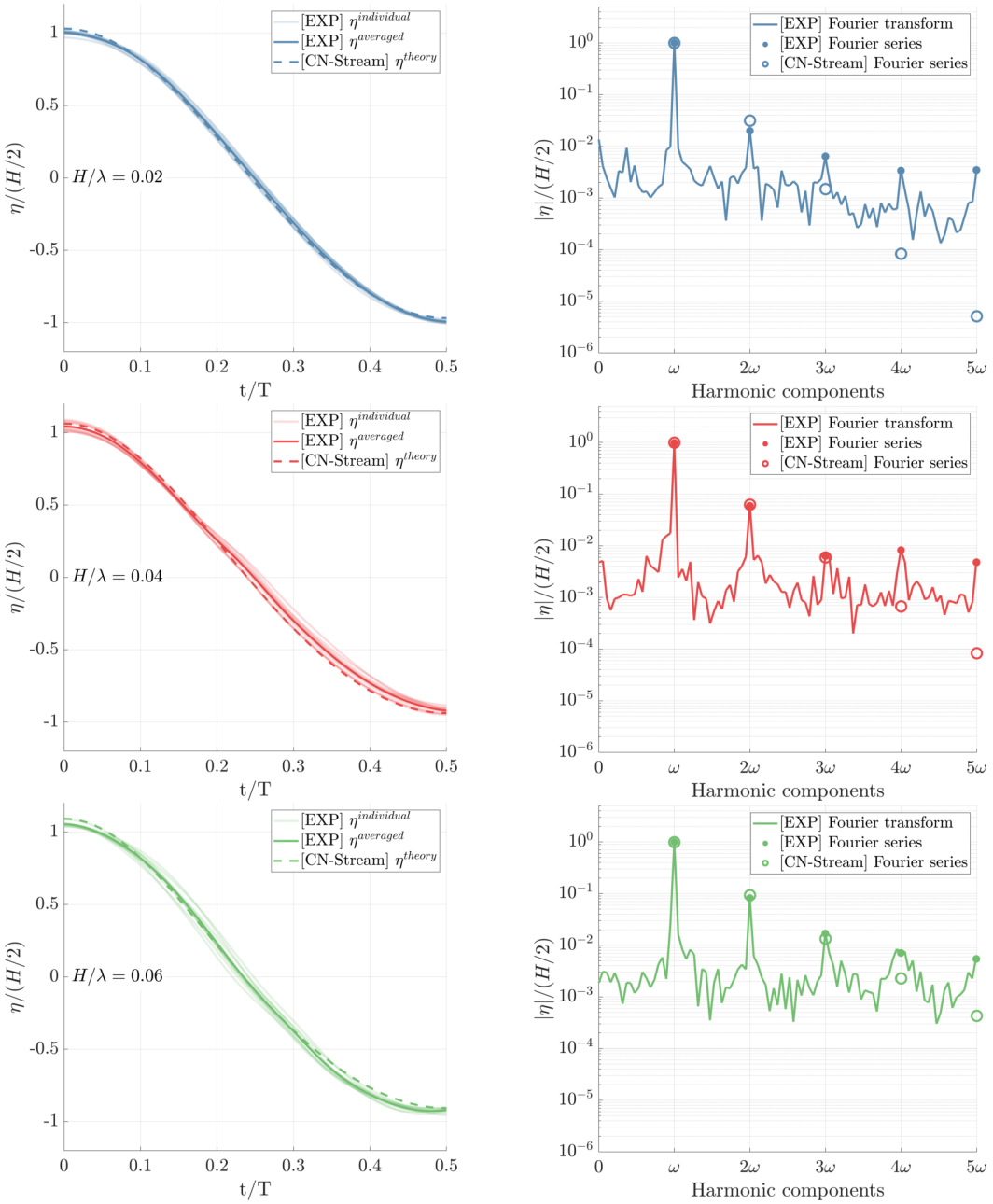

Figure 5.13 – Calibrated wave profiles and harmonics at the wave period 1.2 s with three wave steepnesses ($H/\lambda = 0.02, 0.04, 0.06$).

On the other hand, irregular waves were calibrated in a Numerical Wave Tank (NWT) using the Higher-Order Spectral method (HOS-NWT, Ducrozet et al. (2012)). The dimensions of the numerical tank match the ones of the physical wave tank of the Ecole Centrale Nantes. The characteristics of the wavemaker and reflection beach were also numerically modeled in the simulation.

Two irregular sea states were selected using the JONSWAP spectrum (see Table 5.4). For the irregular wave calibration, 15 realizations of each sea state were considered with different random phases. The time duration of each realization was 1,100 s, which included more than 500 waves. After obtaining an averaged wave spectrum from each realization at the target position, linear amplification parameters, $C^{n+1}(f)$, are computed to correct the wave spectrum for the next iteration $(n+1)$ using the equation below:

$$C^{n+1}(f) = \frac{a_{target}(f)}{a^n_{HOS}(f)} C^n(f) \tag{5.1}$$

where $a_{target}(f)$ is the Fourier amplitude of the target wave spectrum at a given frequency f. $a^n_{hos}(f)$ is the Fourier amplitude of the simulated spectrum in the HOS-NWT at the n^{th} iteration. The detailed procedure can be found in Canard et al. (2020).

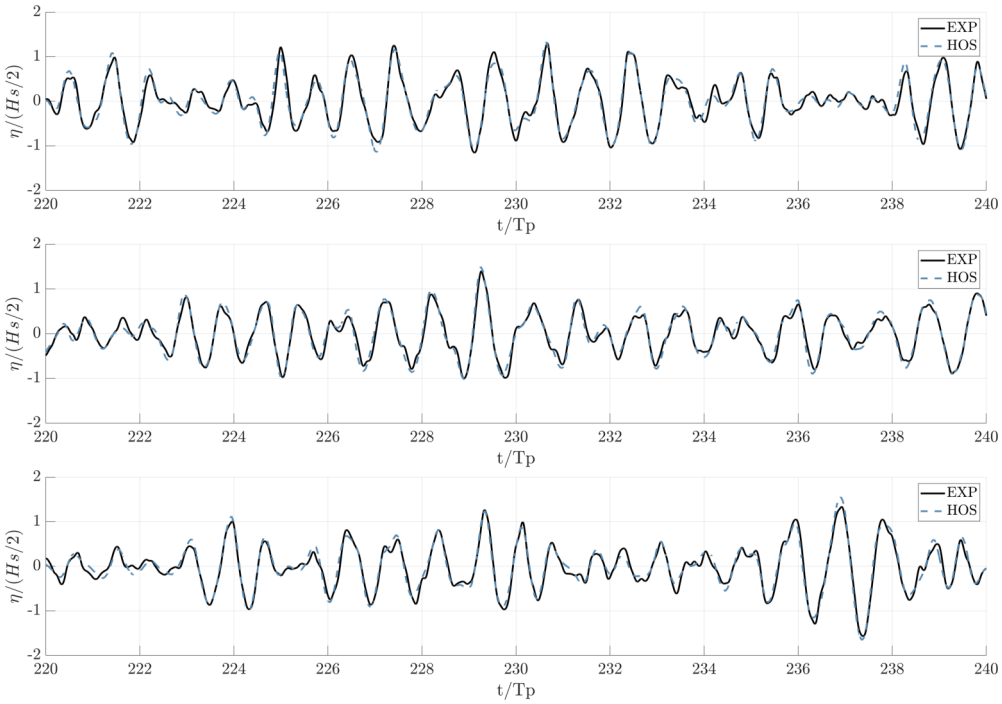

Figure 5.14 – Time series of free surface elevation at the target location for three realizations of the irregular waves ($H_s = 0.125$, $T_p = 2.0$).

Three representative realizations were tested physically in the wave tank after obtaining the calibrated spectrum in the numerical wave tank for each sea state. Figure 5.14 shows the comparison of the computed irregular wave time series and the measured ones at the target location. The waves obtained from the numerical wave tank matched the waves in the physical wave tank in close agreement. An averaged wave spectrum example using the three realizations is provided in Figure 5.15. The measured spectrum shows a good agreement with the target spectrum. Consequently, the spectrum parameters were accurately achieved in a physical wave tank using the corrections derived from the numerical wave tank with a discrepancy of less than 5 %, see Table 5.4.

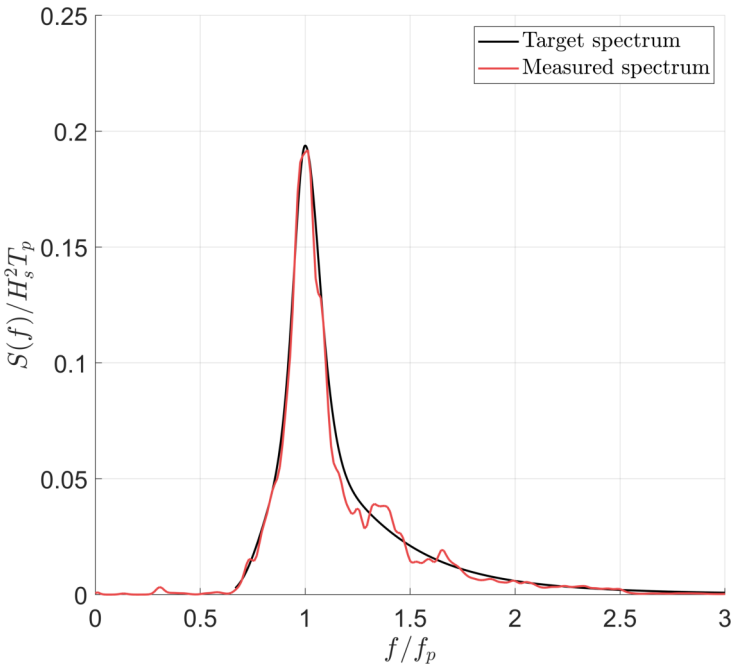

Figure 5.15 – Irregular wave spectrum ($H_s = 0.125$, $T_p = 2.0$) at the target location (black: target spectrum; red: averaged spectrum for the three wave series).

Table 5.4 – Differences in the spectrum parameters between target and measured irregular waves.

Target wave condition				Differences		
H_s [m]	T_p [s]	T_z [s]	γ	H_s^{EXP}/H_s	T_p^{EXP}/T_p	T_z^{EXP}/T_z
0.125	2.0	2.57	3.3	0.97	1.00	1.03
0.250	2.0	2.57	3.3	0.98	0.99	1.00

5.7.2 Hammer tests

The hammer test is a common way to obtain the natural structural modes by imposing an impact load. This test allows for an understanding of how the experimental model responds to the external loads. Furthermore, these natural frequencies need to be identified before the testing as the structural response of the experimental model is one of the possible sources of noise in the measured signals.

The test focused on examining the truncated cylinder with the largest heave plate (Model E with $D_d/D_c = 3.5$) as this configuration is least stiff compared to the others. It was observed that each configuration has different natural frequencies due to variations in total mass and structural stiffness caused by the diameter of the plate. Figure 5.16 represents the structural responses that were measured using an accelerometer installed on the plate. The response was obtained by hitting the plate with a rubber hammer. The time series shows that the structural response highly oscillates over time and decays rapidly after the impact at $t = 52$ seconds.

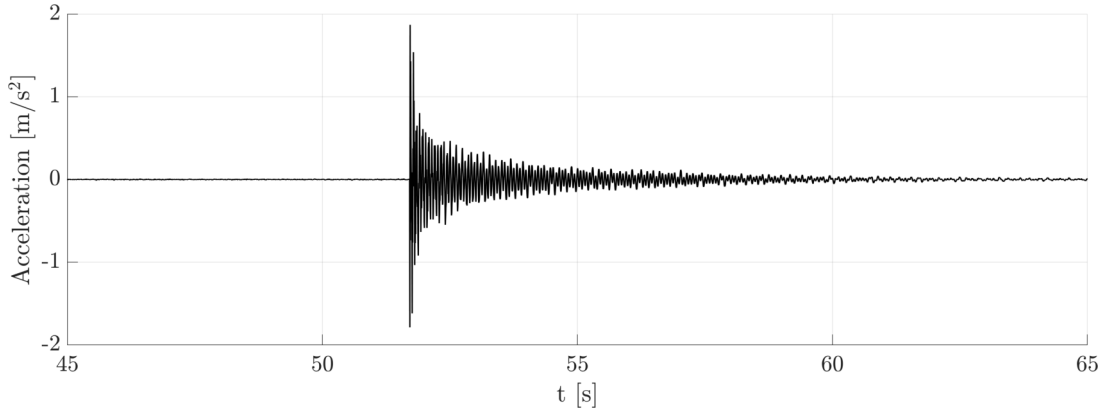

Figure 5.16 – Example of hammer test in the wave tank on the experimental model (D_d/D_c=3.5) at the deep draft (d = 0.775 m).

The study measured the structural responses in both dry and wet conditions using hammer tests that were conducted inside and outside the wave tank. The results of the Fourier transform of the accelerations and strains are shown in Figure 5.17. Multiple peaks are observed with the largest heave plate ($D_d/D_c = 3.5$, Model E). The lowest natural frequency is found at 10.3 Hz for the dry mode and 5.1 Hz for the wet mode. This frequency was confirmed to be due to the first mode of the plate through structural analysis. The peaks measured by the accelerometer are generally aligned with those of the strain gauges. The wet modes appear at lower frequencies than the dry modes due to the hydrodynamic added mass. Therefore, the lowest wet natural frequency serves as a reference for signal processing in Chapters 6, 7.

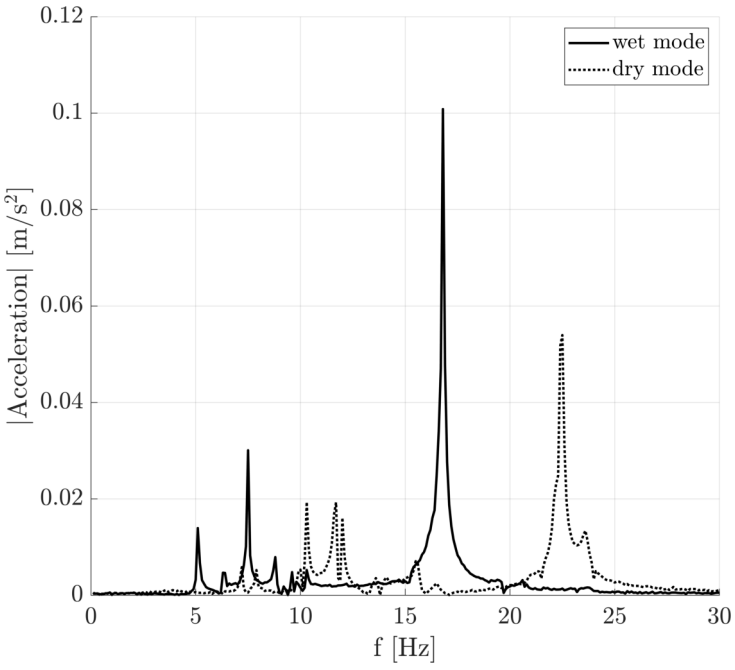

(a) Acceleration

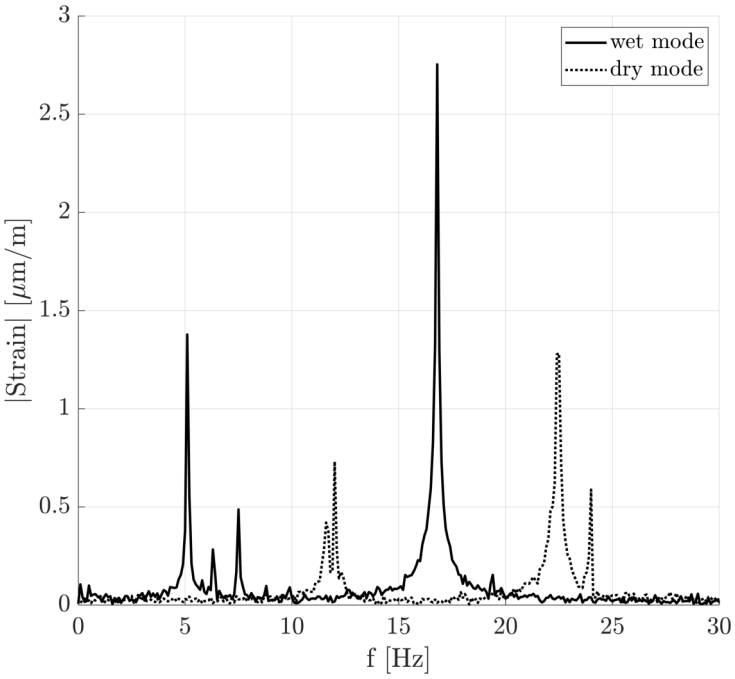

(b) Strain

Figure 5.17 – Measured dry (dashed line) and wet (solid line) natural frequencies of the experimental model (D_d/D_c=3.5) at the deep draft, d = 0.775 m.

5.7.3 Inertia matrix of the model

A procedure to obtain the inertia matrix of the model by imposing motions using the hexapod is presented. Assuming the body is moving in the air, the fluid load is negligible due to the low air density compared to the water density ($\rho_{air} << \rho_{water}$). Therefore, the measured load consists of inertia and gravity loads. The estimation of the position of the center of gravity and of the inertia matrix is made with two series of tests.

Firstly, in quasi-static motions of pure roll and pitch (very low-frequency motion, 0.02 Hz), the contributions of the velocity and acceleration components in the inertia loads can be neglected. This assumption leads to a simplified expression of the equation of motion. The mass and position of the center of gravity can be obtained from the measured forces and moments from the load cell. Then, the moments of inertia are deduced from pure dynamic motions of the roll, pitch, and yaw at higher frequencies (1.0 Hz). The procedure is given in Figure 5.18.

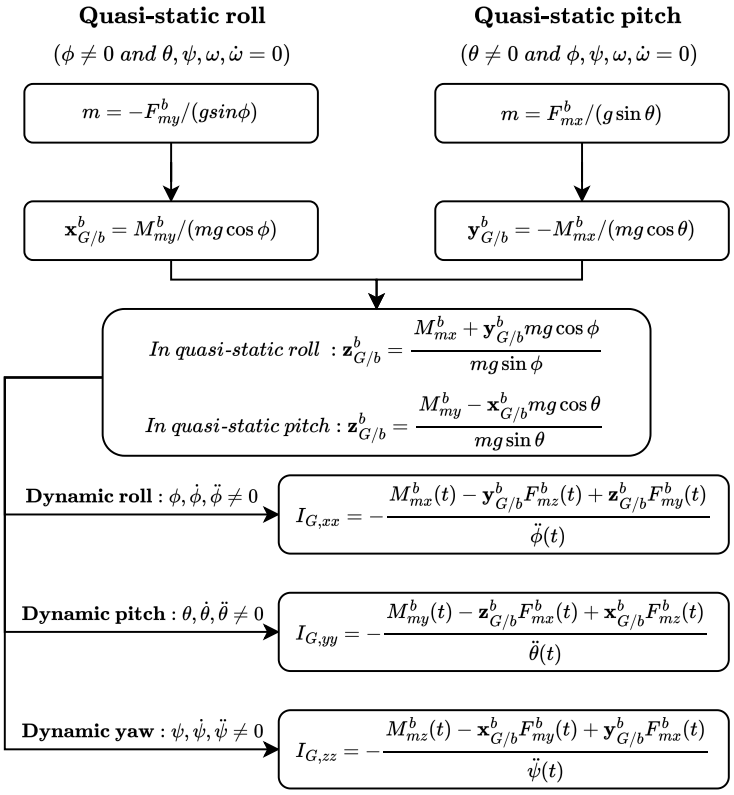

Figure 5.18 – Flow chart for obtaining mass, the center of gravity and moments of inertia of the model from the measurement $\mathbf{F}_m$ and $\mathbf{M}_m$ at O_b. Here, m is the mass, $(\mathbf{x}^b_{G/b}, \mathbf{y}^b_{G/b}, \mathbf{z}^b_{G/b})$ is the vector of the center of gravity from O_b expressed in the body-fixed reference frame and I_G is the moment of inertia at the center of gravity G.

To implement this procedure, tests were conducted on the experimental model configurations before the wave tank testing. An example of a moving cylinder in the air is shown in Figure 5.19 with the test setup installed outside of the wave tank. The force transducer and the Qualisys motion tracking cameras were utilized to measure the loads and motions of the model.

Figure 5.19 – A moving cylinder in the air (outside of the wave tank) to measure the inertia loads.

During the tests, the hexapod imposed two types of motions: quasi-static and dynamic. In the quasi-static tests, the hexapod applied a motion amplitude of 10 degrees for 60 seconds, resulting in negligible angular velocity and accelerations of the inertia components in the measurements. On the other hand, in the dynamic tests, the hexapod applied a 5-degree amplitude motion with a period of 5 seconds. The motion parameters are summarized in Table 5.5.

Table 5.5 – Test matrix for the quasi-static and dynamic rotational motions in the air.

Test type	Motion	T [s]	ω [rad/s]	Motion angle [deg]	Motion angle [rad]	Angular velocity [rad/s]	Angular acceleration [rad/s^2]	Note
Quasi-static	Roll	60.00	0.10	10.00	0.17	0.02	0.00	Mass, $\mathbf{x}_{G/b}$, $\mathbf{z}_{G/b}$
	Pitch	60.00	0.10	10.00	0.17	0.02	0.00	Mass, $\mathbf{y}_{G/b}$, $\mathbf{z}_{G/b}$
Dynamic	Roll	1.00	6.28	6.00	0.10	0.66	4.13	$I_{G,xx}$
	Pitch	1.00	6.28	6.00	0.10	0.66	4.13	$I_{G,yy}$
	Yaw	1.00	6.28	6.00	0.10	0.66	4.13	$I_{G,zz}$

The estimations of the mass, vertical center of gravity, and moments of inertia are summarized in Table 5.6 for all configurations. The results show less than 4 % difference compared to the CAD design tool (SolidWorks). These values are used to calculate the inertial and gravitational loads in Chapter 7.

Table 5.6 – Estimation of the experimental models' mass and moment of inertia from the measurement in the forced oscillation tests in the air.

Model	Draft (d/D_c)	m [kg]	$\mathbf{z}^b_{G/b}$ [m]	$I_{G,xx}$ [kgm^2]	$I_{G,yy}$ [kgm^2]	$I_{G,zz}$ [kgm^2]	Difference (estimation/CAD-1) [%]				
Model A	deep (2.2)	36.9	-0.27	8.7	8.8	0.9	0.2	3.8	-0.1	0.6	0.0
(D_d/D_c=1.0)	shallow (0.7)	24.7	-0.02	2.3	2.3	0.6	1.9	0.0	0.9	0.4	0.0
Model B	deep (2.2)	41.6	-0.33	10.0	10.0	1.1	0.0	3.1	0.0	0.6	0.0
(D_d/D_c=1.5)	shallow (0.7)	29.5	-0.06	2.6	2.6	0.8	1.4	0.0	0.4	0.4	0.0
Model C	deep (2.2)	64.2	-0.48	14.8	14.9	4.8	-0.2	0.0	-0.5	0.5	0.8
(D_d/D_c=2.9)	middle (1.4)	58.1	-0.31	8.8	8.8	4.6	0.3	3.3	-0.5	0.0	0.9
	shallow (0.7)	52.1	-0.14	4.9	4.9	4.5	0.7	0.0	0.6	1.4	0.9
Model D	deep (2.2)	60.9	-0.47	14.3	14.4	4.4	-0.2	2.2	-0.6	0.3	0.9
(D_d/D_c=2.9τ)	shallow (0.7)	48.8	-0.13	4.7	4.7	4.1	0.7	0.0	0.9	1.1	0.7
Model E	deep (2.2)	79.7	-0.54	18.4	18.5	9.8	-0.3	0.0	-0.2	0.6	1.2
(D_d/D_c=3.5)	shallow (0.7)	67.6	-0.17	7.6	7.6	9.4	0.3	0.0	1.6	1.7	1.4

Note 1. $\mathbf{x}^b_{G/b}$ and $\mathbf{y}^b_{G/b} < 0$.

Note 2. $I_b = I_G - m\left(\mathbf{r}^b_{G/b}(\mathbf{r}^b_{G/b})^T - (\mathbf{r}^b_{G/b})^T\mathbf{r}^b_{G/b}I_{3\times3}\right)$ where $I_{3\times3}$ is the identity matrix.

CHAPTER 6

WAVE DIFFRACTION LOADS ON A VERTICAL CIRCULAR CYLINDER WITH A HEAVE PLATE

This chapter focuses on wave diffraction loads influenced by heave plates at deep and shallow submerged depths. It is based on the extensive experimental campaign described in the previous chapter, conducted on a fixed vertical and free-surface piercing circular cylinder with five different circular plates, including a perforated plate. The horizontal and vertical wave forces are examined in monochromatic and bichromatic waves. The results show that the heave plate significantly influences the force time histories and representative harmonics at the zeroth-, first-, second-, sum-, and difference-frequency components. The study also found that wave steepness and submerged depth of the plate contribute to the nonlinearity of the loads and that the porous plate reduces the loads compared to the solid plate. Corresponding results from the BEM solver HydroStar provide a reasonable prediction of the harmonics. However, underprediction of the first harmonic of the vertical forces is found at low frequencies, specifically where the BEM indicates the cancellation of the forces. Dedicated computational fluid dynamics (CFD) simulations are carried out to investigate this discrepancy, and it is observed that flow separation occurs around the edge of the plate. A simplified approach based on the Morison equation is employed to model the flow separation effects as the viscous drag forces. That approach shows that viscous drag is the dominant contributor to vertical wave forces on the heave plate in the low-frequency regime. As a result, the three distinct vertical force regimes with the plates are explained as being a function of the plate diameter and wave frequency. This chapter is written based on the submitted paper, "Experimental study of wave diffraction loads on a vertical circular cylinder with heave plate at deep and shallow drafts" (see Appendix A).

6.1 Introduction

This wave diffraction study aims to experimentally investigate the effect of heave plates on wave diffraction loads and provide as comprehensive an understanding as possible of the domain of validity of engineering models. A fixed vertical and surface-piercing cylinder is studied with and without a circular plate. Five heave-plate configurations, including porosity with varying diameters and a constant plate thickness, are tested with two submerged depths. Two types of waves (monochromatic and bichromatic waves) are used to investigate the influence of the heave plate on wave loads. The monochromatic waves, also known as “regular waves", allow us to measure the loads in different harmonics excited by a single wave frequency, ω. On the other hand, the bichromatic waves are composed of two sets of regular waves (ω_1 and ω_2) designed to obtain the loads occurring at the sum frequency ($\omega^+ = \omega_1 + \omega_2$) and difference frequency ($\omega^- = \omega_1 - \omega_2$) by the interaction of two wave components.

Section 6.2 introduces the wave test parameters for the monochromatic and bichromatic waves, defined by the wave amplitudes and frequencies. Section 6.3 presents experimental data analysis, examining force time series and harmonic content using Fast Fourier Transform (FFT) for all configurations. The measured wave loads are approximated with harmonic components obtained from the monochromatic and bichromatic waves. The correspondence between the measured wave loads and theoretical computations is also presented in this section. The results are provided in Section 6.4. The effects of heave plates on wave loads are investigated with respect to the wave steepness, submerged depths, and porosity. The harmonic content of experimental measurements is systematically compared with the corresponding order from the potential flow theory.

Detailed discussion is made in Section 6.5. The consistency of the present study is first shown on a solitary vertical circular cylinder by comparison with the existing literature. Further investigation employs an incompressible Navier-Stokes (CFD) solver to numerically visualize the flow field around the heave plate, particularly flow separations. A simplified Morison equation is used to model the flow separation as the viscous drag forces. Additionally, we discuss the determination of the drag coefficients for different wave steepnesses and plate diameters. As a result, this section identifies three different vertical wave force regimes based on experimental and numerical investigations, considering wave frequency and heave plate diameter. Finally, the conclusions are given in Section 6.6.

6.2 Test conditions

One single vertical cylinder was tested with all heave plate configurations in two immersed drafts: deep ($d/D_c = 2.2$) and shallow ($d/D_c = 0.7$). Two types of long-crested waves (monochromatic and bichromatic waves) were generated by the wavemaker in the single wave direction of the positive x-axis.

6.2.1 Monochromatic waves

Monochromatic waves allow us to measure the loads in different harmonics excited by a single wave frequency, ω. The regular wave periods T were selected from 0.9 s to 3.0 s, which is under the operation limitation of the wavemaker. The periods correspond to a non-dimensional wave frequency, $\omega^2 D_c/g$ ranging from 0.2 to 1.7. Furthermore, three wave steepnesses ($H/\lambda = 0.02, 0.04, 0.06$, where H and λ stand for wave height and wavelength) were chosen to investigate the non-linear effects on the wave loads. Table 6.1 presents the selected regular wave parameters, including the wave scatter parameter ($\pi D_c/\lambda$) and the Keulegan-Carpenter number ($KC_w = \pi H/D_c$).

Figure 6.1 presents an example of wave field around the cylinder equipped with the largest heave plate ($D_d/D_c = 3.5$) at the shallow draft ($d/D_c = 0.7$) in the regular wave ($\omega^2 D_c/g = 0.4$, $H/\lambda = 0.04$).

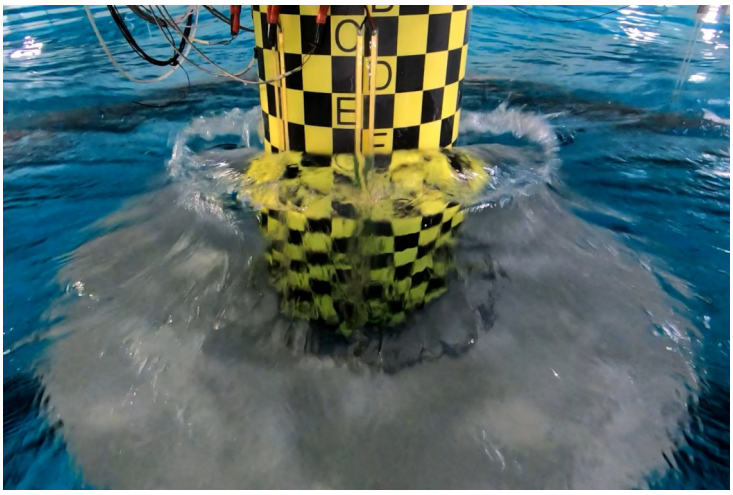

Figure 6.1 – A snapshot of the diffracted waves around the truncated cylinder with the heave plate ($D_d/D_c = 3.5$) at the shallow submerged depth ($d/D_c = 0.7$, $d = 0.25$ m). A regular wave ($\omega^2 D_c/g = 0.35$, $H/\lambda = 0.04$) propagates from the front to the back. The full video is available as supplementary material.

All the wave steepnesses are examined at the deep draft with the solitary cylinder (Model A) and the cylinder with the solid plate (Model C). Only one wave steepness ($H/\lambda = 0.06$) is considered for the other configurations. On the other hand, at the shallow draft, all the steepnesses are tested for all the configurations. However, some wave frequencies could not be tested with the plate due to the large wave amplitude with $H/\lambda = 0.04$ and 0.06.

As mentioned in the previous chapter, the regular waves were first calibrated in the tank without the model. A reference wave gauge was installed at the target position $x_{target} = 17.2$ m. An amplification factor was used to calibrate the waves to ensure that the generated waves reach the target wave heights within a range of 5 % error. These factors depend on the wave frequency and height and aim to correct the small deviation of the wavemaker linear transfer function. The measured wave heights, including all nonlinearities, are used to nondimensionalize the results.

Table 6.1 – Monochromatic waves with three wave steepnesses.

$\omega^2 D_c/g$	$H/\lambda = 0.02$			$H/\lambda = 0.04$			$H/\lambda = 0.06$		
	$\pi D_c/\lambda$	H/D_c	KC_w	$\pi D_c/\lambda$	H/D_c	KC_w	$\pi D_c/\lambda$	H/D_c	KC_w
1.74	0.87	0.07	0.22	0.86	0.15	0.46	0.84	0.22	0.68
1.41	0.70	0.09	0.28	0.69	0.18	0.56	0.68	0.27	0.84
1.16	0.58	0.11	0.34	0.57	0.22	0.68	0.56	0.32	1.02
0.98	0.49	0.13	0.40	0.48	0.26	0.81	0.47	0.39	1.21
0.83	0.42	0.15	0.48	0.41	0.31	0.99	0.40	0.45	1.42
0.63	0.31	0.20	0.63	0.31	0.40	1.26	0.30	0.60	1.89
0.35	0.18	0.34	1.08	0.17	0.71	2.24	0.17	1.07	3.36
0.16	0.08	0.80	2.51	0.08	1.57	4.94			

6.2.2 Bichromatic waves

The bichromatic waves are composed of two sets of regular waves (ω_1 and ω_2) designed to obtain the loads occurring at the sum frequency ($\omega^+ = \omega_1 + \omega_2$) and difference frequency ($\omega^- = \omega_1 - \omega_2$) by using the interaction of two wave components. The heave plate effects on the slowly varying drift loads are studied using bichromatic waves with the solitary cylinder (Model A) and the heave plate (Model C). Three primary wave frequencies ω_1 are selected from the monochromatic waves, and the secondary wave frequencies ω_2 are set to have a difference frequency $\omega^- = 1.2$ rad/s, which corresponds to $\lambda_{\omega^-}/D_c \approx 124$ assuming deep water. The wave steepness of each wave component in bichromatic waves is designed to be 0.02, which corresponds to the one in the monochromatic waves.

The same amplification factors obtained from the regular wave calibration were used to generate bichromatic waves. The bichromatic waves were generated without the model, and the wave elevation was measured at the target position. In contrast to the regular waves, the individual wave heights can not be measured. Hence, the measured first-harmonic amplitude, A_j of each wave frequency ω_j, is used for non-dimensionalization. The test parameters of bichromatic waves are given in Table 6.2.

Table 6.2 – Bichromatic waves with a difference frequency $\omega^- = 1.2$ rad/s.

Primary wave component (ω_1)				Secondary wave component (ω_2)			
$\omega_1^2 D_c/g$	$\pi D_c/\lambda$	H_1/D_c [1]	KC_w	$\omega_2^2 D_c/g$	$\pi D_c/\lambda$	H_2/D_c [1]	KC_w
0.35	0.18	0.31	0.99	0.67	0.33	0.19	0.59
0.83	0.42	0.13	0.41	1.30	0.65	0.08	0.24
1.16	0.58	0.08	0.25	1.70	0.85	0.07	0.21

[1] $H_1 = 2 \times A_1, H_2 = 2 \times A_2$

Figure 6.2 summarizes the wave conditions of the monochromatic waves (symbols with face colors) and bichromatic waves (symbols without face colors). The selected wave conditions are designed to investigate the different wave force regimes introduced by Chakrabarti (1987), including the diffraction, inertia and drag force regimes. All the waves are below the wave-breaking criterion. The wave components of the bichromatic waves are in a similar frequency range as the monochromatic waves.

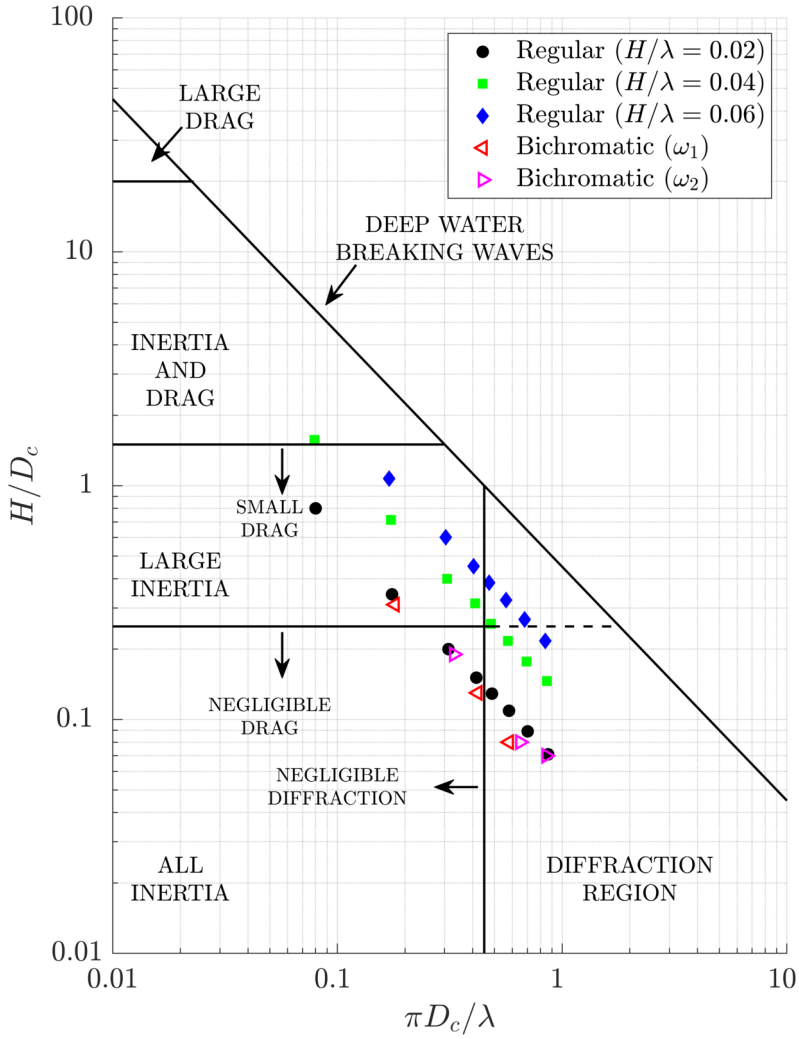

Figure 6.2 – Monochromatic and bichromatic wave conditions in different wave force regimes (Chakrabarti (1987)).

6.3 Analysis of the experimental data

6.3.1 Load convention for the fixed body with incident waves

Figure 6.3 presents the load convention expressed in the body-fixed reference frame $\{b\}$, which is identical to the Galilean reference frame $\{O\}$ for the fixed body. The forces and moments measured by the transducer at O_t are converted to the ones at the origin of the reference system, O_b, located on the free surface. The z-axis of the reference frame is aligned with the cylinder axis and points upward in the positive direction. Additionally, the x-axis is aligned with the wave direction.

The measured loads include the gravity loads $\overline{F}^{(W)} = m\mathbf{g}$ (where m is the model's mass and $\mathbf{g}$ the acceleration due to gravity), the hydrostatic buoyancy at rest $\overline{F}^{(S)}$ and the wave-induced loads. The inertia loads do not contribute to the measured loads since the hexapod firmly restricts body motions. Therefore, the wave loads, hereafter referred to as $\mathbf{F}$, were obtained by subtracting the buoyancy and weight contributions from the measured loads. These unbalanced forces were eliminated from the measurements during the zeroing process, along with the initial offset of the sensor.

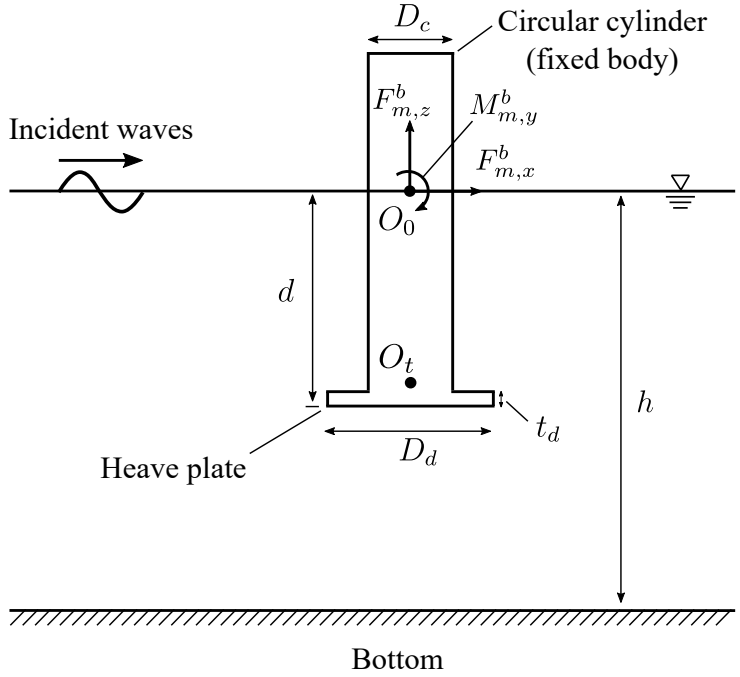

Figure 6.3 – Load convention for the fixed body in the wave tank: $F^b_{m,x}, F^b_{m,z}, M^b_{m,y}$ stand for the measured forces and moments at the origin of the body-fixed reference, O_b, converted from the ones measured by force transducer at O_t.

6.3.2 Data pre-processing

The measured force time series is filtered by a low-pass filter using a 4.5 Hz cut-off frequency. The cut-off frequency is lower than the first wet natural frequency of the plate, which was obtained from the hammer tests (5 Hz for the largest plate, $D_d/D_c = 3.5$ at the deep draft, $d/D_c = 2.2$). This ensures that we keep the harmonics of interest associated with the wave frequency. For instance, the highest frequency wave is 1.1 Hz ($\omega^2 D_c/g = 1.74$), which allows up to the third harmonic. The time series is reduced by selecting a time window with an integer number of wave periods, N. The transient period and wave reflection from the wave-absorbing beach are carefully excluded by considering the first wave arriving time and wave returning time at the model location. For example, in monochromatic waves, the window is $30T$ in length for the short wave period, but for the long wave, the window is limited to $5T$ due to the high group velocity. On the other hand, for the bichromatic waves, the length of the time window is chosen as $10T^-$, where $T^- = 2\pi/\omega^-$.

6.3.3 Wave loads in monochromatic waves

Figure 6.4 shows an example of the horizontal and vertical force time series on Model E ($D_d/D_c = 3.5$) at the deep draft with a single wave frequency ($\omega^2 D_c/g = 1.74$) and the wave steepness ($H/\lambda = 0.06$). The measured signal is compared to the filtered signal, where the higher frequency response is discarded above the cut-off frequency. The filtered signals present satisfactory periodicity, specifically exhibiting sinusoidal behavior in the horizontal forces and secondary peaks in the vertical forces.

Fourier analysis is used to obtain the harmonic content from the raw time history within the selected window (NT), allowing for precise capture of the zeroth harmonic and minimizing energy losses of each harmonic content in regular waves. In Figures 6.4b and 6.4d, the results of Fast Fourier Transform (FFT) clearly show that the wave loads are distributed on the zeroth and higher harmonics of the horizontal and vertical forces. Additional peaks appear in the FFT, which correspond to the wet natural frequencies of the model. The structural response affects the harmonics of the measured loads located near the natural frequencies. However, below the cut-off frequency, these structural contributions are negligible, and this is the limit of our experimental setup.

It is worth noting that the first harmonic in the vertical forces is comparable to the second harmonic, which can be observed as the secondary peak in the time history shown in Figure 6.4c. In general, the first harmonic is the most dominant, and the first four harmonics,

including the zeroth harmonic, account for above 95 % of the total harmonic amplitudes.

Therefore, the wave loads in monochromatic waves can be approximated by the following equation,

$$\mathbf{F}(t) \approx \overline{\mathbf{F}} + \mathfrak{Re}\{\mathbf{F}^{(\omega)} e^{-i\omega t}\} + \mathfrak{Re}\{\mathbf{F}^{(2\omega)} e^{-2i\omega t}\} + \mathfrak{Re}\{\mathbf{F}^{(3\omega)} e^{-3i\omega t}\} + \mathbf{O}(4\omega) \tag{6.1}$$

where $\overline{\mathbf{F}}$ is the hydrodynamic contribution of the mean loads, so-called mean wave drift loads. $\mathbf{F}^{(\omega)}$, $\mathbf{F}^{(2\omega)}$, $\mathbf{F}^{(3\omega)}$ are corresponding to the first-, second-, and third-harmonic components of the Fourier series.

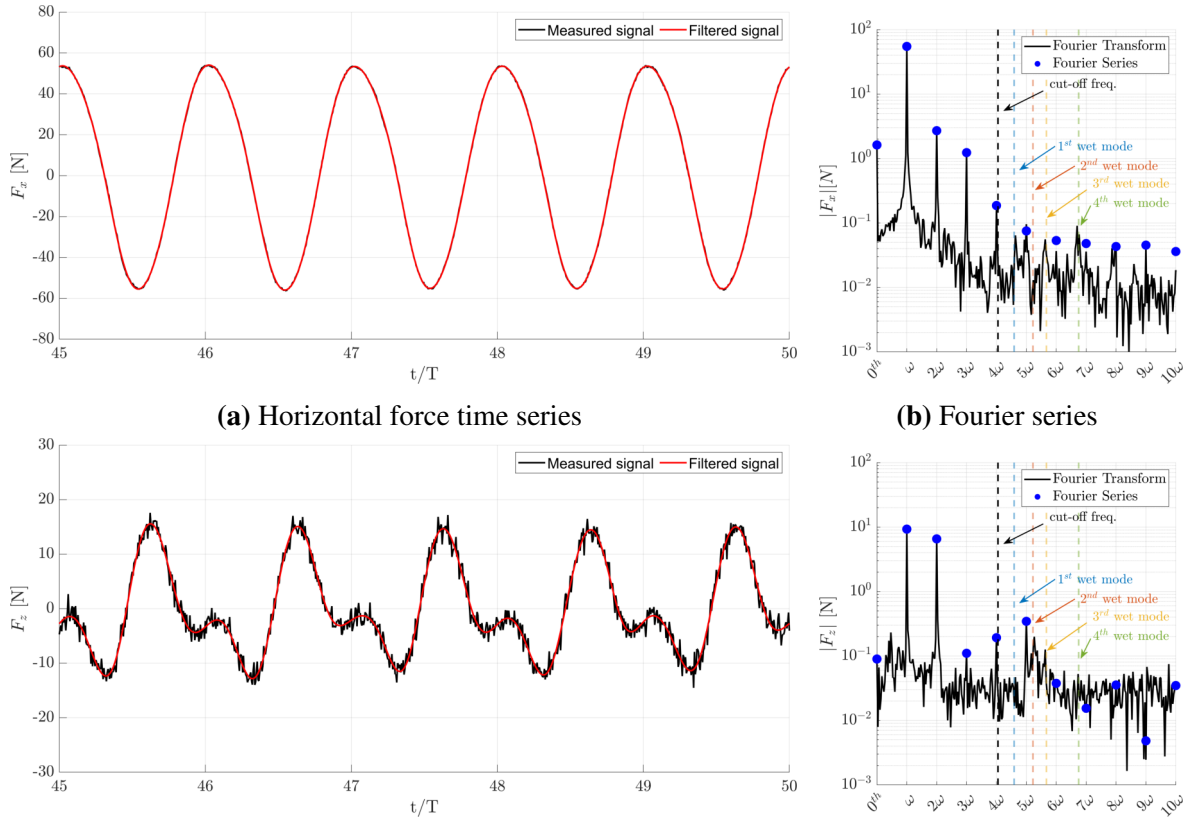

(a) Horizontal force time series

(b) Fourier series

(c) Vertical force time series

(d) Fourier series

Figure 6.4 – Horizontal and vertical wave forces for the vertical circular cylinder with the largest plate $D_d/D_c = 3.5$ (with the lowest natural frequency) in monochromatic waves of nondimensional wave frequency ($\omega^2 D_c/g = 1.74$) and wave steepness ($H/\lambda = 0.06$) at the deep draft ($d/D_c = 2.2$).

6.3.4 Wave loads in bichromatic waves

In Figure 6.5, an example is provided highlighting the difference-frequency contribution in the horizontal and vertical forces acting on Model C ($D_d/D_c = 2.9$) with the bichromatic wave set ($\omega_1^2 D_c/g = 0.83$ and $\omega_2^2 D_c/g = 1.30$) at the shallow draft. In the time series, the interaction between the two wave components can be observed as a beat with frequency ω^-. The forces are slowly varying in time with the difference frequency, which is called the slowly varying wave drift forces. All the peaks identified from FFT in Figures 6.5b and 6.5d correspond to the interactions of two wave components, as shown in x-axis up to the third interaction (e.g., $3\omega_{1,2}$, $|2\omega_1 \pm \omega_2|$, $|2\omega_2 \pm \omega_1|$), which is comparable with the sum and difference frequency contributions. The minor peaks correspond to higher interactions.

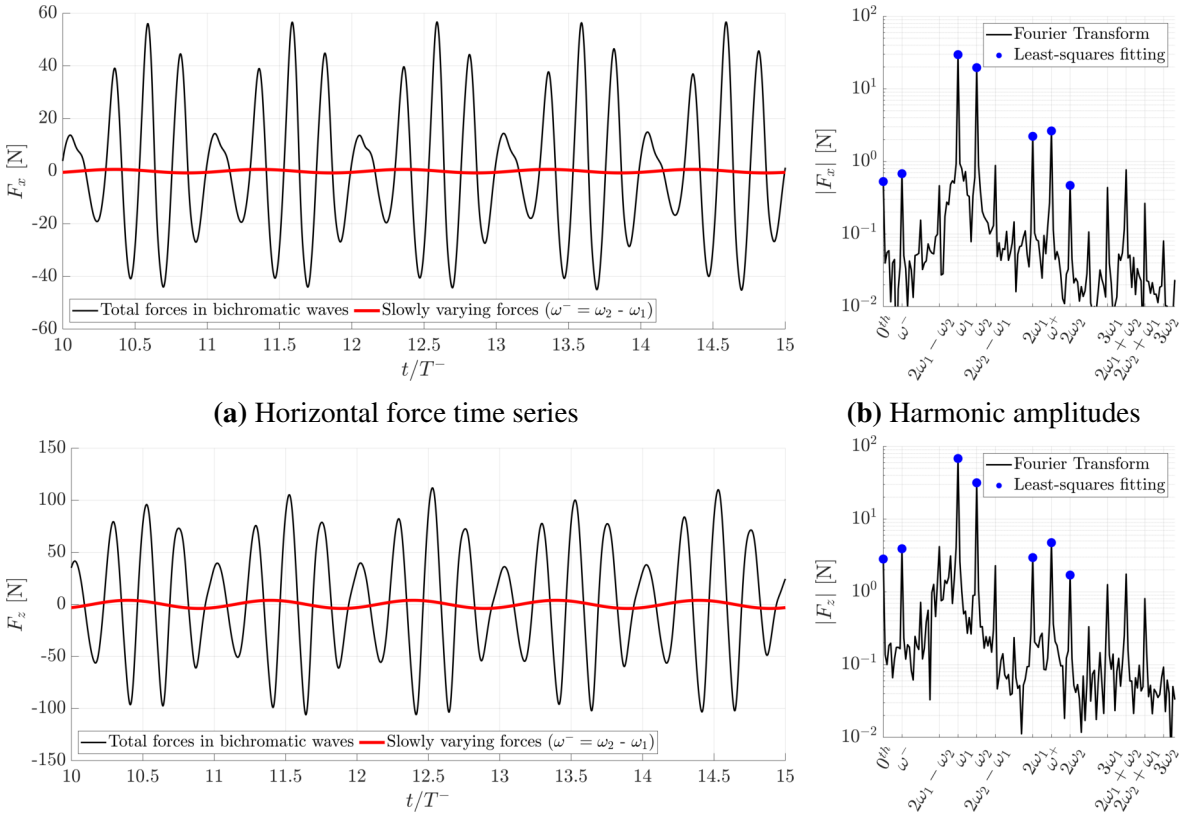

(a) Horizontal force time series

(b) Harmonic amplitudes

(c) Vertical force time series

(d) Harmonic amplitudes

Figure 6.5 – Horizontal and vertical wave forces for the vertical circular cylinder with a heave plate (Model C, D_d/D_c=2.9) in bichromatic waves ($\omega_1^2 D_c/g = 0.83$ and $\omega_2^2 D_c/g = 1.30$) at the shallow draft ($d/D_c = 0.7$).

In bichromatic waves, the least squares procedure (Fonseca et al. (2011); Li and Bachynski-Polić (2021)) is utilized to obtain the first and second harmonic components of ω_1, ω_2, as well as the sum- and difference-frequency components (ω^+,ω^-) from the force-time series. This method is more convenient than standard Fourier analysis for extracting the harmonic components from the time history in bichromatic waves, as there is no condition on the length of the time window.

The following equation then approximates the wave loads in bichromatic waves up to the second interaction of two wave components:

$$\begin{aligned}\mathbf{F}(t) \approx \overline{\mathbf{F}} &+ \mathfrak{Re}\{\mathbf{F}^{(\omega_1)}e^{-i\omega_1 t}\} + \mathfrak{Re}\{\mathbf{F}^{(\omega_2)}e^{-i\omega_2 t}\} + \mathfrak{Re}\{\mathbf{F}^{(2\omega_1)}e^{-i2\omega_1 t}\} + \mathfrak{Re}\{\mathbf{F}^{(2\omega_2)}e^{-i2\omega_2 t}\} \\ &+ \mathfrak{Re}\{\mathbf{F}^{(\omega^+)}e^{-i\omega^+ t}\} + \mathfrak{Re}\{\mathbf{F}^{(\omega^-)}e^{-i\omega^- t}\}\end{aligned} \tag{6.2}$$

where $\mathbf{F}^{(\omega^+)}$, $\mathbf{F}^{(\omega^-)}$ are the sum- and difference-frequency forces.

The harmonic content of interest, i.e. the one present in Eq. (6.2), is well indicated by the least-squares fitting procedure.

6.3.5 Correspondence of wave diffraction loads in potential flow theory and experiments

In the potential flow theory, the wave loads are mathematically described for the monochromatic and bichromatic wave cases. The loads are evaluated with different orders of magnitude by introducing a perturbation series with respect to the wave steepness parameter ($\varepsilon = k_0 A$) as described in Kim and Yue (1989, 1990); Malenica and Molin (1995).

The wave loads are computed by integrating the pressure on the wetted body surface at the rest position, $\overline{S}_B$.

$$\mathbf{F} = \iint_{\overline{S}_B} p\mathbf{n} dS \tag{6.3}$$

where the pressure is from the Bernoulli equation: $p = -\rho g z - \rho \frac{\partial \Phi}{\partial t} - \frac{1}{2}\rho (\nabla\Phi)^2$. In this study, the contribution of the radiation potential induced by the body motion is discarded in total velocity potential.

In monochromatic waves, the wave loads are decomposed with the different orders as,

$$\mathbf{F}(t) = \mathbf{F}^{(0)} + \mathfrak{Re}\{\mathbf{F}^{(1)} e^{-i\omega t}\} + \overline{\mathbf{F}}^{(2)} + \mathfrak{Re}\{\mathbf{F}^{(2)} e^{-2i\omega t}\} + \mathbf{O}(\varepsilon^3) \tag{6.4}$$

where $\mathbf{F}^{(0)}$ is the hydrostatic force at the rest position, and $\mathbf{F}^{(1)}$, $\overline{\mathbf{F}}^{(2)}$, $\mathbf{F}^{(2)}$ stand for the first-order, second-order mean drift and second-order double frequency forces, respectively. The mean drift forces can be evaluated using the near-field method (Pinkster and Van Oortmerssen (1978)), far-field method (Maruo (1960); Newman (1967)), and middle-field method (Chen (2007)). The second-order double frequency loads, $\mathbf{F}^{(2)}$, are dealt with following the bichromatic theory.

Additional terms appear for bichromatic waves due to the interactions of the two wave frequency components.

$$\mathbf{F}(t) = \mathbf{F}^{(0)} + \mathfrak{Re}\{\sum_{j=1}^{2} \mathbf{F}^{(1)}_{\omega_j} e^{-i\omega_j t}\} + \mathfrak{Re}\sum_{j=1}^{2}\sum_{l=1}^{2}\{\mathbf{F}^{(2),-}_{(\omega_j,\omega_l)} e^{-i\omega^- t} + \mathbf{F}^{(2),+}_{(\omega_j,\omega_l)} e^{-i\omega^+ t}\} + \mathbf{O}(\varepsilon^3) \tag{6.5}$$

where $\omega^- = \omega_j - \omega_l$ and $\omega^+ = \omega_j + \omega_l$. Superscripts $+$ and $-$ stand for the sum- and difference-frequency contributions.

The second-order terms in the above Eq. (6.5) can be written in quadratic form,

$$\begin{aligned}\mathbf{F}^{(2)}(t) =& A_1^2\bar{\mathbf{f}}_{\omega_1}^{(2),-} + A_2^2\bar{\mathbf{f}}_{\omega_2}^{(2),-} + \mathfrak{Re}\{2A_1A_2\mathbf{f}_{(\omega_1,\omega_2)}^{(2),-}e^{-i\omega^- t}\} \\ &+ \mathfrak{Re}\{A_1^2\mathbf{f}_{(\omega_1,\omega_1)}^{(2),+}e^{-2i\omega_1 t} + A_2^2\mathbf{f}_{(\omega_2,\omega_2)}^{(2),+}e^{-2i\omega_2 t} + 2A_1A_2\mathbf{f}_{(\omega_1,\omega_2)}^{(2),+}e^{-i\omega^+ t}\}\end{aligned} \tag{6.6}$$

where $\mathbf{f}_{(\omega_1,\omega_2)}^{(2),+}$, $\mathbf{f}_{(\omega_1,\omega_2)}^{(2),-}$ are Quadratic Transfer Functions (QTFs) for sum- and difference-frequency components. $\bar{\mathbf{f}}_{\omega_1}^{(2),-}$, $\bar{\mathbf{f}}_{\omega_2}^{(2),-}$ are the mean drift forces in unit wave amplitude from the difference frequency contribution, and $\mathbf{f}_{(\omega_1,\omega_1)}^{(2),+}$, $\mathbf{f}_{(\omega_2,\omega_2)}^{(2),+}$ are the second-order double frequency loads from the sum-frequency contribution where $\omega_j = \omega_l$.

Therefore, the harmonic components measured in the experiments given in Table 6.3 correspond to the wave loads evaluated at different orders by the theory. This study mainly focuses on the impact of the heave plate on the mean drift forces, the first and second harmonic forces, and the sum and difference frequency forces. These contributions are dominant in the wave loads and are of interest in engineering.

Table 6.3 – Correspondence of wave diffraction loads between harmonics and orders of wave loads up to the second interaction of the wave components in the experiment and potential flow theory.

Wave type	Experiments	Harmonics	Theory	Orders ($\varepsilon = k_0A$)
No waves	$\mathbf{F}^{(W)}$	0^{th} (weight)	-	-
	$\mathbf{F}^{(S)}$	0^{th} (buoyancy)	$\mathbf{F}^{(0)}$	0^{th}
Monochromatic waves	$\overline{\mathbf{F}}$	0^{th} (or mean)	$\overline{\mathbf{F}}^{(2)}$	2^{nd} mean
	$\mathbf{F}^{(\omega)}$	1^{st}	$\mathbf{F}^{(1)}$	1^{st} (linear)
	$\mathbf{F}^{(2\omega)}$	2^{nd}	$\mathbf{F}^{(2)}$	2^{nd} double freq.
Bichromatic waves	$\overline{\mathbf{F}}$	0^{th} (or mean)	$A_1^2\bar{\mathbf{f}}_{\omega_1}^{(2),-} + A_2^2\bar{\mathbf{f}}_{\omega_2}^{(2),-}$	2^{nd} mean
	$\mathbf{F}^{(\omega)}$	1^{st} of ω_1, ω_2	$\mathbf{F}_{\omega}^{(1)}$	1^{st} (linear)
	$\mathbf{F}^{(2\omega)}$	2^{nd} of ω_1, ω_2	$A^2\mathbf{f}_{(\omega,\omega)}^{(2),+}$	2^{nd} double freq.
	$\mathbf{F}^{(\omega^+)}$	1^{st} at ω^+	$2A_1A_2\mathbf{f}_{(\omega_1,\omega_2)}^{(2),+}$	2^{nd} sum freq.
	$\mathbf{F}^{(\omega^-)}$	1^{st} at ω^-	$2A_1A_2\mathbf{f}_{(\omega_1,\omega_2)}^{(2),-}$	2^{nd} difference freq.

In this study, the QTFs are computed numerically using the commercial BEM solver HydroStar (Bureau Veritas (2020)). The middle-field method (Chen (2007)) is used for the difference frequency components to compute the mean drift forces and slowly varying drift

forces. The sum-frequency wave loads are computed by the near-field method. The panel models for the cylinder and heave plate are used by following the description in Section 4.1. The porous parameter $\kappa = 5$ is employed to implement 10 % of the porosity of the plate (Model D) for both deep and shallow drafts.

6.4 Results

6.4.1 Wave loads in monochromatic waves

This section presents the horizontal and vertical wave loads acting on the cylinder without ($D_d/D_c = 1.0$) and with heave plates ($D_d/D_c = 1.5, 2.9, 3.5$), including the perforated plate. All results are obtained with regular waves at deep (d/D_c=2.2) and shallow (d/D_c=0.7) drafts. First, the time series of nondimensional wave loads $F(t)/\rho g D_c^2(H/2)$ is presented together with Fourier series results up to the third harmonic.

Next, the amplitude of the first and second harmonics, as well as the mean value of the forces, are plotted with respect to the nondimensional wave frequency $\omega^2 D_c/g$ called a harmonic operator. The amplitudes of each harmonic are nondimensionalized with

$$F'^{(\omega)} = \frac{F^{(\omega)}}{\rho g D_c^2(H/2)}, \qquad F'^{(2\omega)} = \frac{F^{(2\omega)}}{\rho g D_c(H/2)^2}, \qquad \overline{F}' = \frac{\overline{F}}{\rho g D_c(H/2)^2} \tag{6.7}$$

where superscript indicates the harmonic components, overline stands for the mean value of the forces, and H is the measured wave height of calibrated waves.

Three different wave steepnesses are provided for Model A (D_d/D_c=1.0) and C (D_d/D_c=2.9) at the deep draft and for all configurations at the shallow draft. Each configuration is represented by a different symbol and color. The type of symbol face color describes the wave steepness (H/λ): empty for 0.02, transparent for 0.04, and solid for 0.06. The first-, and second-order hydrodynamic loads computed by HydroStar are given in solid lines for comparison.

a) Time series and harmonic components

One selected time series of wave loads is shown with a single wave component ($\omega^2 D_c/g = 1.0$, $H/\lambda = 0.06$) at deep and shallow drafts. The load time series of all configurations are synchronized and displayed during five wave periods in the periodic state.

The measured forces show good repeatability in time in general. Furthermore, the Fourier series are obtained using the time series of thirty wave periods.

Figure 6.6 presents the horizontal wave forces on the cylinder with all heave plates at deep and shallow drafts. At the deep draft, the behavior of the horizontal forces in time is almost identical in terms of the amplitudes and phase. However, heave plate effects can be clearly recognized in the Fourier series. Especially the first harmonic of the horizontal force increases with the diameter of the heave plate. Furthermore, the forces with the porous plate are slightly lower than with the equivalent solid plate.

The effect of the heave plate on horizontal forces is more noticeable at shallow draft. In the time series, the positive peaks are higher and sharper with the heave plates, while the phase is shifted compared to the solitary cylinder (Model A). The porosity effects are more noticeable in the time series, reducing the amplitude of the forces as compared to the equivalent solid plate ones. sThe effects of the plate can also be seen in the zeroth and higher harmonic components, with same trends as for the first harmonic components.

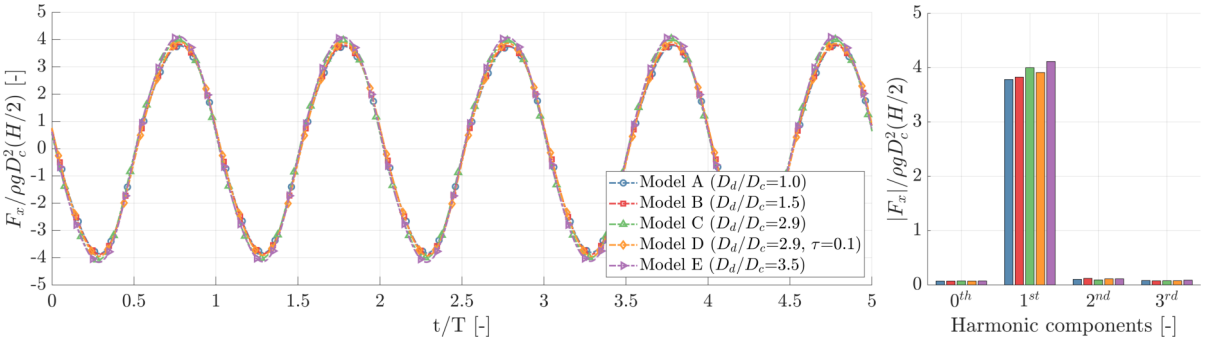

(a) Time series of horizontal wave forces at the deep draft **(b)** Harmonics ($30T$)

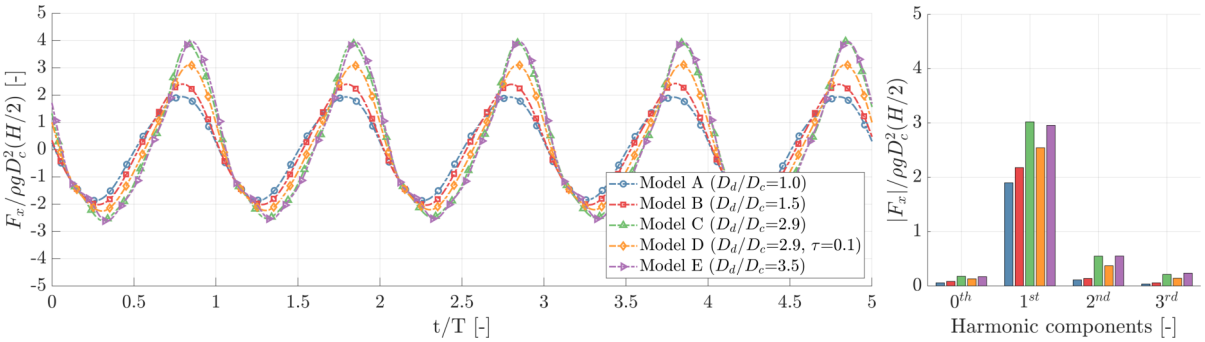

(c) Time series of horizontal wave forces at the shallow draft **(d)** Harmonics ($30T$)

Figure 6.6 – Non-dimensional horizontal wave forces at the deep ($d/D_c = 2.2$) and shallow ($d/D_c = 0.7$) drafts at the non-dimensional wave frequency ($\omega^2 D_c/g = 1.0$) with wave steepness ($H/\lambda = 0.06$).

The corresponding non-dimensional vertical wave forces are given in Figure 6.7. In contrast to the horizontal forces, the effects of the plate can be seen clearly at both deep and shallow drafts. At the deep draft, the peak of vertical forces with the plate appears earlier than for the solitary cylinder. In the time series, the porous plate reduces the forces but also shifts the forces compared to the equivalent solid plate. Moreover, porosity tends to flatten the peaks in the vertical forces for both drafts. In general, the first harmonics of the vertical forces are significantly affected by the plates. Interestingly, the small heave plate (D_d/D_c=1.5) decreases the first harmonic of the vertical forces compared to the solitary cylinder. The porous plate reduces all harmonics of the vertical force compared to the equivalent solid plate.

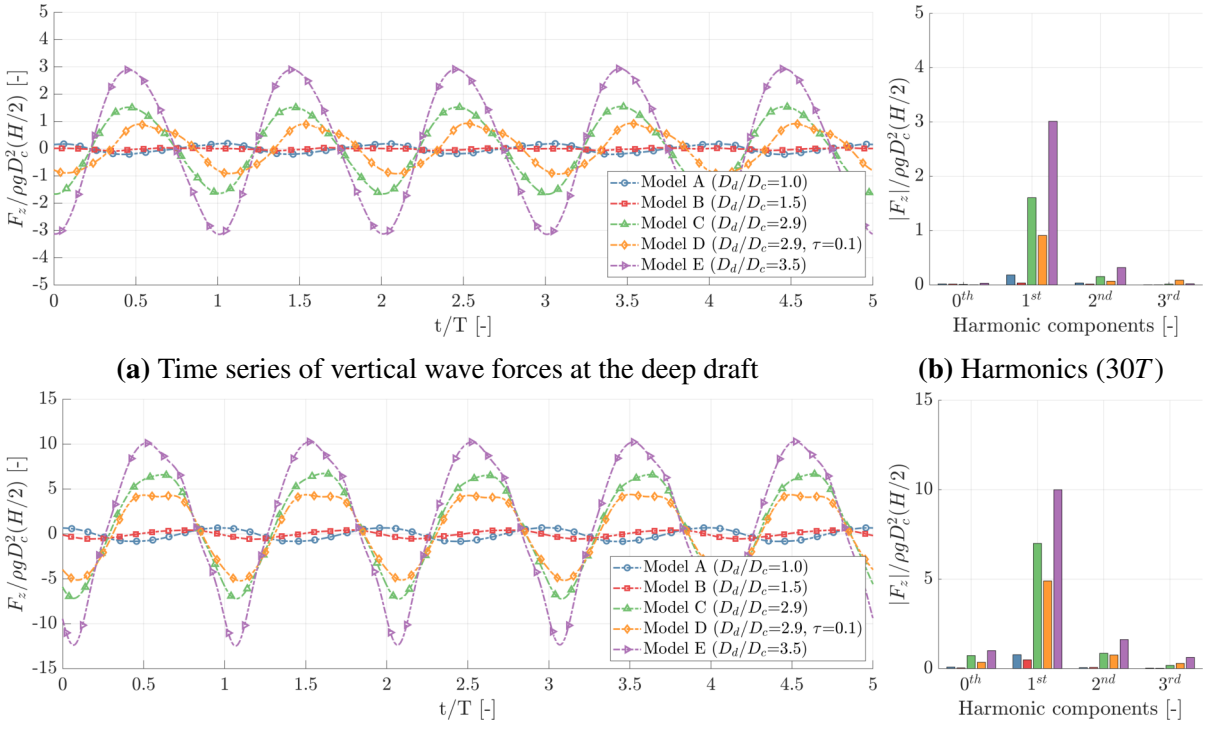

(a) Time series of vertical wave forces at the deep draft

(b) Harmonics ($30T$)

(c) Time series of vertical wave forces at the shallow draft

(d) Harmonics ($30T$)

Figure 6.7 – Non-dimensional vertical wave forces at the deep ($d/D_c = 2.2$) and shallow ($d/D_c = 0.7$) drafts at the non-dimensional wave frequency ($\omega^2 D_c/g = 1.0$) with wave steepness ($H/\lambda = 0.06$).

b) Harmonic operators of horizontal wave forces

Figure 6.8 shows the amplitude of the first-, and second-harmonic components, as well as the mean value of horizontal wave forces at both the deep (d/D_c=2.2) and shallow (d/D_c=0.7) drafts. The measured horizontal forces exerted on the truncated cylinder without the plate (Model A), given in blue color, indicate a monotonic behavior with respect to wave frequency. Generally, wave steepness has minor effects on the non-dimensional horizontal forces compared to the influence of wave frequency. The measured forces are well-described by the first-, and second-order potential theory at both drafts.

The presence of the plate affects the first harmonic components. At deep draft, the plates slightly increase the horizontal forces compared to the solitary cylinder for $0.2 < \omega^2 D_c/g < 1.8$. In contrast, at the shallow draft, the forces increase significantly with increasing the diameter of the plate. Notably, significant wave steepness results in decreased forces for large heave plates at the frequency where nondimensional wave forces are maximized. Therefore, potential flow theory tends to overestimate the forces when $H/\lambda > 0.02$. It is worth noting that the effect of heave plates is mitigated at high wave frequencies where the wavelength is very short compared to the cylinder.

Similar to the first harmonics, the influence of the plate on the second harmonics and mean drift forces is not important at the deep draft. However, at the shallow draft, the plate has also a dominant impact on the second harmonics and the mean of the horizontal forces. Significant peaks are measured around $\omega^2 D_c/g = 0.8$ for the second harmonic horizontal forces at the shallow draft for Model C and E. The peaks increase with increasing the plate diameter and decrease with increasing the wave steepness. The potential flow method predicts the general tendency well, but the magnitude is overestimated around the peak frequency. Furthermore, the plates at the shallow draft strongly affect the horizontal mean drift forces, while there is almost no difference at the deep draft. Increasing the plate size leads to an increase in the mean horizontal force, particularly at the peak frequency ($\omega^2 D_c/g \approx 1.2$). On the other hand, the porosity of the plate has a negligible effect on the mean horizontal force.

However, the perforated plate (Model D), shown in orange, reduces the horizontal forces first and second harmonics compared to the solid plate (Model C) shown in green. The reduction is more visible at the shallow draft: for the wave frequency $\omega^2 D_c/g = 1.2$ the porosity decreases the load by approximately 30%. The potential flow describes well, in general, the first harmonics of the experimental measurements with the porous parameter ($\kappa = 5$) in Darcy's law to represent the porosity factor $\tau = 10\%$.

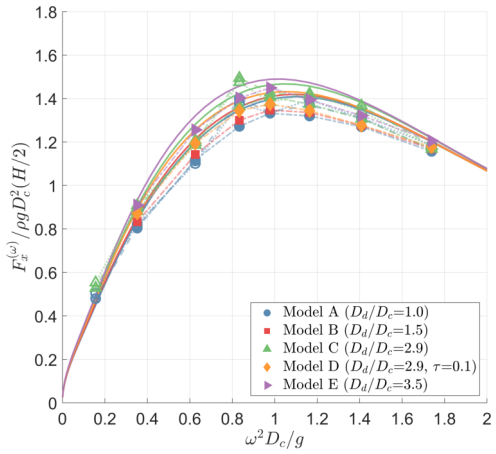

(a) First harmonics at the deep draft

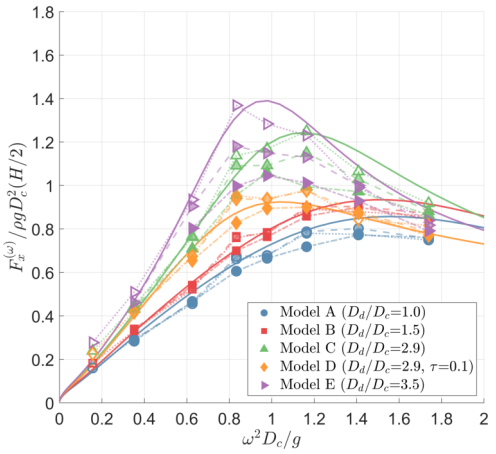

(b) First harmonics at the shallow draft

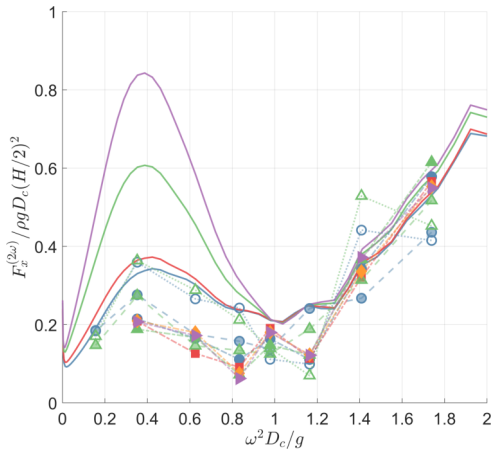

(c) Second harmonics at the deep draft

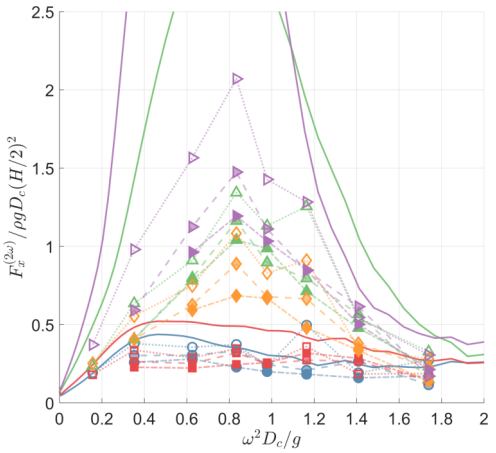

(d) Second harmonics at the shallow draft

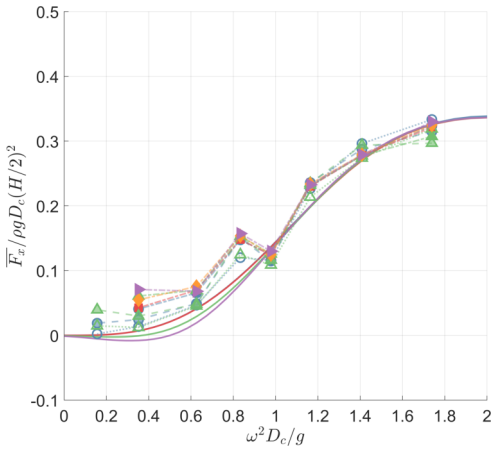

(e) Mean drift at the deep draft

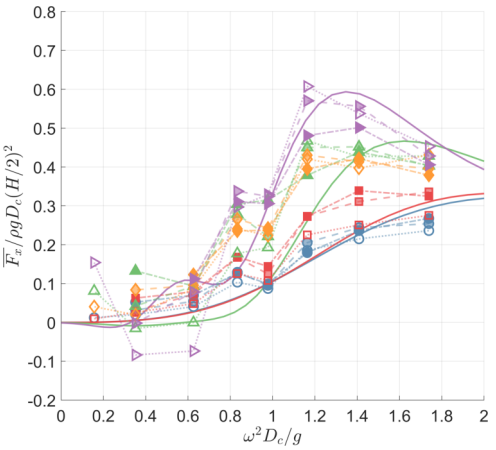

(f) Mean drift at the shallow draft

Figure 6.8 – Non-dimensional horizontal wave loads at the deep ($d/D_c = 2.2$) and shallow ($d/D_c = 0.7$) drafts (symbols without fill: $H/\lambda = 0.02$, symbols with transparent face colors: $H/\lambda = 0.04$, symbols with fill: $H/\lambda = 0.06$, and solid lines: HydroStar).

c) Harmonic operators of vertical wave loads

The measured harmonics of the vertical wave loads are summarized as the harmonic operators in Figure 6.9. The first harmonics are monotonically decreasing with increasing wave frequency on the solitary cylinder (Model A) at the deep and shallow drafts. As the wave frequency increases, the forces decrease and converge to zero. This is because the vertical forces are exerted only on the bottom of the cylinder. The water particle velocity decreases exponentially and cannot influence the cylinder bottom at high frequency. However, at low frequency, the non-dimensional vertical forces reach around 0.8 ($F_z^{(\omega)}/(\rho g A_w(H/2)) = 1$), dominated by incident wave forces known as Froude-Krylov forces.

On the other hand, with the heave plate, the vertical forces not only act on the bottom but also on the top of the plate. As a result, the amplitude of the first harmonics on the small plate (Model B) is lower than that of the solitary cylinder (Model A) at both drafts. In addition, with the large heave plates (Model C, D, and E), the first harmonics of the vertical forces are significantly increased in high-frequency regions. The forces decrease as the wave frequency decreases in low-frequency regions.

Interestingly, the potential theory indicates that the vertical forces are canceled out in these frequency regions, where the forces on the bottom and top of the plate are equal. However, the theory underestimates the forces compared to the experimental measurements around that cancellation frequency. The underestimation of the first harmonic of the vertical forces is more significant with higher wave steepness (H/λ) with the large heave plates. The wave steepness effects are dominantly visible in the low-frequency region with the solid plate. Whereas it is much less significant in the high-frequency region ($\omega^2 D_c/g > 1$).

For the porous plate, the effects are visible in the whole frequency range by decreasing the vertical forces, notably at the shallow draft. The first harmonic on the porous plate (Model D, $\tau = 0.1$) is predicted well by Darcy's law with porous parameter ($\kappa = 5$) in the BEM solver, especially for the lower wave steepness ($H/\lambda = 0.02$). However, significant differences exist in the low-frequency region. Further discussion of the first harmonic of vertical wave forces is provided in Section 6.5.

The presence of a heave plate tends to increase the second-harmonic components at deep and shallow drafts, largely for the larger plates. The second harmonics of the vertical forces at the deep draft generally increase with respect to the frequency. At the shallow draft, on the other hand, only the cylinder alone and with a small heave plate show a similar trend as for the deep draft. With the larger plate, the second harmonics show fluctuations with respect to the frequency. The second-order theory predicts the general trend of the second-harmonic vertical

forces. The porous plate reduces the second-harmonic vertical forces compared to the equivalent solid plate (Model C) at the deep and shallow drafts.

Lastly, the mean drift forces exerted on the solitary cylinder and the cylinder with the small plate (Model B) show negative forces at the deep and shallow drafts. With the large heave plates, the mean drift forces are increasing more significantly at the shallow draft. The porous plate decreases the mean forces by 50% compared to the equivalent solid plate at the shallow draft.

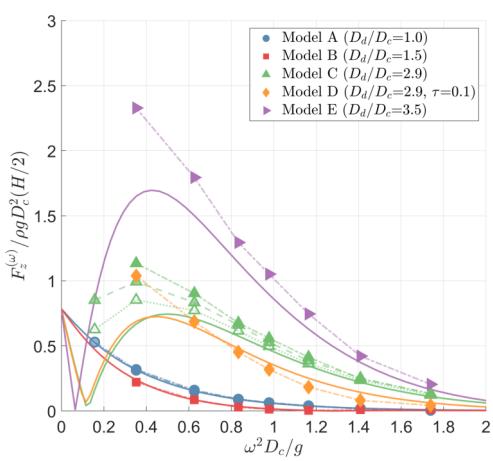

(a) First harmonics at the deep draft

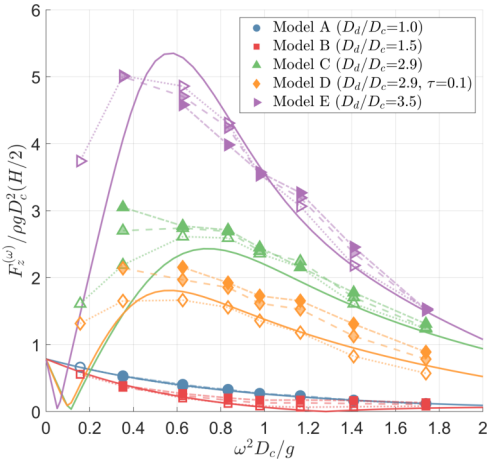

(b) First harmonics at the shallow draft

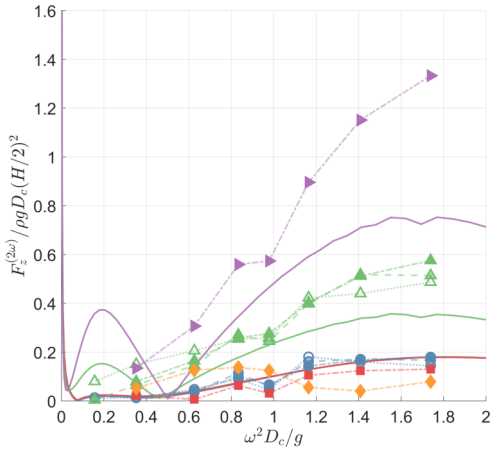

(c) Second harmonics at the deep draft

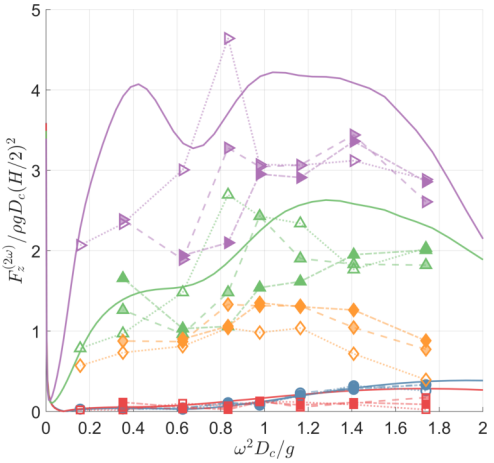

(d) Second harmonics at the shallow draft

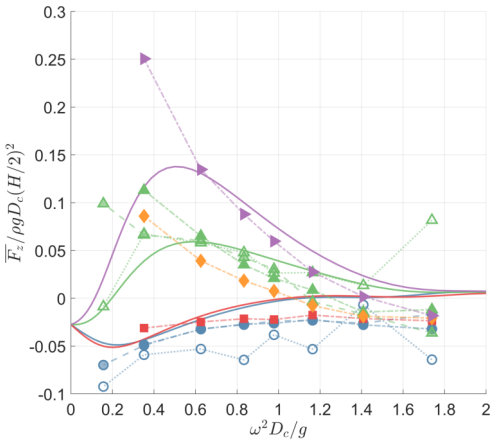

(e) Mean drift at the deep draft

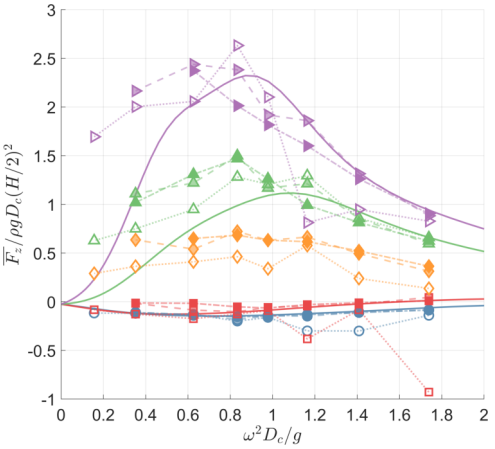

(f) Mean drift at the shallow draft

Figure 6.9 – Non-dimensional vertical wave forces at the deep ($d/D_c = 2.2$) and shallow ($d/D_c = 0.7$) drafts (symbols without fill: $H/\lambda = 0.02$, symbols with transparent colors: $H/\lambda = 0.04$, symbols with fill: $H/\lambda = 0.06$, and solid lines: HydroStar).

6.4.2 Wave loads in bichromatic waves

The horizontal and vertical wave forces acting on the cylinder without (Model A) and with heave plate (Model C) are examined at deep (d/D_c=2.2) and shallow (d/D_c=0.7) drafts in bichromatic waves. The harmonic amplitudes of the forces at $\omega_1, \omega_2, \omega^+, \omega^-$ are nondimensionalized with,

$$F'^{(\omega_j)} = \frac{F^{(\omega_j)}}{\rho g D_c^2 A_j}, \qquad F'^{(\omega^{+,-})} = \frac{F^{(\omega^{+,-})}}{\rho g D_c A_1 A_2} \tag{6.8}$$

where ω_j represents the wave frequency components. A_1 and A_2 are the first harmonics of the wave amplitude corresponding to each wave frequency.

a) Time series and harmonic components

Figures 6.10 - 6.11 show one example of wave-loads time series in bichromatic waves together with the amplitudes of first-, and second-harmonics of ω_1 and ω_2 as well as the sum- and difference-frequency components, ω^+ and ω^-. The amplitudes of the forces are obtained using the least-square method using Eq. (6.2). In the time series, it is clear that the behavior of horizontal forces presents envelopes repeated with period T^-, regardless of the presence of the plate and of the drafts. At the deep draft, the forces are almost the same without or with the plate. However, at the shallow draft, the forces are significantly influenced by the plate, resulting in an increased amplitude. On the other hand, the amplitude and the phase of vertical forces of Model C are increased and shifted compared to Model A in both drafts. This is consistent with the trends observed with monochromatic waves.

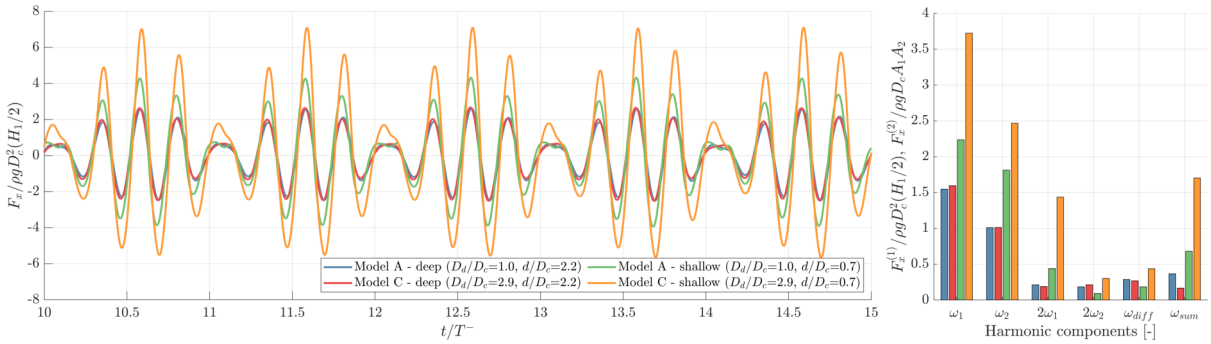

(a) Time series of horizontal wave forces in bichromatic waves **(b)** Harmonics

Figure 6.10 – Non-dimensional horizontal wave forces on the vertical circular cylinder without ($D_d/D_c = 1.0$) and with the heave plate ($D_d/D_c = 2.9$) in bichromatic waves ($\omega_1^2 D_c/g = 0.83$ and $\omega_2^2 D_c/g = 1.30$) at deep ($d/D_c = 2.2$) and shallow ($d/D_c = 0.7$) drafts.

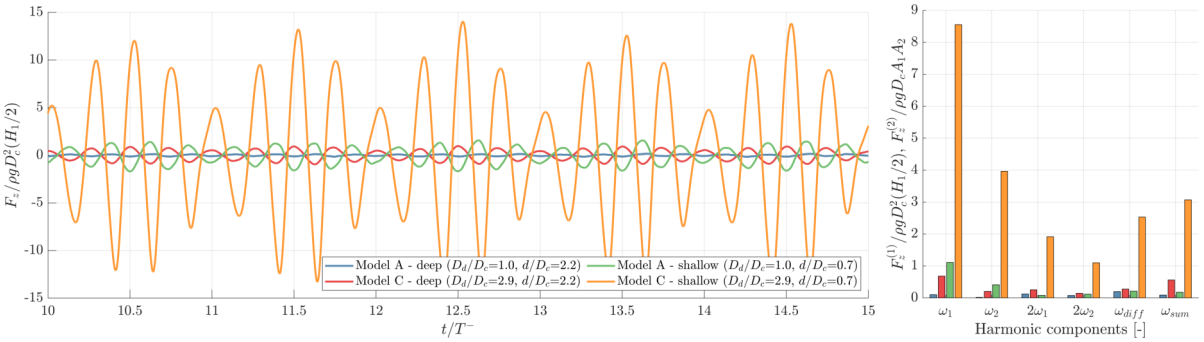

(a) Time series of vertical wave forces in bichromatic waves **(b)** Harmonics

Figure 6.11 – Non-dimensional vertical wave forces on the vertical circular cylinder without ($D_d/D_c = 1.0$) and with the heave plate ($D_d/D_c = 2.9$) in bichromatic waves ($\omega_1^2 D_c/g = 0.83$ and $\omega_2^2 D_c/g = 1.30$) at deep ($d/D_c = 2.2$) and shallow ($d/D_c = 0.7$) drafts.

b) Harmonic operators of the first harmonics

Figure 6.12 shows the first harmonics of horizontal and vertical wave forces in bichromatic waves represented by the symbols with solid face colors. For comparison, the first harmonics from the monochromatic waves with the wave steepness of $H/\lambda = 0.02$ are plotted with symbols without face color. The first-order wave forces from potential flow theory are presented in solid lines with colors corresponding to the configuration and the draft.

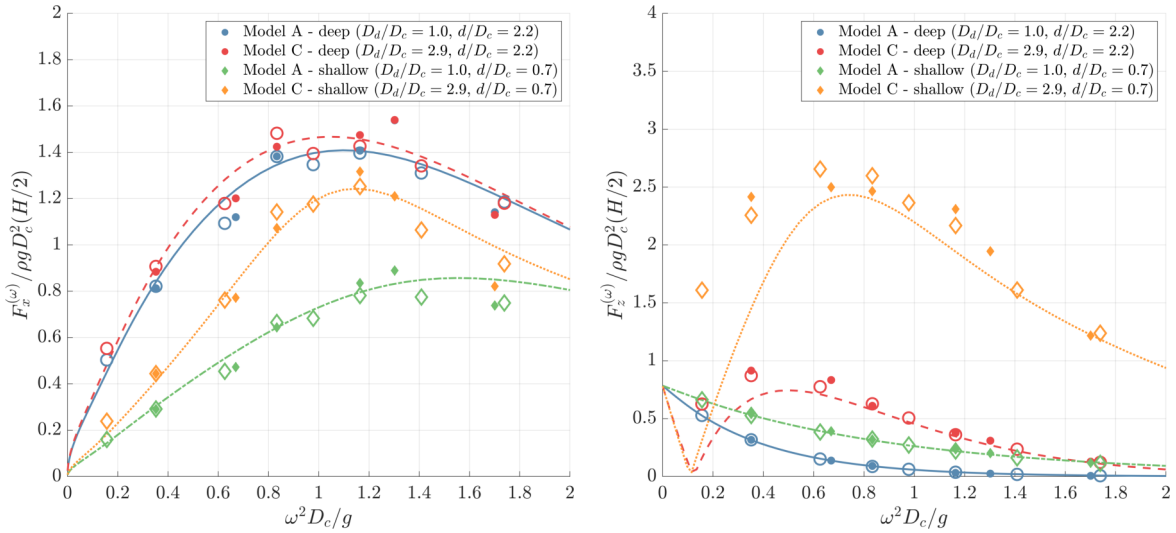

(a) Horizontal wave forces **(b)** Vertical wave forces

Figure 6.12 – The first harmonic wave forces on the vertical circular cylinder with and without the heave plate at the deep and shallow drafts (lines: HydroStar, symbols without fill: monochromatic waves $H/\lambda = 0.02$, symbols with fill: bichromatic waves).

In bichromatic waves, the first harmonics of the forces are generally close to the measurements in monochromatic waves. As the frequency increases, the vertical forces on the solitary cylinder decrease and converge to zero. It is important to note that the vertical forces on the heave plate (Model C) are similar in magnitude to the regular wave ones at low frequency, where the potential flow theory underestimates the forces.

c) Sum- and difference-frequency components

Wave loads at the sum and difference frequencies in bichromatic waves are shown with symbols in Figures 6.13 - 6.14. The second-order sum- and difference-frequency wave forces evaluated by QTFs using HydroStar are given in solid lines for comparison. Similar to the second harmonic in the monochromatic waves, the horizontal forces are less affected by the presence of the plate at the deep draft but significantly affected at the shallow draft. The effect of the plate is noticeable on the vertical forces at both deep and shallow drafts.

In the difference-frequency components, the slowly varying forces on the solitary cylinder and cylinder with the plate are identical at the deep draft. The forces on the cylinder with the plate are significantly increased at the shallow draft, which is a similar tendency to the mean drift forces in monochromatic waves.

In general, the potential flow theory predicts well the horizontal and vertical wave forces at the sum and difference frequencies. However, the theory tends to overestimate the horizontal forces of the sum frequency and underestimate the vertical forces of the difference frequency. This is again similar to what was obtained for the second harmonic and mean of monochromatic waves, where the second-order horizontal forces were higher than those in the measured second harmonic, and the zeroth-order vertical forces were lower than the measurements in the low-frequency region.

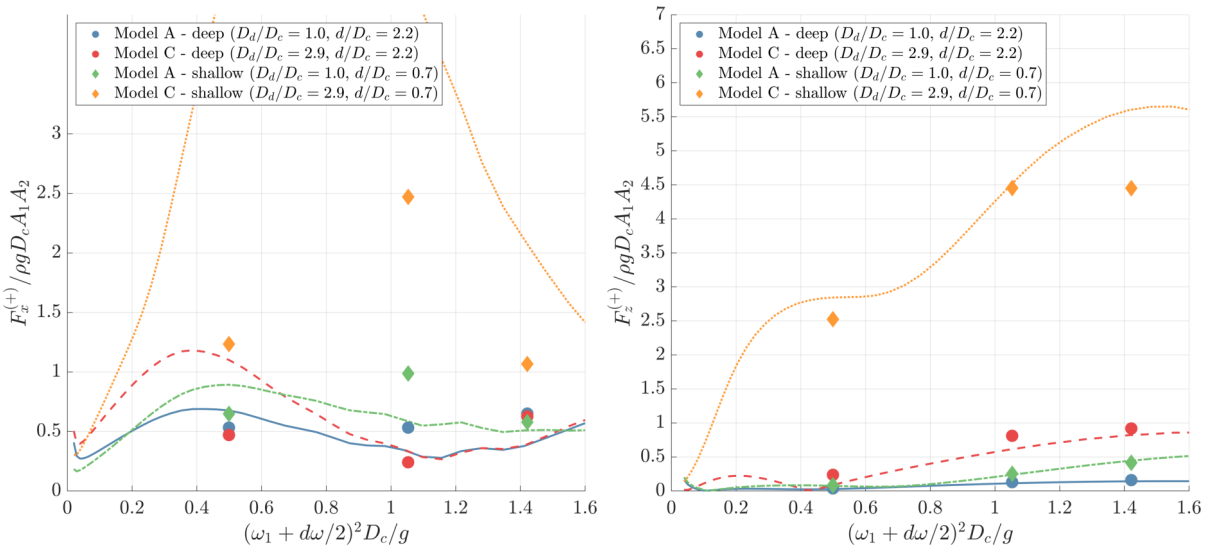

(a) Horizontal wave forces **(b)** Vertical wave forces

Figure 6.13 – Wave forces at sum frequency ω^+ on the vertical circular cylinder with and without the heave plate at the deep and shallow drafts in bichromatic waves (lines: HydroStar (near-field), symbols with colors: bichromatic waves).

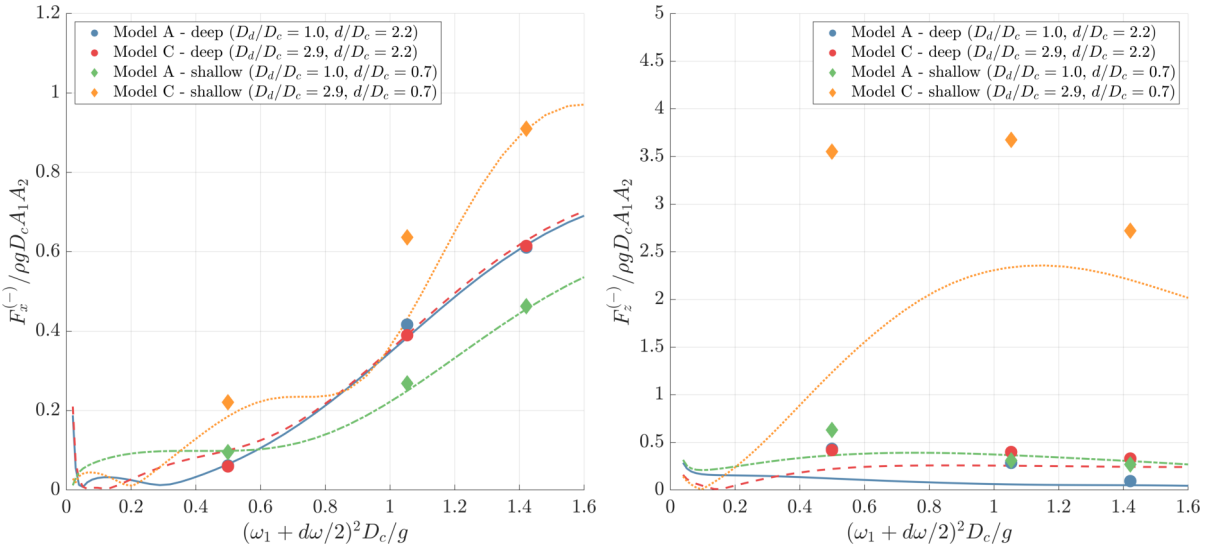

(a) Horizontal wave forces **(b)** Vertical wave forces

Figure 6.14 – Wave forces at difference frequency ω^- on the vertical circular cylinder with and without the heave plate at the deep and shallow drafts in bichromatic waves (lines: HydroStar (middle field), symbols with colors: bichromatic waves).

6.5 Discussion

In the previous section, the potential flow theory, commonly employed in engineering models, was seen to generally predict the wave loads at the 0^{th}, 1^{st}, and 2^{nd} harmonics. However, there are differences between the experimental measurements and theoretical predictions when the cylinder is equipped with the heave plate. Of particular interest is the underestimation of the first harmonics that dominate the wave loads. Therefore, the focus of this section is to provide a more detailed understanding of the first harmonic wave loads.

6.5.1 Wave loads on a vertical circular cylinder in the literature

This section places the present experiments on a truncated vertical circular cylinder (Model A) within relevant experimental databases in the literature. The experimental databases available in the literature mainly concentrate on horizontal wave forces, with only limited discussion on vertical wave forces.

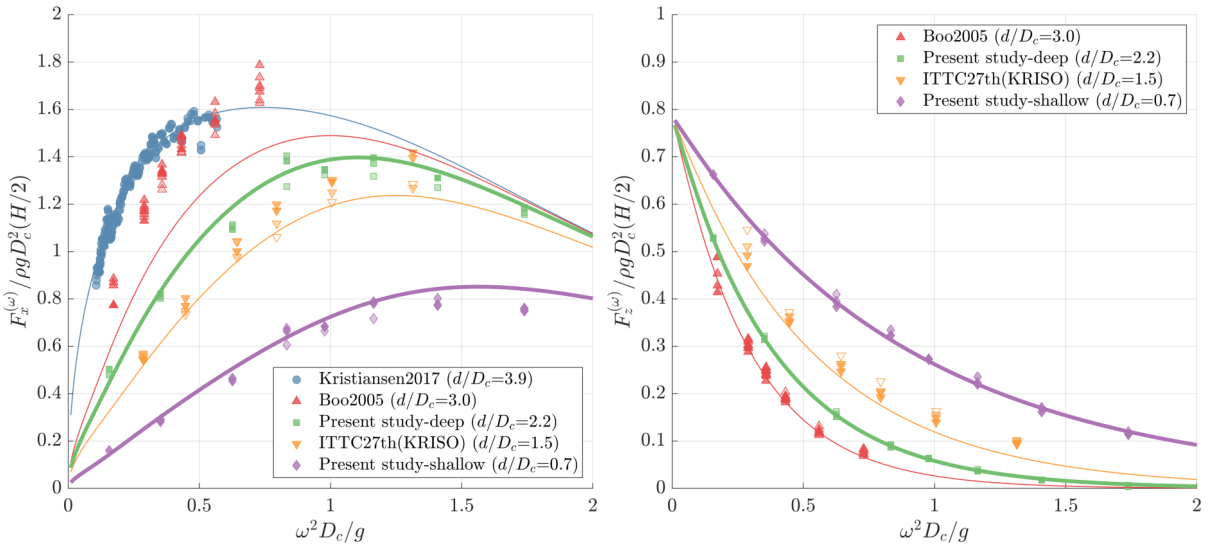

(a) Horizontal wave forces **(b)** Vertical wave forces

Figure 6.15 – Non-dimensional first harmonics of horizontal and vertical wave forces on the vertical circular cylinder. Lines are the results using the linear theory: a) McCamy and Fuchs (1954) for a bottom-mounted cylinder and Garrett (1971) for the truncated cylinder. Symbols are the experimental measurements: 1) Kristiansen and Faltinsen (2017) for the bottom-mounted cylinder (○), 2) Boo (2006) (△), 3) ITTC 27th OEC (2014); Sung et al. (2007) (▽), and 4) the present study (□, ◊) for the truncated cylinder. The transparency of the face color means the wave steepness.

Figure 6.15 illustrates the first harmonics of wave loads exerted on the vertical circular cylinder with respect to the nondimensional wave frequency $\omega^2 D_c/g$. The cylinder configurations in the literature are represented by the draft ratio d/D_c. For instance, the present study considers two draft ratios: deep draft ($d/D_c = 2.2$) and shallow draft ($d/D_c = 0.7$). Previous studies examined the bottom-mounted cylinder ($d/D_c = 3.9$, Kristiansen and Faltinsen (2017)) and the truncated cylinder ($d/D_c = 1.5$, Sung et al. (2007) and $d/D_c = 3.0$, Boo (2006)). For comparison, the potential flow theory on the bottom-mounted circular cylinder (McCamy and Fuchs (1954)) and on the truncated cylinder (Garrett (1971)) are presented in solid lines. In general, the first harmonic wave loads, nondimensionalized as $F^{(\omega)}/\rho g D_c^2(H/2)$, are described well by the linear potential flow theory, which evaluates the forces analytically.

The outcomes of the present experiment are consistent with the general trend in the literature. Increasing the draft ratio increases the nondimensional horizontal forces. This can be attributed to the increase in the wetted body surface. Eventually, the horizontal forces acting on the truncated cylinder are close to those acting on the bottom-mounted cylinder. Conversely, decreasing the draft ratio leads to an increase in the nondimensional vertical wave forces. As confirmed in Section 6.4, the vertical forces on the solitary cylinder decrease with increasing wave frequency and converge to zero.

6.5.2 Wave loads on a vertical circular cylinder with a heave plate

In this section, we focus on the underestimation of the first harmonics of the vertical wave forces in the low-frequency region, as observed in Section 6.4. To begin with, we investigate the flow field by solving the incompressible Navier-Stokes equations (with a CFD solver) for the cylinder with the heave plate (Model C, $D_d/D_c = 2.9$) in regular waves. The flow is visualized around the heave plate, where flow separation is expected. The vertical wave forces evaluated in CFD are compared with the experimental measurements. Furthermore, attempts are made to overcome the underprediction of potential flow solutions by introducing the viscous drag term of Morison equation. Finally, a classification into different regimes of vertical wave forces is proposed based on the wave frequency and diameter ratio.

a) CFD simulations

The CFD simulations are carried out using the foamStar solver (see Section 4.2). The regular waves are generated using wave2Foam with the free surface $k-\omega$ SST turbulence model as well as the Crank-Nicolson time integration scheme to minimize the wave dissipation during

its propagation.

Spatial refinement is considered around the free surface as $\lambda/\Delta x = \lambda/\Delta y > 80$ and $H/\Delta z > 15$. Relaxation zones are used with length λ for the incoming waves, 2λ for wave reflections at the back of the domain and 0.5λ on the side. In total, about 5 million cells are used within the symmetric computational domain. The time step dt is taken as $T/dt = 500$.

Figure 6.16 presents the flow field with Model C ($D_d/D_c = 2.9$) in the regular waves ($\omega^2 D_c/g = 0.35$, $H/\lambda = 0.04$) at the deep draft. The magnitude of the flow velocity field is illustrated along with the vectors of the flow velocity. A strong flow separation is observed at the edge of the plate in CFD. This flow separation is not considered in the potential flow theory.

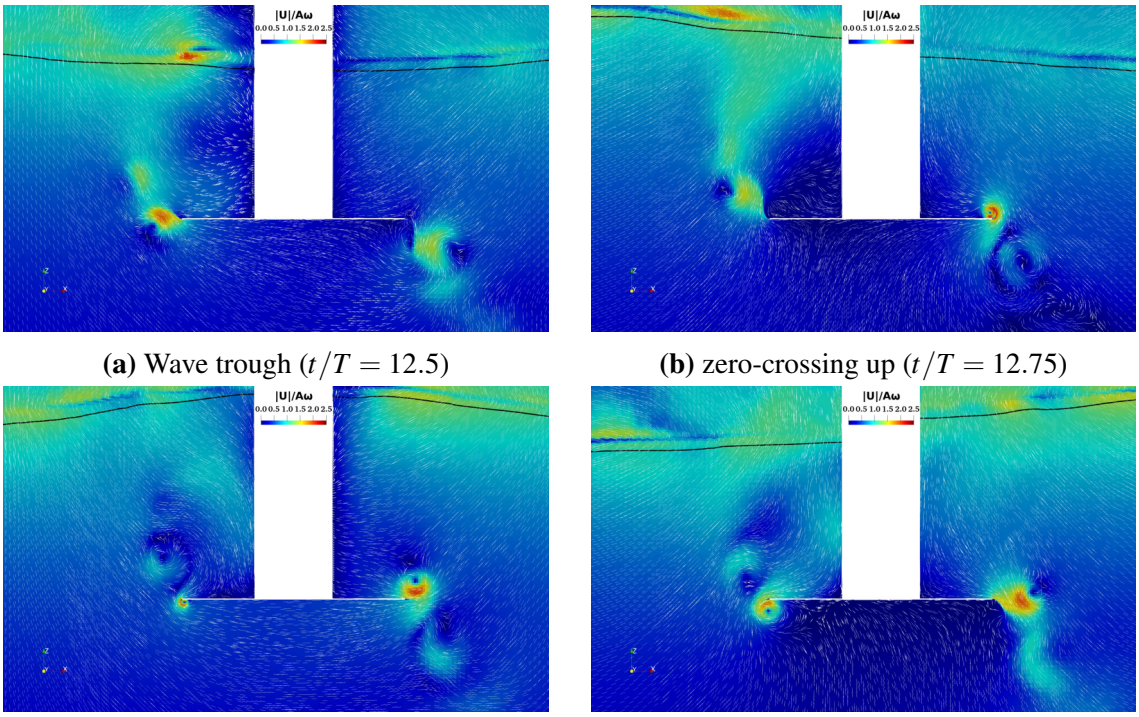

(a) Wave trough ($t/T = 12.5$)

(b) zero-crossing up ($t/T = 12.75$)

(c) Wave crest ($t/T = 13.0$)

(d) Zero-crossing down ($t/T = 13.25$)

Figure 6.16 – Magnitude of non-dimensional flow velocity ($|\mathbf{U}|/(H/2)\omega$) and free surface (black solid line) around the cylinder with the heave plate ($D_d/D_c = 2.9$) at the deep draft in the monochromatic waves ($\omega^2 D_c/g = 0.35$, $H/\lambda = 0.04$) propagating in positive x-direction (left to right).

b) Simplified viscous model

A simplified method is presented to investigate the effect of the vertical wave forces resulting from flow separation. The contribution of the flow separation can be modeled using

viscous drag forces from Morison equation. The first-order vertical wave forces can be defined here as,

$$F_z^{(1)} = F_z^p + F_z^v \tag{6.9}$$

where F_z^p is the first-order hydrodynamic forces computed by the potential flow theory (Han et al. (2024)) and F_z^v is the viscous drag force from the Morison equation defined as

$$F^v = \frac{1}{2}\rho C_D S_d U_z |U_z| \tag{6.10}$$

where $S_d = 1/4\pi D_d^2$ is the plate's surface area and C_D stands for the drag coefficient. The flow velocity U_z is computed using the linear velocity potential of the incident wave, ϕ_I,

$$U_z(t) = \frac{\partial \phi_I}{\partial z} = \Re\mathfrak{e}\left\{ \frac{-igAk_0}{\omega} \frac{\sinh k_0(z+h)}{\cosh k_0 h} e^{i(k_0 x - \omega t)} \right\} \tag{6.11}$$

where the wave number k_0 is obtained from the linear dispersion relation, $\omega^2 = k_0 g \tanh k_0 h$. The reference position is at the center of the submerged circular plate ($x = 0$, $z = -d$).

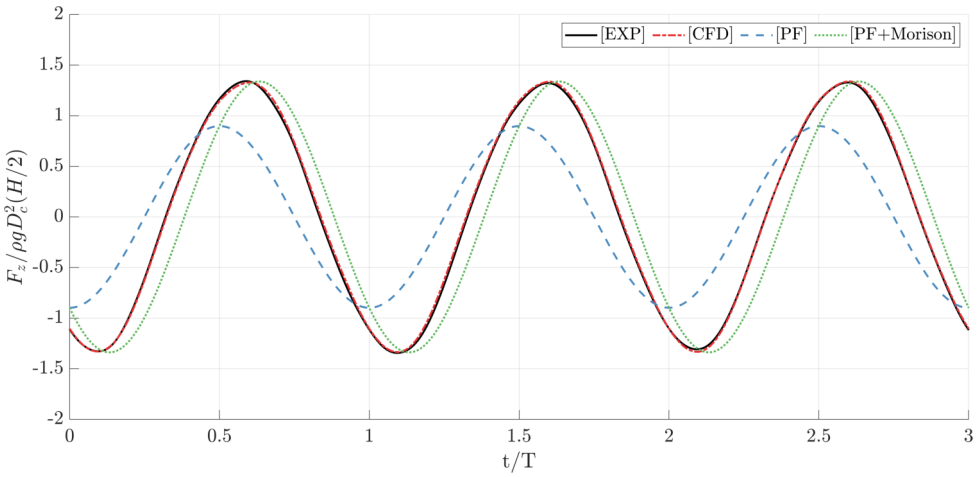

Figure 6.17 – Time series of non-dimensional vertical wave forces on the cylinder with heave plate ($D_d/D_c = 2.9$) at the deep draft ($d/D_c = 2.2$) in the regular waves ($\omega^2 D_c/g$=0.35, H/λ = 0.04): experiment (solid line), CFD (dashed-dot line), potential flow theory (dashed line), and simplified method with $C_D = 23.0$ (dotted line).

Figure 6.17 shows an example of the vertical force time history on Model C in regular waves with non-dimensional wave frequency ($\omega^2 D_c/g = 0.35$) and wave steepness (H/λ = 0.04) at the deep draft ($d/D_c = 2.2$). The drag coefficients for Model C ($D_d/D_c = 2.9$) are obtained iteratively by targeting the amplitude of the measured vertical forces, resulting in

constant values of 17, 23, and 28 for the three wave steepnesses, respectively.

The CFD result is in very close agreement with the experiment, while the potential flow theory largely underestimates the amplitude and has a phase discrepancy. An important improvement of the potential flow prediction is obtained by including the viscous drag forces (Eq. (6.9)), but there is still some inconsistency in the phase. There are two possible reasons for this difference. The first reason is a time lag due to the distribution of vortices, which has a certain inertia inducing a force not in phase with the excitation velocity. The second reason is the reference position of the flow velocity. The drag forces are related to the flow separation that occurs at the edge of the plate, which is far from the reference position. This aspect is left for future research focusing on engineering design models.

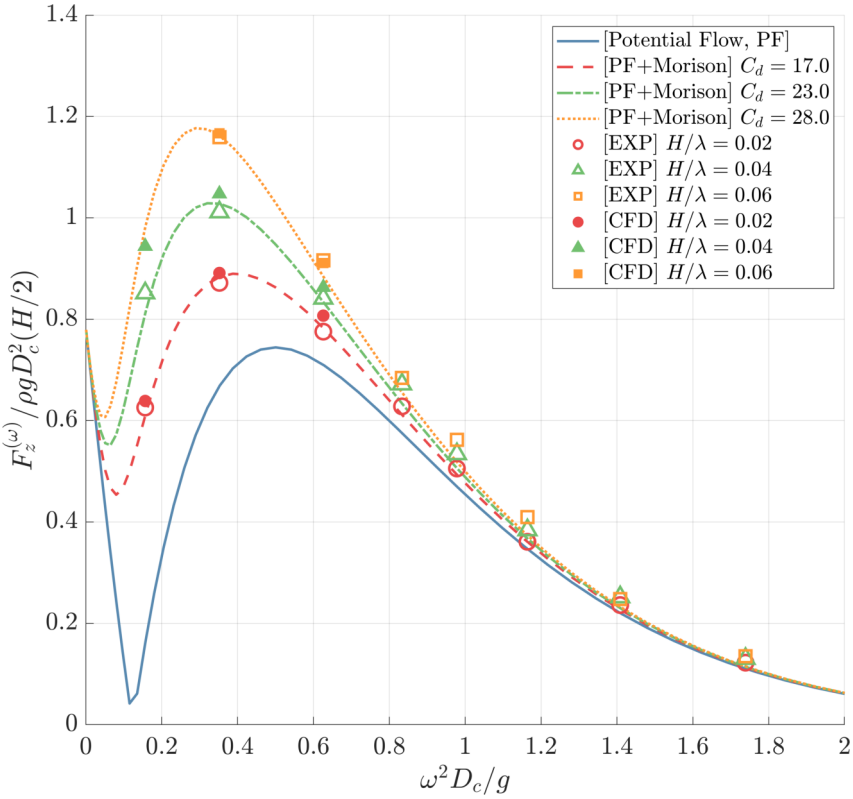

Figure 6.18 – Non-dimensional vertical wave forces on the cylinder with heave plate ($D_d/D_c = 2.9$) at the deep draft ($d/D_c = 2.2$): potential flow theory (solid lines), potential flow theory with added viscous drag (dashed, dashed-dot, and dotted lines), experiments (symbols with face colors), CFD (symbols without face colors).

Figure 6.18 shows the prediction of the first harmonic operator for vertical forces in three wave steepnesses using the simplified method, i.e. potential flow with added viscous drag, and CFD. CFD simulations were performed only in the low-frequency domain. It accurately captured the vertical forces in that low-frequency region as well as the effects of wave steepness. Similarly, the simplified method accurately predicts the first harmonic amplitude over the entire frequency range using the constant drag coefficient corresponding to each wave steepness. It is worth noting that at deep draft, the drag coefficient depends on wave steepness and not frequency. The contribution of viscous drag forces appears in the low-frequency region ($\omega^2 D_C/g < 1.0$), and it is most significant at the cancelation frequency of about $\omega^2 D_c/g = 0.1$.

c) Vertical force regimes on a cylinder with a heave plate at the deep draft

This section examines the vertical wave forces based on the size of the heave plate. The CFD simulations, described in Section a), are conducted with seven representative plate diameter ratios: $D_d/D_c = 1.0, 1.5, 2.0, 2.5, 2.9, 3.5, 4.0$. A single regular wave, with wave steepness $H/\lambda = 0.04$ and nondimensional frequency $\omega^2 D_c/g = 0.35$, is considered where strong flow separation is observed. This study is limited to the deep draft $d/D_c = 2.2$.

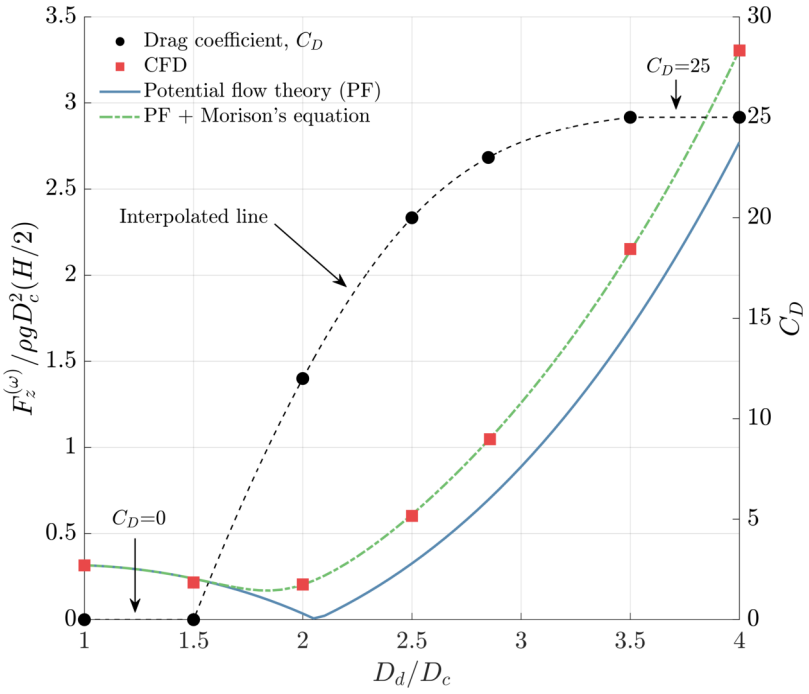

Figure 6.19 – Determination of drag coefficients for diameter ratios D_d/D_c ranging from 1.0 to 4.0 with a regular wave of frequency $\omega^2 D_c/g$=0.35 and wave steepness H/λ=0.04 at the deep draft d/D_c=2.2.

The drag coefficients for different plate diameter ratios are provided in Figure 6.19. The coefficients are determined using the simplified method described in Equations (6.9-6.11) with reference to the CFD results. The values are interpolated for diameter ratios ranging from 1.0 to 4.0. For small plates ($D_d/D_c \leq 1.5$), where the difference between the diffraction theory and CFD is negligible, the coefficients are set to zero. It is also noted that the coefficient is converged to a constant value for large plates ($D_d/D_c \geq 3.5$).

The simplified method provides global responses that correspond to the wave frequency as shown in Figure 6.20. From the results, three distinct force regimes can be identified:

- Region I: Diffraction. This region is governed by the potential flow theory. This is valid for the high-frequency region $\omega^2 D_c/g \geq 1.0$ for all plate diameters, and over the whole range of frequency for small heave plates with $D_d/D_c < 1.5$.
- Region II: Viscous drag. This is where viscous drag dominates, and the plate cancels out the linear hydrodynamic vertical forces ($0.1 \leq \omega^2 D_c/g \leq 0.5$).
- Region III: Diffraction + viscous drag. In this region, both potential and drag forces contribute to the vertical wave forces.

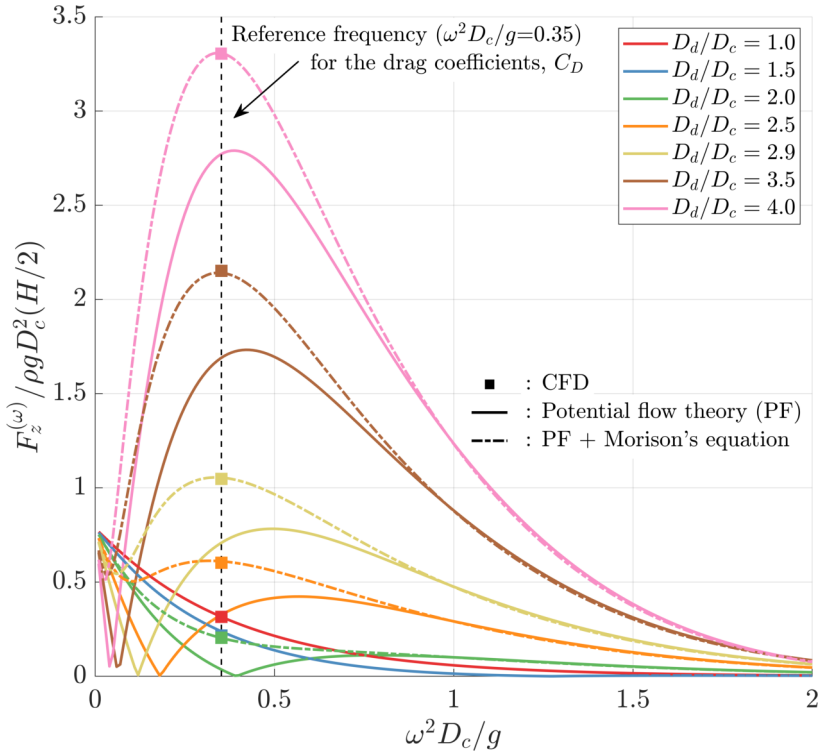

Figure 6.20 – Vertical wave excitation forces for nondimensional wave frequency $\omega^2 D_c/g$ at the deep draft.

In summary, Figure 6.21 illustrates these three vertical wave force regimes acting on the cylinder with heave plate. Note that this analysis is limited to the case of wave steepness H/λ=0.04 and the deep draft. It is worth noting that the size of the drag region II depends on the wave steepness as the drag coefficient changes, as discussed in Section b).

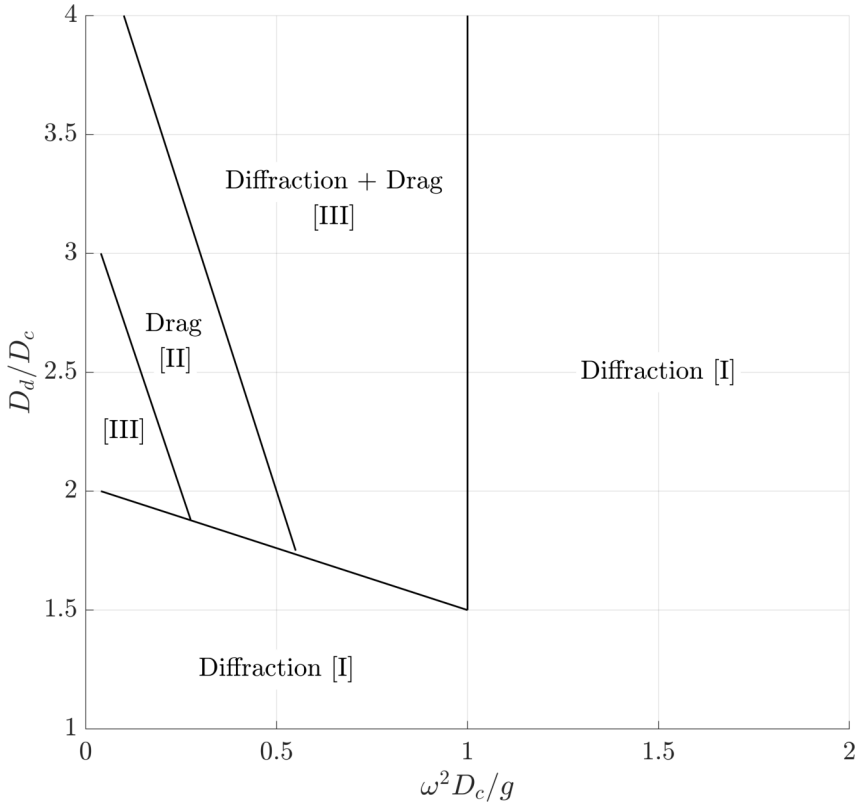

Figure 6.21 – Vertical wave force regimes of a vertical circular cylinder with a heave plate at the deep draft ($d/D_c = 2.2$): Region I: diffraction regime, Region II: viscous drag regime, and Region III: diffraction and viscous drag regimes.

6.6 Conclusions

Wave loads on a fixed vertical and surface-piercing circular cylinder with a circular plate were investigated experimentally. The study examined five different plate configurations, including a perforated plate, at deep and shallow submerged depths ($d/D_c = 2.2, 0.7$). The waves used in the experiment were monochromatic waves with three wave steepnesses ($H/\lambda = 0.02, 0.04, 0.06$) and bichromatic waves. The waves were carefully calibrated before testing. A force transducer was used to measure wave loads, mitigating sources of error from wave reflection and structural responses.

Horizontal and vertical wave forces exerted on the cylinder with the heave plate were of particular interest. Measured force time histories were examined to provide insights into the influence of the plate diameter and submerged depth. Fourier analysis and least-squares fitting were utilized to obtain the harmonic content from the load time series induced by the monochromatic and bichromatic waves.

A boundary element method solver based on the potential flow theory (HydroStar) was used to evaluate the first- and second-order loads for comparison. Panel models for solid plates were made by considering the plate's thickness, and the source distribution method was used to solve a boundary integral equation. The perforated plate was modeled using Darcy's law by assuming a zero-thickness plate with a porous parameter, with a mixed approach (dipole + source methods).

In the present study, a significant impact of the heave plate was observed on the wave loads, particularly on the harmonic contents. The following outcomes can be highlighted:

- Heave plate diameter: The diameter ratio of the plate (D_d/D_c) significantly affects wave loads by altering the force amplitude and shifting the phase. The boundary element method used in this study provides reasonable agreement with the corresponding harmonics of experimental measurements. However, there are some inconsistencies observed in the harmonic content, particularly in the first harmonic of the vertical force. The BEM solver predicts the cancellation of first-order vertical forces in low-frequency regions but the experimental results show significant amounts of first-harmonic forces at these frequencies.
- Wave steepness: The nondimensional horizontal forces tend to decrease as the wave steepness increases. This trend is more pronounced for the large plates ($D_d/D_c = 2.9, 3.5$) whereas it is negligible for the solitary cylinder. On the other hand, the first harmonic of vertical forces with the large plates increases with increasing wave

steepness in low-frequency regions.

- Submerged depth: The effect of the submerged depth is closely related to the wave steepness, as there is an interaction between the plate and the free surface. At deep draft, horizontal forces are less affected by the heave plate and the wave steepness, but at shallow draft, it becomes significant. Additionally, the harmonic content of the wave loads is notably increased at the shallow draft compared to the deep draft.
- Perforated plate: The perforated plate with 10 % porosity effectively decreases the wave loads, which is more noticeable at shallow drafts. The panel method with porous parameter predicts well the first harmonic of the wave loads at the deep and shallow drafts.

Further investigation of the first harmonics of wave loads was carried out. The results from the present experiment on the solitary cylinder (Model A) were found to be consistent with the general trends in the literature.

CFD simulations were carried out to investigate the vertical forces on the heave plate (Model C) at low wave frequency, configuration for which the potential flow solver did not predict well the experimental result. It was observed that flow separation occurred around the edge of the plate. A simplified viscous approach using Morison's equation was used to model the contribution of the flow separation. The drag coefficient of Morison's equation was determined using experimental and numerical (CFD) results for the desired wave steepness at low frequencies where viscous drag is dominant. This approach permitted to provide an accurate prediction of the first harmonic vertical force amplitude compared to the experiment despite some remaining inconsistencies in the phase of the time series.

In conclusion, a classification of vertical force regimes at deep draft was proposed as a function of the nondimensional wave frequency and the plate diameter ratio: (I) diffraction regime, (II) viscous drag regime, and (III) diffraction and viscous drag regime.

CHAPTER 7

HYDRODYNAMIC LOADS ON AN OSCILLATING CIRCULAR CYLINDER WITH A HEAVE PLATE

This chapter presents the hydrodynamic loads for surge, heave, and pitch oscillations of a vertical and surface-piercing circular cylinder with the heave plate. The study considers flow parameters (motion amplitude and frequency) and heave-plate characteristics, including plate diameter and porosity. Furthermore, the proximity of the free surface is of interest with various submersion depths. Dedicated experiments were carried out with extensive test campaigns to address the behavior of the hydrodynamic loads and the harmonic contents. As described in Chapter 5, a captive model technique was employed to impose the motions using a hexapod as a forced motion generator. The hydrodynamic loads were obtained by subtracting the inertia, gravity, and linear hydrostatic loads from the measured loads using a six-component force transducer. This chapter is written based on the submitted paper, "Experimental study of hydrodynamic loads induced by the motion of a vertical circular cylinder with heave plates in proximity of the free surface" (see Appendix A).

7.1 Introduction

First, the test matrix is provided in the following section for the pure surge, heave, and pitch motions, with the proximity of the free surface. Section 7.3 introduces the method that is used to obtain the hydrodynamic loads from the measurements. A procedure is introduced to obtain mass and moment of inertia experimentally, and a mathematical description is given for the fluid loads by defining the dynamic and static contributions. The experimental results are presented in Sections 7.4 to 7.6 for forced heave, surge, and pitch motions, respectively. The hydrodynamic loads are examined at various submerged drafts first, and observation of the harmonic content of the loads is discussed. Furthermore, the influence of the characteristics of

the heave plate geometry, including diameter ratio and porosity, is discussed. In particular, the first harmonics are interpreted as added mass and damping coefficients. The coefficients are investigated by studying the influence of flow parameters, plate geometry and submerged plate depth. Lastly, conclusions are drawn in Section 7.8.

7.2 Test conditions

7.2.1 Prescribed motions

In this study, prescribed motions are defined with a periodic function with 30 motion periods T in total duration, with a function of amplitude ξ_j and angular frequency ω as follows,

$$\begin{bmatrix} \mathbf{r}^0_{b/0}(t) \\ \Theta_{0b}(t) \end{bmatrix} = \xi_j \cos(\omega t + \varepsilon), \qquad j = 1-6 \tag{7.1}$$

where $\mathbf{r}^0_{b/0}(t) = [\mathbf{x}^0_{b/0}(t), \mathbf{y}^0_{b/0}(t), \mathbf{z}^0_{b/0}(t)]^T$ is the translational vector expressed in the global reference frame $\{0\}$. $\Theta_{0b}(t) = [\phi(t), \theta(t), \psi(t)]^T$ is the Euler angle vector that takes $\{0\}$ into the body reference frame $\{b\}$. ξ_j is the motion amplitude for surge, sway, and heave for $j = 1-3$, and roll, pitch, and yaw for $j = 4-6$. $\omega = 2\pi/T$ is a circular frequency, t is time, and ε is a phase of the motion. In the following prescribed motions, only one motion amplitude of the six is non-zero in each configuration.

As illustrated in Figure 7.1, a ramp function was considered at the beginning and end of the prescribed motions to minimize the transient behavior of the response. Before the beginning of the motions, the experimental model moves slowly to achieve the target submerged depth with an initial offset and pauses for $t_{zero} = 50$ s to get the zeroing signals. The center of rotation was defined at O_b, which is on the free surface at rest.

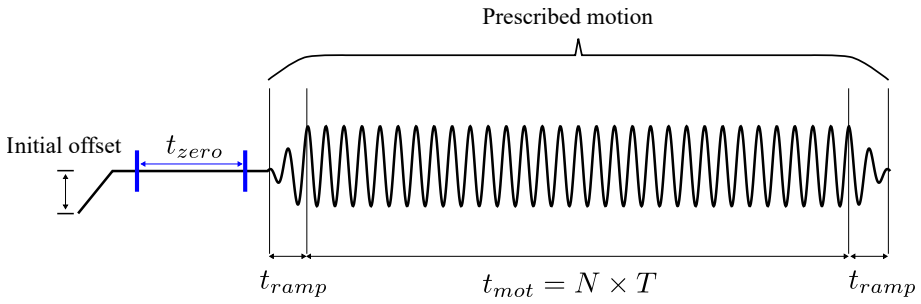

Figure 7.1 – Prescribed motions including times for zeroing, ramp up and down.

7.2.2 Surge, heave and pitch motion parameters

A single vertical cylinder with heave plates oscillating in surge, heave, and pitch motions was tested without incident waves to obtain the hydrodynamic loads induced by the prescribed motion. Two distinct test campaigns were conducted with different flow parameters. First, various motion periods from 0.9 s to 3.0 s were considered with a single amplitude of 0.05 m for surge and heave and 0.05 rad (3.0 deg) for pitch. These small amplitude motions were intended to minimize the nonlinearity due to the motion amplitude.

The nonlinearity of the loads was then addressed with different motion amplitudes at a single motion frequency ($\omega^2 D_c/g$=0.35, T = 2.0 s). For the translational motions, the amplitudes range from 0.0125 m to 0.19 m, which corresponds to the translational KC_c number

$$KC_c = 2\pi\xi_{1,3}/D_c \tag{7.2}$$

which ranges from 0.2 to 3.6.

Regarding the pitch amplitudes, they were chosen from 0.02 rad (1.0 deg) to 0.16 rad (9.0 deg). The rotational KC_c number is introduced as,

$$KC_c = 2\pi\xi_5 d/D_c \tag{7.3}$$

which differs depending on the submerged depth.

Furthermore, deep (0.775 m), middle (0.500 m) and shallow (0.250 m) drafts were considered to investigate the free surface proximity. The middle draft was only tested for Model C (solid plate with $D_d/D_c = 2.9$), which is the reference model. In addition, two more submerged drafts were added for the heave motions: the intermediate (0.375 m) and very shallow (0.125 m) drafts. All the heave plate configurations were tested with surge and heave motions. For the pitch motions, only the effect of the presence of the heave plate, including the perforated plate, was studied using Models A, C and D. The test condition parameters are listed in Table 7.1.

Figure 7.2 presents examples of disturbed free surface in forced heave oscillation with the largest heave plate ($D_d/D_c = 3.5$) at the shallow draft. Strong interactions between the free surface and the heave plate were observed during the experiments.

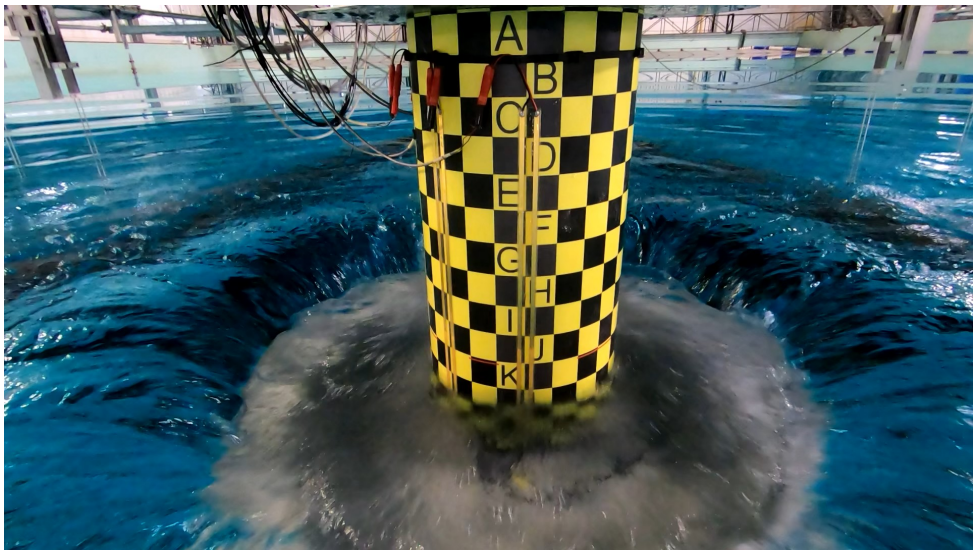

(a) Disturbed free surface by the heave plate.

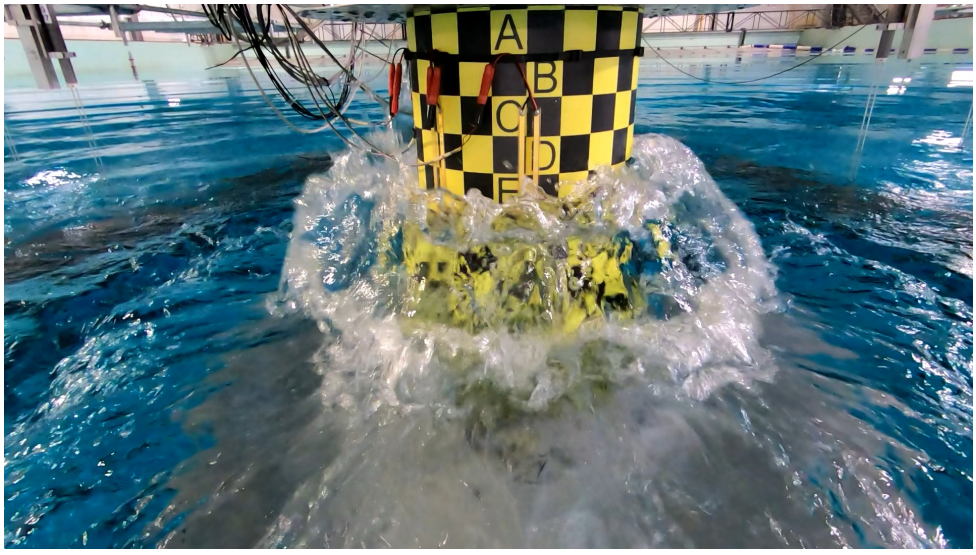

(b) Free surface jump-up after the disturbance.

Figure 7.2 – Snapshots of the radiated waves around the truncated cylinder with heave plate ($D_d/D_c = 3.5$) at the shallow submerged depth ($d/D_c = 0.7$, $d = 0.775$ m). A regular heave motion ($KC_c = 1.8$, $\omega^2 D_c/g = 1.41$) is imposed by the hexapod.

Table 7.1 – Test parameters for the forced oscillation in surge, heave, and pitch motions.

Motions	Test type	T [s]	$\omega^2 D_c/g$	ξ [m or deg]	KC_c	D_d/D_c (model)	d/D_c (draft)
Heave	freq.	3.0	0.16	0.050	0.9	1.0 (A) 1.5 (B) 2.9 (C) 2.9τ (D) 3.5 (E)	2.2 (deep) 1.4 (middle) 1.1 (intermediate) 0.7 (shallow) 0.4 (very shallow)
		2.0	0.35				
		1.5	0.63				
		1.3	0.83				
		1.2	0.98				
		1.1	1.16				
		1.0	1.41				
		0.9	1.74				
	amp.	2.0	0.35	0.0125	0.22	1.0 1.5 2.9 2.9τ 3.5	2.2 1.4 1.1 0.7 0.4
				0.025	0.45		
				0.050	0.90		
				0.075	1.35		
				0.100	1.80		
				0.125	2.24		
				0.150	2.69		
				0.175	3.14		
				0.190	3.41		
	amp. & freq.	4.0	0.09	0.0125	0.22	2.9	1.1 0.7
		3.0	0.16	0.025	0.45		
		2.5	0.23	0.050	0.90		
				0.075	1.35		
				0.100	1.80		
				0.125	2.24		
				0.150	2.69		
				0.175	3.14		
				0.190	3.41		
Surge	freq.	3.0	0.16	0.050	0.9	1.0 1.5 2.8 2.9τ 3.5	2.2 1.4 0.7
		2.0	0.35				
		1.5	0.63				
		1.3	0.83				
		1.2	0.98				
		1.1	1.16				
		1.0	1.41				
		0.9	1.74				
	amp.	2.0	0.35	0.025	0.45	1.0 1.5 2.9 2.9τ	2.2 1.4 0.7
				0.050	0.90		
				0.075	1.35		
				0.100	1.80		
				0.125	2.24		
				0.150	2.69		
				0.175	3.14		
				0.190	3.59		
Pitch	freq.	3.0	0.16	3.0	0.73/0.47/0.23 (deep/middle/shallow)	1.0 2.9 2.9τ	2.2 1.4 0.7
		2.0	0.35				
		1.5	0.63				
		1.3	0.83				
		1.2	0.98				
		1.1	1.16				
		1.0	1.41				
		0.9	1.74				
	amp.	2.0	0.35	1.0	0.24/0.16/0.08	1.0 2.9 2.9τ	2.2 1.4 0.7
				3.0	0.73/0.47/0.23		
				5.0	1.21/0.78/0.39		
				7.0	1.70/1.10/0.55		
				9.0	2.19/1.41/0.70		
				12.0	2.91/1.88/0.94		

7.3 Analysis of the experimental data

7.3.1 Load convention for the moving body

Figure 7.3 presents the reference frames and load conventions in the forced oscillation tests. The Galilean reference frame $\{O\}$ is fixed on the free surface at rest, while the body-fixed reference frame $\{b\}$ is attached to the moving body. The instantaneous state of the reference frame $\{b\}$ is described based on the reference frame $\{O\}$, using the distance vector $\mathbf{r}^0_{b/0}$ and the Euler angles Θ_{0b}. In this test, $\mathbf{r}^0_{b/0}$ and Θ_{0b} are imposed by the hexapod, while the Qualysis system measures these motions to verify they correspond to the prescription.

The loads acting on the moving body are measured by the force transducer located at O_t. Since the transducer is fixed on the rigid body, the loads are expressed in the body-fixed reference frame $\{b\}$. Therefore, the measured loads are expressed at the origin of the body-fixed reference frame $\{b\}$, O_b, using the equation below:

$$\begin{aligned} \mathbf{F}^b_m &= \mathbf{F}^b_t \\ \mathbf{M}^b_m &= \mathbf{M}^b_t + \mathbf{r}^b_{t/b} \times \mathbf{F}^b_t \end{aligned} \tag{7.4}$$

where $\mathbf{F}^b_t$ and $\mathbf{M}^b_t$ are the measured force and moment vectors about O_t and $\mathbf{r}^b_{t/b}$ is the position vector from O_b to O_t expressed in $\{b\}$.

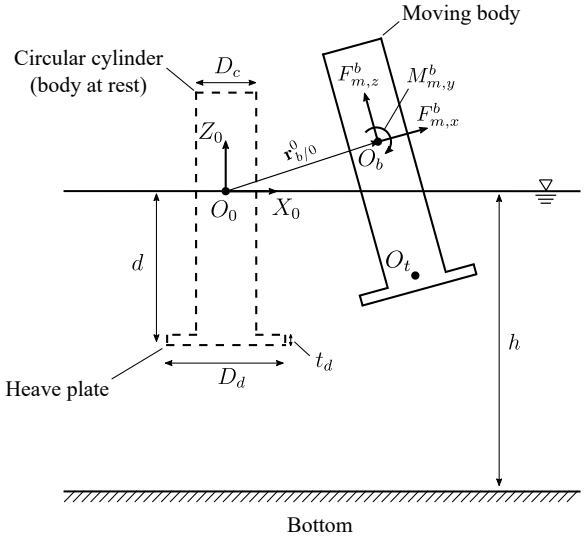

Figure 7.3 – Load convention of the moving body in the wave tank: $F^b_{m,x}, F^b_{m,z}, M^b_{m,y}$ stand for the measured forces and moments at the origin of the body-fixed reference, O_b, converted from the force transducer located at O_t.

7.3.2 Fluid loads from the measurements

The main objective of these experiments is to investigate the hydrodynamic loads on an oscillating body. Since the force measurement contains the inertia, gravity and fluid loads, the first two terms need to be handled in order to obtain the fluid loads using the Newton-Euler equation of motion at the given point O_b shown as:

$$\begin{aligned} m\left(\frac{d\mathbf{V}^b_{b/0}}{dt}+\boldsymbol{\omega}^b_{b/0}\times\mathbf{V}^b_{b/0}+\frac{d\boldsymbol{\omega}^b_{b/0}}{dt}\times\mathbf{r}^b_{G/b}+\boldsymbol{\omega}^b_{b/0}\times(\boldsymbol{\omega}^b_{b/0}\times\mathbf{r}^b_{G/b})\right)&=\mathbf{F}^b_g+\mathbf{F}^b_f+\mathbf{F}^b_c \\ I_b\frac{d\boldsymbol{\omega}^b_{b/0}}{dt}+\boldsymbol{\omega}^b_{b/0}\times I_b\boldsymbol{\omega}^b_{b/0}+m\mathbf{r}^b_{G/b}\times\left(\frac{d\mathbf{V}^b_{b/0}}{dt}+\boldsymbol{\omega}^b_{b/0}\times\mathbf{V}^b_{b/0}\right)&=\mathbf{M}^b_g+\mathbf{M}^b_f+\mathbf{M}^b_c \end{aligned} \tag{7.5}$$

where m is the mass of the model, I_b is the moment of inertia at position O_b, $\mathbf{r}^b_{G/b}$ is the vector from O_b to the center of gravity O_G, $\mathbf{V}^b_{b/0}$ is the body velocity and $\boldsymbol{\omega}^b_{b/0}$ is the angular velocity. The superscript b means the body-fixed reference frame, and the subscripts g, f and c stand for the gravity, fluid and constraint loads. Here, we are following the notation of Fossen (2011).

The LHSs of Equation (7.5) are defined as the inertia forces and moments: $\mathbf{F}^b_i$, $\mathbf{M}^b_i$. On the other hand, the constraint loads on the RHSs are treated as the measured loads from the load cell as $\mathbf{F}^b_c=-\mathbf{F}^b_m$ and $\mathbf{M}^b_c=-\mathbf{M}^b_m$. Then, the equation of motion is simplified for the measured loads as follows,

$$\begin{aligned} \mathbf{F}^b_f(t)&=\mathbf{F}^b_m(t)+\mathbf{F}^b_i(t)-\mathbf{F}^b_g(t) \\ \mathbf{M}^b_f(t)&=\mathbf{M}^b_m(t)+\mathbf{M}^b_i(t)-\mathbf{M}^b_g(t) \end{aligned} \tag{7.6}$$

where the subscript m stands for the measured loads.

From these last equations, the fluid loads acting on the body are obtained by subtracting the inertial and gravity loads from the measurements. The general expressions of the inertia, gravity and hydrostatic loads are summarized in Section 2.1.

7.3.3 Hydrodynamic loads on the vertical circular cylinder with the heave plate

When a free surface piercing body oscillates in calm water, the fluid loads involve dynamic and static contributions. The hydrodynamic loads are considered as the dynamic contributions in fluid loads and are obtained by subtracting the static contribution as given in Section 2.2.2. Therefore, the fluid forces in Equation (7.6) can be decomposed into hydrodynamic and hydrostatic forces. In the case of the vertical circular cylinder, the linear hydrostatic loads are appropriate for modelling hydrostatic loads due to the simplicity of the geometry. Thus, the equations for hydrodynamic loads can be simplified for the pure surge, heave, and pitch motions as below.

- Horizontal hydrodynamic force in pure surge motion:

$$F^b_{hd,x}(t) = F^b_{m,x}(t) + m\ddot{\mathbf{x}}^b_{b/0}(t) \tag{7.7}$$

  where $\ddot{\mathbf{x}}^b_{b/0}$ is the x-acceleration (surge) vector of O_b from O_0 expressed in the body-fixed reference frame. For the surge motion, there is no hydrostatic contribution to the fluid forces.

- Vertical hydrodynamic force in pure heave motion:

$$F^b_{hd,z}(t) = F^b_{m,z}(t) + m\ddot{\mathbf{z}}^b_{b/0}(t) + mg - \rho g\nabla + \rho g A_w \mathbf{z}^b_{b/0}(t) \tag{7.8}$$

  where $\ddot{\mathbf{z}}^b_{b/0}$ is the z-acceleration (heave) vector of O_b from O_0 expressed in the body-fixed frame, ∇ is a submerged volume under the free surface at rest and A_w is the water plane area of the cylinder.

- Hydrodynamic moment in pure pitch motion at the center of rotation:

$$\begin{aligned} M^b_{hd,y}(t) =& M^b_{m,y}(t) + I_b\ddot{\theta}(t) - mg\left(\mathbf{x}^b_{G/b}\cos\theta(t) + \mathbf{z}^b_{G/b}\sin\theta(t)\right) \\ &+ \rho g\left(\nabla\mathbf{z}^b_{B/b} + \frac{\pi}{64}D_c^4\right)\sin\theta(t) \end{aligned} \tag{7.9}$$

  where $\ddot{\theta}(t)$ is an angular acceleration of pitch motion and $\mathbf{z}^b_{B/b}$ is the vertical center of buoyancy at rest.

The mass m, center of gravity $\mathbf{r}^b_{G/b} = [\mathbf{x}^b_{G/b}, \mathbf{y}^b_{G/b}, \mathbf{z}^b_{G/b}]^T$, and moment of inertia of each configuration were obtained from the forced oscillation tests in the air with quasi-static and dynamic motions. Detailed procedures and results are given in 5.7.3.

7.3.4 Harmonics of hydrodynamic loads and hydrodynamic coefficients

An example of the vertical hydrodynamic forces acting on the cylinder with the heave plate in forced heave oscillation is shown in Figure 7.4. The hydrodynamic loads induced by sinusoidal motions show a periodic oscillatory behavior over time. The signal obtained after the application of a low-pass filter with a cut-off frequency of 4.5 Hz displays a satisfactory periodicity.

The harmonic content from the time history is obtained using Fourier analysis within the selected window of $10T$ integer periods to minimize the energy losses from the hydrodynamic loads. The results clearly demonstrate that higher harmonics are visible up to the 10th harmonic, even with linear imposed motion. The first harmonic is the most dominant, but higher harmonics also contribute significantly to the overall load.

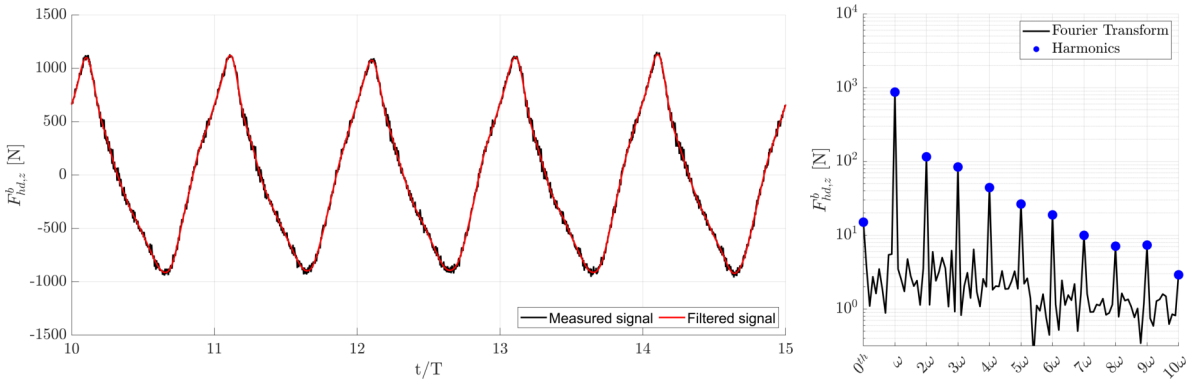

(a) Vertical hydrodynamic force time series at deep draft

(b) Harmonics ($10T$)

Figure 7.4 – Time histories of vertical hydrodynamic forces on the vertical circular cylinder with the solid plate ($D_d/D_c = 2.9$) and its harmonic content. The model oscillates in heave motion with a single amplitude $KC_c = 2.7$ and frequency $\omega^2 D_c/g = 0.4$.

The contribution of the first harmonic depends on the motion amplitude. As shown in Figure 7.5, the first-harmonic contribution accounts for over 90 % of the harmonics up to the fifth ($\sum_{n=0}^{5} F_{hd,z}^{(n\omega)}$) when the KC_c number is less than 0.5. However, as the KC_c number increases, the relative contribution of higher harmonics gradually increases, resulting in a decrease in the relative contribution of the first harmonic; this is important to bear in mind when analyzing the first harmonic only. Additionally, the submerged depth also affects the first harmonic contribution. For the drafts deeper than ($d/D_c > 1.1$), the contribution of the first harmonic shows a similar trend in general. Interestingly, for shallow drafts close to the free surface, the contribution of the first harmonic rapidly decreases to approximately 55% at $KC_c = 2.7$ at the draft $d/D_c = 0.7$, for example.

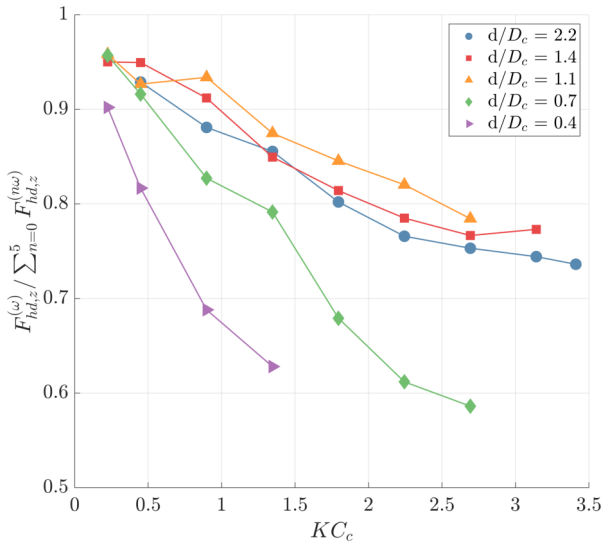

Figure 7.5 – Relative contribution of the first harmonic to the vertical hydrodynamic loads acting on the vertical cylinder with the solid plate ($D_d/D_c = 2.9$) in the heave oscillation with varying the proximity to the free surface.

With periodic behavior hypothesis, the fluid loads can be modelled with Equation (7.10), where f_{hd} is a general expression of the hydrodynamic loads expressed in the body-fixed reference frame. The least-square method is used to obtain the amplitudes of each harmonic.

$$\begin{aligned} f_{hd}(t) \approx & \overline{f}_{hd} + \mathfrak{Re}\{f_{hd}^{(\omega)} e^{-i(\omega t+\varepsilon)}\} + \mathfrak{Re}\{f_{hd}^{(2\omega)} e^{-2i(\omega t+\varepsilon)}\} + \mathfrak{Re}\{f_{hd}^{(3\omega)} e^{-3i(\omega t+\varepsilon)}\} \\ & + \mathfrak{Re}\{f_{hd}^{(4\omega)} e^{-4i(\omega t+\varepsilon)}\} + \mathfrak{Re}\{f_{hd}^{(5\omega)} e^{-5i(\omega t+\varepsilon)}\} \end{aligned} \tag{7.10}$$

where the superscript indicates the corresponding harmonic component. For example, $f_{hd}^{(n\omega)}$ is a complex amplitude of the n^{th} harmonic, where $f_{hd}^{(n\omega)} = f_{hd}^{c,(n\omega)} + i f_{hd}^{s,(n\omega)}$ with $i = \sqrt{-1}$.

In marine hydrodynamics, the first harmonic component of the oscillating body is often considered the only contribution and is further interpreted as in-phase and out-of-phase components with the body motion. The in-phase component leads to the added mass, and the other means damping.

$$A_{ij} = \frac{1}{\xi_j \omega^2} f_{hd,i}^{c,(\omega)}, \qquad B_{ij} = \frac{1}{\xi_j \omega} f_{hd,i}^{s,(\omega)} \tag{7.11}$$

where A_{ij} and B_{ij} are the added mass (kg or kgm^2) and the total (or equivalent) damping (kg/s or kgm^2/s) from the first harmonic. This study presents only the diagonal components of the added mass and damping where $i = j$.

7.4 Results I: forced heave oscillations

This section shows the vertical hydrodynamic force time series and its harmonic content. Firstly, the frequency effect is examined, and then the influence of KC_c is presented with various drafts of a solid plate with $D_d/D_c = 2.9$ (Model C). The harmonic content for the porous plate with the same diameter ratio (Model D) is compared to that for this solid plate. The hydrodynamic coefficients, i.e., added mass and damping, are analyzed as the first harmonic in the hydrodynamic forces. Finally, the behavior of these coefficients in terms of frequency, KC_c, plate diameter, and submerged drafts are provided.

7.4.1 Time series and harmonic content of vertical hydrodynamic forces

A single configuration with a heave plate ($D_d/D_c = 2.9$) is examined to address the effects of motion amplitude and frequency on the hydrodynamic forces. The deep ($d/D_c = 2.2$) and shallow ($d/D_c = 0.7$) drafts are selected to highlight the influence of the free surface's proximity. The time histories are displayed in 5 cycles, and the harmonic content is given up to fifth harmonics obtained from 10 cycles. The hydrodynamic forces are nondimensionalized as $F_{hd}/\rho g D_c^3$. The results cover the magnitude of the forces as well as in- and out-of-phase components, which are physically interpreted as the added mass and damping components in the following.

a) Influence of the motion frequency

In Figure 7.6, time histories of vertical hydrodynamic forces are presented for several motion frequencies with a single single motion amplitude ($KC_c = 0.9$) at the deep and shallow drafts. Generally, the hydrodynamic forces are shifted compared to the imposed heave motion given as a black dashed line. The measured force amplitudes are increased with increasing motion frequency, which can be observed in both time series and harmonics. The first harmonic is dominant in the harmonic content, and the amplitudes of the zeroth and higher harmonics are negligibly small compared to the first harmonic. Furthermore, the amplitude of the first harmonic linearly increases with the motion frequency at the deep draft, but the linearity is broken at the shallow draft.

The evolution of the first harmonic with the motion frequency is investigated in Figure 7.7, where the magnitude, in-phase and out-of-phase components are presented at five different submerged depths for the solid plate ($D_d/D_c = 2.9$). Additionally, it compares the

first-harmonic components of hydrodynamic loads on the porous plate with the same diameter ratio.

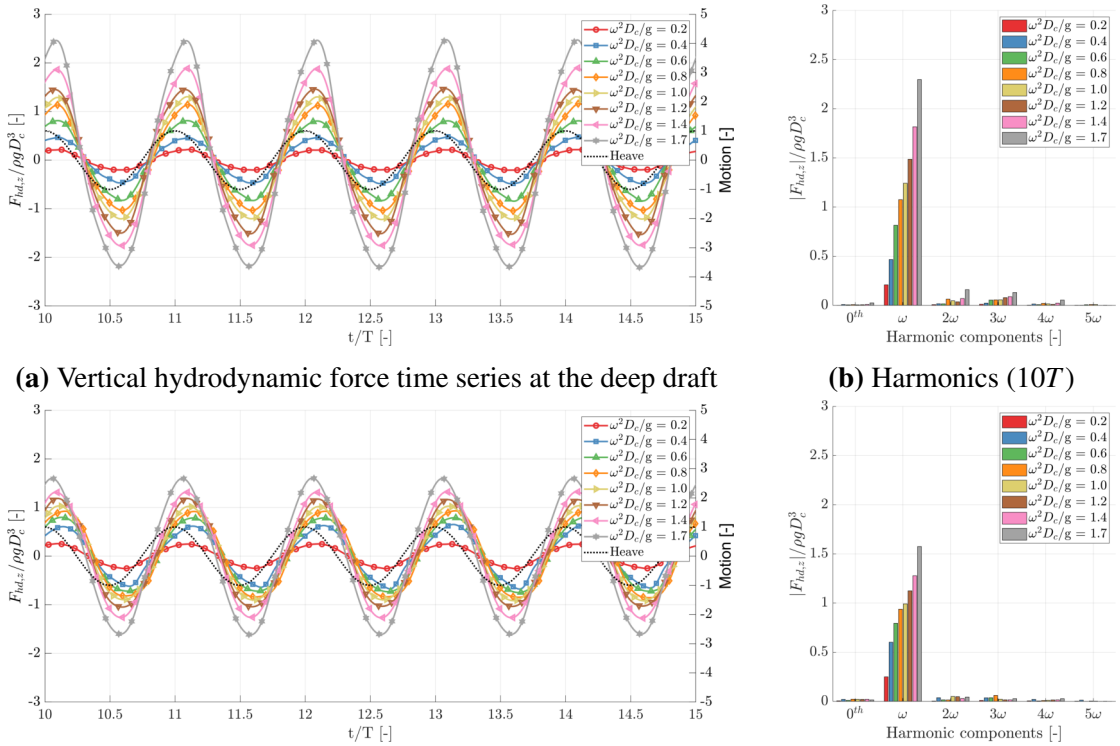

(a) Vertical hydrodynamic force time series at the deep draft

(b) Harmonics ($10T$)

(c) Vertical hydrodynamic force time series at the shallow draft

(d) Harmonics ($10T$)

Figure 7.6 – Time series and harmonic content of vertical hydrodynamic forces on the solid plate (D_d/D_c = 2.9) at the deep ($d/D_c = 2.2$) and shallow ($d/D_c = 0.7$) drafts. Heave motions are imposed with a single amplitude ($KC_c = 0.9$) and various frequencies ($\omega^2 D_c/g = 0.2 \sim 1.7$).

The magnitude of the first harmonic increases with increasing frequency at the deep draft $d/D_c = 2.2$. The in- and out-of-phase components follow the tendency of the magnitude, although the increasing rates are different. By decreasing the submerged depth, the magnitude of the first harmonics stops to increase linearly. Interestingly, $\omega^2 D_c/g = 0.6$ looks like a critical frequency, and the general trend of the magnitude of the first harmonic is distinct before and after this value. At lower frequencies, the magnitude increases with decreasing draft, while at higher frequencies, it decreases.

The in-phase component of forces shows similarity at low frequencies up to the third draft, but differences become larger as the frequency increases. As the submerged depth becomes shallower, the increase rate with frequency decreases, but it can still be seen that the component increases with frequency. In contrast to the magnitude of the out-of-phase

component increasing linearly at deep drafts, the slope begins to flatten at low drafts. At the shallow draft, $d/D_c = 0.25$, there is no change in frequency above 0.8, and it tends to decrease at the lowest draft, $d/D_c = 0.125$. The general trend of the out-of-phase component is distinct at the frequency $\omega^2 D_c/g = 1.41$. The value increases due to the proximity of the free surface below this frequency but decreases at the highest motion frequency.

The perforated plate shows a similar tendency compared to the solid plate. At the low motion frequency ($\omega^2 D_c/g \leq 0.35$), the first harmonics of solid and porous plates have similar magnitudes. However, as the frequency increases, the difference between the two becomes more apparent. Generally, the in-phase component of the porous plate is lower than that of the solid plate at all submerged depths. Meanwhile, the out-of-phase component is larger at deeper drafts and smaller at shallower drafts.

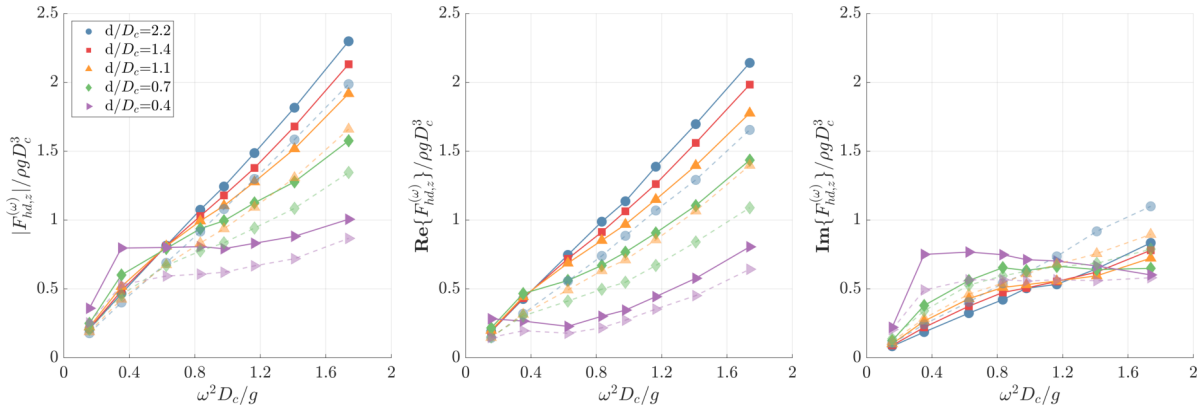

(a) Magnitude **(b)** In phase **(c)** Out of phase

Figure 7.7 – The amplitude of the first harmonic component of the vertical hydrodynamic forces on the solid plate (D_d/D_c = 2.9) given in solid lines (——) at various drafts. Heave motions are imposed with a single amplitude ($KC_c = 0.9$) and various frequencies ($\omega^2 D_c/g = 0.2 \sim 1.7$). The first harmonic loads on the perforated plate ($D_d/D_c = 2.9$) given in dashed lines (- - -) are compared, except for the middle draft ($d/D_c = 1.4$, red color).

b) Influence of motion amplitudes

Figure 7.8 presents the effects of motion amplitudes given in KC_c on the force time series. At the deep draft, the amplitude of the forces increases with the motion amplitude, which is similar to what is observed when varying the motion frequency. Notably, the positive and negative peaks are sharpened with increasing the motion amplitude. The linear increase of all harmonics can be clearly seen in the zeroth, first, and higher harmonics according to the KC_c. A similar trend is observed at the shallow draft up to KC_c = 2.2. It is worth noting that the

positive peaks of the time series are flattened at the $KC_c = 2.7$ compared to that of the deep draft.

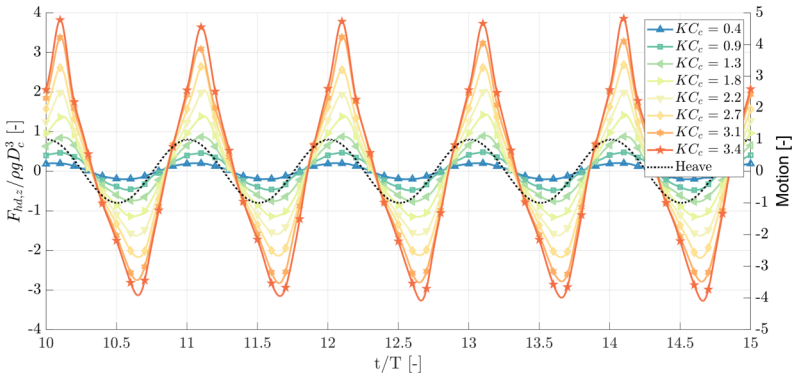

(a) Vertical hydrodynamic force time series at the deep draft

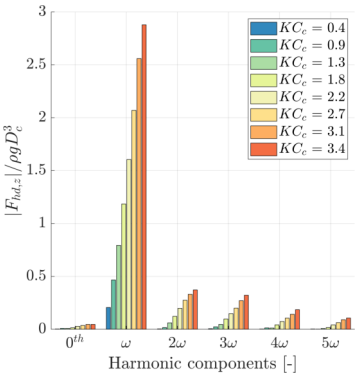

(b) Harmonics ($10T$)

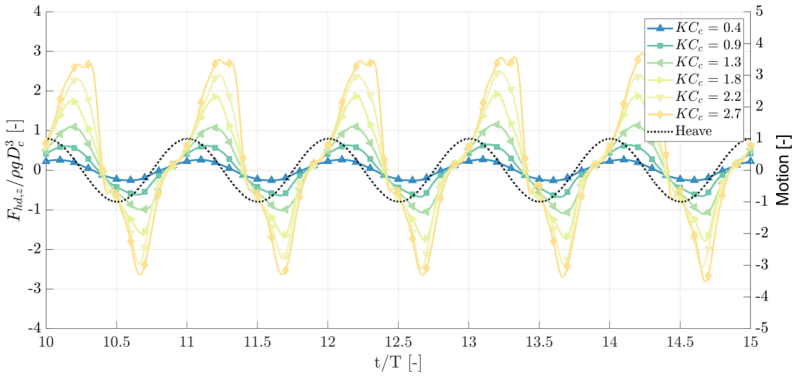

(c) Vertical hydrodynamic force time series at the shallow draft

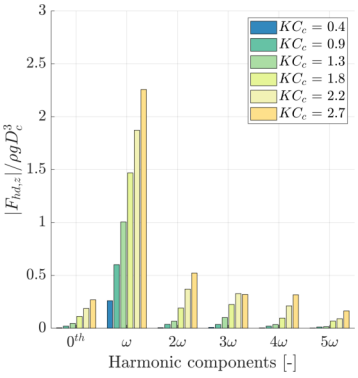

(d) Harmonics ($10T$)

Figure 7.8 – Time series and harmonic content of vertical hydrodynamic forces on the solid plate (D_d/D_c = 2.9) at the deep ($d/D_c = 2.2$) and shallow ($d/D_c = 0.7$) drafts. Heave motions are imposed with a single frequency ($\omega^2 D_c/g = 0.4$) and various amplitudes ($KC_c = 0.4 \sim 3.4$).

Figure 7.9 presents harmonic content up to the third harmonic in magnitude, in- and out-of-phase components on the solid and perforated plates. The magnitude of the first harmonics increases with an increase of the KC_c number and slightly increases with a decrease in the submerged depth. The in-phase components of the first harmonic show a similar trend up to the draft ratio d/D_c = 1.1. However, differences appear when the draft ratio falls below 0.7 and $KC_c \leq 1.8$, corresponding to ξ_3/d = 0.4. Similarly, the difference is clearly visible at the very shallow draft ($d/D_c = 0.35$) after KC_c number 0.9, which corresponds also to ξ_3/d = 0.4. The value starts to decrease after this KC_c number.

The out-of-phase components of the first harmonic force show a distinct effect of submerged depth with respect to the KC_c. The growth rate increases with the vicinity of the free

surface. Interestingly, there is no difference at very low KC_c numbers, but for higher KC_c large differences appear depending on the submerged depth. Furthermore, the magnitude, in-phase and out-of-phase components generally increase monotonically for the higher harmonics at the deep draft. It can be seen that the in-phase and out-of-phase components of the second and third harmonics decrease with a decrease in the submergence. In general, the higher harmonic values are negative when the draft ratio is $d/D_c \leq 0.7$, except in the in-phase component of the third harmonic, where the values are mostly negative regardless of the depth.

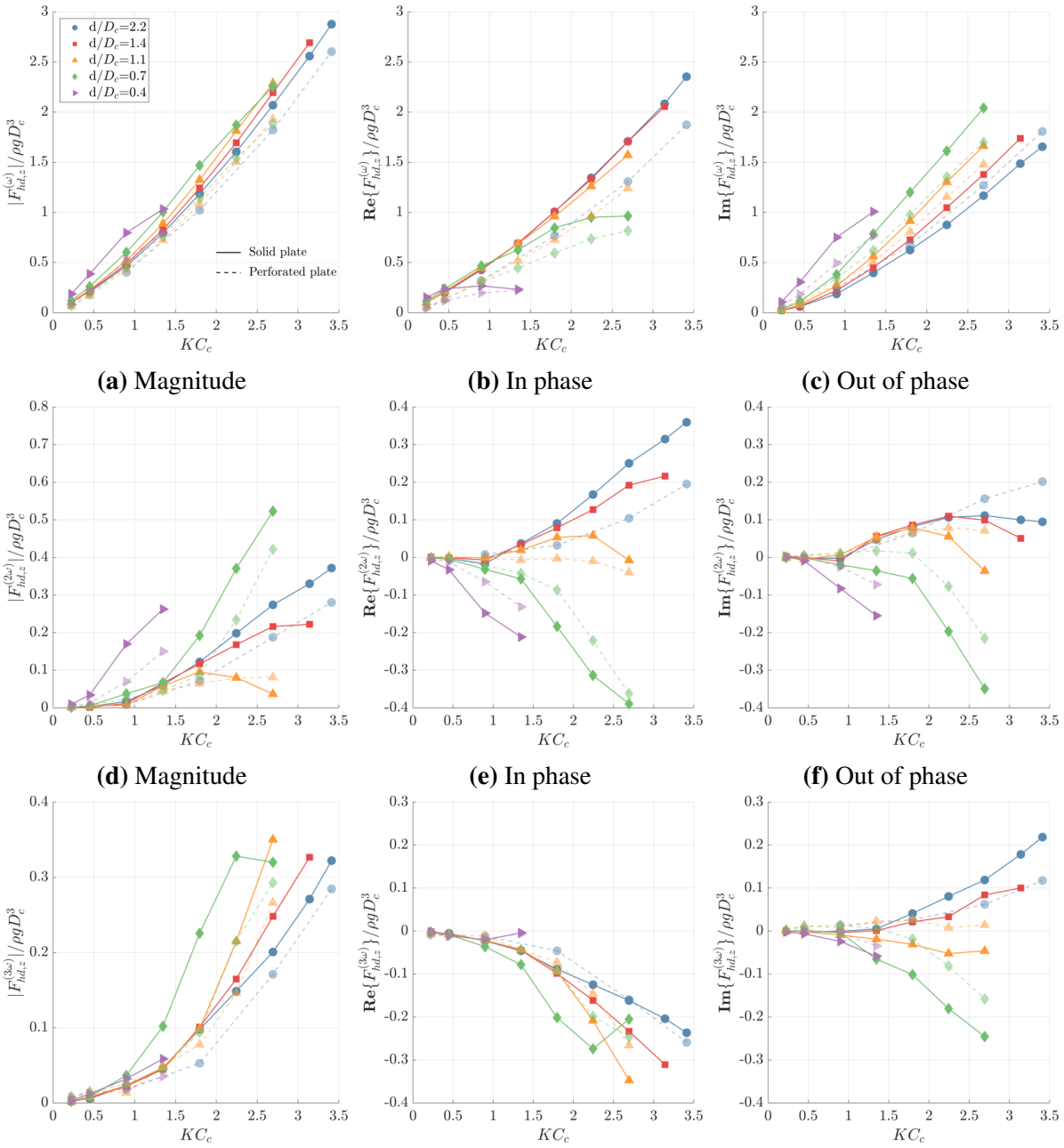

(a) Magnitude **(b)** In phase **(c)** Out of phase

(d) Magnitude **(e)** In phase **(f)** Out of phase

(g) Magnitude **(h)** In phase **(i)** Out of phase

Figure 7.9 – The amplitude of the first three harmonic components of the vertical hydrodynamic forces on the solid plate ($D_d/D_c = 2.9$) given in solid lines (——) at various drafts. Heave motions are imposed with a single frequency ($\omega^2 D_c/g = 0.4$) and various amplitudes ($KC_c = 0.2 \sim 3.4$). The harmonic loads on the perforated plate ($D_d/D_c = 2.9$, Model D) given in dashed lines (- - -) are compared except for the middle draft ($d/D_c = 1.4$, red color).

7.4.2 Hydrodynamic coefficients for the heave motion

The first harmonics examined in the previous section are now used to compute the added mass and damping coefficients, which are in- and out-of-phase components as given in Equation (7.11). The results of a linear potential flow theory model (Han et al. (2024)) are compared to the experimental measurements. An investigation is carried out on the hydrodynamic coefficients of the heave plates ($D_d/D_c = 2.9$) with and without porosity. The motion frequency and amplitude effects are studied by varying submerged depth. Lastly, the effect of the diameter ratio is presented.

a) Influence of the motion frequency for the solid and perforated plates

Figure 7.10 presents the non-dimensional added mass and damping on the heave plate case ($D_d/D_c = 2.9$) for various motion frequencies ranging in $0.16 \leq \omega^2 D_c/g \leq 1.74$. Motion frequency does not affect the added mass and damping at the deep draft, as reported in Lopez-Pavon and Souto-Iglesias (2015). When the draft decreases, the added mass drops significantly at low frequencies $\omega^2 D_c/g < 0.6$ but gradually increases with increasing motion frequency. The decrement of the added mass was also reported in McIver and Evans (1984); Greenhow and Ahn (1988) with a submerged body. In particular, according to McIver and Evans (1984) based on potential flow analysis, the added mass is related to both the kinetic and potential energies of the fluid motion. The kinetic energy decreases with the reduction of submergence, while the potential energy is only affected by the deformation of the free surface. This results in the reduction of the added mass due to the proximity of the free surface.

At the deep draft ($d/D_c = 2.2$), the added mass from the experiment is higher than the results of the potential flow theory (shaded solid lines), which is close to a theoretical value ($A_{33}/\rho D_c^3 = 7.1$ for the Model C) computed using a formulation proposed by Tao et al. (2007). In the shallower draft, the potential theory is able to predict that the added mass is strongly dependent on the frequency but underpredicts the value compared to the measurements.

Meanwhile, the non-dimensional damping increases as the draft decreases, particularly at a frequency below 1.4. Notably, at the highest frequency $\omega^2 D_c/g = 1.74$, the damping decreases when the draft decreases. Furthermore, the motion frequency strongly affects the damping with the proximity of the free surface, and the maximum damping appears around $\omega^2 D_c/g \simeq 0.35$.

During the experiments, it was observed that the heave motion of the plate at the shallow drafts generated significant radiated waves during the tests, while there were almost no radiated

waves at the deep draft. Potential flow theory is consistent with the findings, demonstrating that there is no wave damping at the deep draft, but significant wave damping when the submerged depth decreases. This suggests that in the case of deep drafts, the damping is dominated by vortices. However, in the case of shallow drafts, the damping is composed of vortices and radiated waves.

The added mass for the perforated plate is less than that for the solid plate with the tested motion frequency range and shows a similar trend according to the frequency for the solid plate. The perforated plate produces more damping than the solid plate at the draft ratios of 2.2 and 1.1. For ratios below 0.7, the damping of the porous plate is lower than that of the solid plate. Interestingly, we observed that the amplitude of the radiated waves by the perforated plate is lower than that of the solid plate at the shallow draft.

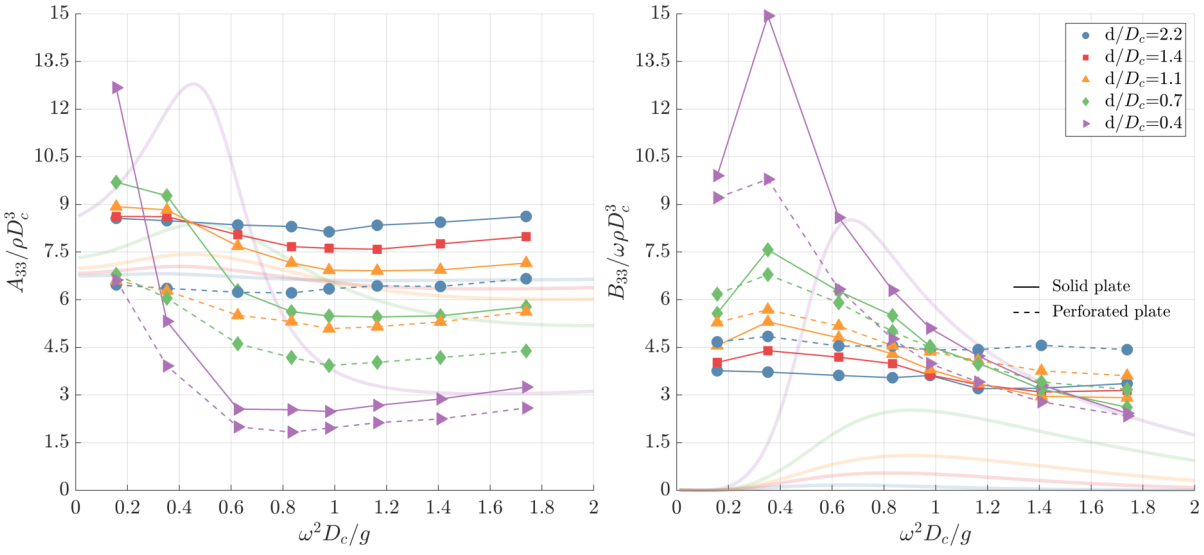

(a) Added mass, A_{33} **(b)** Damping, B_{33}

Figure 7.10 – Non-dimensional heave added mass and damping coefficients on the solid plate (——) and perforated plate (- - -) with a single amplitude ($KC_c = 0.9$) and various frequencies ($\omega^2 D_c/g = 0.2 \sim 1.7$) at various drafts. Note: the perforated plate at the middle draft, $d/D_c = 1.4$ (red), is not tested. Shaded lines without markers are the results of the potential flow theory.

b) Influence of the motion amplitude, KC_c, for the solid and perforated plates

Figure 7.11 presents non-dimensional heave added mass and damping on the heave plate (D_d/D_c = 2.9) with various KC_c numbers at a single motion frequency $\omega^2 D_c/g = 0.4$. At the deep draft (d/D_c = 2.2), the added mass and damping on the solid plate are linearly increased with increasing the KC_c number. This aligns with the findings of Thiagarajan and Troesch (1998). However, it is interesting to note that the growth rate of the added mass decreases as the draft becomes shallower. On the other hand, the damping increases as the draft decreases, and the slope of damping increases with respect to the KC_c number. At the very shallow draft $d/D_c = 0.4$, the maximum peak occurs at $KC_c = 0.9$, followed by a decrease in the damping. Garrido-Mendoza et al. (2014) also found similar results in their CFD simulations.

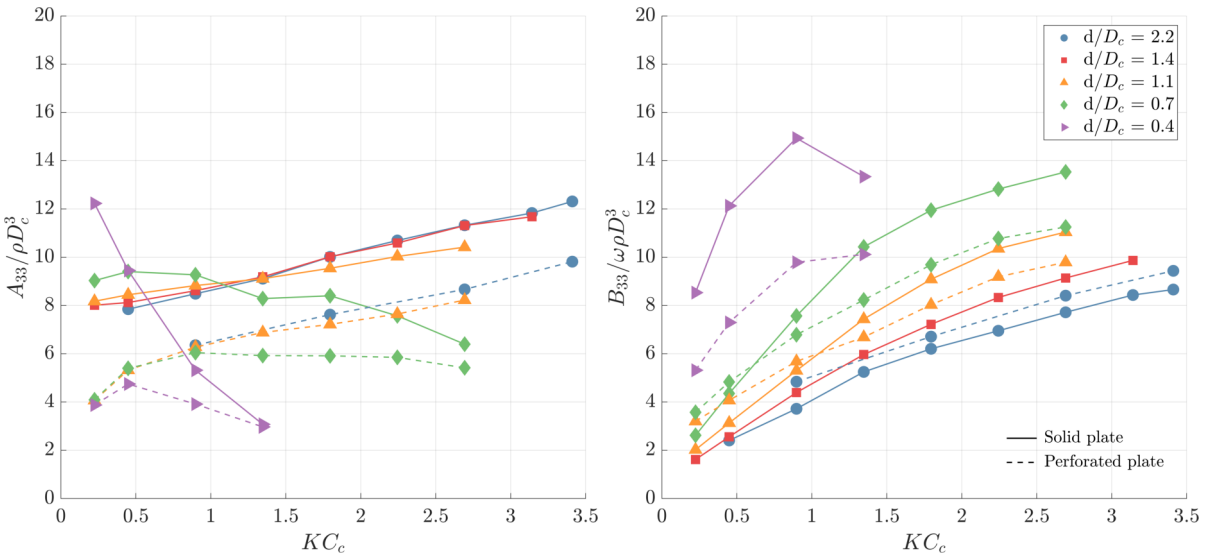

(a) Added mass, A_{33} **(b)** Damping, B_{33}

Figure 7.11 – Non-dimensional heave added mass and damping coefficients on the solid plate (——) and perforated plate (- - -) with a single frequency ($\omega^2 D_c/g = 0.4$) and various amplitudes ($KC_c = 0.2 \sim 3.4$) at various drafts. Note: the perforated plate at the draft, $d/D_c = 1.4$ (red), is not tested.

In general, the porous plate produces less added mass than the solid plate. The slope of the porous plate is similar to that of the solid plate at the deep draft but differs when decreasing the draft ratio. However, the rate of change is less steep than that of the solid plate. The damping with the perforated plate is larger than with the solid plate at the deep draft in whole KC_c numbers. On the other hand, at the draft ratios of 1.1 and 0.7, the damping of the perforated

plate is larger at low KC_c numbers but lower at high KC_c numbers. This result is consistent with the findings of Tian et al. (2017). Notably, at the very shallow draft, the damping of the solid plate is larger than that of the perforated plate, even at low KC_c.

c) Influence of motion frequency and amplitude for the solid plate

Further investigation is made on a solid plate with $D_d/D_c = 2.9$ by considering three additional motion frequencies $\omega^2 D_c/g$ = 0.09, 0.16, 0.23, to complete the study otherwise limited to the single motion frequency ($\omega^2 D_c/g$ = 0.4). The additional frequencies correspond to the motion periods T = 4.0, 3.0, 2.5 s at the model scale.

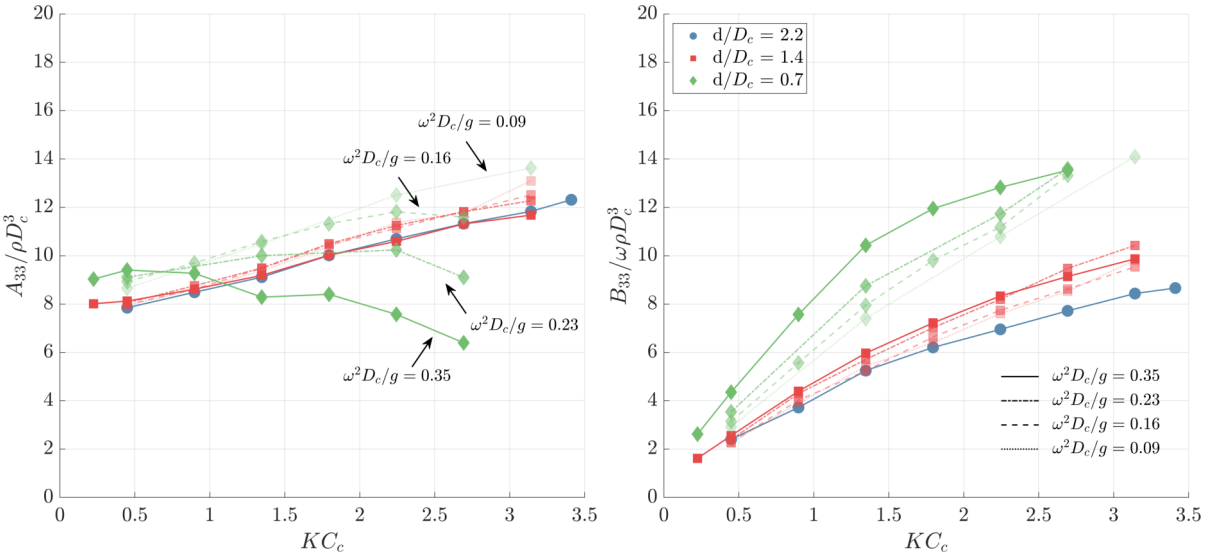

(a) Added mass, A_{33} **(b)** Damping, B_{33}

Figure 7.12 – Non-dimensional heave added mass and damping coefficients on the solid plate ($D_d/D_c = 2.9$) with the motion amplitudes ($KC_c = 0.2 \sim 3.4$) and frequencies ($\omega^2 D_c/g = 0.1 \sim 0.4$) at the deep (●), middle (■), and shallow (⧫) drafts.

Figure 7.12 shows the non-dimensional added mass and damping with varying motion amplitudes and frequencies. The additional results are illustrated with distinguished lines and transparency. The added mass and damping at the middle draft linearly increase with an increase of the KC_c number and present an identical slope when changing the motion frequencies. At the shallow draft (d/D_c = 0.7), the slope increases from a negative value to a positive one with decreasing motion frequency. Eventually, with the motion frequency $\omega^2 D_c/g$ = 0.09, the slope of the added mass at the shallow draft is almost identical to that of the middle and deep drafts.

This effect can be seen in the damping by changing the slope according to the KC_c number. It means that when the motion frequency is very low ($\omega^2 D_c/g < 0.1$), the slope of the added mass at the shallow draft is similar to the one at the deeper draft. These effects are more pronounced at the shallow draft, while there is no difference at the middle draft due to the motion frequency.

d) Influence of heave plate diameter

This section presents the added mass and damping with various heave plate ratios (D_d/D_c) ranging from 1.0 to 3.5. Two submerged depths are examined: deep ($d/D_c = 2.2$) and shallow ($d/D_c = 0.7$) drafts. Figure 7.13 presents the non-dimensional hydrodynamic coefficients with various motion frequencies.

The hydrodynamic coefficients are not influenced by the motion frequency at the deep draft for all plate configurations. For the solitary cylinder and the cylinder with the small heave plate ($D_d/D_C = 1.5$), the added mass and damping are almost identical at both deep and shallow drafts. However, for the largest heave plate ($D_d/D_c = 3.5$), the behavior of the coefficients is affected by the motion frequency in a similar way to the plate $D_d/D_c = 2.9$. At the peak frequency $\omega^2 D_c/g = 0.35$, the damping of the plate with $D_d/D_c = 3.5$ is more strongly influenced by the motion frequency than the plate with $D_d/D_c = 2.9$.

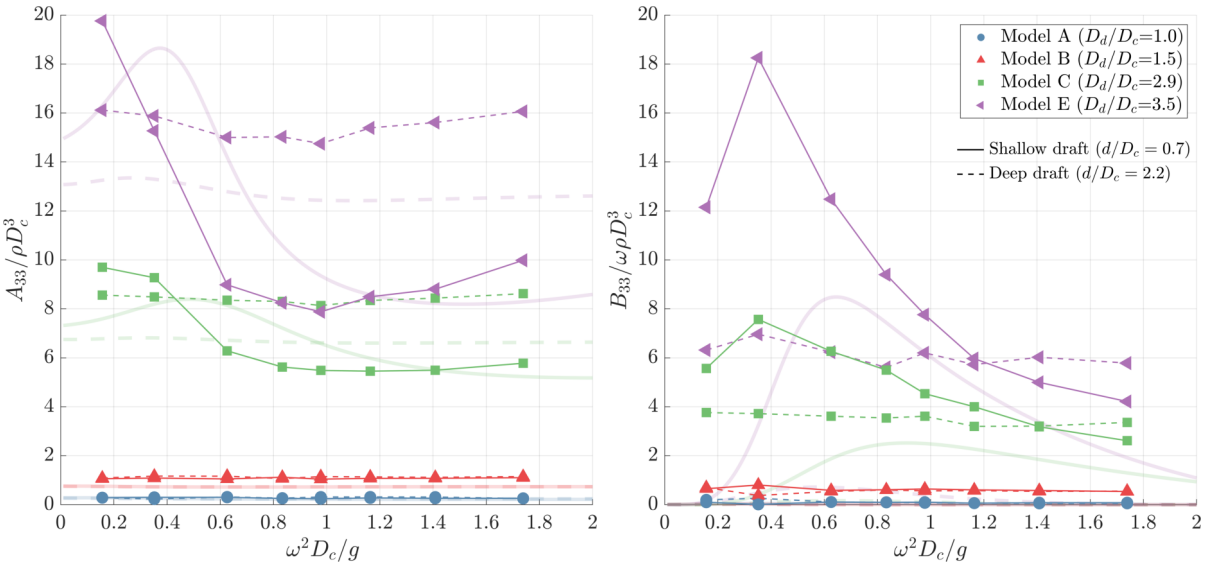

(a) Added mass, A_{33} **(b)** Damping, B_{33}

Figure 7.13 – Non-dimensional heave added mass and damping coefficients on the various solid plates ($D_d/D_c = 1.0, 1.5, 2.9, 3.5$) at the deep (- - -) and shallow (——) drafts with a single amplitude ($KC_c = 0.9$) and various frequencies. Shaded lines without markers are the results of the potential flow theory.

The potential flow theory predicts that the influence of frequency is negligible at the deep draft and significant at the shallow draft, similar to the experimental findings. The wave damping and its dependency on the motion frequency are very significant at the shallow draft with the large heave plates (Models C and E).

Similarly, the influence of the submerged depth on the added mass and damping with respect to the KC_c for the solitary cylinder and the small heave plate ($D_d/D_c = 1.5$) is negligible, as shown in Figure 7.13. However, for larger heave plates, the added mass increases with an increase in KC_c at the deep draft, but decreases at the shallow draft by showing a negative slope according to the KC_c. On the other hand, damping increases at both deep and shallow drafts, but the slope is more significant at the shallow draft than at the deep draft. It is worth noting that larger plates provide more added mass and damping than smaller plates at both deep and shallow drafts with a given frequency and KC_c.

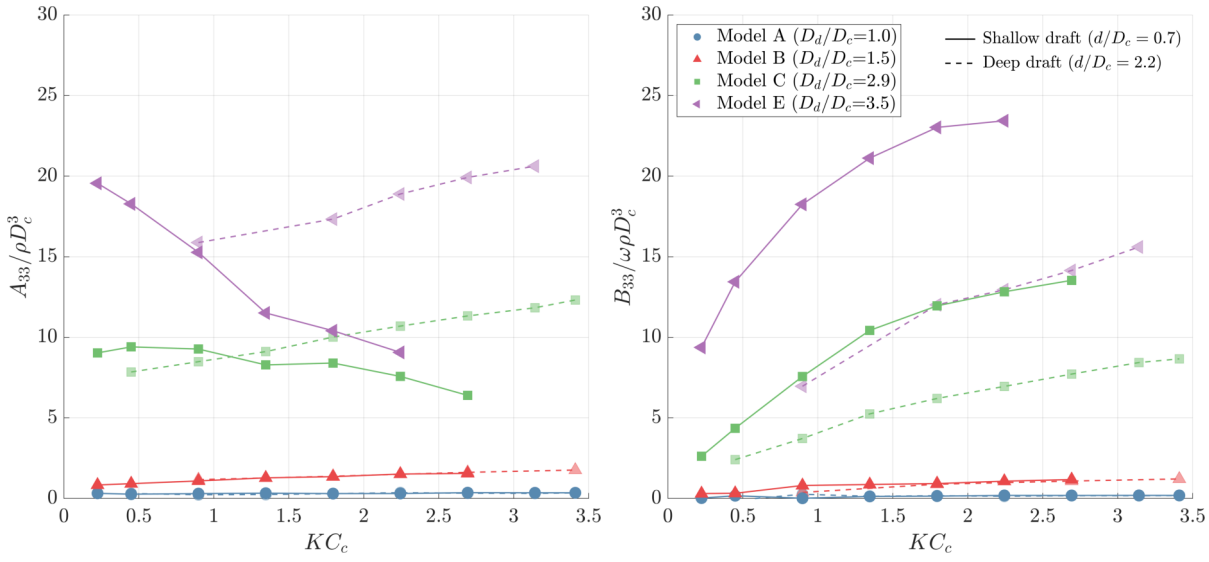

(a) Added mass **(b)** Damping

Figure 7.14 – Non-dimensional heave added mass and damping coefficients on the various solid plates ($D_d/D_c = 1.0, 1.5, 2.9, 3.5$) at the deep (- - -) and shallow (——) drafts with a single frequency ($\omega^2 D_c/g = 0.4$) and various amplitudes ($KC_c = 0.2 \sim 3.4$).

7.5 Results II: forced surge oscillations

This section examines the hydrodynamic forces in forced surge oscillation.

7.5.1 Time series and harmonic content of horizontal hydrodynamic forces

The non-dimensional horizontal forces time histories ($F_{hd,x}/\rho g D_c^3$) are presented for the circular cylinder with the heave plate ($D_d/D_c = 2.9$, Model C) at the deep ($d/D_c = 2.2$) and shallow ($d/D_c = 0.7$) drafts. The first harmonics observed at the three studied drafts are also presented. The harmonics for the solid plate are compared to those for the solitary cylinder and the perforated plate.

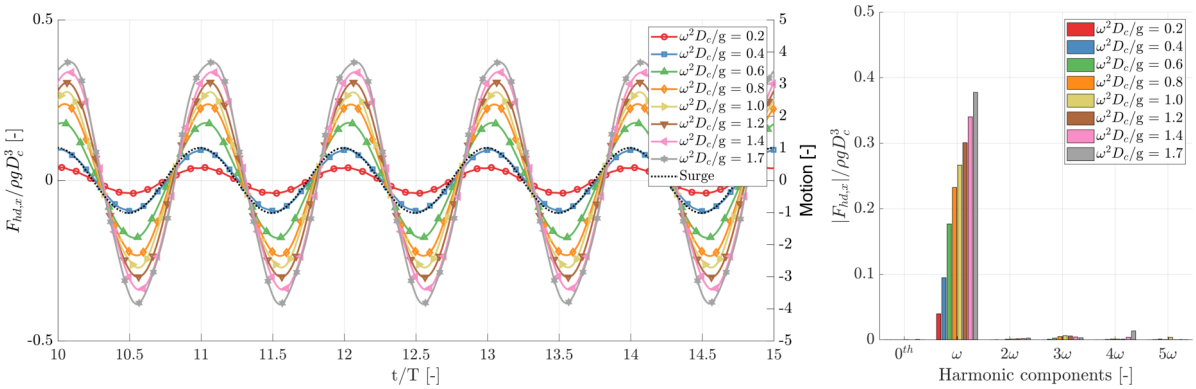

(a) Horizontal hydrodynamic force time series at the deep draft

(b) Harmonics ($10T$)

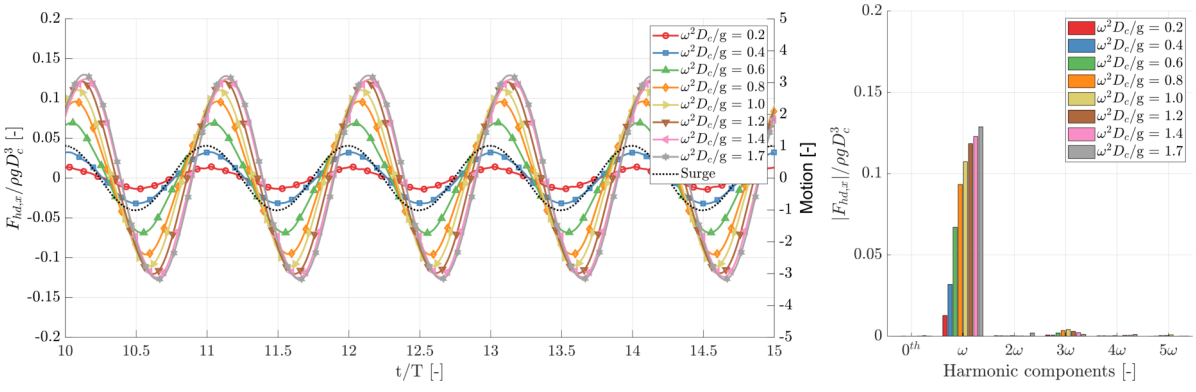

(c) Horizontal hydrodynamic force time series at the shallow draft

(d) Harmonics ($10T$)

Figure 7.15 – Time series and harmonic content of horizontal hydrodynamic forces on the solid plate ($D_d/D_c = 2.9$) at the deep ($d/D_c = 2.2$) and shallow ($d/D_c = 0.7$) drafts. Surge motions are imposed with a single amplitude ($KC_c = 0.9$) and various frequencies ($\omega^2 D_c/g = 0.2 \sim 1.7$).

a) Influence of the motion frequency

The following observations are made from Figure 7.15, which shows horizontal time histories in changing the motion frequency at deep and shallow drafts. At low frequency ($\omega^2 D_c/g \leq 0.4$), the force behavior follows the imposed surge motion depicted by a black dashed line. However, as the frequency increases, the forces tend to shift, and their amplitude increases. At the shallow draft, the maximum and minimum peaks of the time series are more significantly shifted. The dominant harmonic content is the first harmonic, while the amplitudes of the zeroth and higher harmonics are very small compared to the first harmonic.

The harmonic content at the deep, middle, and shallow drafts is summarized in Figure 7.16. At deep and middle drafts, the magnitude of the first harmonic increases with frequency. Meanwhile, the tendency is flattened at high frequency at the shallow draft, which is also pronounced in the in-phase components. Both the magnitude and in-phase components decrease significantly by decreasing the submerged depth, but not for the out-of-phase components. The out-of-phase component gradually increases as foreseen in Figure 7.15.

Similar trends are observed with the solitary cylinder (Model A) and the cylinder with the perforated plate (Model D). The magnitude of the first harmonic of the perforated plate is slightly lower than that of the solid plate. Interestingly, the out-of-phase components of each configuration are close to each other at the deep draft, but differences are noticeable at the shallow draft.

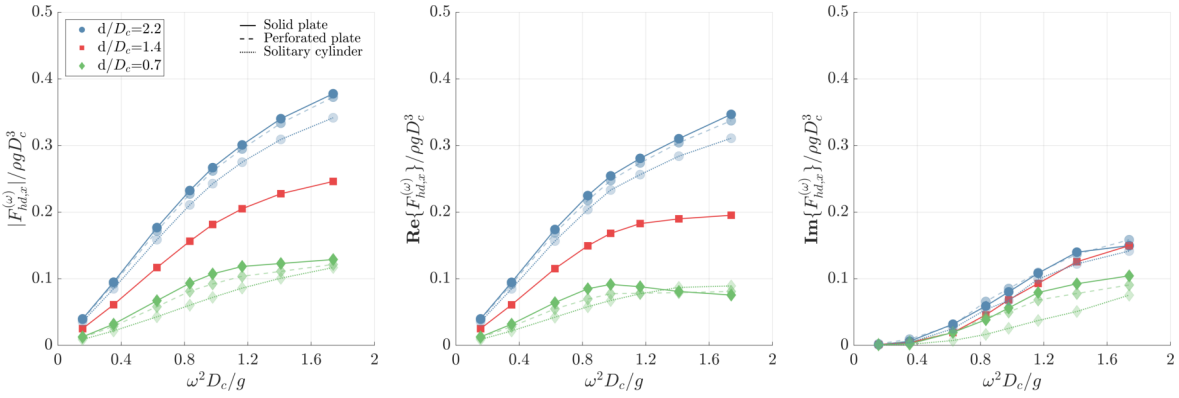

(a) Magnitude **(b)** In phase **(c)** Out of phase

Figure 7.16 – The amplitude of the first harmonic component of the horizontal hydrodynamic forces on the solid plate ($D_d/D_c = 2.9$) at the deep (●), middle (■), and shallow (♦) drafts. Surge motions are imposed with a single amplitude ($KC_c = 0.9$) and various frequencies ($\omega^2 D_c/g = 0.2 \sim 1.7$). The first harmonic loads on the perforated plate ($D_d/D_c = 2.9$) and solitary cylinder ($D_d/D_c = 1.0$) are compared, except for the middle draft ($d/D_c = 1.4$, red color).

b) Influence of the motion amplitude

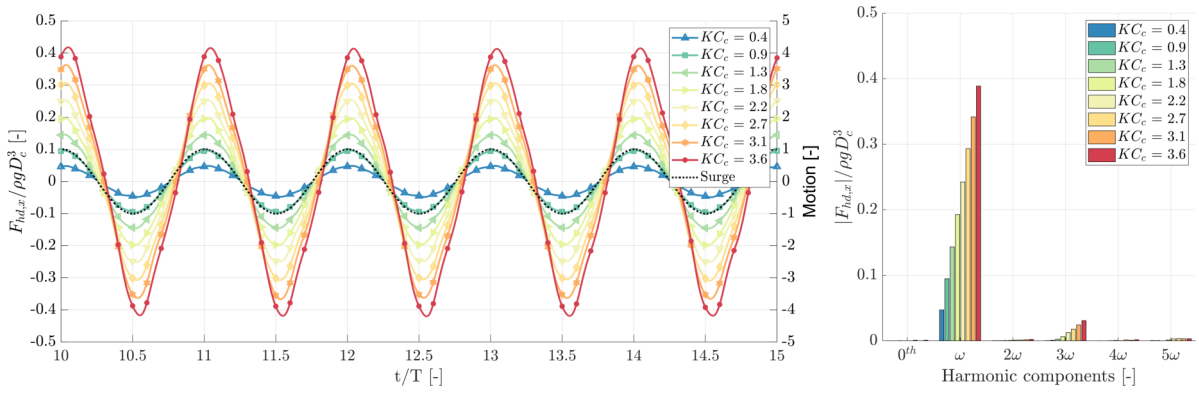

(a) Horizontal hydrodynamic force time series at the deep draft

(b) Harmonics ($10T$)

(c) Horizontal hydrodynamic force time series at the shallow draft

(d) Harmonics ($10T$)

Figure 7.17 – Time series and harmonic content of horizontal hydrodynamic forces on the solid plate ($D_d/D_c = 2.9$) at the deep ($d/D_c = 2.2$) and shallow ($d/D_c = 0.7$) drafts. Surge motions are imposed with a single frequency ($\omega^2 D_c/g = 0.4$) and various amplitudes ($KC_c = 0.4 \sim 3.6$)

The effects of the motion amplitude on the horizontal forces are shown in Figure 7.17. Depending on the motion amplitude, the increase in the forces is more pronounced than the phase shift. It is observed that the first harmonic dominates the horizontal hydrodynamic forces. Interestingly, the third harmonic becomes prominent as the KC_c number increases, while the other components remain insignificant.

In Figure 7.18, the first and third harmonics are provided. By increasing the KC_c, the magnitudes of the first and third harmonics show a monotonic increase. It is also noticeable that the first harmonic of the forces is due to in-phase components, and they are clearly distinguished by the draft. In contrast, the out-of-phase components are similar regardless of the draft. At low KC_c numbers, the magnitude of the first harmonic component is almost

identical for the single cylinder and the cylinder with the heave plate. However, as KC_c increases, the differences due to the heave plate presence become more important.

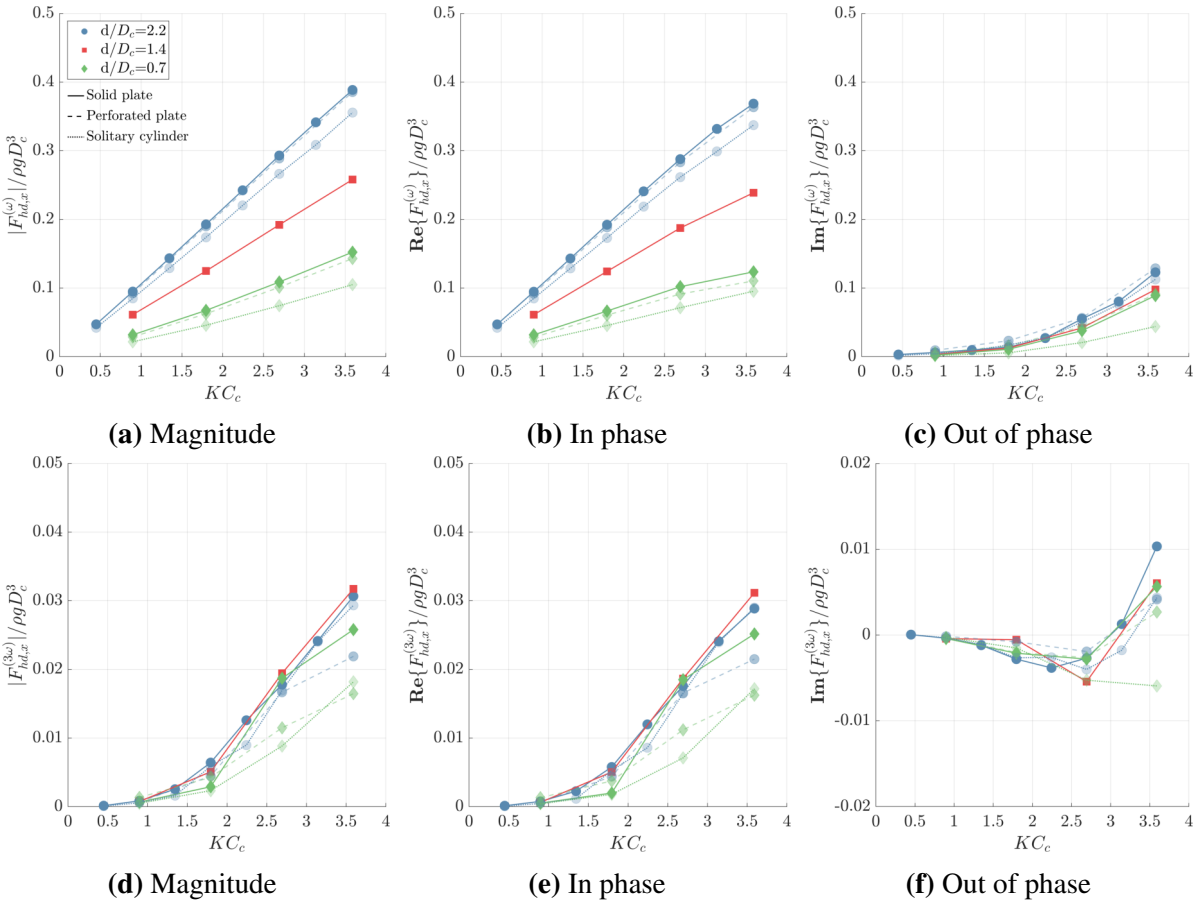

(a) Magnitude **(b)** In phase **(c)** Out of phase

(d) Magnitude **(e)** In phase **(f)** Out of phase

Figure 7.18 – The amplitude of the first (top) and third (bottom) harmonic components of horizontal hydrodynamic forces on the solid plate (D_d/D_c = 2.9) at the deep (●), middle (■), and shallow (♦) drafts. Surge motions are imposed with a single frequency ($\omega^2 D_c/g = 0.4$) and various amplitudes ($KC_c = 0.5 \sim 3.6$). The harmonic loads on the perforated plate ($D_d/D_c =$ 2.9) and solitary cylinder ($D_d/D_c = 1.0$) are compared, except for the middle draft ($d/D_c = 1.4$, red color).

7.5.2 Hydrodynamic coefficients for the surge motions

The surge added mass and damping of the first harmonics are non-dimensionalized as $A_{11}/\rho D_c^3$ and $B_{11}/\omega\rho D_c^3$, respectively. Figure 7.19 shows the effects of motion frequency of the heave plates on the hydrodynamic coefficients for all configurations at two different drafts: deep and shallow drafts. The surge added mass is dependent on the motion frequency. In the deep draft, the added mass presents similar behavior for all configurations, with larger plates showing slightly higher added mass. Conversely, in the case of the shallow draft, the opposite is shown at high frequency.

The dampings from the different heave plates at the deep draft are similar to each other. The plate effects are more pronounced at the shallow draft, showing that, in general, the larger plates produce more damping than the smaller ones. It is worth noting that the damping for the porous plate is slightly lower than that for the solid plate. In general, the potential flow theory predicts well the hydrodynamic coefficients in surge motion at both the deep and shallow drafts. This means that in the surge motion, the total damping is dominated by the wave damping.

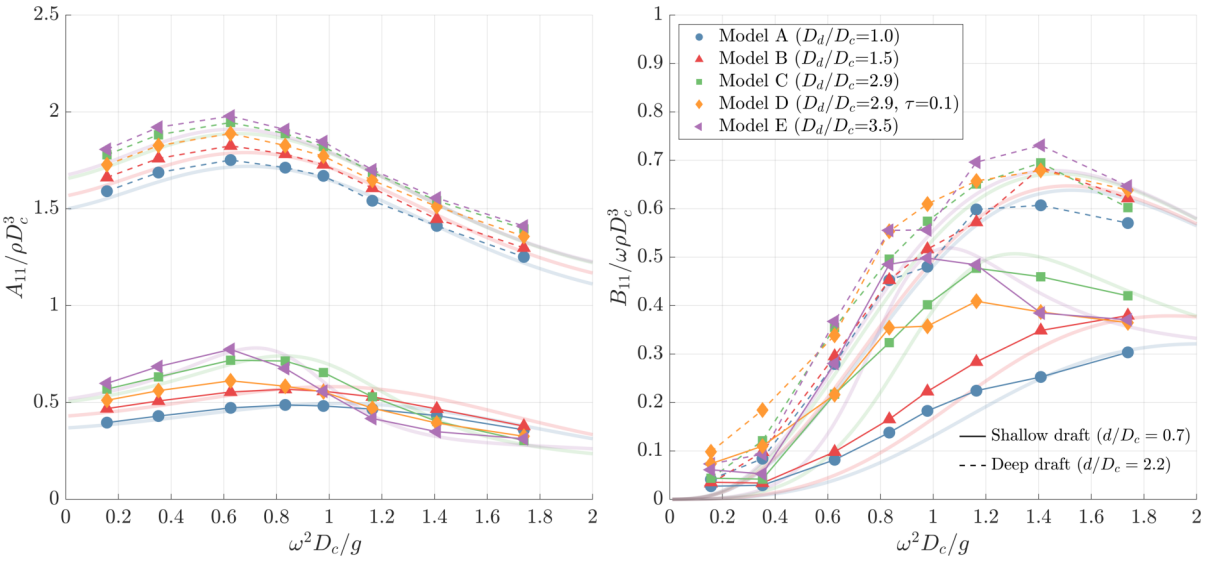

(a) Added mass, A_{11} **(b)** Damping, B_{11}

Figure 7.19 – Non-dimensional surge added mass and damping coefficients for the different heave plates with a single amplitude ($KC_c = 0.9$) and various frequencies ($\omega^2 D_c/g = 0.2 \sim 1.7$) at the deep (- - -) and shallow (——) drafts. Shaded lines without markers are the results of the potential flow theory considered only for the solid plates.

The effects of KC_c on the coefficients at the given motion frequency ($\omega^2 D_c/g = 0.35$) are shown in Figure 7.20. For both deep and shallow drafts, surge added mass is clearly differentiated by plate diameter, but the difference with KC_c is small. However, surge damping is strongly influenced by KC_c, as its magnitude increases. At the deep draft, the damping is similar for all plate configurations. At the shallow draft, Model C ($D_d/D_c = 2.9$) produces more damping compared to Model A and B ($D_d/D_c \leq 1.5$), and the porous plate gives more damping compared to the solid plate.

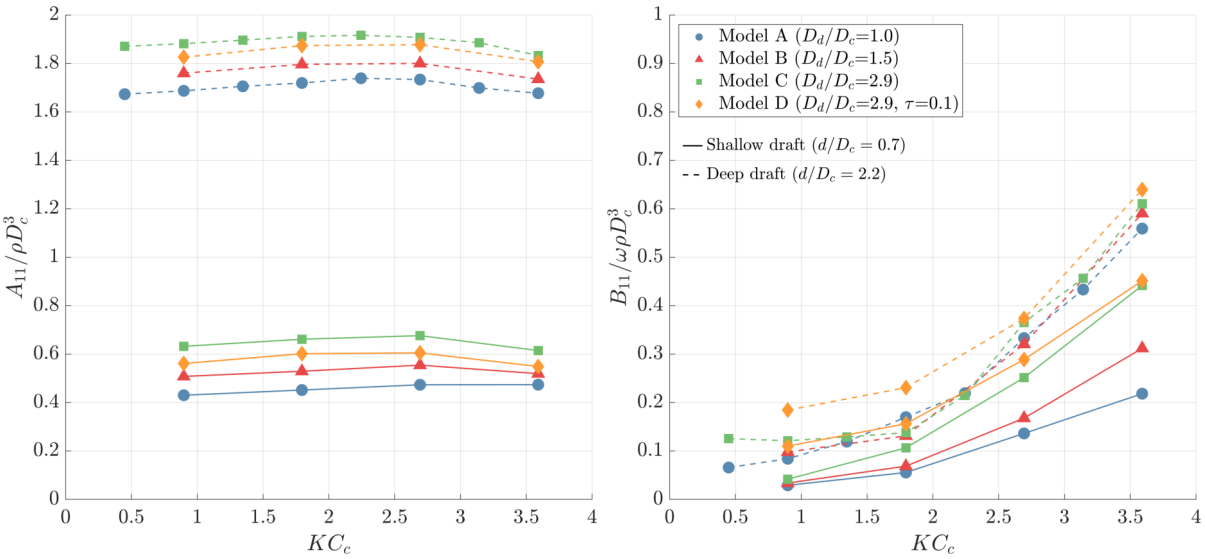

(a) Added mass, A_{11} **(b)** Damping, B_{11}

Figure 7.20 – Non-dimensional surge added mass and damping coefficients for the different heave plates with a single frequency ($\omega^2 D_c/g = 0.4$) and various amplitudes at the deep (- - -) and shallow (——) drafts.

7.6 Results III: forced pitch oscillations

The results of the non-dimensional hydrodynamic pitch moments ($M_{hd,y}/\rho g D_c^5$) are presented. Three plate configurations (Models A, C, and D) are examined to address the presence of the heave plate and porosity.

7.6.1 Time series of hydrodynamic loads

Figure 7.21 presents the time histories of the moments on the heave plate (Model C, $D_d/D_c = 2.9$) at the deep and shallow drafts. For the deep draft, it can be observed that an increase in frequency leads to an increase in the amplitude of the load and a change in phase. A similar trend can be seen at low drafts, but the forces do not increase above a certain frequency ($\omega^2 D_c/g = 1.0$). In general, the first harmonic dominates, and the contribution of other harmonics is negligibly small.

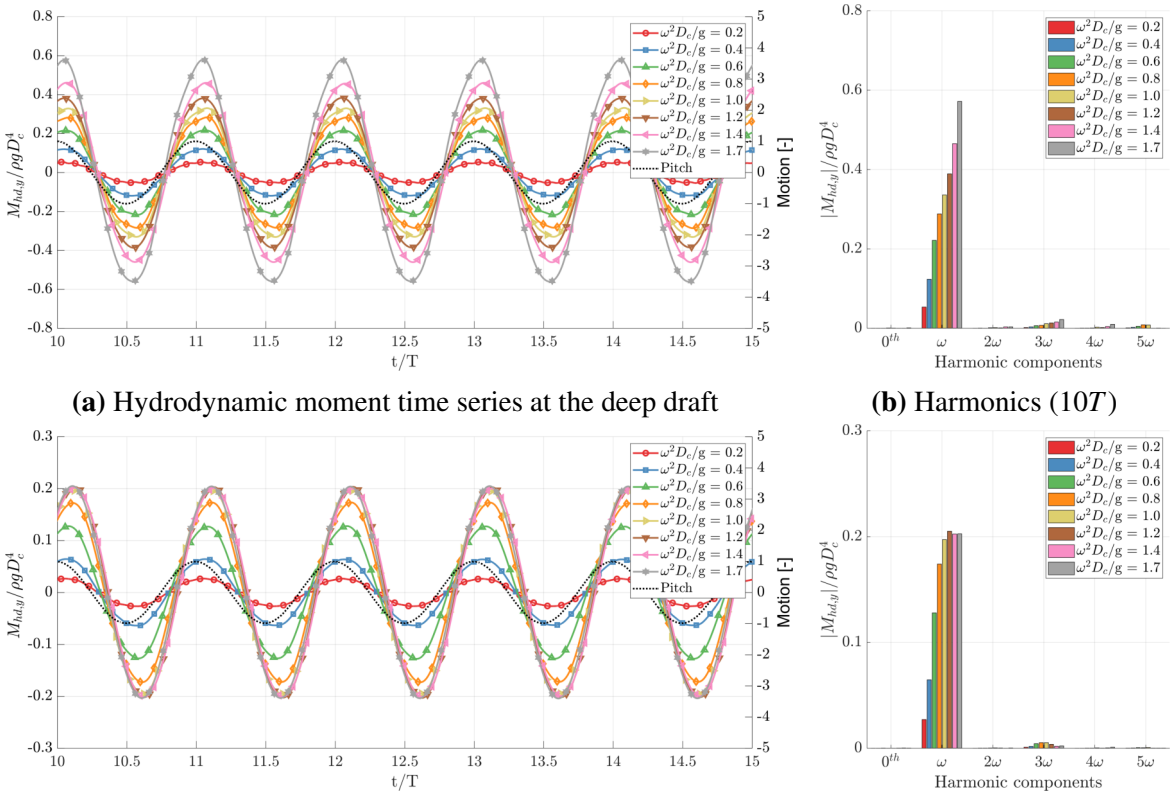

(a) Hydrodynamic moment time series at the deep draft

(b) Harmonics ($10T$)

(c) Hydrodynamic moment time series at the shallow draft

(d) Harmonics ($10T$)

Figure 7.21 – Time series and harmonic content of hydrodynamic moments on the solid plate ($D_d/D_c = 2.9$) at the deep ($d/D_c = 2.2$) and shallow ($d/D_c = 0.7$) drafts. Pitch motions are imposed with a single amplitude (ξ_5 = 3.0 deg) and various frequencies ($\omega^2 D_c/g = 0.2 \sim 1.7$).

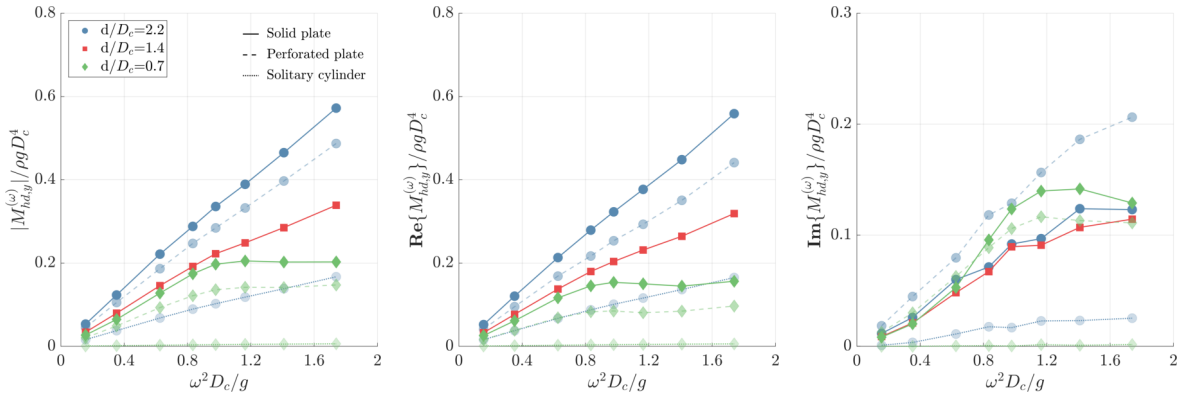

(a) Magnitude **(b)** In phase **(c)** Out of phase

Figure 7.22 – The amplitude of the first harmonic component of the hydrodynamic moments on the solid plate ($D_d/D_c = 2.9$) at the deep (●), middle (■), and shallow (⧫) drafts. Pitch motions are imposed with a single amplitude ($\xi_5 = 3.0$ deg) and various frequencies ($\omega^2 D_c/g = 0.2 \sim 1.7$). The first harmonic loads on the perforated plate ($D_d/D_c = 2.9$) and solitary cylinder ($D_d/D_c = 1.0$) are compared, except for the middle draft ($d/D_c = 1.4$, red color).

The results for the first harmonic are summarized in Figure 7.22. At deep and middle drafts, the magnitude of the harmonic increases linearly with frequency. However, at the shallow draft, it can be seen that the load magnitude no longer increases after a certain frequency. This trend is similar to the perforated plate. In terms of the magnitude of the first harmonic force and the in-phase component, the perforated plate has smaller values than that of the solid plate for both deep and low drafts. Interestingly, at the deep draft, the out-of-phase component for the perforated plate is higher than that for the solid plate, and vice versa at the shallow draft. It is also worth noting that the presence of the heave plate increases the pitch moment compared to a single cylinder.

Figure 7.23 presents the hydrodynamic pitch moment time histories and their harmonics with different amplitudes ranging in $1.0^\circ \leq \xi_5 \leq 9.0^\circ$. Corresponding KC_c (Eq. (7.3)) differ depending on the submerged draft. At the deep and shallow drafts, the forces increase by increasing the motion amplitude, and the phase is shifted compared to the prescribed pitch motion given in the dashed line. The first harmonics contribute significantly, and the third harmonics are visible but negligibly small compared to the first harmonics. The variation of the first harmonics into in- and out-of-phase components is given in Figure 7.24. At the deep draft, the magnitude of the first harmonic with the heave plate is linearly increased and distinctively higher than for the solitary cylinder. The perforated plate follows a similar tendency but slightly lower than the solid plate. At the deep draft, the out-of-phase component for the perforated plate is higher than that for the solid plate, but there is no difference at the shallow draft.

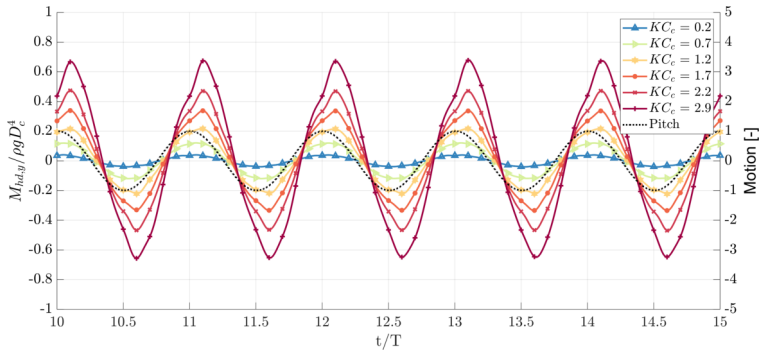

(a) Hydrodynamic moment time series at the deep draft

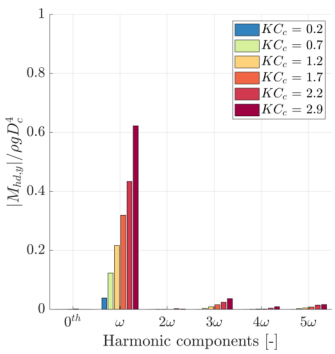

(b) Harmonics ($10T$)

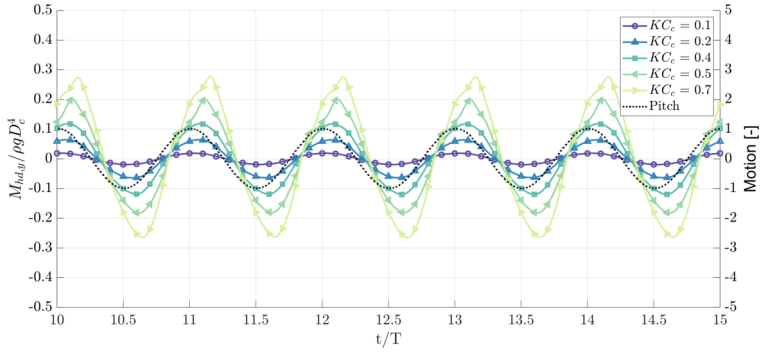

(c) Hydrodynamic moment time series at the shallow draft

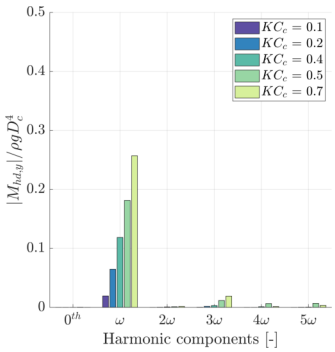

(d) Harmonics ($10T$)

Figure 7.23 – Time series and harmonic content of the hydrodynamic moments on the solid plate ($D_d/D_c = 2.9$) at the deep ($d/D_c = 2.2$) and shallow ($d/D_c = 0.7$) drafts. Pitch motions are imposed with a single frequency ($\omega^2 D_c/g = 0.4$) and various amplitudes ($\xi_5 = 1.0° \sim 9.0°$)

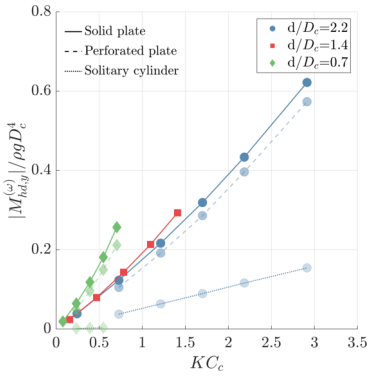

(a) Magnitude

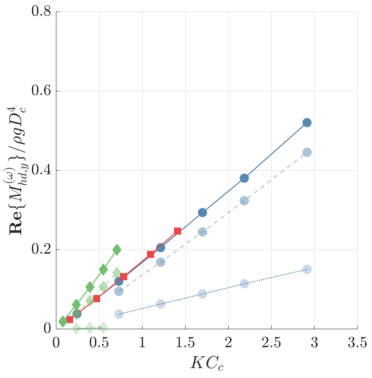

(b) In phase

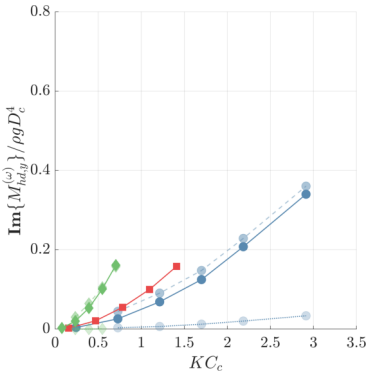

(c) Out of phase

Figure 7.24 – The amplitude of the first harmonic component of the hydrodynamic moments on the solid plate ($D_d/D_c = 2.9$) at the deep (●), middle (■), and shallow (♦) drafts. Pitch motions are imposed with a single frequency ($\omega^2 D_c/g = 0.4$) and various amplitudes ($\xi_5 = 1.0° \sim 9.0°$). The first harmonic loads on the perforated plate ($D_d/D_c = 2.9$) and solitary cylinder ($D_d/D_c = 1.0$) are compared, except for the middle draft ($d/D_c = 1.4$, red color).

7.6.2 Hydrodynamic coefficients for pitch motions

The effects of motion frequency and amplitude on the pitch added mass and damping are presented in Figures 7.25 and 7.26, respectively. The added mass and damping are nondimensionalized as $A_{55}/\rho D_c^5$ and $B_{55}/\omega\rho D_c^5$.

Based on the results obtained from the experiments conducted on the solid plate (Model C), it can be observed that the pitch added mass is less affected by the frequency at the deep and middle drafts. However, at shallow draft, it is more pronounced. The results of the potential flow theory are aligned with the experimental findings, even though the predictions are slightly lower than the measurement. Notably, the theory provides a good agreement for added mass and damping on the solitary cylinder.

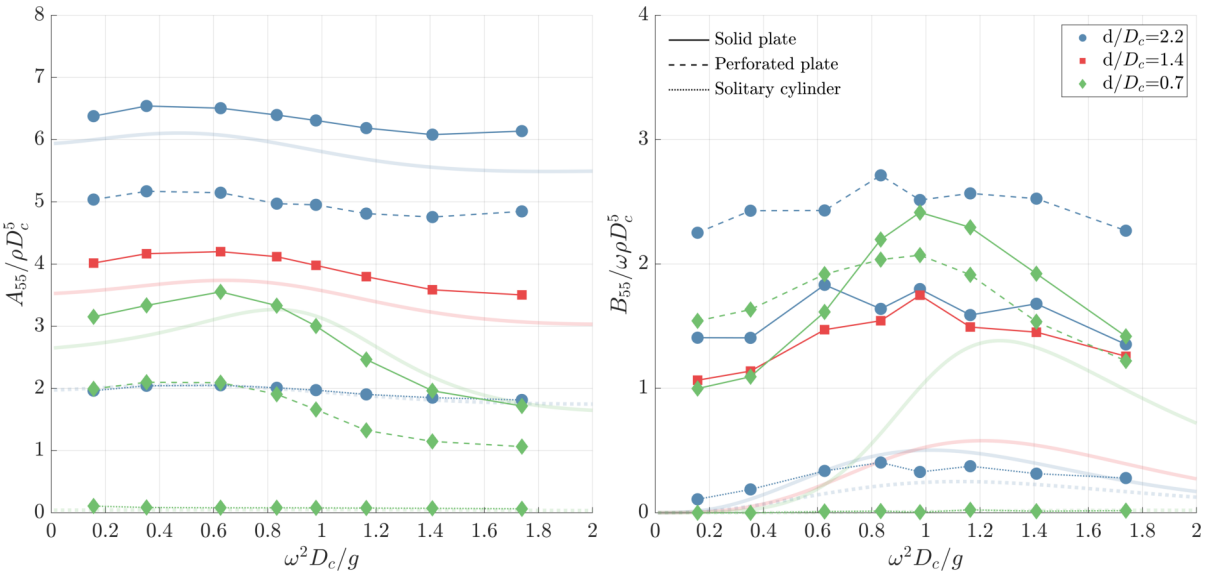

(a) Added mass, A_{55} **(b)** Damping, B_{55}

Figure 7.25 – Non-dimensional pitch added mass and damping coefficients with a single amplitude ($\xi_5 = 3.0°$) and various frequencies ($\omega^2 D_c/g = 0.2 \sim 1.7$) for the solid plate (——), perforated plate (---) and solitary cylinder (·····) at the deep (●), middle (■), and shallow (⧫) drafts. Lines with markers indicate the experimental results and shaded lines without markers are the results of the potential flow theory given for the cylinder with and without the solid plate (Model A, C).

For the solitary cylinder, the added mass shows an almost constant value even with varying KC_c. On the other hand, the added mass with the heave plate gradually increases as KC_c increases. Meanwhile, the reduction of the draft results in a decrease in the added mass.

The pitch damping is less affected by the motion frequency at deeper drafts ($d/D_c >$

1.1). However, at the shallow draft, it is observable. Particularly, when the frequency is higher than 0.8, the damping at the shallow draft is higher than at the deep and middle drafts. Furthermore, the increase of KC_c significantly affects the damping, and the rate of the damping is also increased by reducing the submergence. Similar to heave damping, the potential flow theory generally underpredicts pitch damping.

The presence of the plate results in the increase of the added mass and damping, which is consistent with the other motions. The porosity produces less added mass than the solid plate at the deep and shallow drafts. Notably, the damping for the perforated plate is higher than that for the solid plate at the deep draft but varies with frequency and KC_c at shallow drafts.

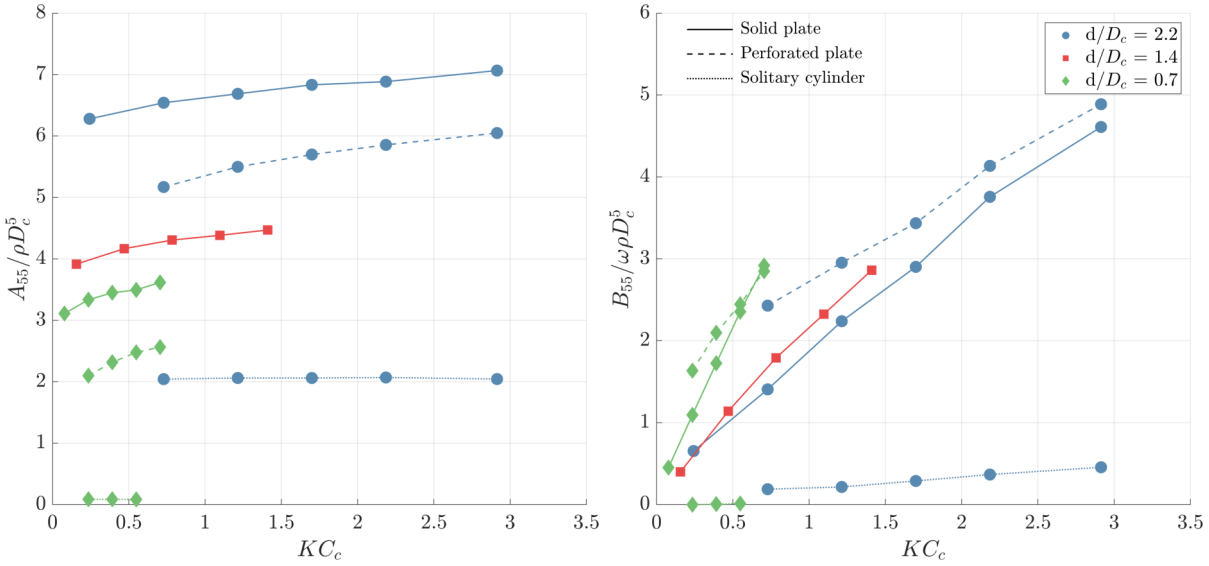

(a) Added mass, A_{55} **(b)** Damping, B_{55}

Figure 7.26 – Non-dimensional pitch added mass and damping coefficients with a single frequency ($\omega^2 D_c/g = 0.4$) and various amplitudes ($\xi_5 = 1.0° \sim 9.0°$) for the solid plate (——), perforated plate (---) and solitary cylinder (·····) at the deep (●), middle (■), and shallow (⧫) drafts.

7.7 Discussion

In the previous Section 7.4.2, it was observed that vertical hydrodynamic loads induced by heaving plates exhibit different behaviors depending on submerged drafts. Although various motion parameters and submerged depths were tested, the flow characteristics and free surface behaviors were not completely understood based on the present experimental setup. Therefore, this section presents further investigation using numerical simulations based on the numerical setup validated in Section 4.2.

The main objective of this section is to provide a more detailed understanding of the flow and free surface behaviors for a single heave plate configuration ($D_d/D_c = 2.2$, Model C). Selected test parameters are given in Table 7.2 involving three representative submerged drafts: deep, middle, and shallow. Finally, the contributions of the heave damping components are discussed using the dissipation of enstrophy, free surface and wave radiation, as presented in Section 2.2.4.

Table 7.2 – Test parameters for forced heave oscillations in numerical simulations.

Config	d	d/D_c	D_d/D_c	$\omega^2 D_c/g$				
Deep	0.775	2.2	2.9	0.16	0.35	0.63	0.98	1.41
Middle	0.500	1.4	2.9	0.16	0.35	0.63	0.98	1.41
Shallow	0.250	0.7	2.9	0.16	0.35	0.63	0.98	1.41

Note. Only a small heave motion amplitude ($KC_c = 0.9$) is considered.

7.7.1 Numerical setup for heaving cylinder with a heave plate

Figure 7.27 displays an axisymmetric computational domain and its boundaries. The length of the axisymmetric domain is set as 10 times the diameter of the plate ($10D_d$), with a wedge angle of 5 deg, which is sufficient as discussed in Pinguet et al. (2022). The distance between the bottom and free surface at rest is defined as 5 times D_d, which is identical to the 5-meter water depth of the hydrodynamic and ocean engineering tank at the Ecole Centrale Nantes.

An example of mesh for the deep draft configuration $d/D_c = 2.2$ is illustrated in Figure 7.28. In order to capture radiated waves, the free surface is resolved, and various levels of grid resolution are applied around the heave plate to investigate the flow behavior with high resolution. A $5D_d$-long relaxation zone is defined to absorb radiated waves, which is around 3

times larger than the shortest wave at $\omega^2 D_c/g = 1.4$ and 0.5 larger than the longest wave at $\omega^2 D_c/g = 0.16$. The mesh generation schemes and dimensions of the computational domain remain constant for all submerged depths and motion frequencies.

In this study, the numerical schemes described in Section 4.2 are utilized. One notable difference from the previous setting is the use of a free surface $k-\omega$ SST turbulence model along with a Crank-Nicolson time integration scheme (0.95) to resolve radiated waves caused by body motions. The time step is fixed at $dt = 0.001$. The boundary conditions are listed in Table 7.3.

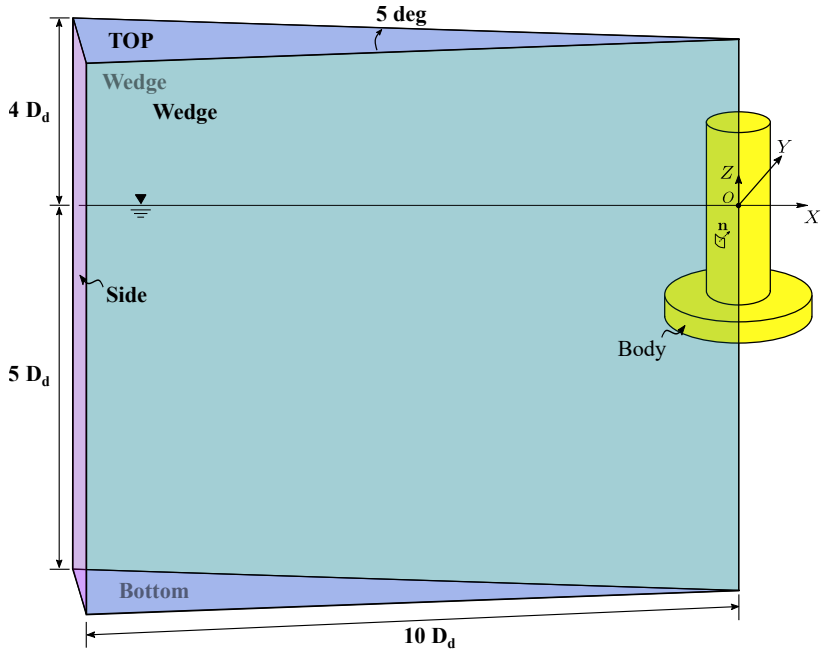

Figure 7.27 – Numerical axisymmetric domain for a truncated circular cylinder with a heave plate at the bottom.

Table 7.3 – Boundary conditions of the axisymmetric domain used for forced heave oscillations.

	Top	Side/Bottom	Body	Wedge
U	InletOutlet	fixedVlaue	movingWallVelocity	Wedge
p_rgh	totalPressure	ZeroGradient	fixedFluxPressure	Wedge
α	inletOutlet	ZeroGradient	ZeroGradient	Wedge
k	zeroGradient	zeroGradient	kqRWallFunction	Wedge
ω	zeroGradient	zeroGradient	omegaWallFunction	Wedge
ν_t	calculated	calculated	nutUSpaldingWallFunction	Wedge

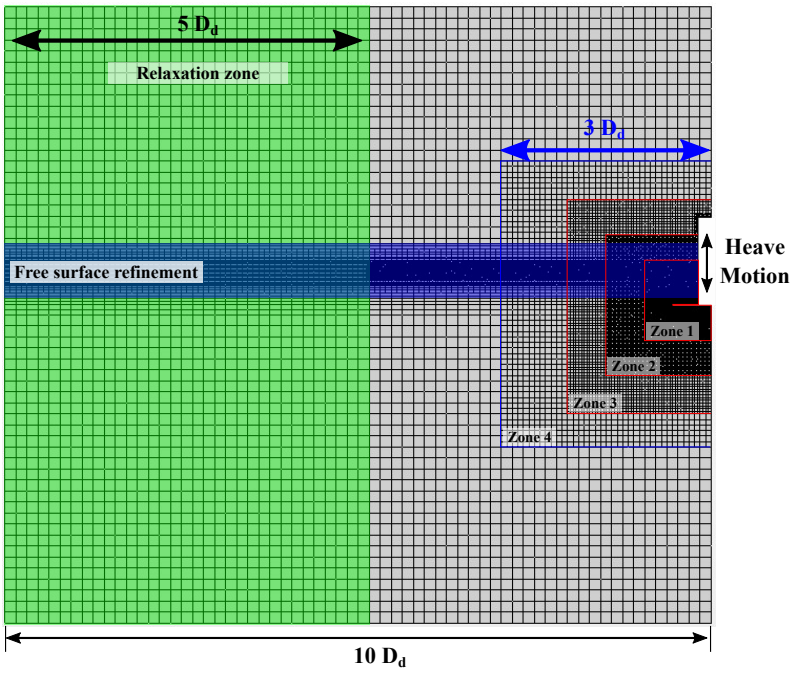

Figure 7.28 – Grid refinements and relaxation zone for forced heave oscillation simulation.

7.7.2 Flow field around heave plates

Figure 7.29 illustrates the flow velocity fields around the heave plate, which was not obtained in the experiment. Four representative positions are examined with a motion frequency $\omega^2 D_c/g = 0.35$: zero-crossing up (zero up), top, zero-crossing down (zero down), and bottom. The figure presents different drafts at each position in the same row, making it easy to compare the effects of ambient flow and free surface according to the submerged depth. The free surface, defined as the surface where the VoF function $\alpha = 0.5$, is indicated by a black solid line in the figure. The color legend is used to describe the strength of non-dimensional flow velocity, and white arrows display flow vectors.

Based on this flow visualization, there is a significant interaction between the free surface and the vortices released by the plate at the shallow draft. This interaction causes a noticeable effect on the deformation of the free surface. When the plate moves downward, it causes the flow to curl, generating a strong flow velocity that is located very close to the free surface. Additionally, the fluid surrounding the plate tends to follow the plate's movement.

However, this phenomenon does not occur for the deep draft. At the deep draft, the fluid flow is divided into two main patterns. Specifically, when the plate moves down (zero-crossing

down), the fluid above the plate goes down and follows the plate, whereas the fluid near the free surface moves in the opposite direction in a counter rotation towards the free surface with small velocity. As a result, the free surface is less deformed at the deep draft.

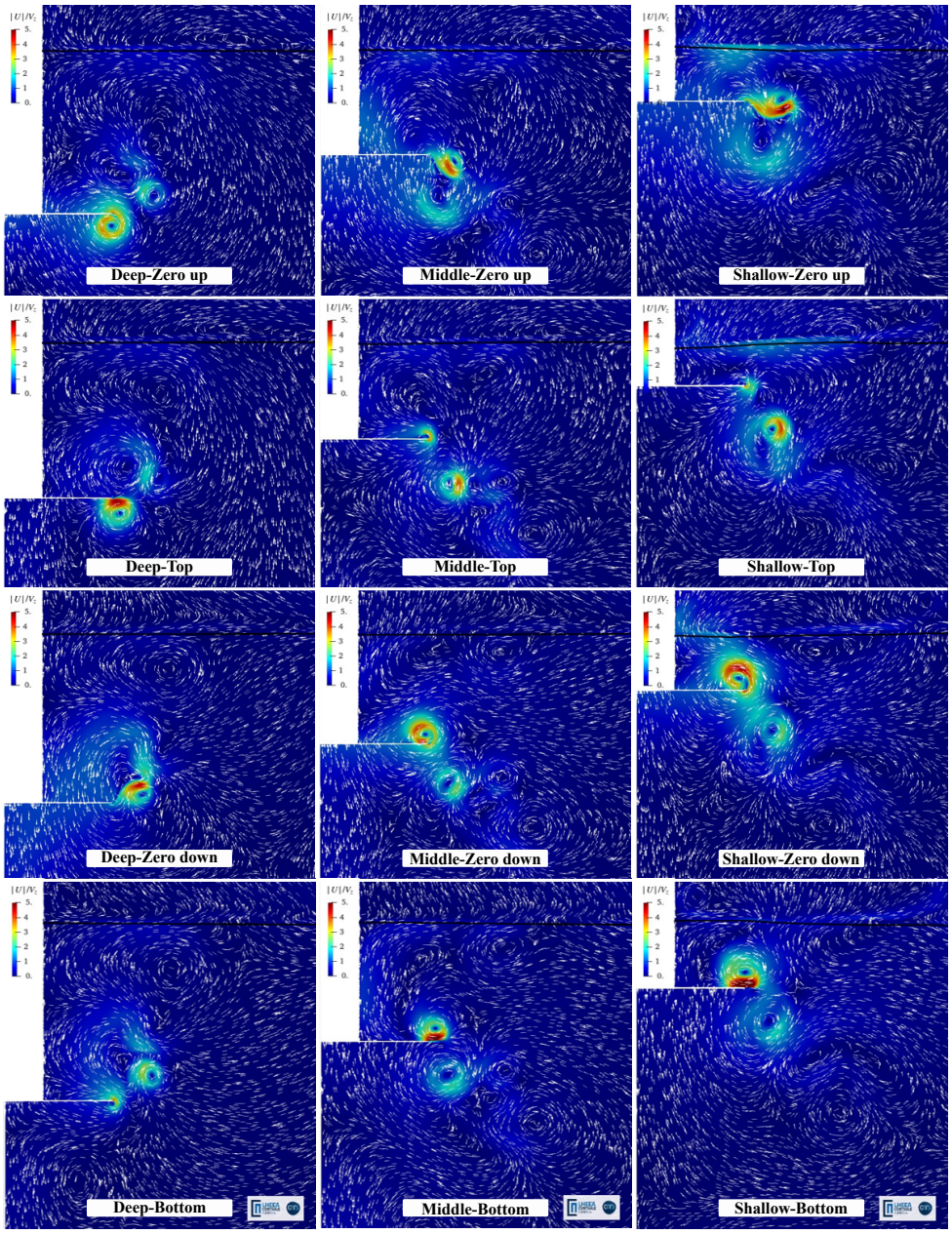

Figure 7.29 – Non-dimensional flow velocity field ($0 \leq |\mathbf{u}|/V_z \leq 5$) during a heave oscillation ($KC_c = 0.9$, $\omega^2 D_c/g = 0.35$) for deep, middle, and shallow drafts at zero up, top, zero down, and bottom positions. White arrows indicate flow vectors, and black solid lines give the free surface position.

7.7.3 Radiated waves in forced heave oscillations

Radiated waves measured by wave gauges 3 and 5 are further investigated in this section. These wave measurements are situated at angular intervals of 120 degrees and located 2.1 m ($r/D_d = 2.1$) away from the cylinder center (see Figure 5.1). First, a radiated wave time series is investigated with two heave motion frequencies: low frequency ($\omega^2 D_c/g = 0.35$) and high frequency ($\omega^2 D_c/g = 1.4$). Then response amplitude operators (RAOs) of the first harmonic radiated wave are presented.

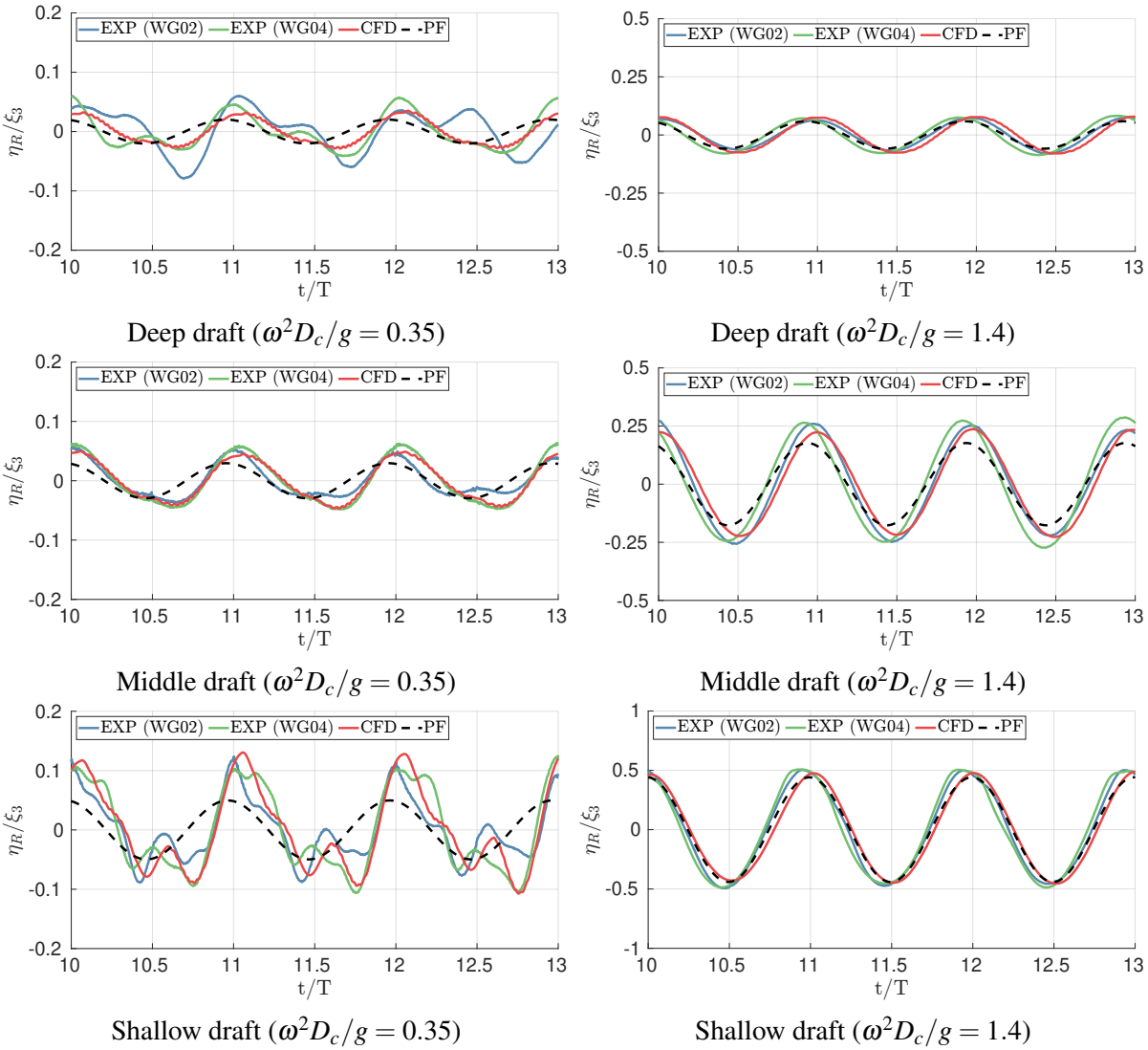

Figure 7.30 – Non-dimensional radiated waves with $\omega^2 D_c/g = 0.35$ obtained (or measured) 2.1 m ($r/D_d = 2.1$) far away from the center of the cylinder.

In Figure 7.30, the waves measured experimentally are compared with the numerical simulation and potential flow model developed in Chapter 3. The results obtained from both wave gauges are almost identical except for the deep draft with the lowest frequency where the amplitude of the radiated waves is very small. As expected, the radiated waves increase as the submerged depth reduces. The numerical simulation shows good agreement with the experimental results. Moreover, the first-order radiated wave from the potential flow model also shows acceptable agreement but tends to underestimate wave heights compared to experiments and numerical simulations. Particularly, at low drafts with low-frequency motion ($\omega^2 D_c/g = 0.35$), where nonlinearity is prominent, the first-order potential radiated wave shows significant differences with the experiments and CFD simulations. This is compatible with the observation in flow fields that show a strong interaction between vortices and free surface.

Figure 7.31 presents the RAOs of the first harmonic obtained from the radiated waves. Similar to the previous comparison in time series, the results of the numerical simulations (CFD) align with those of experiments. The first-order results from the potential flow model (dashed line) predict the general trend of the first harmonic of the wave, showing very good agreement for the shallow draft. Notably, there are some discrepancies at the deep and middle drafts, especially around the peak of the RAOs.

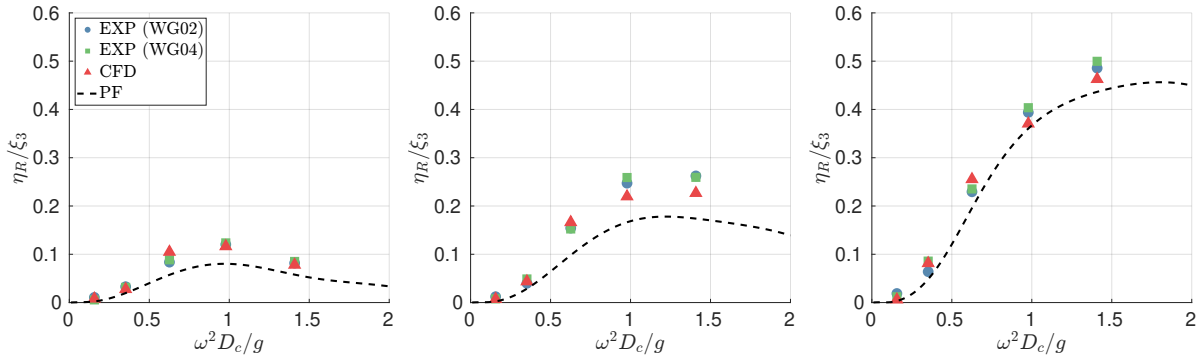

(a) Deep draft **(b)** Middle draft **(c)** Shallow draft

Figure 7.31 – RAOs of radiated waves obtained (or measured) 2.1 m ($r/D_d = 2.1$) far away from the center of the cylinder.

7.7.4 Heave damping and its components

As described in Section 2.2.4, the hydrodynamic linearized damping B comprises three main components: damping due to the dissipation of enstrophy B_ω, damping caused by free surface effects B_{FS} and radiated damping on the lateral surface B_C.

$$B = B_\omega + B_{FS} + B_C \tag{7.12}$$

Furthermore, by putting the lateral boundary far from the body, "far-field" ($\dot{\mathscr{E}}_C \to \dot{\mathscr{E}}_\infty$), the damping B_c is interpreted as the wave radiated damping B_w, assuming the flow is potential there. Therefore, the damping components in Equation (7.12) can be expressed as,

$$\begin{aligned} B_\omega &= -\frac{2}{\omega^2\overline{\xi}^2}\left\langle \dot{\mathscr{E}}_\omega \right\rangle = \frac{2}{\omega^2\overline{\xi}^2}\left\langle \iiint_{\Omega_C} \mu\boldsymbol{\omega}^2 dV \right\rangle \\ B_{FS} &= -\frac{2}{\omega^2\overline{\xi}^2}\left\langle \dot{\mathscr{E}}_{FS} \right\rangle = \frac{4}{\omega^2\overline{\xi}^2}\left\langle \iint_{\partial\Omega_F} \mu(\nabla \boldsymbol{u}\boldsymbol{u})\cdot\boldsymbol{n} dS \right\rangle \\ B_C &= B_w \end{aligned} \tag{7.13}$$

The first two components B_ω and B_{FS} can be computed in the numerical simulation, as explained in detail in Garrido-Mendoza Carlos A. (2015). To compute these terms numerically, a control volume is defined using *topoSet* in OpenFOAM, along with a radius, $r = 5D_d$, that is large enough to account for all significant flow behavior. It could be noticed, as shown in Figure 7.29, that the flow induced by the plate remains around the plate while only the waves propagate away from the body. Fortunately, the latter can be addressed by using the potential flow method with the far-field assumption. In this study, the analytical model developed in Chapter 3 is thus used to compute the wave damping, B_w.

Figure 7.32 (left) shows heave damping obtained from experiments (Section 7.10) and from the present numerical simulations. In this figure, $B_{33}^{F_{hd}}$ denotes the damping obtained from the hydrodynamic forces and $B_{33}^{\mathscr{E}_{total}}$ stands for the total damping computed using Equation (7.13). From the results, it can be seen that both dampings computed from the hydrodynamic forces (CFD and EXP) agree. The damping computed from the flow fields is close to the one computed from the forces showing that the domain is sufficiently discretized. The numerical results show that the damping at the deep draft is less influenced by the motion frequency but pronounced as the submerged draft reduces.

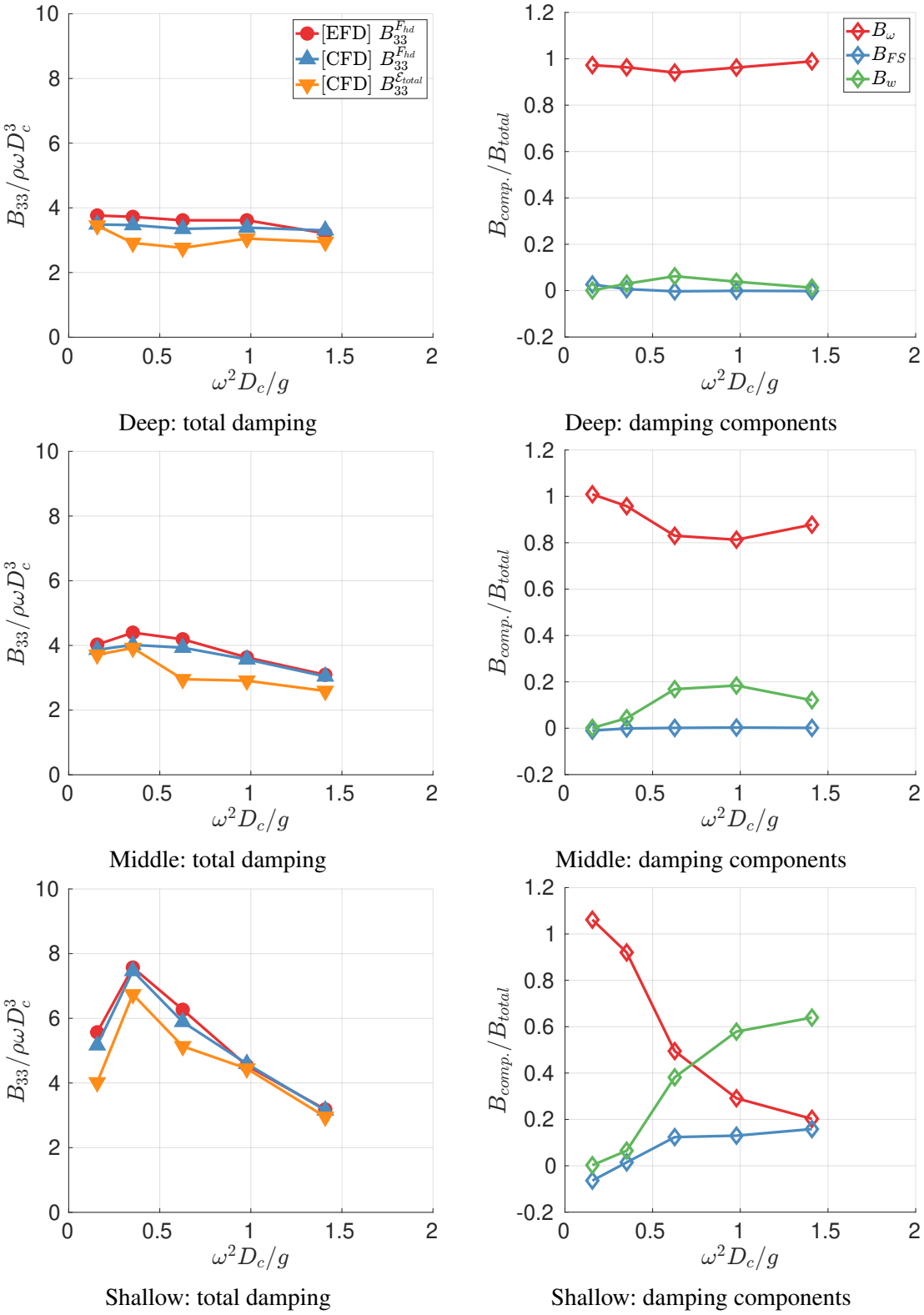

Deep: total damping | Deep: damping components

Middle: total damping | Middle: damping components

Shallow: total damping | Shallow: damping components

Figure 7.32 – Non-dimensional heave damping (left) and its components (right) on a heaving cylinder with a heave plate at deep, middle and shallow drafts.

The contribution of each dissipation term to the total damping ($B_{component}/B_{total}$) is examined in Figure 7.32 (right). The result of damping at the deep draft is aligned with the literature (Garrido-Mendoza Carlos A. (2015)), as the damping from the free surface dissipation B_{FS} and wave damping B_w are negligible. The damping from the enstrophy terms dominates the total damping. Therefore, in this regime, a possible modelling using drag coefficients (quadratic) could be suitable.

On the other hand, as the draft decreases, the contribution of wave damping increases, while the enstrophy contribution decreases. Surprisingly, even at the shallow draft, B_ω is still dominant at the low frequency ($\omega^2 D_c/g = 0.16$). As the frequency increases, the wave damping contribution begins to take over the contribution from enstrophy and eventually surpasses it at high frequencies $\omega^2 D_c/g \geq 0.98$. The damping from the free surface dissipation remains nearly zero up to the middle draft and the damping B_{FS} contributes more than 10 % of the total damping at the shallow draft at high frequency. This could be an indication of breaking, or some uncertainty in the evaluation of the term. Therefore, to model the damping with drag coefficients, it is important to consider first the contribution of the linear wave damping, in particular for lower submerged depth ($d/D_c \leq 1.4$).

The damping from the free surface dissipation, B_{FS}, shows negative values at shallow draft and low frequency ($\omega^2 D_c/g = 0.16$), probably again because of the difficulty of evaluating this term. In this area, the heave plate generates significant radiated waves with long wavelengths ($\lambda/\mathrm{D}_d \approx 14$) that cannot be captured by the current computational domain. Therefore, a more detailed investigation is required to validate this result. A study with higher spatial and temporal resolutions (or a larger computational domain) might be interesting for this attribute, as the present study was only carried out with a constant time step and identical grid resolutions.

7.8 Conclusions

The hydrodynamic loads have been investigated for surge, heave, and pitch oscillations of a vertical and surface-piercing circular cylinder with a heave plate mounted at the bottom. It was observed that the harmonically oscillating cylinder causes hydrodynamic loads with various harmonic content. This is true with the plate at different submerged depths, but presents stronger at the shallow draft. The amplitude and frequency of the motion highly affected the magnitude and phase of the harmonics. The study demonstrated that the first harmonic is the predominant harmonic in the hydrodynamic loads. The first harmonic was further interpreted as added mass and damping coefficients.

The experimental results indicate that the proximity of the free surface affects the hydrodynamic coefficients, as follows:

- **Heave motion:** The heave damping of plates is greatly affected by the motion frequency when the draft is reduced. The damping generally increases as the draft decreases. However, decreasing the submerged depth significantly reduces the added mass, which is consistent with the theoretical studies of McIver and Evans (1984); Greenhow and Ahn (1988).

  The added mass increases linearly with KC_c for the deep draft. In contrast, for the shallow draft, the added mass decreases as KC_c increases. It is worth noting that this decreasing tendency depends on the motion frequency. Conversely, the slope of damping with respect to KC_c increases by reducing the submergence. In the very shallow draft ($d/D_c = 0.4$), a peak of damping occurs where the damping starts to decrease with increasing KC_c.
- **Surge and pitch motions:** The surge added mass and damping is strongly influenced by the motion frequency at both deep and shallow drafts. These are well predicted by potential flow theory in a small $KC_c = 0.9$. It is worth noting that surge added mass is less dependent on KC_c, whereas the damping is significantly affected by KC_c.

  On the other hand, for the pitch motion, the characteristics of the hydrodynamic coefficients are similar to those of the heave motions. It was observed that the added mass and damping are affected by the motion frequency at the shallow draft and less at the deeper drafts. For the solitary cylinder, the potential flow theory describes the hydrodynamic coefficients well. However, this theoretical model underpredicts the hydrodynamic coefficients when the plate is mounted at the bottom of the cylinder.
- **Plate characteristics:** The presence of a heave plate increases the added mass and

damping for surge, heave, and pitch motions in general. A larger heave plate provides even more damping. Using a porous plate reduces the added mass, but the plate has more damping than the solid plate at deep drafts. However, at shallow drafts, the porous plate exhibits less damping. This may be because the wave damping, which makes a significant contribution to the total damping at the shallow draft, is greater with the solid plate.

In the present study, the primary focus was on examining the first harmonics of hydrodynamic loads, i.e., added mass and equivalent damping. However, as the results indicate, higher harmonics become more prominent as the motion amplitude increases, and the contribution of the first harmonic decreases when the plate approaches the free surface. Therefore, to accurately model the hydrodynamic loads on heave plates, it is necessary to conduct further studies of higher harmonics. It is also important to analyze the interaction between the free surface and vorticity by visualizing the flow through PIV experiments or numerical analysis to supplement the results of this study. Furthermore, it is beneficial to determine the contribution of wave, vorticity and other energy dissipation terms to the damping term. Therefore, a further parametric numerical study (CFD) is planned with a combination of motion amplitudes, frequencies and submerged depths toward a comprehensive understanding. Finally, the understanding needs to be expanded to the real design of floating substructures, which can be geometrically more complicated, involving multiple columns, pontoons, braces and reinforcements such as stiffeners or webs.

CHAPTER 8

CONCLUSIONS

8.1 Heave plates on floating wind turbine foundations

Wave loads greatly influence the design of the substructure, mooring lines, and power cables of the floating systems. The loads can cause extreme responses, drift motions, and vibrations due to system resonance, which pose a significant challenge in designing and operating FWTs in harsh offshore environments. A practical solution to mitigate these dynamic responses is to install heave plates. The plates are widely used on semi-submersible floaters (Roddier et al. (2010); Lopez-Pavon and Souto-Iglesias (2015); Pegalajar-Jurado et al. (2018); Robertson et al. (2020)) as well as in box-type floaters (Choisnet et al. (2016)). The heave plates serve to increase the hydrodynamic damping of the system as well as the added mass. Therefore, an accurate assessment of these effects is important to optimize the floaters and estimate the capital expenditures (CAPEX) of FWTs during the design phase. For example, the substructure and foundation represent the most considerable portion of CAPEX, accounting for 37.5 %, according to the 2021 Cost of Wind Energy Review by the National Renewable Energy Laboratory (Stehly and Duffy (2021)).

In the engineering design tool of FWT, evaluating the hydrodynamic loads due to the heave plate remains a challenge. Numerous engineering tools are time-domain solvers based on the potential flow theory. That method requires assistance in modelling the heave plates of floaters and often needs calibration based on high-fidelity models, such as experiments or computational fluid dynamics (CFD) simulations. While hydrodynamic databases are available in the literature for different shapes and flow properties, they mostly come from classical offshore engineering with structures relatively different from those developed in the floating wind community. Therefore, consideration of a wide range of flow and geometric parameters is necessary to account for the flexibility and diversity of the FWT platform design. In particular, the free surface effect needs to be carefully addressed in engineering applications since the floating substructure of FWT has a relatively low draft compared to conventional offshore platforms.

8.2 Overview of the present work

The objective of this study was to investigate the effects of the heave plate on hydrodynamic loads. To accomplish this, a single vertical, surface-piercing circular cylinder was used with and without a heave plate mounted at the bottom. This model shape is commonly found in offshore structures, specifically in semi-submersibles for FWTs. The study focused on the physical quantities of interest using simple geometry while minimizing any interference caused by geometrical complexity. The main effort was to analyze the hydrodynamic loads based on extensive tank testing as well as numerical and analytical studies.

One of the major tasks in this study was to conduct experiments. In the tests, a captive model technique was utilized with a forced motion generator, called hexapod. A six-component force transducer was used to measure the resulting hydrodynamic loads. This test setup enabled us to carry out two experimental approaches: (1) a fixed model with incident waves and (2) a forced oscillating model without incident waves. This separation of diffraction and radiation loads was based on a linear theory that decomposes a single problem into diffraction and radiation problems, respectively. The loads were categorized into the hydrodynamic loads induced by waves and motions. In engineering models, the former is modeled as wave diffraction loads or wave excitation loads. The latter is often interpreted as the added mass, damping, or viscous drag contribution. We successfully measured the loads separately and analyzed the effects of the heave plates on the loads in terms of force time series and harmonic content using Fourier analysis. This analysis is helpful in identifying the contribution of the heave plate to each hydrodynamic load component.

The decomposed problems were implemented into a first-order analytical model and numerical simulations. The analytical model was developed based on the potential flow theory and presented generalized first-order solutions for a truncated circular cylinder with a heave plate at the bottom. These solutions covered linear diffraction and radiation of water wave problems, including surge, heave, and pitch motions. In addition, a Navier-Stokes equations solver (CFD) was validated using experimental data from the HiPRWind project and the present study. By using the $k-\omega$ turbulence model, the numerical method was able to capture the flow separation and provide a good resolution of the hydrodynamic forces compared to the experimental measurements.

8.3 Major findings

In this study, the hydrodynamic loads on a truncated circular cylinder with a heave plate have been extensively investigated using three different approacheswhich have different levels of fidelity: potential flow theory, computational fluid dynamics (CFD), and physical wave tank testing. The major findings are highlighted below.

First-order wave diffraction/radiation solutions

A first-order analytical method has been developed to solve wave diffraction and radiation problems on a truncated circular cylinder with a circular plate. This method is able to efficiently compute linear hydrodynamic loads, including wave loads, added mass and damping for surge, heave and pitch motions. These linear hydrodynamic coefficients are significant parameters used to solve an equation of motion to compute the responses in an engineering model, which is a low-fidelity model capable of efficiently computing the entire design scenario. However, adjustments may need to be made to enhance the resolution of such a low-fidelity model by modelling additional viscous or nonlinear effects, which maintains efficiency while improving the accuracy of results. Therefore, this first-order method is expected to provide a robust basis for a comprehensive hydrodynamic database that can be used to model the viscous or nonlinear effects toward high-fidelity models utilizing experimental data.

Numerical modelling of heave plates

1. The BEM solver is a common practice to solve a seakeeping problem. This approach is both robust and efficient and is particularly suitable for complex geometries where analytical expressions are not applicable. However, for some specific applications, such as for a thin plate, verifications might be needed using analytical solutions. From the present validation study, the BEM solver's source method shows good agreement with analytical methods for thick heave plates. However, the source method tends to underestimate the vertical hydrodynamic component for thin plates. By using the dipole method, the BEM solver is capable of improving the prediction of heave damping in that case.
2. In the CFD solver, the turbulence model is crucial to accurately resolve the flow field around the oscillating heave plate. From validation with the experiments of (Lopez-Pavon and Souto-Iglesias (2015); Anglada-Revenga et al. (2020)), using

axisymmetric and symmetric models with $k-\omega$ SST turbulence model permitted to predict both flow field and vertical hydrodynamic forces as well as the added mass and damping.

Heave plate effects on wave diffraction loads in monochromatic and bichromatic waves

1. The diameter ratio of the plate (D_d/D_c) significantly affects the wave loads. In particular, with the large plates ($D_d/D_c = 2.9, 3.5$), the vertical forces increase significantly. Interestingly, the BEM solver indicates the cancellation of first-order vertical forces in the low-frequency region, however, the experimental results show significant amounts of the first-harmonic forces there.
2. The perforated plate with 10 % porosity effectively decreases the wave loads, which is more noticeable at shallow drafts. The panel method with added porous parameter predicts well the first harmonics of the wave loads at the deep and shallow drafts.
3. As the steepness of the wave increases, the non-dimensional horizontal forces tend to decrease. This trend is more noticeable with the large plates, but negligible for the solitary cylinder. On the other hand, in low-frequency regions, the first harmonic of vertical forces with the large plate increases as the wave steepness increases.
4. The effect of the submerged depth is closely related to the wave steepness, as there is an interaction between the plate and the free surface. At the deep draft, horizontal forces are less affected by the heave plate and the wave steepness, but at the shallow draft, it becomes significant. Additionally, the harmonic content of the wave loads is notably increased at the shallow draft compared to the deep draft.
5. The underestimation of vertical wave forces on the plate is identified due to the flow separation occurring around the edge of the plate through CFD simulations. Using the simplified Morison's equation to estimate the drag coefficients and add them to the potential flow prediction permits getting a prediction much closer to experimental or CFD results, compared to using only potential flow theory. Identification of vertical forces regimes at the deep draft was proposed according to the nondimensional wave frequency and the plate diameter ratio, with three regimes: (I) diffraction regime, (II) viscous drag regime, and (III) diffraction and viscous drag regime.

Heave plate effects on hydrodynamic loads in forced oscillations

1. From extensive experiments, it has been observed that harmonically oscillating

cylinders with plates at different submerged depths cause hydrodynamic loads with various harmonic content. In particular, for heaving plates, the contribution of the first harmonic on vertical hydrodynamic forces decreases in proximity to the free surface. In addition, with large KC_c, the contribution of the second or third harmonics to the total hydrodynamic loads is significant. Therefore, it is important to note that while modelling the hydrodynamics of a heave plate through added mass and damping, which are mainly based on the first harmonic content, one should be careful since higher harmonics can also play a significant role.

2. The presence of a heave plate increases the added mass and damping for surge, heave, and pitch motions. In general, a larger heave plate provides even more damping. Using a porous plate reduces the added mass, but the plate has more damping than the solid plate at deep drafts. However, at shallow drafts, the porous plate exhibits less damping. This may be because wave damping significantly contributes to the total damping at the shallow draft.
3. The added mass and damping coefficients of the surge are affected by the motion frequency at deep and shallow drafts. The potential flow theory can accurately predict these effects, but only for limited motion amplitude. It is noted that surge damping is significantly influenced by KC_c compared to the added mass.
4. The added mass and damping coefficients of the heave at the deep draft confirmed that the motion amplitude represented by the KC number is more predominant than the frequency. This tendency is consistent with the findings in the literature (Lopez-Pavon and Souto-Iglesias (2015)). Notably, the heave added mass tends to be significantly reduced due to the proximity to the free surface. On the other hand, the damping is increased due to the vicinity of the free surface and is strongly influenced by the motion frequency.
5. Hydrodynamic pitch coefficients have similar trends to that for heave motions. Added mass and damping depend on motion frequency, especially at shallow drafts. The potential theory gives accurate prediction for a solitary cylinder, but underpredicts the hydrodynamic coefficients when the cylinder is equipped with the heave plate.

8.4 Future work and recommendations

This study conducted extensive tank testing to provide the FWT community with a comprehensive understanding of the hydrodynamic characteristics of heave plates. The experimental findings were complemented by numerical and analytical studies. The results confirmed that hydrodynamic loads are highly dependent on geometrical and flow parameters, particularly the motion frequency and submerged depth. Therefore, a parametric study using high-fidelity numerical simulation (CFD) is expected to further explore the relationships between the loads and the parameters.

The present study of hydrodynamic loads has mainly focused on regular waves and motions. The loads can be represented through hydrodynamic coefficients in frequency domain analysis in engineering applications. However, it is also important to investigate the hydrodynamic loads in irregular waves and motions evolving in time as they represent more realistic environmental conditions. Notably, when it comes to radiation problems, the memory effects play a significant role as the present flow is heavily influenced by the flow induced in the past. Therefore, it is necessary to conduct further research on the added mass and damping in irregular motions to model the heave plate in irregular sea states accurately.

Further research is necessary to establish a complete hydrodynamic database for an engineering model. This will help the engineering model provide a more accurate assessment of the effects of heave plates by modelling viscous and nonlinear effects. As a result, it will improve the hydrodynamic modelling of floating systems and optimize their performance. Additionally, it would be interesting to validate the engineering model using the hydrodynamic coefficients obtained from the database to address the limit of assumptions made in the engineering model. However, it's important to acknowledge that this approach through coefficients (of the first harmonics) has inherent strong limitations. The results obtained from the present study show a strong variability and dependence of these coefficients on different parameters, indicating that this simplified approach based on the use of coefficients is probably ineffective and impractical for complex problems involving strong nonlinearities.

Lastly, a simple circular cylinder with a circular plate geometry is considered in this study. However, the floating structure is often more complex in reality. The geometry of the floater can be intricate, involving multiple columns, braces and reinforcements such as stiffeners or webs. This geometrical complexity affects the differences in fluid dynamics and needs further investigation. A fully designed model equipped with several columns and mooring lines needs further investigation in irregular seas.

BIBLIOGRAPHY

A. Abazari, M. Behzad, and K. Thiagarajan. Hydrodynamic damping enhancement by implementing a novel combined rigid-elastic heave plate. *Journal of Marine Science and Technology*, 26(1):216–232, 3 2021. ISSN 0948-4280. doi: 10.1007/s00773-020-00732-7.

S. An and O. M. Faltinsen. An experimental and numerical study of heave added mass and damping of horizontally submerged and perforated rectangular plates. *Journal of Fluids and Structures*, 39:87–101, 5 2013. ISSN 08899746. doi: 10.1016/j.jfluidstructs.2013.03.004.

E. Anglada-Revenga, A. Bezunartea-Barrio, A. Maron-Loureiro, E. Molinelli-Fernandez, J. Oria-Escudero, L. Saavedra-Ynocente, C. Soriano-Gomez, D. Duque-Campayo, J. Gomez-Goni, and A. Souto-Iglesias. Scale effects in heave plates: PIV investigation. In *International Conference on Offshore Mechanics and Arctic Engineering*, 2020.

A. Bezunartea-Barrio, S. Fernandez-Ruano, A. Maron-Loureiro, E. Molinelli-Fernandez, F. Moreno-Buron, J. Oria-Escudero, J. Rios-Tubio, C. Soriano-Gomez, A. Valea-Peces, C. Lopez-Pavon, and A. Souto-Iglesias. Scale Effects on Heave Plates for Semi-Submersible Floating Offshore Wind Turbines: Case Study With a Solid Plain Plate. *Journal of Offshore Mechanics and Arctic Engineering*, 142(3), 6 2020. ISSN 0892-7219. doi: 10.1115/1.4045374.

D. D. Bhatta. Computations of hydrodynamic coefficients, displacement-amplitude ratios and forces for a floating cylinder due to wave diffraction and radiation. *International Journal of Non-Linear Mechanics*, 46(8):1027–1041, 10 2011. ISSN 0020-7462. doi: 10.1016/J.IJNONLINMEC.2011.04.022.

D. D. Bhatta and M. Rahman. On scattering and radiation problem for a cylinder in water of finite depth. *International Journal of Engineering Science*, 41(9):931–967, 5 2003. ISSN 0020-7225. doi: 10.1016/S0020-7225(02)00381-6.

S. Y. Boo. Measurements of higher harmonic wave forces on a vertical truncated circular cylinder. *Ocean Engineering*, 33(2):219–233, 2 2006. ISSN 0029-8018. doi: 10.1016/J.OCEANENG.2005.03.006.

B. Bouscasse. *Dynamic interactions between solids and viscous liquids with free surface*. PhD thesis, Universidad Politécnica de Madrid, 2015.

Bureau Veritas. HydroStar for experts user manual, version 8.10. Technical report, Bureau Veritas, 2020.

Bureau Veritas Rule Note (NI572). Rule Note NI-572: Classification and Certification of Floating Offshore Wind Turbines. Technical report, Bureau Veritas.

M. Canard, G. Ducrozet, and B. Bouscasse. Generation of 3-hr Long-Crested Waves of Extreme Sea States With HOS-NWT Solver. In *Volume 6B: Ocean Engineering*. American Society of Mechanical Engineers, 8 2020. ISBN 978-0-7918-8438-6. doi: 10.1115/OMAE2020-18930.

S. K. Chakrabarti. *Hydrodynamics of offshore structures*. WIT press, 1987.

X.-B. Chen. Middle-field formulation for the computation of wave-drift loads. *Journal of Engineering Mathematics*, 59(1):61–82, 7 2007. ISSN 0022-0833. doi: 10.1007/s10665-006-9074-x.

Y. Cheng, L. Fu, S. Dai, M. Collu, L. Cui, Z. Yuan, and A. Incecik. Experimental and numerical analysis of a hybrid WEC-breakwater system combining an oscillating water column and an oscillating buoy. *Renewable and Sustainable Energy Reviews*, 169:112909, 11 2022a. ISSN 13640321. doi: 10.1016/j.rser.2022.112909.

Y. Cheng, L. Fu, S. Dai, M. Collu, C. Ji, Z. Yuan, and A. Incecik. Experimental and numerical investigation of WEC-type floating breakwaters: A single-pontoon oscillating buoy and a dual-pontoon oscillating water column. *Coastal Engineering*, 177:104188, 10 2022b. ISSN 03783839. doi: 10.1016/j.coastaleng.2022.104188.

C. M. Chiang, M. Stiassnie, and D. K.-P. Yue. *Theory and Applications of Ocean Surface Waves*, volume 23. World Scientific, 7 2005. ISBN 978-981-238-893-3. doi: 10.1142/5566.

Y.-M. Choi, Y. J. Kim, B. Bouscasse, S. Seng, L. Gentaz, and P. Ferrant. Performance of different techniques of generation and absorption of free-surface waves in Computational Fluid Dynamics. *Ocean Engineering*, 214:107575, 10 2020. ISSN 00298018. doi: 10.1016/j.oceaneng.2020.107575.

T. Choisnet, B. Geschier, and G. Vetrano. Initial comparison of concrete and steel hulls in the case of Ideol's square ring floating substructure. In *the 15th World Wind Energy Conference and Exhibition*, Tokyo, 2016.

Choisnet Thomas. FLOATGEN deliverable 3.1: Report on the requirements of the floating structure. Technical report, 2013.

A. T. Chwang. A porous-wavemaker theory. *Journal of Fluid Mechanics*, 132:395–406, 7 1983. ISSN 0022-1120. doi: 10.1017/S0022112083001676.

A. Colagrossi, B. Bouscasse, and S. Marrone. Energy-decomposition analysis for viscous free-surface flows. *Physical Review E*, 92(5):053003, 11 2015. ISSN 1539-3755. doi: 10.1103/PhysRevE.92.053003.

P. Cong, Y. Liu, Y. Gou, and B. Teng. Theoretical modeling of hydrodynamic characteristics of a compound column-plate structure based on a novel derivation of mean drift force formulation. *Proceedings of the Institution of Mechanical Engineers, Part M: Journal of Engineering for the Maritime Environment*, 233(4):1022–1036, 11 2019. ISSN 1475-0902. doi: 10.1177/1475090218808019.

H. Cozijn, Ries Uittenbogaard, and Erik ter Brake. Heave, roll and pitch damping of a deepwater CALM buoy with a skirt. In *ISOPE International Ocean and Polar Engineering Conference*, 2005.

S. M. Damián and N. M. Nigro. An extended mixture model for the simultaneous treatment of small-scale and large-scale interfaces. *International Journal for Numerical Methods in Fluids*, 75(8):547–574, 7 2014. ISSN 0271-2091. doi: 10.1002/fld.3906.

L. Deike, M. Berhanu, and E. Falcon. Decay of capillary wave turbulence. *Physical Review E*, 85(6):066311, 6 2012. ISSN 1539-3755. doi: 10.1103/PhysRevE.85.066311.

T. Descamps. *Numerical analysis and development of accurate models in a CFD solver dedicated to naval applications with waves*. PhD thesis, Ecole Centrale de Nantes, 2023.

DNV-RP-C205. ENVIRONMENTAL CONDITIONS AND ENVIRONMENTAL LOADS. Technical report, 2010.

M. J. Downie, J. M. Graham, C. Hall, A. Incecik, and I. Nygaard. An experimental investigation of motion control devices for truss spars. *Marine Structures*, 13(2):75–90, 3 2000. ISSN 0951-8339. doi: 10.1016/S0951-8339(00)00010-1.

G. Ducrozet, F. Bonnefoy, D. Le Touzé, and P. Ferrant. A modified High-Order Spectral method for wavemaker modeling in a numerical wave tank. *European Journal of Mechanics - B/Fluids*, 34:19–34, 7 2012. ISSN 09977546. doi: 10.1016/j.euromechflu.2012.01.017.

G. Ducrozet, B. Bouscasse, M. Gouin, P. Ferrant, and F. Bonnefoy. CN-Stream: Open-source library for nonlinear regular waves using stream function theory. Technical report, 1 2019.

O. M. Faltinsen. *Sea loads on ships and offshore structures*. 1990.

O. M. Faltinsen, J. N. Newman, and T. Vinje. Nonlinear wave loads on a slender vertical cylinder. *Journal of Fluid Mechanics*, 289:179–198, 4 1995. ISSN 0022-1120. doi: 10.1017/S0022112095001297.

N. Fonseca, J. Pessoa, S. Mavrakos, and M. Le Boulluec. Experimental and numerical investigation of the slowly varying wave exciting drift forces on a restrained body in bi-chromatic waves. *Ocean Engineering*, 38(17-18):2000–2014, 12 2011. ISSN 00298018. doi: 10.1016/j.oceaneng.2011.09.017.

N. Fonseca, S. Nybø, J. M. Rodrigues, A. Gallego, and C. Garrido. Identification of Wave Drift Forces on a Floating Wind Turbine Sub-Structure With Heave Plates and Comparison With Predictions. In *Volume 8: Ocean Renewable Energy*. American Society of Mechanical Engineers, 6 2022. ISBN 978-0-7918-8593-2. doi: 10.1115/OMAE2022-81467.

T. I. Fossen. *Handbook of marine craft hydrodynamics and motion control*. John Wiley & Sons, 2011.

C. J. R. Garrett. Wave forces on a circular dock. *Journal of Fluid Mechanics*, 46(1):129–139, 3 1971. ISSN 0022-1120. doi: 10.1017/S0022112071000430.

C. Garrido-Mendoza, K. Thiagarajan, A. Souto-Iglesias, B. Bouscasse, and A. Colagrossi. Numerical investigation of the flow features around heave plates oscillating close to a free surface or seabed. In *International Conference on Offshore Mechanics and Arctic Engineering*, 2014.

C. A. Garrido-Mendoza, K. P. Thiagarajan, A. Souto-Iglesias, A. Colagrossi, and B. Bouscasse. Computation of flow features and hydrodynamic coefficients around heave plates oscillating near a seabed. *Journal of Fluids and Structures*, 59:406–431, 11 2015. ISSN 08899746. doi: 10.1016/j.jfluidstructs.2015.10.003.

Garrido-Mendoza Carlos A. *Hydrodynamic forces on heave plates for offshore systems oscillating close to the seabed or the free surface*. PhD thesis, Technical University of Madrid (UPM), 2015.

J. M. R. Graham. The forces on sharp-edged cylinders in oscillatory flow at low Keulegan–Carpenter numbers. *Journal of Fluid Mechanics*, 97(02):331, 3 1980. ISSN 0022-1120. doi: 10.1017/S0022112080002595.

M. Greenhow and S. Ahn. Added mass and damping of horizontal circular cylinder sections. *Ocean Engineering*, 15(5):495–504, 1 1988. ISSN 00298018. doi: 10.1016/0029-8018(88)90012-1.

S.-Y. Han, B. Bouscasse, J.-C. Gilloteaux, and D. Le Touzé. Validation study of a cfd numerical solver for the oscillatory flow features around heave plates. American Society of Mechanical Engineers, 6 2022. ISBN 978-0-7918-8593-2. doi: 10.1115/OMAE2022-81116.

S.-Y. Han, B. Bouscasse, V. Leroy, and D. Le Touzé. Linear diffraction and radiation theory of water waves by a truncated vertical circular cylinder with heave plate in deep and shallow drafts. *International Journal of Naval Architecture and Ocean Engineering*, page 100580, 1 2024. ISSN 20926782. doi: 10.1016/j.ijnaoe.2023.100580.

H. Haslum and O. Faltinsen. Alternative Shape of Spar Platforms for Use in Hostile Areas. In *All Days*. OTC, 5 1999. doi: 10.4043/10953-MS.

J. He, H. Wu, C.-J. Yang, R.-C. Zhu, W. Li, and F. Noblesse. Diffraction–radiation of regular water waves and irregular frequencies: A straightforward flow-modeling approach and analysis. *European Journal of Mechanics - B/Fluids*, 90:7–14, 11 2021. ISSN 09977546. doi: 10.1016/j.euromechflu.2021.07.011.

Y. Himeno. Prediction of Ship Roll Damping - A State of the Art. Technical report, 1981.

C. Hirt and B. Nichols. Volume of fluid (VOF) method for the dynamics of free boundaries. *Journal of Computational Physics*, 39(1):201–225, 1 1981. ISSN 00219991. doi: 10.1016/0021-9991(81)90145-5.

J. B. Huang and R. E. Taylor. Semi-analytical solution for second-order wave diffraction by a truncated circular cylinder in monochromatic waves. *Journal of Fluid Mechanics*, 319(-1):171, 7 1996. ISSN 0022-1120. doi: 10.1017/S0022112096007306.

A. Hulme. The wave forces acting on a floating hemisphere undergoing forced periodic oscillations. *Journal of Fluid Mechanics*, 121(-1):443, 8 1982. ISSN 0022-1120. doi: 10.1017/S0022112082001980.

ITTC. Estimation of Roll Damping. Technical report, 2021.

ITTC 27th OEC. Final Report and Recommendations to the 27th ITTC. Technical report, 2014.

J. Kim and I.-H. Cho. Wave power extraction by multiple wave energy converters arrayed in a water channel resonator. *International Journal of Naval Architecture and Ocean Engineering*, 13:178–186, 2021. ISSN 20926782. doi: 10.1016/j.ijnaoe.2021.02.004.

M.-H. Kim and D. K. P. Yue. The complete second-order diffraction solution for an axisymmetric body Part 1. Monochromatic incident waves. *Journal of Fluid Mechanics*, 200:235–264, 3 1989. ISSN 0022-1120. doi: 10.1017/S0022112089000649.

M.-H. Kim and D. K. P. Yue. The complete second-order diffraction solution for an axisymmetric body Part 2. Bichromatic incident waves and body motions. *Journal of Fluid Mechanics*, 211:557–593, 2 1990. ISSN 0022-1120. doi: 10.1017/S0022112090001690.

Y. J. Kim. *Numerical improvement and validation of a naval hydrodynamics CFD solver in view of performing fast and accurate simulation of complex ship-wave interaction*. PhD thesis, Ecole Centrale de Nantes, 2022.

H. J. Koh and I. H. Cho. Heave motion response of a circular cylinder with the dual damping plates. *Ocean Engineering*, 125:95–102, 10 2016. ISSN 0029-8018. doi: 10.1016/J.OCEANENG.2016.07.037.

T. Kristiansen and O. M. Faltinsen. Higher harmonic wave loads on a vertical cylinder in finite water depth. *Journal of Fluid Mechanics*, 833:773–805, 12 2017. ISSN 0022-1120. doi: 10.1017/jfm.2017.702.

V. Kurian, C. Ng, and M. Liew. Dynamic Responses of Truss Spar Due to Wave Actions. *Research Journal of Applied Sciences, Engineering and Technology*, 5(3):812–818, 1 2013. ISSN 20407459. doi: 10.19026/rjaset.5.5026.

R. Kurnia and G. Ducrozet. NEMOH: Open-source boundary element solver for computation of first- and second-order hydrodynamic loads in the frequency domain. *Computer Physics Communications*, 2023.

B. Le Méhauté. *An Introduction to Hydrodynamics and Water Waves*. Springer Berlin Heidelberg, Berlin, Heidelberg, 1976. ISBN 978-3-642-85569-6. doi: 10.1007/978-3-642-85567-2.

C.-H. Lee, J. N. Newman, and X. Zhu. AN EXTENDED BOUNDARY INTEGRAL EQUATION METHOD FOR THE REMOVAL OF IRRELEGULAR FREQUENCY EFFECTS. *International Journal for Numerical Methods in Fluids*, 23(7):637–660, 10 1996. ISSN 0271-2091. doi: 10.1002/(SICI)1097-0363(19961015)23:7<637::AID-FLD437>3.0.CO;2-3.

A.-j. Li and Y. Liu. New analytical solutions to water wave diffraction by vertical truncated cylinders. *International Journal of Naval Architecture and Ocean Engineering*, 11(2): 952–969, 7 2019. ISSN 20926782. doi: 10.1016/j.ijnaoe.2019.04.006.

H. Li and E. E. Bachynski-Polić. Analysis of difference-frequency wave loads and quadratic transfer functions on a restrained semi-submersible floating wind turbine. *Ocean Engineering*, 232:109165, 7 2021. ISSN 00298018. doi: 10.1016/j.oceaneng.2021.109165.

J. Li, S. Liu, M. Zhao, and B. Teng. Experimental investigation of the hydrodynamic characteristics of heave plates using forced oscillation. *Ocean Engineering*, 66:82–91, 7 2013. ISSN 0029-8018. doi: 10.1016/J.OCEANENG.2013.04.012.

C. Linton. Radiation and diffraction of water waves by a submerged sphere in finite depth. *Ocean Engineering*, 18(1-2):61–74, 1 1991. ISSN 00298018. doi: 10.1016/0029-8018(91)90034-N.

C. Linton and P. McIver. *Handbook of Mathematical Techniques for Wave/Structure Interactions*. Chapman and Hall/CRC, 2 2001a. ISBN 9780429123603. doi: 10.1201/9781420036060.

C. M. Linton and P. McIver. *Handbook of mathematical techniques for wave/structure interactions*. CRC Press, 2001b.

C. Lopez-Pavon and A. Souto-Iglesias. Hydrodynamic coefficients and pressure loads on heave plates for semi-submersible floating offshore wind turbines: A comparative analysis using large scale models. *Renewable Energy*, 81:864–881, 9 2015. ISSN 0960-1481. doi: 10.1016/J.RENENE.2015.04.003.

C. Lopez-Pavon, R. A. Watai, F. Ruggeri, A. N. Simos, and A. Souto-Iglesias. Influence of Wave Induced Second-Order Forces in Semisubmersible FOWT Mooring Design. *Journal of Offshore Mechanics and Arctic Engineering*, 137(3), 6 2015. ISSN 0892-7219. doi: 10.1115/1.4030241.

S. Malenica. Semi-Analytical Methods for Different Problems of Diffraction-Radiation by Vertical Circular Cylinders. *International Journal of Ocean System Engineering*, 2(2): 116–138, 5 2012. ISSN 2233-6478. doi: 10.5574/IJOSE.2012.2.2.116.

S. Malenica and X. Chen. On the Irregular Frequencies Appearing in Wave Diffraction-Radiation Solutions. In *International Journal of Offshore and Polar Engineering*, 1998.

S. Malenica and B. Molin. Third-harmonic wave diffraction by a vertical cylinder. *Journal of Fluid Mechanics*, 302:203–229, 11 1995. ISSN 0022-1120. doi: 10.1017/S0022112095004071.

H. Maruo. The drift of a body floating on waves. *Journal of Ship Research*, 4(3):1–11, 1960.

S. A. Mavrakos and Grigoropoulos. Numerical and experimental investigation of the exciting wave loads on a vertical truncated cylinder. *WIT Transactions on Ecology and the Environment*, 1994.

R. C. McCamy and R. A. Fuchs. Wave forces on piles: a diffraction theory. *Tech. Memo No. 69, Beach Erosion Board, U.S. Army Corps of Engineers*, 1954.

P. McIver and D. V. Evans. The occurrence of negative added mass in free-surface problems involving submerged oscillating bodies. *Journal of Engineering Mathematics*, 18(1):7–22, 3 1984. ISSN 0022-0833. doi: 10.1007/BF00042895.

B. Molin. *Offshore Structure Hydrodynamics*. Cambridge University Press, 1 2023. ISBN 9781009198059. doi: 10.1017/9781009198059.

B. Molin, F. Remy, and T. Rippol. Experimental study of the heave added mass and damping of solid and perforated disks close to the free surface. In *International Maritime Association of the Mediterranean*, 2007.

C. Monroy, S. Seng, and S. Malenica. Développements et validation de l'outil CFD OpenFOAM pour le calcul de tenue à la mer. In *Conference: 15èmes journées de l'hydrodynamique*, 2016.

M. Moreau, T. Kristiansen, B. Ommani, and B. Molin. An upright bottomless vertical cylinder with baffles floating in waves. *Applied Ocean Research*, 119:102934, 2 2022. ISSN 0141-1187. doi: 10.1016/J.APOR.2021.102934.

J. N. Newman. The Drift Force and Moment on Ships in Waves. *Journal of Ship Research*, 11 (01):51–60, 3 1967. ISSN 0022-4502. doi: 10.5957/jsr.1967.11.1.51.

A. Pegalajar-Jurado, H. Bredmose, M. Borg, J. G. Straume, T. Landbø, H. S. Andersen, W. Yu, K. Müller, and F. Lemmer. State-of-the-art model for the LIFES50+ OO-Star Wind Floater Semi 10MW floating wind turbine. *Journal of Physics: Conference Series*, 1104:012024, 10 2018. ISSN 1742-6588. doi: 10.1088/1742-6596/1104/1/012024.

R. Pinguet, M. Benoit, B. Molin, and F. Rezende. CFD analysis of added mass, damping and induced flow of isolated and cylinder-mounted heave plates at various submergence depths using an overset mesh method. *Journal of Fluids and Structures*, 109:103442, 2 2022. ISSN 08899746. doi: 10.1016/j.jfluidstructs.2021.103442.

J. Pinkster and G. Van Oortmerssen. Computation of the first and second order wave forces on oscillating bodies in regular waves. In *the 2nd International Conference on Numerical Ship Hydrodynamics*, 1978.

A. Robertson and L. Wang. OC6 Phase Ib: Floating Wind Component Experiment for Difference-Frequency Hydrodynamic Load Validation. *Energies*, 14(19):6417, 10 2021. ISSN 1996-1073. doi: 10.3390/en14196417.

A. Robertson, J. Jonkman, M. Masciola, H. Song, A. Goupee, A. Coulling, and C. Luan. Definition of the semisubmersible floating system for phase II of OC4. Technical report, National Renewable Energy Lab.(NREL), Golden, CO (United States), 2014.

A. N. Robertson, F. Wendt, J. M. Jonkman, W. Popko, H. Dagher, S. Gueydon, J. Qvist, F. Vittori, J. Azcona, E. Uzunoglu, C. G. Soares, R. Harries, A. Yde, C. Galinos, K. Hermans, J. B. de Vaal, P. Bozonnet, L. Bouy, I. Bayati, R. Bergua, J. Galvan, I. Mendikoa, C. B. Sanchez, H. Shin, S. Oh, C. Molins, and Y. Debruyne. OC5 Project Phase II: Validation of Global Loads of the DeepCwind Floating Semisubmersible Wind Turbine. *Energy Procedia*, 137:38–57, 10 2017. ISSN 18766102. doi: 10.1016/j.egypro.2017.10.333.

A. N. Robertson, S. Gueydon, E. Bachynski, L. Wang, J. Jonkman, D. Alarcón, E. Amet, A. Beardsell, P. Bonnet, B. Boudet, C. Brun, Z. Chen, M. Féron, D. Forbush, C. Galinos, J. Galvan, P. Gilbert, J. Gómez, V. Harnois, F. Haudin, Z. Hu, J. L. Dreff, M. Leimeister, F. Lemmer, H. Li, G. Mckinnon, I. Mendikoa, A. Moghtadaei, S. Netzband, S. Oh, A. Pegalajar-Jurado, M. Q. Nguyen, K. Ruehl, P. Schünemann, W. Shi, H. Shin, Y. Si, F. Surmont, P. Trubat, J. Qwist, and S. Wohlfahrt-Laymann. OC6 Phase I: Investigating

the underprediction of low-frequency hydrodynamic loads and responses of a floating wind turbine. *Journal of Physics: Conference Series*, 1618(3):032033, 9 2020. ISSN 1742-6588. doi: 10.1088/1742-6596/1618/3/032033.

D. Roddier, C. Cermelli, A. Aubault, and A. Weinstein. WindFloat: A floating foundation for offshore wind turbines. *Journal of Renewable and Sustainable Energy*, 2(3):033104, 5 2010. ISSN 1941-7012. doi: 10.1063/1.3435339.

H. Rusche. *Computational fluid dynamics of dispersed two-phase flows at high phase fractions*. PhD thesis, Imperial College London (University of London), 2003.

T. S. Sarpkaya. *Wave Forces on Offshore Structures*. Cambridge University Press, 2 2010. ISBN 9780521896252. doi: 10.1017/CBO9781139195898.

W. Sheng, E. Tapoglou, X. Ma, C. Taylor, R. Dorrell, D. Parsons, and G. Aggidis. Hydrodynamic studies of floating structures: Comparison of wave-structure interaction modelling. *Ocean Engineering*, 249:110878, 4 2022. ISSN 00298018. doi: 10.1016/j.oceaneng.2022.110878.

A. N. Simos, F. Ruggeri, R. A. Watai, A. Souto-Iglesias, and C. Lopez-Pavon. Slow-drift of a floating wind turbine: An assessment of frequency-domain methods based on model tests. *Renewable Energy*, 116:133–154, 2 2018. ISSN 09601481. doi: 10.1016/j.renene.2017.09.059.

T. Stehly and P. Duffy. 2020 Cost of Wind Energy Review. Technical report, National Renewable Energy Laboratory (NREL), Golden, CO (United States), 12 2021.

S. Sudhakar and S. Nallayarasu. Influence of Heave Plate on Hydrodynamic Response of Spar. In *Volume 1: Offshore Technology; Polar and Arctic Sciences and Technology*, pages 437–447. ASMEDC, 1 2011. ISBN 978-0-7918-4433-5. doi: 10.1115/OMAE2011-49565.

H. Sung, Y. S. Kim, B. W. Nam, and S. Y. Hong. Experimental investigation of wave loads on a truncated vertical circular cylinder. In *The Korean Society of Ocean Engineering Conference*, 2007.

L. Tao and D. Dray. Hydrodynamic performance of solid and porous heave plates. *Ocean Engineering*, 35(10):1006–1014, 7 2008. ISSN 0029-8018. doi: 10.1016/J.OCEANENG.2008.03.003.

L. Tao and K. Thiagarajan. Low KC flow regimes of oscillating sharp edges. II. Hydrodynamic forces. *Applied Ocean Research*, 25(2):53–62, 4 2003a. ISSN 01411187. doi: 10.1016/S0141-1187(03)00046-4.

L. Tao and K. Thiagarajan. Low KC flow regimes of oscillating sharp edges I. Vortex shedding observation. *Applied Ocean Research*, 25(1):21–35, 2 2003b. ISSN 0141-1187. doi: 10.1016/S0141-1187(03)00031-2.

L. Tao, B. Molin, Y. M. Scolan, and K. Thiagarajan. Spacing effects on hydrodynamics of heave plates on offshore structures. *Journal of Fluids and Structures*, 23(8):1119–1136, 11 2007. ISSN 0889-9746. doi: 10.1016/J.JFLUIDSTRUCTS.2007.03.004.

B. Teng and S. Kato. Third order wave force on axisymmetric bodies. *Ocean Engineering*, 29 (7):815–843, 6 2002. ISSN 00298018. doi: 10.1016/S0029-8018(01)00047-6.

K. Thiagarajan and J. Moreno. Wave Induced Effects on the Hydrodynamic Coefficients of an Oscillating Heave Plate in Offshore Wind Turbines. *Journal of Marine Science and Engineering*, 8(8):622, 8 2020. ISSN 2077-1312. doi: 10.3390/jmse8080622.

K. P. Thiagarajan and A. W. Troesch. Hydrodynamic heave damping estimation and scaling for tension leg platforms. *Journal of Offshore Mechanics and Arctic Engineering*, 1994.

K. P. Thiagarajan and A. W. Troesch. Effects of Appendages and Small Currents on the Hydrodynamic Heave Damping of TLP Columns. *Journal of Offshore Mechanics and Arctic Engineering*, 120(1):37–42, 2 1998. ISSN 0892-7219. doi: 10.1115/1.2829518.

K. P. Thiagarajan, I. Datta, A. Z. Ran, L. Tao, and J. E. Halkyard. Influence of Heave Plate Geometry on the Heave Response of Classic Spars. In *21st International Conference on Offshore Mechanics and Arctic Engineering, Volume 1*, pages 621–627. ASMEDC, 1 2002. ISBN 0-7918-3611-8. doi: 10.1115/OMAE2002-28350.

X. Tian, L. Tao, X. Li, and J. Yang. Hydrodynamic coefficients of oscillating flat plates at $0.15 \leq KC \leq 3.15$. *Journal of Marine Science and Technology*, 22(1):101–113, 3 2017. ISSN 0948-4280. doi: 10.1007/s00773-016-0401-2.

H. Wadhwa and K. Thiagarajan. Experimental assessment of hydrodynamic coefficients of disks oscillating near a free surface. In *International Conference on Offshore Mechanics and Arctic Engineering*, 2009.

H. Wadhwa, B. Krishnamoorthy, and K. Thiagarajan. Variation of heave added mass and damping near seabed. In *International Conference on Offshore Mechanics and Arctic Engineering*, 2010.

R. W. Yeung. Added mass and damping of a vertical cylinder in finite-depth waters. *Applied Ocean Research*, 3(3):119–133, 7 1981. ISSN 0141-1187. doi: 10.1016/0141-1187(81)90101-2.

L. Zhang, W. Shi, Y. Zeng, C. Michailides, S. Zheng, and Y. Li. Experimental investigation on the hydrodynamic effects of heave plates used in floating offshore wind turbines. *Ocean Engineering*, 267:113103, 1 2023. ISSN 00298018. doi: 10.1016/j.oceaneng.2022.113103.

S. Zhang and T. Ishihara. Numerical study of hydrodynamic coefficients of multiple heave plates by large eddy simulations with volume of fluid method. *Ocean Engineering*, 163: 583–598, 9 2018. ISSN 00298018. doi: 10.1016/j.oceaneng.2018.03.060.

L. Zhu and H.-C. Lim. Hydrodynamic characteristics of a separated heave plate mounted at a vertical circular cylinder. *Ocean Engineering*, 131:213–223, 2 2017. ISSN 00298018. doi: 10.1016/j.oceaneng.2017.01.007.

APPENDIX A

LIST OF RESEARCH ACTIVITIES

A.1 Journal papers

S.-Y. Han, B. Bouscasse, V. Leroy, and D. Le Touzé, Linear diffraction and radiation theory of water waves by a truncated vertical circular cylinder with heave plate in deep and shallow draft, International Journal of Naval Architecture and Ocean Engineering, 2024.

S.-Y. Han, B. Bouscasse, V. Leroy, S. Delacroix, F. Bonnefoy, E. Bachynski-Polić, and D. Le Touzé, Experimental study of wave diffraction loads on a vertical circular cylinder with heave plate at deep and shallow drafts, Ocean Engineering (under review).

S.-Y. Han, B. Bouscasse, V. Leroy, S. Delacroix, F. Bonnefoy, J.-C. Gilloteaux, and D. Le Touzé, Experimental study of hydrodynamic loads induced by the motion of a vertical circular cylinder with heave plates in proximity of the free surface, Ocean Engineering (under review).

A.2 Conferences

S.-Y. Han, B. Bouscasse, J.-C. Gilloteaux, and D. Le Touzé, Hydrodynamic analysis and numerical modelling of heave-plates dedicated to the design of floating WT, Wind Energy Science Conference, 2021. (presentation)

S.-Y. Han, B. Bouscasse, J.-C. Gilloteaux, and D. Le Touzé, Validation study of a CFD numerical solver for the oscillatory flow features around heave plates, International Conference on Offshore Mechanics and Arctic Engineering (OMAE), 2022. (conference proceeding)

S.-Y. Han, S. Delacroix, B. Bouscasse, V. Leroy, F. Bonnefoy, and D. Le Touzé, Experimental and numerical study on wave diffraction by a circular cylinder with a heave plate, EERA DeepWind conference, 2023. (poster)

S.-Y. Han, S. Delacroix, D. Lestari, B. Bouscasse, V. Leroy, F. Bonnefoy, J.-C. Gilloteaux, and D. Le Touzé, Study of hydrodynamic loads on a truncated circular cylinder

with a heave plate in irregular seas, International Conference on Computational Methods in Marine Engineering (MARINE), 2023. (presentation)

S.-Y. Han, B. Bouscasse, V. Leroy, S. Delacroix, F. Bonnefoy, and D. Le Touzé, Experimental investigation of the radiation loads of a heave plate with tilt angle, International Conference on Offshore Mechanics and Arctic Engineering (OMAE), 2024. (conference proceeding)

A.3 Secondments

1st secondment

Subject: Study on hydrodynamic loads on heave plates for barge-like platforms
Host institution: BW-Ideol (industry)
Supervisor: Riccardo Mariani
Duration: 2022.07.11 - 2022.09.09.
Location: La Ciotat, France

2nd secondment

Subject: Study on wave diffraction loads on heave plates
Host institution: Norwegian University of Science and Technology, NTNU (academia)
Supervisor: Erin E. Bachynski-Polić
Duration: 2023.07.31 - 2023.08.25.
Location: Trondheim, Norway

A.4 List of trainings

Table A.4.1 – List of trainings.

No	Courses	Organizations	Date	Note
1	Engineering with enough redundancy; avoided engineering, focus on HSE topics, certifaction	Univ. Rostock and Univ. Stuttgart	08.12.2020 - 10.12.2020 (online)	FLOAWER 1st Training
2	Aeroelastic, stability analyses and design of wind turbines	Politecnico di Milano	29.06.21 - 02.07.2021 (online)	FLOAWER 2nd Training
3	Experimental techniques at lab scale & sea test site management (+GWO: Sea survival & Boat transfer by Centre d'etude et de partique de la survie)	Ecole Centrale Nantes	12.09.2021 - 17.09.2021 (Nantes)	FLOAWER 3rd Training
4	Effective research dissemination, safety management, communication skills	Univ. of Oldenburg	07.03.2022 - 11.03.2022 (Oldenburg)	FLOAWER 4th Training
5	Environment, Licensing, Marine Spatial Planning and Economics of Floating Offshore Wind	WavEC	19.09.2023 - 23.09.2023 (Lisbon)	FLOAWER 5th Training
6	Responsible Research and Innovation (RRI), Scientific Ethics, Career Development Planning, Communication Skills	NTNU	20.01.2023 - 24.01.2023 (Trondheim)	FLOAWER 6th Training
7	Cours de français débutant	Association Chercheurs étrangers à Nantes	29.09.2021 - 24.11.2021	FLE Maison de chercheurs
8	Water Waves and Sea States Modelling	Ecole Centrale Nantes	2021 - 2022	
9	Introduction à l'éthique de la recherche et à l'intégrité scientifique	Ecole doctorale (ED SIS)	2022	
10	Séminaire de présentations par les doctorant. e.s SIS de 2ème année	Ecole doctorale (ED SIS)	2023	
11	Réunion de rentrée 1ère année	Ecole doctorale (ED SIS)	2022	
12	Une action de médiation scientifique à destination d'élèves de lycée	le Cercle FSER	2022	Declics

APPENDIX B

ANALYTICAL METHODS

B.1 Matrix for determining unknown coefficients

The matrices $\mathbb{L}$ and $\mathbb{R}$ from the linear system of equations (3.34) consist of submatrices as,

$$\mathbb{L} = \begin{bmatrix} \mathbb{L}^{11} & \mathbb{L}^{12} & \mathbb{L}^{13} & \mathbb{L}^{14} \\ \mathbb{L}^{21} & \mathbb{L}^{22} & 0 & 0 \\ \mathbb{L}^{31} & 0 & \mathbb{L}^{33} & \mathbb{L}^{34} \\ 0 & 0 & \mathbb{L}^{43} & \mathbb{L}^{44} \end{bmatrix}, \qquad \mathbb{R} = \begin{bmatrix} \mathbb{R}^{1} \\ \mathbb{R}^{2} \\ \mathbb{R}^{3} \\ \mathbb{R}^{4} \end{bmatrix} \tag{B.1}$$

where the first row is established from the normal velocity continuity on $r = R_d$ and $-h \leq z \leq 0$ in Equation (3.30),

$$\mathbb{L}^{11}_{i,i} = U^{'}_{mi}(R_d) \int_{-h}^{0} f_i^2(z) dz \tag{B.2}$$

where $i = 0 \sim N_1$.

$$\mathbb{L}^{12}_{i,j} = -V^{'}_{mj}(R_d) \int_{-h}^{-d} Z_j(z) f_i(z) dz \tag{B.3}$$

where $i = 0 \sim N_1$, and $j = 0 \sim N_2$.

$$\mathbb{L}^{13}_{i,j} = -X^{'}_{mj}(R_d) \int_{-d_c}^{0} F_j(z) f_i(z) dz \tag{B.4}$$

where $i = 0 \sim N_1$, and $j = 0 \sim N_3$.

$$\mathbb{L}^{14}_{i,j} = -W^{'}_{mj}(R_d) \int_{-d_c}^{0} F_j(z) f_i(z) dz \tag{B.5}$$

where $i = 0 \sim N_1$, and $j = 0 \sim N_3$.

The second row comes from the pressure continuity on $r = R_d$ and $-h \leq z \leq -d$ in Equation (3.31),

$$\mathbb{L}^{21}_{i,j} = U_{mj}(R_d) \int_{-h}^{-d} f_j(z) Z_i(z) dz \tag{B.6}$$

where $i = 0 \sim N_2$, and $j = 0 \sim N_1$.

$$\mathbb{L}_{i,i}^{22} = -V_{mi}(R_d) \int_{-h}^{-d} Z_i^2(z) dz \tag{B.7}$$

where $i = 0 \sim N_2$.

The third row comes from the pressure continuity on $r = R_d$ and $-d_c \leq z \leq 0$ in Equation (3.32),

$$\mathbb{L}_{i,j}^{31} = U_{mj}(R_d) \int_{-d_c}^{0} f_j(z) F_i(z) dz \tag{B.8}$$

where $i = 0 \sim N_3$, and $j = 0 \sim N_1$.

$$\mathbb{L}_{i,i}^{33} = -X_{mi}(R_d) \int_{-d_c}^{0} F_i^2(z) dz \tag{B.9}$$

where $i = 0 \sim N_3$.

$$\mathbb{L}_{i,i}^{34} = -W_{mi}(R_d) \int_{-d_c}^{0} F_i^2(z) dz \tag{B.10}$$

where $i = 0 \sim N_3$.

Lastly, the no-penetration condition on the cylinder surface $r = R_c$ and $-d_c \leq z \leq 0$ in Equation (3.33) gives the fourth row as,

$$\mathbb{L}_{i,i}^{43} = X_{mi}^{'}(R_c) \int_{-d_c}^{0} F_i^2(z) dz \tag{B.11}$$

where $i = 0 \sim N_3$.

$$\mathbb{L}_{i,i}^{44} = W_{mi}^{'}(R_c) \int_{-d_c}^{0} F_i^2(z) dz \tag{B.12}$$

where $i = 0 \sim N_3$.

On the other hand, the matrix $\mathbb{R}$ in diffraction problems is established based on the contribution of the incident wave potential as,

$$\mathbb{R}_i^1 = -J_m^{'}(k_0 R_d) \int_{-h}^{0} f_0(z) f_i(z) dz \tag{B.13}$$

where $i = 0 \sim N_1$.

$$\mathbb{R}_i^2 = -J_m(k_0 R_d) \int_{-h}^{-d} f_0(z) Z_i(z) dz \tag{B.14}$$

where $i = 0 \sim N_2$.

$$\mathbb{R}_i^3 = -J_m(k_0 R_d) \int_{-d_c}^{0} f_0(z) F_i(z) dz \tag{B.15}$$

where $i = 0 \sim N_3$.

$$\mathbb{R}_i^4 = 0_{(N_3+1)\times 1} \tag{B.16}$$

In radiation problems, the matrix $\mathbb{R}$ is determined by the particular solutions and forcing terms on the body boundary condition as,

$$\mathbb{R}_i^1 = \frac{1}{\varepsilon_m} \int_{-d}^{-d_c} Q_p^I f_i(z) dz \tag{B.17}$$

where $i = 0 \sim N_1$.

$$\mathbb{R}_i^2 = \frac{1}{\varepsilon_m} \int_{-h}^{-d} \psi_p^{II} Z_i(z) dz \tag{B.18}$$

where $i = 0 \sim N_2$.

$$\mathbb{R}_i^3 = \frac{1}{\varepsilon_m} \int_{-d_c}^{-0} \psi_p^{III} F_i(z) dz \tag{B.19}$$

where $i = 0 \sim N_3$.

$$\mathbb{R}_i^4 = \frac{1}{\varepsilon_m} \int_{-d_c}^{0} Q_p^{III} F_i(z) dz \tag{B.20}$$

where $i = 0 \sim N_3$. Here, $p = 1$, 3, and 5 are for surge, heave, and pitch, respectively.

B.2 Analytical expression of the hydrodynamic loads

By inserting the diffraction potentials in Equations (3.10), (3.11), (3.14), and (3.16) into Equation (3.35), the analytical expressions of the wave excitation forces and moments are obtained as below.

Linear horizontal wave force:

$$\begin{aligned} F_x = -2\pi i \rho g A \Bigg[R_d \Bigg\{ J_1(k_0 R_d) \int_{-d}^{-d_c} f_0(z) dz + \sum_{n=0}^{N_1} A_{1n} U_{1n}(R_d) \int_{-d}^{-d_c} f_n(z) dz \Bigg\} \\ + R_c \sum_{n=0}^{N_3} (C_{1n} + D_{1n}) \int_{-d_c}^{0} F_n(z) dz \Bigg] \end{aligned} \tag{B.21}$$

where the integrations of the vertical functions are given by,

$$\int_{-d}^{-d_c} f_n(z)dz = \begin{cases} \frac{1}{k_0 \cosh k_0 h}\Big(\sinh k_0(h-d_c) - \sinh k_0(h-d)\Big), & n=0 \\ \frac{1}{k_n \cos k_n h}\Big(\sin k_n(h-d_c) - \sin k_n(h-d)\Big), & n \geq 1 \end{cases} \tag{B.22}$$

$$\int_{-d_c}^{0} F_n(z)dz = \begin{cases} \frac{1}{\beta_0}\tanh \beta_0 d_c, & n=0 \\ \frac{1}{\beta_n}\tan \beta_n d_c, & n \geq 1 \end{cases} \tag{B.23}$$

Linear vertical wave force:

$$\begin{aligned} F_z = 2\pi\rho g A \Bigg[& \sum_{n=0}^{N_2} B_{0n} Z_n(-d) \int_0^{R_d} r V_{0n}(r)dr \\ & - \sum_{n=0}^{N_3} F_n(-d_c)\Big\{ C_{0n}\int_{R_c}^{R_d} r X_{0n}(r)dr + D_{0n}\int_{R_c}^{R_d} r W_{0n}(r)dr \Big\} \Bigg] \end{aligned} \tag{B.24}$$

where the integrations of the radial functions are evaluated as,

$$\int_0^{R_d} r V_{0n}(r)dr = \begin{cases} \frac{1}{2}R_d^2, & n=0 \\ \frac{1}{\alpha_n} R_d I_1(\alpha_n R_d), & n \geq 1 \end{cases} \tag{B.25}$$

$$\int_{R_c}^{R_d} r X_{0n}(r)dr = \begin{cases} \frac{1}{\beta_0}\Big(R_d J_1(\beta_0 R_d) - R_c J_1(\beta_0 R_c)\Big), & n=0 \\ \frac{1}{\beta_n}\Big(R_d I_1(\beta_n R_d) - R_c I_1(\beta_n R_c)\Big), & n \geq 1 \end{cases} \tag{B.26}$$

$$\int_{R_c}^{R_d} r W_{0n}(r)dr = \begin{cases} \frac{1}{\beta_0}\Big(R_d Y_1(\beta_0 R_d) - R_c Y_1(\beta_0 R_c)\Big), & n=0 \\ \frac{1}{\beta_n}\Big(-R_d K_1(\beta_n R_d) + R_c K_1(\beta_n R_c)\Big), & n \geq 1 \end{cases} \tag{B.27}$$

Linear wave moment:

$$\begin{aligned} M_y = -2\pi i\rho gA \Bigg[& R_d \Bigg\{ J_1(k_0 R_d) \int_{-d}^{-d_c} z f_0(z) dz + \sum_{n=0}^{N_1} A_{1n} U_{1n}(R_d) \int_{-d}^{-d_c} z f_n(z) dz \Bigg\} \\ & + R_c \sum_{n=0}^{N_3} (C_{1n} + D_{1n}) \int_{-d_c}^{0} z F_n(z) dz \\ & + \sum_{n=0}^{N_2} B_{1n} Z_n(-d) \int_0^{R_d} r^2 V_{1n}(r) dr \\ & - \sum_{n=0}^{N_3} F_n(-d_c) \Bigg\{ C_{1n} \int_{R_c}^{R_d} r^2 X_{1n}(r) dr + D_{1n} \int_{R_c}^{R_d} r^2 W_{1n}(r) dr \Bigg\} \Bigg] \end{aligned} \tag{B.28}$$

where the integrations of radial and vertical functions are provided as follows,

$$\int_0^{R_d} r^2 V_{1n}(r) dr = \begin{cases} \frac{1}{4} R_d^3, & n = 0 \\ \frac{1}{\alpha_n} R_d^2 I_2(\alpha_n R_d), & n \geq 1 \end{cases} \tag{B.29}$$

$$\int_{R_c}^{R_d} r^2 X_{1n}(r) dr = \begin{cases} \frac{1}{\beta_0} \Big(R_d^2 J_2(\beta_0 R_d) - R_c^2 J_2(\beta_0 R_c) \Big), & n = 0 \\ \frac{1}{\beta_n} \Big(R_d^2 I_2(\beta_n R_d) - R_c^2 I_2(\beta_n R_c) \Big), & n \geq 1 \end{cases} \tag{B.30}$$

$$\int_{R_c}^{R_d} r^2 W_{1n}(r) dr = \begin{cases} \frac{1}{\beta_0} \Big(R_d^2 Y_2(\beta_0 R_d) - R_c^2 Y_2(\beta_0 R_c) \Big), & n = 0 \\ \frac{1}{\beta_n} \Big(-R_d^2 K_2(\beta_n R_d) + R_c^2 K_2(\beta_n R_c) \Big), & n \geq 1 \end{cases} \tag{B.31}$$

$$\begin{aligned} & \int_{-d}^{-d_c} z f_n(z) dz \\ & = \begin{cases} \dfrac{1}{k_0^2 \cosh k_0 h} \Big(-k_0 d_c \sinh k_0(h - d_c) - \cosh k_0(h - d_c) \\ \qquad + k_0 d \sinh k_0(h - d) + \cosh k_0(h - d) \Big), & n = 0 \\ \dfrac{1}{k_n^2 \cos k_n h} \Big(-k_n d_c \sin k_n(h - d_c) + \cos k_n(h - d_c) \\ \qquad + k_n d \sin k_n(h - d) - \cos k_n(h - d) \Big), & n \geq 1 \end{cases} \end{aligned} \tag{B.32}$$

$$\int_{-d_c}^{0} zF_n(z)dz = \begin{cases} \frac{-1}{\beta_0^2 \cosh \beta_0 d_c}(\cosh \beta_0 d_c - 1), & n = 0 \\ \frac{1}{\beta_n^2 \cos \beta_n d_c}(\cos \beta_n d_c - 1), & n \geq 1 \end{cases} \tag{B.33}$$

In the radiation problem, substituting the unit amplitude velocity potential (Equations (3.23), (3.25), and (3.28)) into Equation (3.37), gives the analytical expression for surge, heave, and pitch motions as,

$$\iint_{S_B} \phi_1 \cos\theta n_1 dS = -2\pi \left\{ R_d \sum_{n=0}^{N_1} A_{1n} U_{1n}(R_d) \int_{-d}^{-d_c} f_n(z)dz + R_c \sum_{n=0}^{N_3} (C_{1n} + D_{1n}) \int_{-d_c}^{0} F_n(z)dz \right\} \tag{B.34}$$

$$\begin{aligned} \iint_{S_B} \phi_3 n_3 dS =& 2\pi \left[\sum_{n=0}^{N_2} B_{0n} \cos(n\pi) \int_0^{R_d} rV_{0n}(r)dr - \frac{1}{4(h-d)} \left(\frac{R_d^4}{4} - (h-d)^2 R_d^2 \right) \right. \\ & - \sum_{n=0}^{N_3} F_n(-d_c) \left\{ C_{0n} \int_{R_c}^{R_d} rX_{0n}(r)dr + D_{0n} \int_{R_c}^{R_d} rW_{0n}(r)dr \right\} \\ & \left. + \frac{1}{2} \left(d_c - \frac{g}{\omega^2} \right) \left(R_d^2 - R_c^2 \right) \right] \end{aligned} \tag{B.35}$$

$$\begin{aligned} \iint_{S_B} \phi_5 \cos\theta n_5 dS = -2\pi \Bigg[& R_d \sum_{n=0}^{N_1} A_{1n} U_{1n}(R_d) \int_{-d}^{-d_c} zf_n(z)dz \\ & + \sum_{n=0}^{N_2} B_{1n} \cos(n\pi) \int_0^{R_d} r^2 V_{1n}(r)dr \\ & + R_c \sum_{n=0}^{N_3} (C_{1n} + D_{1n}) \int_{-d_c}^{0} zF_n(z)dz \\ & - \sum_{n=0}^{N_3} F_n(-d_c) \left\{ C_{1n} \int_{R_c}^{R_d} r^2 X_{1n}(r)dr + D_{1n} \int_{R_c}^{R_d} r^2 W_{1n}(r)dr \right\} \\ & + \frac{1}{16(h-d)} \left(\frac{R_d^6}{6} - R_d^4 (h-d)^2 \right) \\ & - \frac{1}{8} \left(d_c - \frac{g}{\omega^2} \right) \left(R_d^4 - R_c^4 \right) \\ & - \frac{R_c^2}{2} \left(\frac{d_c^3}{3} - \frac{1}{2} \frac{g}{\omega^2} d_c^2 \right) \Bigg] \end{aligned} \tag{B.36}$$

APPENDIX C

DRAWINGS FOR HEAVE PLATES

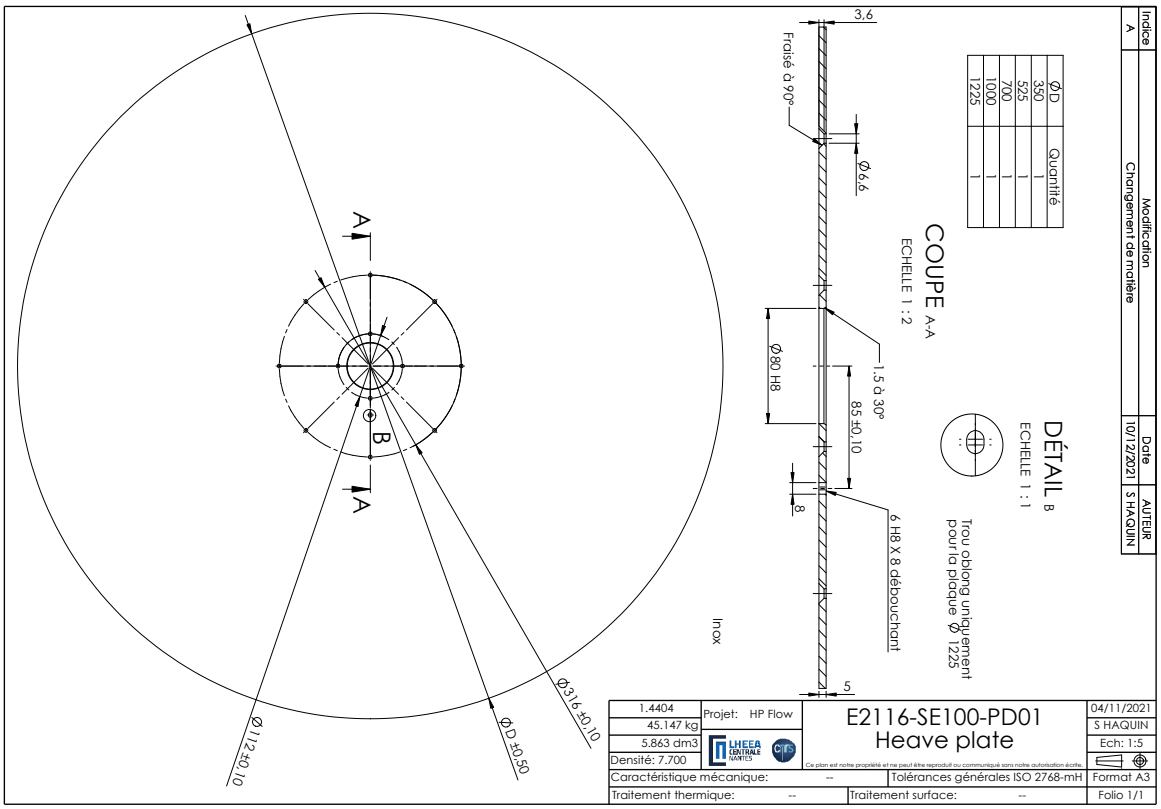

Figure C.0.1 – Drawing of a heave plate.

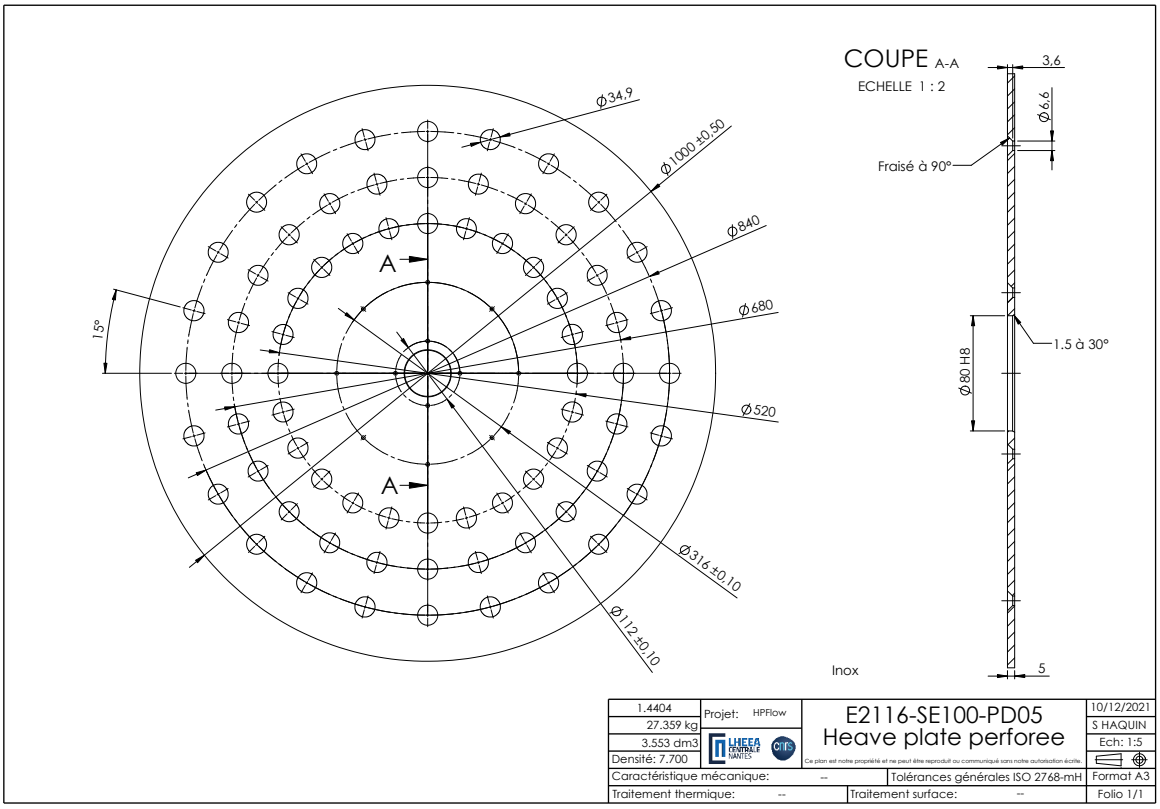

Figure C.0.2 – Drawing of the perforated plate with diameter 1.0 m.

COLLEGE SCIENCES
DOCTORAL DE L'INGENIERIE
PAYS DE LA LOIRE ET DES SYSTEMES

CENTRALE NANTES

Titre : Analyse hydrodynamique et modélisation numérique des plaques anti-pilonnement pour l'éolien flottant

Mot clés : Éolienne flottante ; Plaques anti-pilonnement ; Expériences, CFD ; Potential flow theory

Résumé : Cette thèse vise à étudier les chargements hydrodynamiques exercés sur les plaques anti-pilonnement en se concentrant sur le cas des éoliennes flottantes qui ont un tirant d'eau plus faible et des mouvements plus importants que les plateformes offshore conventionnelles. Pour atteindre cet objectif, plusieurs campagnes expérimentales sont menées sur un cylindre circulaire tronqué équipé d'une plaque anti-pilonnement dans le bassin océanique de l'Ecole Centrale de Nantes. L'étude examine les chargements hydrodynamiques induits par des vagues monochromatiques et bichromatiques, ainsi que par les mouvements de cavalement, de pilonnement et de tangage. Différents diamètres de plaques sont étudiés pour différents tirants d'eau. Une plaque avec porosité est également testée. De plus, une méthode analytique basée sur la théorie linéaire des écoulements potentiels est développée pour résoudre les problèmes de diffraction et de radiation. Le domaine de validation est discuté en comparant avec les résultats expérimentaux et ceux de solveurs développés sur la base de la méthode des éléments frontières (Boundary Element Method, BEM). Enfin, des simulations haute fidelité qui résolvent les équations de Navier Stokes (CFD) sont réalisées. Il a été montré qu'un modèle de turbulence doit être implémenté grâce à des comparaisons avec des champs de vitesse expérimentaux. Les résultats montrent notamment la présence d'une forte séparation des écoulements autour du bord de la plaque lors des essais en présence de vagues incidentes ou avec des oscillations verticales de pilonnement. Un modèle Morison simplifié est suggéré pour modéliser la séparation des écoulements pour les chargements liés à la diffraction.

Title: Hydrodynamic analysis and numerical modelling of heave plates for floating wind turbines

Keywords: Floating wind turbine; Heave plates; Experiments; CFD; Potential flow theory

Abstract: This thesis aims to investigate hydrodynamic loads exerted on heave plates with a focus on the design characteristics of floating wind turbines with a lower submerged depth and a significant motion response compared to conventional offshore platforms. To achieve this goal, extensive experimental campaigns are conducted on a truncated circular cylinder with a heave plate in the hydrodynamic and ocean engineering tank of Ecole Centrale Nantes. The study examines the hydrodynamic loads induced by mono- and bi-chromatic waves, as well as surge, heave, and pitch motions. Various diameters of the plates are studied also considering the porosity and proximity of the free surface across a wide range of flow parameters. Furthermore, a first-order analytical method based on the potential flow theory is developed to solve the wave diffraction and radiation problems. The validation is discussed in comparison with the experimental results and the Boundary Element Method (BEM) solvers. Lastly, dedicated computational fluid dynamics (CFD) simulations are carried out to model the heave plate numerically. It has been confirmed that a turbulence model needs to be implemented through flow visualization. Notably, the results show the presence of strong flow separation around the edge of the plate during the waves and heave oscillations. Consequently, a simplified Morison model is suggested to model the flow separation for the vertical wave diffraction loads.